The Acute and Chronic Effects of Palmitic Acid-Rich Triacylglycerols on Cardiovascular Risk

Filippou, Androulla

Awarding institution:
King's College London

Title: The Acute and Chronic Effects of Palmitic Acid-Rich Triacylglycerols on Cardiovascular Risk

Author: Androulla Filippou

Blood-CNS transport mechanisms in pathophysiology and drug delivery

Mehmet Fidanboylu

Institute of Pharmaceutical Science
King's College London

A thesis submitted for the degree of
Philosophiæ Doctor (PhD)
February 2013

Declaration by candidate

I, Mehmet Fidanboylu, hereby declare that this thesis is my own work and effort and that it has not been submitted anywhere for any award. Where other sources of information have been used, they have been acknowledged.

Signed:

Date:

The most exciting phrase to hear in Science, the one that heralds new discoveries, is not "Eureka!" but "That's funny..."

- Isaac Asimov

Abstract

The blood-CNS barriers form a highly selective biological firewall; regulating the passage of solutes between the blood and cerebral microenvironment. This thesis modelled the blood-CNS barriers *in vivo* to determine the transport of nutrients, metabolic products and drugs across these barriers, and was split into two main parts:

1. ***L*-arginine and ADMA transport** - Circulating levels of the cationic amino acid *L*-arginine and its endogenously produced homologue asymmetric dimethylarginine (ADMA) are in delicately poised equilibrium. Dysregulation of this balance has well-documented implications in cardiovascular disease and also more recently conditions of the brain, as ADMA is a potent inhibitor of nitric oxide synthase (NOS) enzymes, including the endothelial (eNOS) and neuronal (nNOS) isoforms. Until now it has been postulated that ADMA competes for transport across membranes *via* the same cationic transport system as *L*-arginine (system y^+), however this hypothesis has surprisingly never been tested.

The major contributors to transport of both amino acids were investigated to determine how their respective intracellular and extracellular concentrations affect transport across the blood-CNS barriers. These data also have strong relevance to other research areas due to the widespread influence of NO in physiological pathways in health and disease.

At the time of writing, this study represents the first true characterisation of ADMA transport across any physiological membrane *in vivo* and reveals a likely mechanism for explaining 'the *L*-arginine paradox' – the clinical observation that NO-deficient patients

respond well to oral supplementation with *L*-arginine even though $[\text{arginine}]_{\text{plasma}}$ is easily sufficient to saturate eNOS.

2. **'NanoHAT'** - Efflux transporters expressed at the blood-CNS barriers remain one of the biggest hurdles for the efficient delivery of therapeutic agents to the brain. The anti-trypanosomal drug pentamidine was shown previously by our group to be a substrate for efflux from the blood-CNS barriers and does not ordinarily accumulate to pharmacologically relevant levels in the brain. Pluronic® co-polymers are known biological response modifiers that are approved for use in humans and have generated a great deal of interest due to their ability to inhibit efflux transporters and spontaneously form micelles in solution. In this study, a co-formulation of pentamidine and Pluronic® P85 was evaluated as a potential future treatment for CNS-stage Human African Trypanosomiasis, using a combination of *in silico*, *in vitro*, and *in vivo* methodologies.

Combining our group's knowledge and expertise in blood-brain barrier research with colleagues in Molecular Biophysics and Materials & Molecular Modelling has resulted in the creation of a 'mini formulation-development pathway' that can be utilised to optimise and develop formulations in the future.

To my parents:

Thank you for your guidance, patience, encouragement, and especially for always asking why I hadn't got 100/100 in my tests at school! Anything I have ever achieved has been because of, and is dedicated to you both.

And to my fiancé, Simay:

Your persistent support throughout my rollercoaster ride over the past few years has been both a revelation and my inspiration. Thank you for being my ever-present crutch, and my biggest cheerleader – I couldn't have done it without you.

Acknowledgements

I would like to thank:

Dr Sarah A Thomas	Your expertise, support and sense of humour have made my PhD genuinely fun. I am massively grateful for your guidance in overcoming all of the challenges we were presented with, and for the opportunity to work in your lab. It has been exciting to see how the projects have evolved and I have many fond memories to look back on in the future.
Mr Murat Doğruel	One of the nicest, most genuine people I have ever met. Thank you for your wealth of experience and tips during the first months of my PhD. I hope we will keep in touch in the future.
Dr Christopher P Watson	My partner in crime for the three years our PhD studentships overlapped. It was a pleasure to share a lab and office with you, and to swap and share knowledge and plan experiments throughout.
Miss Ann-Charlott Berglar	The best MSc project student anyone could hope for – I'm very glad you are now pursuing a PhD project of your own!
Dr Cécile Dreiss	Thank you for your wisdom and guidance with all things Pluronic®.
Dr Margarita Valero	I sincerely appreciate your help in decoding the disparities and different expressions in calculating the biophysical properties copolymers.

Dr Christian Lorenz Thank you for the *in silico* simulations – these have provided and will continue to provide an incredibly valuable new dimension to our investigations.

Dr Shanta Persaud Your wise input in directing, planning and providing reagents for the islet toxicity experiments is much appreciated.

Dr Bo Liu Many thanks for your supervision when performing the islet toxicity experiments.

Dr Marie-Christine Jones Thank you for your provision of workspace and equipment for the zetasizing experiments.

Contents

List of Figures

List of Tables

Glossary

ABC ATP-binding cassette (superfamily of transporters)

AMT Adsorptive-mediated transcytosis

ADMA Asymmetric dimethylarginine

ARAMI *L*-arginine in acute myocardial infarction (a human clinical study)

atm Atmosphere (measure of atmospheric pressure)

ATP Adenosine-5'-triphosphate

BAATs Broad-scope amino acid transporters

CAATs Cationic amino acid transporters

BBB Blood-brain barrier

BCECs Brain capillary endothelial cells

BCH 2-aminobicyclo-(2, 2, 1)-heptane-2-carboxylic acid – specific inhibitor of system L and system $B^{0,+}$ transport

BCRP Breast cancer-resistance protein

BCSFB Blood-cerebrospinal fluid barrier

CAAs Cationic amino acids

CaM Calmodulin

CaMKII Calmodulin kinase II

CAT Cationic amino acid transporter

cDNA Complementary deoxyribonucleic acid

cGMP 3',5'-cyclic guanosine monophosphate

CHARMM Chemistry at HARvard Macromolecular Mechanics (a group of force fields used in molecular dynamics simulations)

CMC Critical micelle concentration

CNS Central nervous system

CSF Cerebrospinal fluid

CVO Circumventricular organ

DDAH *NG*,*NG*-dimethylarginine dimethylaminohydrolase

FAD Flavin adenine dinucleotide

FMD Flavin adenine mononucleotide

GABA γ-aminobutyric acid

GLUT Glucose transporter

GTP Guanosine triphosphate

H4B Tetrahydrobiopterin

hCMEC-D3 Human Cerebral Microvascular Endothelial Cell line (human *in vitro* model of the BBB)

hnRNP Heterogenous nuclear ribonuclear protein

ISF Interstitial fluid

$\boldsymbol{K_{in}}$ Unidirectional transfer constant

$\boldsymbol{K_m}$ Half-saturation constant

LAMMPS Large-scale Atomic/Molecular Massively Parallel Simulator (molecular dynamics simulations software)

***L*-NMMA** *NG*-monomethyl-*L*-arginine

LOX-1 Lectin-like oxidised low-density lipoprotein receptor-1

MCT Monocarboxylate transporter

MDR Multidrug resistance

MRI Magnetic resonance imaging

mRNA	Messenger ribonucleic acid
MRP	Multidrug resistance-related protein
NADPH	Reduced nicotinamide adenine dinucleotide phosphate
N_{agg}	Aggregation number (of micelle)
NBD	Nucleotide binding domain (sub-domain of P-glycoprotein)
NF-$\varkappa$B	Nuclear factor kappa B
NMDA	*N*-methyl-*D*-aspartate
NO	Nitric oxide
NOS	Nitric oxide synthase (of which there are endothelial, inducible and neuronal subtypes)
OAT	Organic anion transporter
OATP	Organic anion-transporting polypeptides
(ox-)LDL	(Oxidised) low density lipoprotein
P	Partition coefficient
P-gp	P-glycoprotein
PKC	Protein kinase C
PKG	Protein kinase G
PRMT	Protein arginine methyltransferase
RMT	Receptor-mediated trsanscytosis
SBP	Substrate-binding pocket (sub-domain of P-glycoprotein)
SDMA	Symmetric dimethylarginine
sGC	Soluble guanylate cyclase
SLC	Solute carrier (superfamily of transporters)
TEER	Trans-endothelial electrical resistance
TJs	Tight junctions
V_i	Initial volume of distribution
V_{max}	Maximal rate of transport
ZO	*Zonula occludens*, (of which there are -1, -2 and -3 isotypes), scaffold proteins found in tight junctional complexes

1

General Introduction

The central nervous system (CNS) represents the most significant development in the course of metazoan evolution. The abundance and diversity of animals that possess a CNS in some shape or form is testament to the evolutionary advantage that the CNS, and its ability to efficiently process information, confers. High fidelity neuronal signalling is enabled, in part, by the maintenance of a stable microenvironment in the immediate surroundings of the CNS. A high degree of homeostatic regulation of this microenvironment, and its separation from the highly variable and potentially neurotoxic contents of the blood, is brought about by the barriers of the CNS.

1.1 The barriers of the CNS

The barriers of the CNS can be thought of as a 'biological firewall' for the brain – tightly controlling movement of molecules and cells (both self and foreign) between the blood and compartments of the CNS. The barrier interfaces involved in this process are:

i. **The blood-brain barrier** – Separates the brain interstitial fluid (ISF) from blood.

ii. **The blood-cerebrospinal fluid barrier** – Separates the cerebrospinal fluid (CSF) from the choroid plexus ISF.

The main roles of these barriers are to prevent the free, unregulated movement of molecules between the brain fluids and blood, to provide specific transport routes for ions and essential nutrients required by the CNS, as well as the removal of metabolic waste products. The adult brain has very little potential for repair and regeneration, and thus protection from neurotoxic substances both in the blood and from metabolism is crucial. Both barriers display specific morphological features that contribute to these processes, and are described below.

1.1.1 The blood-brain barrier (BBB)

Evidence that a barrier may exist between the blood and the brain was first observed in 1885, when Ehrlich intravenously injected Trypan Blue and other intravital dyes into peripheral veins and arteries. Ehrlich found that the brain and other CNS tissues were poorly stained, while other organs were heavily stained ((Ehrlich, 1885), as cited in (Bradbury, 1993)). However, at this time, both Ehrlich and others incorrectly inferred from these data that internal organs merely had varying affinities for the different dyes. The concept of a barrier was not hypothesised until several years later, when it was observed by a student of Ehrlich that injecting Trypan Blue dye into the CSF resulted in only the brain being stained ((Goldman, 1913), as cited in (Bradbury, 1993)).

The crude light microscopy techniques of the time proved insufficient to identify the precise location of the blood-brain barrier (BBB). It was not until the development of scanning electron microscopes several decades later that light was shed onto the precise morphology of the cerebral vasculature and its associated molecular and cellular components.

1.1.1.1 Characteristics and components of the BBB

There are many features (either cellular or otherwise), at the blood-brain interface that could conceivably contribute to a ‘barrier-like’ phenotype - a basal lamina that is made up of type IV collagen, laminin and fibronectin, with pericytes embedded within its structure; astrocyte processes that intimately surround the basal lamina; and brain

capillary endothelial cells (**Figure 1-1**). This multi-faceted nature of the so-called 'neurovascular unit' initially led to a debate surrounding the precise location of the BBB. It was initially and correctly proposed to be at the brain capillary endothelium (Reese & Karnovsky, 1967), while other hypotheses suggested that the BBB-phenotype was due to astrocyte processes surrounding brain capillaries (Pappenheimer, 1970). This was definitively settled upon by demonstration of the low ion-conductance of brain capillary endothelium (Crone & Olesen, 1982), which has a net resistance of approximately 1900 $\Omega \cdot cm^2$ (compared to resistance as low as 1-2 $\Omega \cdot cm^2$ in some peripheral capillaries).

Important anatomical features that help distinguish brain capillary endothelial cells (BCECs) from endothelial cells found elsewhere in the body are outlined here, and detailed in the sections that follow:

A. Presence of complex tight junctions
B. Adherens junctions
C. Lack of fenestrations
D. Minimal pinocytotic activity
E. High mitochondrial content
F. Enzyme activity

Sections that follow these relate to the additional cellular and non-cellular components of the neurovascular unit shown in **Figure 1-1**:

G. Basal lamina and basement membrane
H. Astrocytes
I. Pericytes
J. Microglia

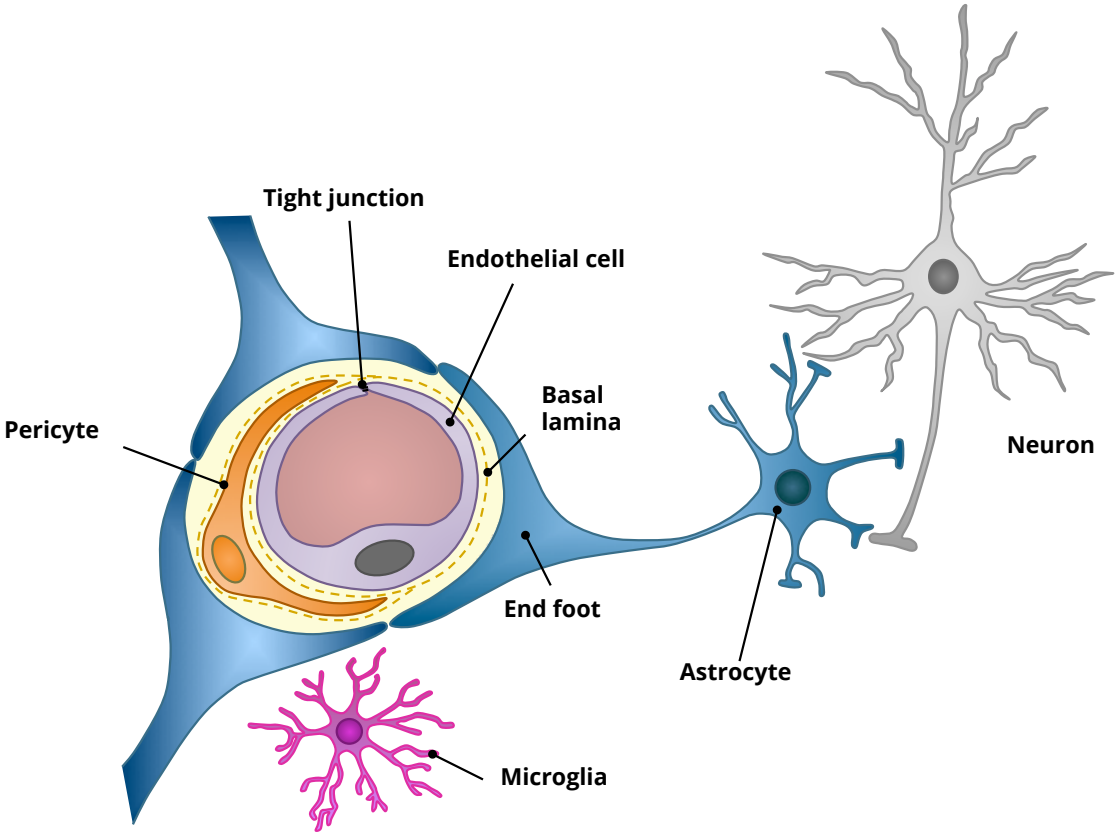

Figure 1-1: The neurovascular unit. The neurovascular unit is composed of several cell types in close association, working together to maintain optimal brain function. Cerebral endothelial cells, the building blocks of the BBB, form tight junctions that restrict the paracellular pathway. Pericytes partially envelop the endothelial cells and share a common basal lamina with them. Astroglial end-feet ensheath the microvessel wall; astrocytes are important in barrier induction and provide links to neurons. Microglia are CNS resident immune cells. Modified, with permission, from Dr S Yusof.

1.1.1.1A Presence of complex tight junctions

The low ion-conductance of the brain capillary endothelium relative to endothelia elsewhere in the body is predominantly due to the presence of tight junctions (TJs) between adjacent BCECs (Romero *et al.*, 2003). In addition to limiting paracellular permeability to ions and other polar compounds, a secondary function of TJs is to separate the membranes of brain capillary endothelial cells into the brain (abluminal) and blood (luminal) sides (van Meer & Simons, 1986); facilitating the spatial segregation of functionally distinct lipids (Tewes & Galla, 2001) and proteins (Betz & Goldstein, 1978; Betz *et al.*, 1980) (including transporters). TJs are intricate structures that span the intercellular space between BCECs, and are formed by a complex of transmembrane proteins and cytoplasmic accessory proteins that both cluster the transmembrane proteins and serve as a platform for interacting signalling and scaffold proteins (**Figure 1-2**). TJs are found throughout the whole of the paracellular cleft in BCECs.

The transmembrane components of TJs include the proteins occludin, claudins and junctional adhesion molecules (JAMs).

Occludin is a 60-65 kDa protein with four transmembrane domains, two extracellular loops and three cytoplasmic domains (two of which are the N- and C-terminal domains (Furuse *et al.*, 1993). It is the extracellular loops that confer the occluding function of occludin, and particularly the second loop that determines the trans-endothelial electrical resistance (TEER) (Feldman *et al.*, 2005). The C-terminal domain consists of 150 amino acids, and associates with the scaffold proteins *zonula occludens* (ZO)-1, ZO-2 and ZO-3 for anchoring to the actin cytoskeleton (Fanning *et al.*, 1998), and regulatory proteins such as protein kinase C (Andreeva *et al.*, 2006). Occludin contains many phosphorylation sites on the hydroxyl groups of serine and threonine residues, with phosphorylation or dephosphorylation of these sites regulating the association of occludin with ZO proteins and consequently its membrane localisation (Andreeva *et al.*, 2001; Kale *et al.*, 2003). The N-terminal domain of occludin also has an integral role in the assembly of TJs, as its deletion in BCEC monolayers grown *in vitro* results in low

TEER values and increased paracellular permeability to small polar molecules (Bamforth *et al.*, 1999).

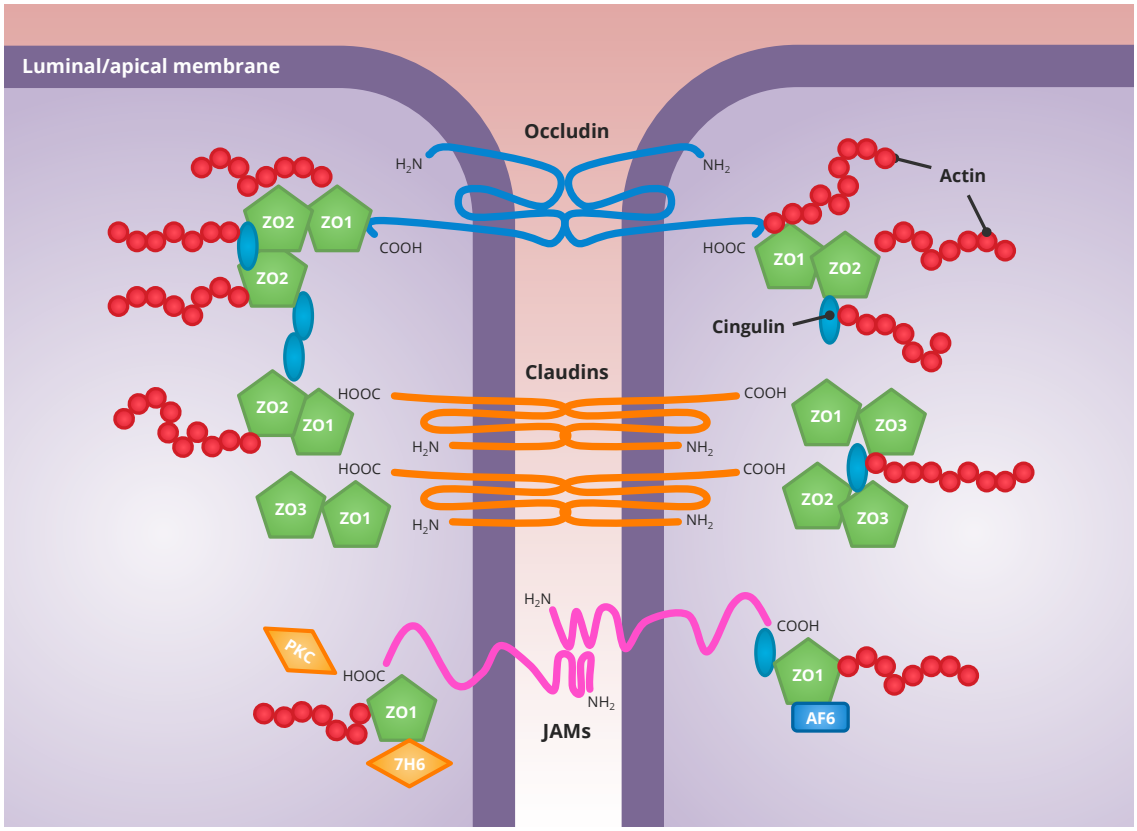

Figure 1-2: Simplified schematic representation of the tight junctional complex found between the majority of brain capillary endothelial cells. Transmembrane proteins occludin, claudins and JAMs span the intercellular cleft between adjacent endothelial cells. Scaffold ZO and cingulin proteins are closely associated and facilitate anchoring to the actin cytoskeleton and myosin, while additional regulatory proteins such as protein kinase C (PKC), 7H6 and AF6 are involved in the regulation of TJ assembly.

Claudins are another essential structural component of TJs, and a multi-gene family of 2024 kDa transmembrane proteins, of which 24 have been identified in mammals (Furuse *et al.*, 1998). Sequence and structural homology within the claudin family is highly conserved; with four transmembrane domains, two extracellular loops and two cytoplasmic domains (a long C-terminal sequence, and short N-terminal sequence) (Heiskala *et al.*, 2001). It is thought that the baseline seal of TJs arises from claudins, which is then augmented by occludin, since overexpression of claudins in fibroblasts results in TJ-like strands, and occludin only localizes to the TJ if claudin is also present (Kubota *et al.*, 1999). Similar to the case with occludin, the C-terminal domain of

claudins also binds ZO proteins (as shown in **Figure 1-2**). The extracellular loops of claudins from neighbouring cells can interact either via homophilic (Piontek *et al.*, 2008) or heterophilic (Furuse *et al.*, 1999) interactions within a single TJ. It is the extracellular loops that determine the charge and size selectivity for paracellular permeability, and it is thought that differences in the claudin content between the BBB and BCSFB could explain why TEER values for the BBB are typically significantly higher than those observed for the BCSFB (Matter & Balda, 2003; Van Itallie & Anderson, 2004). It is generally accepted that claudins 3, 5, and 12 are present at the BBB; while there is some evidence that claudin 1 may also be present (Morcos *et al.*, 2001; Nitta *et al.*, 2003; Wolburg *et al.*, 2003). It should be noted that while TJ strands can be formed without occludin (Balda *et al.*, 1996; Saitou *et al.*, 1998), the absence of claudin-5 at the BBB in double knockout (-/-) mice results in a size-selective increase in paracellular permeability to molecules with a molecular weight of less than 800 Da (Nitta *et al.*, 2003). The identity of claudins present in TJs at the BCSFB will be discussed in ***section 1.1.2.1 - The choroid plexuses***.

JAMs belong to the immunoglobulin superfamily and have a single transmembrane domain, a single extracellular domain, extracellular N-terminal domain and cytoplasmic C-terminal domain (Bazzoni & Dejana, 2004) (**Figure 1-2**). JAMs form homophilic and heterophilic interactions with other JAMs on neighbouring cells to form dimers (Bazzoni *et al.*, 2000). The C-terminal domain of JAMs typically associates with ZO-1, cingulin, junction-associated protein (AF6), tight-junction-associated protein antigen (7H6) and other scaffold proteins (Itoh *et al.*, 2001), while also containing residues that are phosphorylated by protein kinase C (Suzuki *et al.*, 2002). It is thought that phosphorylation of JAMs may be involved in the recruitment of ZO proteins and occludin into TJ complexes (Bazzoni & Dejana, 2004), while scaffold proteins such as cingulin promote binding to the actin cytoskeleton, which can also bind directly to both claudin and occludin (Huber *et al.*, 2001).

1.1.1.1B Adherens junctions

Adherens junctions at the BBB, like TJs, are formed between adjacent endothelial cells. In contrast to TJs however, adherens junctions are formed through associations between cadherins and catenins; transmembrane proteins which in turn bind actin (Vestweber, 2008). Adherens junctions form a paracellular 'zipper-like' structure along the cell border (Dejana, 2004), and in the case of endothelial cells typically contain vascular endothelial (VE)-cadherin (Bazzoni *et al.*, 2000). Adherens junctions are not unique to endothelial cells, but appear to have a critical function in the assembly of TJs and function of BCECs. Binding of VE-cadherin in adherens junctional complexes has been shown to result in the modulation of TJs by both inhibiting FoxO1 activity (a repressor of claudin-5 transcription) and by sequestering β-catenin (a stabiliser of FoxO1 activity) (Taddei *et al.*, 2008). Furthermore, β-catenin has been shown to directly control claudin gene expression – a process that is dependent on the Wnt signalling pathway (Liebner *et al.*, 2008).

1.1.1.1C Lack of fenestrations

Fenestrations are ultramicroscopic pores in the plasma membranes of endothelial cells that facilitate the rapid but non-specific exchange of molecules between blood vessels and surrounding tissues. Fenestrations are present in highly permeable tissues such as the glomerulus (Deen *et al.*, 2001). However, fenestrations are very scarcely found in BCECs – no doubt an adaptation to prevent the non-specific transcellular movement of polar molecules between the blood and brain, as was demonstrated with the molecule, α-aminoisobutyric acid (Fenstermacher *et al.*, 1988).

1.1.1.1D Minimal pinocytotic activity

Pinocytosis is a form of endocytosis, whereby extracellular fluid (and any contents) is taken up by the cell in a non-specific manner following membrane invagination. Since un-regulated, non-specific uptake of solutes is undesirable at the BBB, it is easy to imagine that pinocytic activity at the BBB is low. Indeed, this has been demonstrated by a number of different studies (Brightman & Reese, 1969; Sedlakova *et al.*, 1999).

However, it should be noted that increased pinocytic activity is frequently observed at the BBB in pathological conditions (Tuomanen *et al.*, 1985; Kondo & Suzuki, 1993).

1.1.1.1E High mitochondrial content

Endothelial cells of the BBB have been found to contain a significantly higher density of mitochondria relative to other endothelial cells elsewhere in the body (Oldendorf & Brown, 1975), or indeed non-BBB endothelia in the brain (Fenstermacher *et al.*, 1988). It has been proposed that this confers a large capacity for work, since this greater density of mitochondria can be expected to have a higher output of ATP production (Oldendorf *et al.*, 1977). Indeed, BCECs are highly metabolically active (see ***section 1.1.1.1F - Enzyme systems*** below), and also express a large number of transport systems, some of which require energy either directly (primary active transport) or indirectly (secondary active transport); making use of ion gradients that are maintained by energy-requiring ion pumps (see ***section 1.2 - Transport across the BBB***).

1.1.1.1F Enzyme systems

In addition to serving as a physical barrier (as described above in ***sections A-D***), the BBB also serves as a metabolic (enzymatic) barrier. This is an important consideration in the design of CNS drugs, since metabolism often leads to pharmacological inactivation, and ultimately elimination from the circulation. While drug metabolism primarily falls under the remit of the hepatic and renal systems, it is known to also occur at the level of the BBB (el-Bacha & Minn, 1999). Extracellular (ecto-) enzymes such as peptidases and nucleotidases that respectively metabolise peptides and ATP have been described at the BBB (el-Bacha & Minn, 1999). Furthermore, both phase I enzymes (*e.g.* cytochrome P450-1A and -2B) and phase II enzymes (*e.g.* glutathione S-transferase and UDP-glucouronosyltransferase) have been identified at the BBB in both rodents and humans (Strazielle & Ghersi-Egea, 2005).

1.1.1.1G Basal lamina and basement membrane

BCECs are completely encompassed by a basal lamina – a perivascular extracellular matrix excreted by BCECs typically between 40-50 nm thick. The basal lamina is predominantly made up of collagen IV, heparin sulphate, laminin, fibronectin, tenascin

and proteoglycans secreted by endothelial cells (Farkas & Luiten, 2001). The basal lamina is a constituent of the basement membrane, which is composed of two layers; one separating pericytes from endothelial cells, while the other compartmentalises pericytes from astrocyte endfeet in the neurovascular unit (**Figure 1-1**). The basement membrane is regulated and maintained by pericytes (Kose *et al.*, 2007).

1.1.1.1H Astrocytes

Astrocytes are star-shaped glial cells, with multiple cytoplasmic fibrils predominantly made up of glial acidic fibrillary protein (Walz, 2000). Two distinct types of astrocytes are typically found in the CNS:

i. **Type-1** – Protoplasmic astrocytes, mainly located in grey matter, with fewer cytoplasmic filaments, which are not stained by the A2B5 antibody (Black *et al.*, 1993)
ii. **Type-2** – Fibrous astrocytes, mainly located in white matter, with numerous cytoplasmic filaments, which are positively stained by the A2B5 antibody (Black *et al.*, 1993)

As was alluded to earlier, astrocytes are intimately associated with BCECs; so much so that it was initially astrocytic end-feet that were proposed to be directly responsible for the 'physical barrier' element of the BBB phenotype (De Robertis & Gerschenfeld, 1961). This hypothesis was later discounted on the observation that horseradish peroxidase did not penetrate the luminal walls of the brain microvasculature when injected *i.v.*, but could diffuse through the 20 nm gaps between astrocyte end-feet to reach the abluminal surface of the endothelium if injected directly into the brain (Brightman & Reese, 1969). Several discoveries since these early experiments lead to the re-examination of the role of astrocytes in the induction and maintenance of the BBB.

Astrocytes are the most abundant cell of the human brain, and do not initiate or propagate action potentials along their processes, despite expressing potassium and sodium channels (Nedergaard *et al.*, 2003; Seifert *et al.*, 2006). Astrocytes do, however,

exhibit an inducible increase in the intracellular concentration of Ca^{2+} ions, which is thought to be of functional significance in astrocyte-astrocyte and astrocyte-neuron communication (Cornell-Bell *et al.*, 1990; Charles *et al.*, 1991).

One of the earliest astrocytic functions to be described was the homeostatic maintenance of CNS ion concentrations – particularly K^+ (Kuffler *et al.*, 1966). Astrocytic processes are also involved in neurotransmitter homeostasis; clearing neurotransmitters from the synaptic space *via* specific transporters for glutamate, γ-aminobutyric acid (GABA) and glycine. It is believed that these neurotransmitters are first converted into precursors by enzymes in the astrocytes, before recycling back into the synaptic space for uptake and reconversion by neurons (Seifert *et al.*, 2006).

Astrocytes are also known to provide metabolic support for surrounding cells - storing glycogen granules particularly in regions of high synaptic density (Phelps, 1972). These glycogen stores have been shown to be necessary and sufficient to sustain neurons in hypoglycaemic conditions; a process that is modulated by glutamate (Brown & Ransom, 2007). Other studies have shown that astrocytic glycogen can be broken down into lactate and transferred to neuronal synapses or axons (Voutsinos-Porche *et al.*, 2003; Brown *et al.*, 2004; Brown & Ransom, 2007).

Astrocytes also have an integral role in the developing brain, as molecular boundaries formed by astrocytes are required to guide the growth of developing neuronal axons and neuroblasts (Powell & Geller, 1999). There is also accumulating evidence that astrocytes are required for the maturation of the neuronal synapse during synaptogenesis, a role mediated *via* the release of extracellular signalling molecules such as thrombospondin (Christopherson *et al.*, 2005; Barres, 2008). More recently, astrocytes have been implicated in the regulation of breathing *via* the release of ATP in response to physiological decreases in pH (Gourine *et al.*, 2010).

Astrocytes are more recently implicated in the regulation of cerebral blood flow at a local level. In making such a large number of contacts with cerebral blood vessels, astrocytes are ideally positioned to directly influence the perivascular milieu; releasing

known regulators of vascular tone, such as prostaglandins, nitric oxide, and arachidonic acid (Gordon *et al.*, 2007). It has also been proposed that astrocytes are responsible for regional changes in cerebral blood flow due to synaptic activity – indeed, astrocytes have been directly implicated in changes in blood flow in the visual cortex following visual stimulation, as detected by fMRI (Schummers *et al.*, 2008; Wolf & Kirchhoff, 2008).

In context of the astrocytic influence on BBB development, there is strong *in vitro* evidence to suggest that astrocytes are involved in the induction of the BBB phenotype (Beck *et al.*, 1984; Abbott *et al.*, 2006; Savidge *et al.*, 2007). Conversely, there are some aspects of the BBB that become functional during CNS development *in vivo* before the appearance of astrocytes (Haseloff *et al.*, 2005), and embryonic neural progenitor cells induce BBB properties in BCECs (Weidenfeller *et al.*, 2007).

1.1.1.1l Pericytes

Pericytes were first described almost 150 years ago (Diaz-Flores *et al.*, 2009), but their functions are only just beginning to become clearer. Pericytes are found within the basal lamina, often in close association to BCECs (**Figure 1-1**), and are attached to extracellular matrix proteins of the basal lamina *via* integrins (Stratman *et al.*, 2009). Pericytes are morphologically distinct from BCECs by virtue of their nuclei – pericytes have a circular nucleus, while endothelial cells have an elongated nucleus (Dore-Duffy & Cleary, 2011). Pericytes can also form gap junctions with endothelial cells, created by the mutual expression of connexin-43 (CX43) in the plasma membranes, facilitating the intercellular transfer of nutrients, metabolites, secondary messengers and ions (Bobbie *et al.*, 2010).

An integral role for pericytes in BBB development has recently come to light, where it was demonstrated that BBB formation early in embryonic development coincides with the recruitment of pericytes, before the differentiation of astrocytes from progenitor cells (previously thought to be responsible for induction of the BBB phenotype) (Daneman *et al.*, 2010). Pericytes are now known to be crucial for the development of TJs, and the downregulation of transcytosis – two highly characteristic features of the

BBB (Daneman *et al.*, 2010). The same study, which utilised pericyte-deficient mice, has revealed that pericytes are required for the downregulation of genes linked to increased vascular permeability that are ordinarily attenuated at the BBB, including as plasmalemma vesicle-associated protein (*Plvap*) and angiopoietin-2 (*Angpt2*) (Daneman *et al.*, 2010). Other genes that appear to be downregulated by pericytes at the BBB during development include intercellular cell adhesion molecule 1 (*Icam1*), and activated leukocyte adhesion molecule (*Alcam*) – implying that pericytes also suppress the infiltration of immune cells into the CNS (the proinflammatory responses of which could stunt the development of the BBB) (Daneman *et al.*, 2010). Interestingly, the development of other characteristic features of the BBB, such as the high expression of the glucose transporter, GLUT-1, appear unaffected by the absence of pericytes (Armulik *et al.*, 2010).

The involvement of pericytes in the maintenance of BBB integrity appears to continue through to adulthood and even the aging CNS (Bell *et al.*, 2010). The loss of pericytes during adulthood results both in increased paracellular transport due to the breakdown of TJs, and also increased transendothelial fluid flow (Bell *et al.*, 2010). Furthermore, the study also identified that the loss of pericytes in adult mice resulted in increased in the CNS-infiltration of blood-derived macrophages, and eventual complete loss of some cerebral capillaries, as is observed in the aging human brain (Bell *et al.*, 2010). However, in contrast with the reported differences in gene expression during embryogenesis described above, a loss of pericytes does not appear to result in the upregulation of genes such as *Icam1*.

Pericytes have long been hypothesised to be involved in the control of capillary blood flow - likely mediated by their stellate-shaped, finger-like processes that are wrapped around the capillary wall – however this has only recently been confirmed experimentally (Peppiatt *et al.*, 2006; Bell *et al.*, 2010). This process is likely regulated by contractility mediated by Ca^{2+} influx into the pericyte (Kamouchi *et al.*, 2004), possibly stimulated by the binding of receptors to endothelin-1, vasopressin or

angiotensin II, which are all known to be expressed on the cell surface of pericytes (Diaz-Flores *et al.*, 2009; Hamilton *et al.*, 2010).

1.1.1.1J Microglia

The BBB is a major contributing factor in creating an "immunoprivileged" environment for the CNS, and while immune cells can transmigrate from the blood into the brain under certain conditions, the primary form of active immune defence in the CNS are the microglia. Microglia make up approximately 20% of the total glial cell population in the brain and serve as the resident macrophages (Lawson *et al.*, 1992). Microglia survey the CNS for plaques, damaged cells and foreign bodies, all of which can be phagocytosed before presenting antigens to T-cells (Gehrmann *et al.*, 1995).

1.1.2 The blood-cerebrospinal fluid barrier (BCSFB)

The blood-cerebrospinal fluid barrier (BCSFB) separates the CSF from the choroid plexus ISF, and is made up of the choroid plexuses and arachnoid membrane, described in the following sections.

1.1.2.1 The choroid plexuses

There are four choroid plexuses in total – one in each of the lateral ventricles (I and II), one in the third ventricle (III) and one in the fourth (IV), just beneath the cerebellum. The implication of the choroid plexuses in some barrier function between the blood and CSF was first hypothesised almost 100 years ago, when Trypan Blue dye was found to stain the choroid plexuses when injected systemically, while the rest of the CNS remained unstained ((Goldman, 1913), as cited in (Bradbury, 1993)).

1.1.2.1A Choroid plexus structure

The barrier function of the choroid plexuses is secondary to the main function of secreting CSF, and this is reflected in the morphology of the choroid plexuses. At the macro level, the choroid plexuses are formed from invaginations of the *pia mater* – the innermost layer of the meninges, and are made up of several villous processes (**Figure 1-3**). The choroid plexuses float within the CSF, and are attached to the ventricular ependyma by a stalk. The ependyma is a continuation of the epithelial layer of the choroid plexuses, formed by a single layer of modified cuboidal epithelial cells filled with mitochondria (Del Bigio, 1995), forming approximately 15% of the total cytoplasmic volume in primates (Cornford *et al.*, 1997). Within each villus is a single capillary branched from either the anterior or posterior choroidal arteries, however, unlike capillaries of the BBB, endothelial cells of the choroid plexus capillaries are termed as being "leaky", since they are fenestrated, do not have any TJs, and thus do not contribute to the barrier function of the BCSFB.

The apical (brain-facing) surface of choroid plexus epithelial cells are densely coated with microvilli, with very few kinocilia (Strazielle & Ghersi-Egea, 2000). This is a

distinguishing feature of epithelial cells from the ependymal cells, which have a large number of kinocilia, and very few microvilli (Scott *et al.*, 1974). The surface area of the plasma membrane between the lateral walls of choroid plexus epithelial cells is increased by the presence of infoldings, which are particularly discernible at the basolateral (blood-facing) side of the epithelial cell layer (Keep & Jones, 1990).

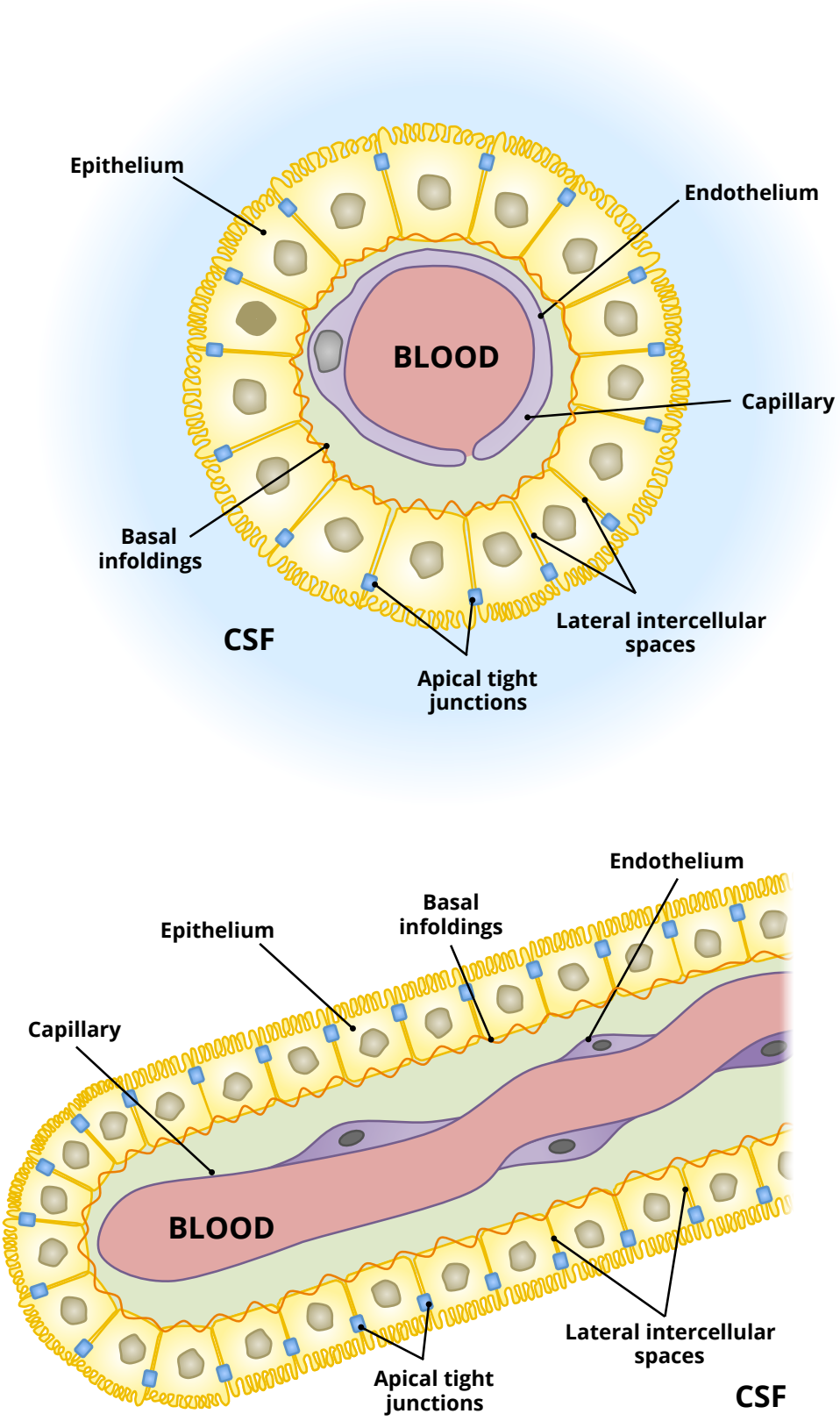

Figure 1-3: Cross-section (top) and longitudinal (bottom) views of a single villus of the choroid plexus. Endothelial cells are shown in purple and epithelial cells in yellow.

1.1.2.1B Barrier characteristics

While choroid plexus epithelial cells are not as finely tuned to serving as a barrier as BCECs, they do display both structural and metabolic characteristics that confer barrier properties to the choroid plexus. As with BCECs, the primary anatomical adaptation preventing the paracellular diffusion of molecules between choroid plexus epithelial cells are TJs, which form a continuous fence at the choroid plexus (Brightman & Reese, 1969). However, in contrast to BCECs, TJs do not line the entire paracellular cleft of choroid plexus epithelium; and are located only between the apical (CSF-facing) side of the epithelial cells (Brightman & Reese, 1969). In structural terms, the components of TJs between choroid plexus epithelia are very similar to those already described between brain capillary endothelia (***section 1.1.1.1A - Presence of complex tight junctions***), with the most obvious differences being in the claudins. The most abundant claudin in choroid plexus epithelial cell TJs is claudin-3 (Wolburg *et al.*, 2009), however claudins 1, 2 and 11 are also expressed to complete the full repertoire in mice (Wolburg *et al.*, 2001). Thus far, only claudin-1 has been characterised at the apical side of the human choroid plexus (Anstrom *et al.*, 2007). The difference in claudins may explain the lower TEER value for the choroid plexus epithelium, which has been recorded at approximately 24 Ω cm^2 *in vivo* in the bull frog (Zeuthen & Wright, 1981). Measurement of choroid plexus TEER *in vivo* is technically difficult to achieve, however, measurements taken from cultured mouse choroid plexus epithelial cells estimate TEER values of between 150-200 Ω cm^2 (Zheng & Zhao, 2002). The "leaky" description of choroid plexus endothelial cells can therefore also be applied to the epithelial cells, at least when comparing to BCECs, since paracellular permeability is significantly higher at the choroid plexus epithelium, as demonstrated by the ability of lanthanum ions to cross from the blood into the ventricular lumen, but not between BCECs (Bouldin & Krigman, 1975). TJs between choroid plexus epithelial cells do, however, appear to prevent paracellular flux, since large proteins such as horseradish peroxidase in the blood have been shown to permeate through the capillary walls, and fill the extracellular space of the choroid plexus stroma; diffusing up to, but not beyond the apical TJs (Reese *et al.*, 1971).

The choroid plexuses, like the BBB, are also active as enzymatic barriers; containing enzymes that break down xenobiotics into less toxic or less pharmacologically-active products (Strazielle *et al.*, 2004). Since drug metabolising enzymes are expressed at significantly higher levels in the choroid plexuses relative to the brain cortex, it has been hypothesised that the BCSFB may play a more prominent role in the detoxification of the CNS than the BBB (Ghersi-Egea *et al.*, 1994). The rabbit, mouse and human choroid plexus epithelium has been shown to contain enzymes that metabolise monoamine neurotransmitters (monoamine oxidase and catechol-o-methyltransferase) (Lindvall & Owman, 1980; Kalaria *et al.*, 1988; Vitalis *et al.*, 2002), in addition to other enzymes that are more implicitly associated with drug metabolism (*i.e.* cytochrome P-450, uridine-5'-diphosphoglucuronosyl transferase and glutathione-S-transferases) (Cammer *et al.*, 1989; Volk *et al.*, 1991; Johnson *et al.*, 1993; Ghersi-Egea *et al.*, 1994; Philbert *et al.*, 1995).

1.1.2.1C CSF secretion

CSF fills the ventricles of the brain, subarachnoid spaces, and around the spinal cord; serving to mechanically and immunologically protect the brain, as well as in the autoregulation of cerebral blood flow. CSF has slightly altered concentrations of Na^+, K^+, Cl^- and Ca^{2+}, but far lower protein levels relative to plasma, and was originally thought to merely be an ultrafiltrate of plasma. It is now clear that CSF is not an ultrafiltrate, and is in fact actively secreted by the choroid plexuses (Ernst *et al.*, 1986; Speake *et al.*, 2001). The total volume of CSF in humans is estimated at 140-150 mL, a volume that is completely replaced four times each day, placing total daily CSF production at approximately 600 mL (Wright, 1978).

CSF secretion is facilitated by a polarised distribution of ion transporters in the apical and basolateral membranes of choroid plexus epithelial cells working in concert to bring about the net movement of ions across the epithelium. This creates an osmotic gradient favouring the movement of water into the cerebral ventricles; a process that is driven by the pump (Na^+/K^+)-ATPase, which is expressed in the membranes of the microvilli at the apical surface of the choroid plexus (Ernst *et al.*, 1986).

Following secretion by the choroid plexuses, CSF circulates around the CNS, before being reabsorbed into the venous system *via* the *superior saggital sinus* (**Figure 1-4**). CSF from the lateral ventricles flows into the third ventricle, through the cerebral aqueduct and then into the fourth ventricle. From here, the fluid passes through median and lateral apertures (not shown in **Figure 1-4**), to the *cisterna magna* before circulating into the cerebral and spinal subarachnoid spaces. The flow of CSF is not continuous, but more pulsatile in nature. This is thought to ensure the one-way flow of CSF from the subarachnoid spaces into the venous sinuses, and is linked to arterial pulse pressure (Takizawa *et al.*, 1986a; Takizawa *et al.*, 1986b).

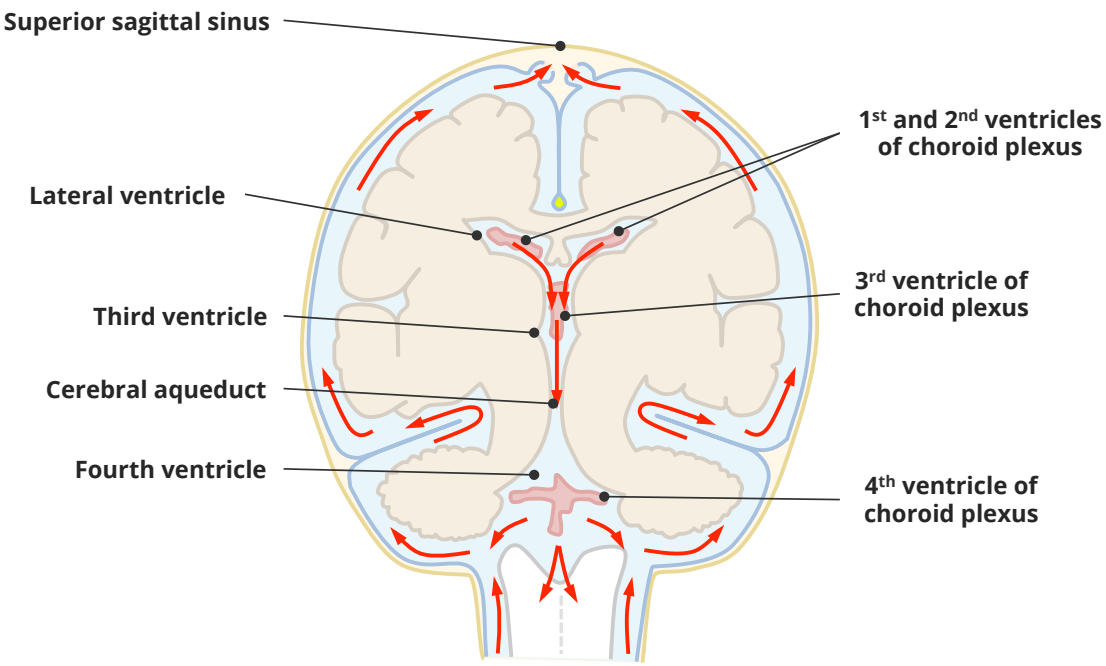

Figure 1-4: Circulation of CSF. CSF (blue) is secreted by the choroid plexuses (which are located in the cerebral ventricles), before circulating through the ventricular cavities and entering the subarachnoid space.

1.1.2.2 The arachnoid membrane

The arachnoid membrane lies beneath the *dura mater* and above the *pia mater*, collectively known as the meninges. The arachnoid membrane is the only member of the three meninges that contributes to the blood-CSF barrier, and contains TJs between the outermost arachnoid epithelial cells (closest to the *dura mater*) (Nabeshima *et al.*, 1975). Early studies have demonstrated amino acid transport at the arachnoid membrane in both mammals (Wright *et al.*, 1971; Lorenzo & Snodgrass, 1972) and amphibia (Wright, 1974). However, its relatively low surface area compared to that of the choroid plexuses and BBB suggests that the overall contribution of the arachnoid membrane to the transport of amino acids into the brain is low.

1.1.3 The circumventricular organs (CVOs)

Circumventricular organs (CVOs) are excluded from the BBB and are characterised by their extensive vasculature (Fry & Ferguson, 2007). The endothelium of CVOs closely resembles that of the choroid plexus, where the 'leaky' capillaries serve to aid their function – namely to either secrete substances (*e.g.* hormones (Macchi & Bruce, 2004)), or detecting chemical signals in the blood (*e.g.* area postrema detecting toxins in the blood to induce vomiting (Brizzee & Neal, 1954)). The choroid plexus is sometimes considered as a CVO due to its similarities in terms of vasculature and fenestrated capillaries, however this is debatable since the choroid plexus does not contain the neural tissues that CVOs do (Cottrell & Ferguson, 2004). CVOs include the *area postrema*, *organum vasculosum* of the *lamina terminalis*, subfornical organ, subcommissural organ, pituitary gland, median eminence and pineal gland, however, (due to the ease of locating these tissues) only the pineal and pituitary glands were studied for the purposes of this thesis.

1.1.3.1 Pineal gland

The morphology and location of the pineal gland varies greatly among mammals. The human pineal gland is located within 1-2 mm of the midline of the brain, and weighs between 100-180 mg (Macchi & Bruce, 2004), while the pineal gland in mice were typically found to weigh up to 300 µg (MF, personal observations). The pineal gland is highly vascularised and is supplied by branches of the posterior choroidal arteries derived from cerebral arteries in the posterior mesencephalon (Macchi & Bruce, 2004). Innervation of the pineal gland includes both the peripheral parasympathetic and sympathetic systems, as well as nerve fibres from the CNS (Wurtman & Axelrod, 1965).

The main function of the pineal gland is the secretion of the hormone melatonin in a circadian manner, in response to stimulation by the suprachiasmatic nuclei, which is regulated by light/dark cycles (Macchi & Bruce, 2004). A role for the pineal gland in

reproduction is also hypothesised, since pineal tumours can affect sexual development (Macchi & Bruce, 2004).

1.1.3.2 Pituitary gland

The pituitary gland can be divided into two lobes – the anterior lobe and posterior lobe (Steel & Polak, 1997). While technically not a part of the brain, the pituitary gland is connected to the hypothalamus *via* a stalk-like structure called the infundibular stem. Indeed, the posterior lobe of the pituitary gland develops from the hypothalamus itself, and is located just below the hypothalamus, in the sella turcica of the sphenoid bone at the base of the skull (Amar & Weiss, 2003). Collectively, the anterior and posterior lobes of the pituitary gland are involved in maintaining homeostasis and influencing the activity of other glands (Amar & Weiss, 2003) *via* the secretion of signalling molecules such as oxytocin and vasopressin produced by the hypothalamus (Steel & Polak, 1997).

1.2 Transport across the BBB

Estimates of the total length of perfused cerebral vasculature in the adult human brain have been placed at approximately 600-700 km (Zlokovic, 2005). No single neuronal cell body is ever further than 15 µm from a capillary (Tsai *et al.*, 2009). The total surface area formed by brain capillaries has been calculated to be approximately 100-150 cm^2 g^{-1}, which when scaled up to a typical adult brain mass of 2 kg equates to 20-30 m^2 (Begley & Brightman, 2003). This constitutes a massive surface for the exchange of molecules between the blood and brain ISF.

It was initially proposed that metabolites passively diffuse through the BBB by facilitative transport alone, and that the saturation of these transporters was responsible, in part, for the regulation of brain metabolism (Pardridge, 1983). It has since emerged that there are several routes by which a molecule can cross the BBB; summarised in **Figure 1-5**.

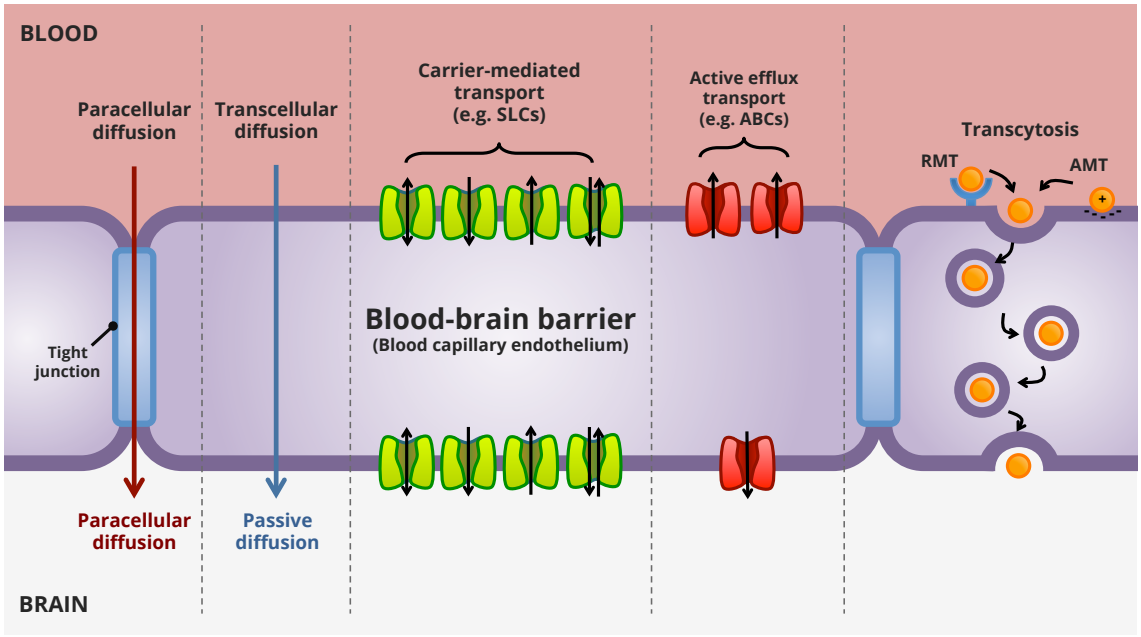

Figure 1-5: Simplified schematic diagram summarising possible routes of crossing the blood-brain barrier. Paracellular movement of hydrophilic molecules is typically blocked by tight junctions. Small lipophilic (lipid-soluble) molecules and some gases can diffuse across the plasma membranes of the capillary endothelial cells. Transport can be facilitated by transport proteins embedded in the plasma membrane that can be bi-directional, uni-directional, symport or antiport in their transport activity, and with varying degrees of ion-dependence. Efflux transporters such as P-glycoprotein (P-gp) are also known to exist at the blood-brain barrier and are vital in contributing to the metabolic barrier phenotype. Transport across the blood-brain barrier can also be receptor-mediated (RMT) in the case of insulin or transferrin, or absorptive-mediated (AMT) through electrostatic interactions between positively charged substances and the negatively charged glycocalyx.

1.2.1 Paracellular diffusion

Paracellular diffusion relates to the movement of water-soluble molecules by passive diffusion through the intercellular space between cells, largely driven by electrochemical, hydrostatic and osmotic gradients. Low paracellular permeability of the BBB is predominantly maintained by TJs, which form a balance between the contractile forces generated at the endothelial cytoskeleton, and the adhesive forces between TJ proteins of neighbouring cells to exclude the passage of polar molecules through the BBB (Garcia & Schaphorst, 1995; van Hinsbergh & van Nieuw Amerongen, 2002). The increase in paracellular permeability at the BBB resulting from the breakdown of TJs is observed in a large number of CNS diseases (Hawkins & Davis, 2005).

1.2.2 Transcellular diffusion

Since the paracellular route from the blood into the brain is essentially blocked by TJs, any molecular traffic across the BBB is forced to go through the cell, *via* the so-called transcellular route. Any molecules utilising the transcellular route across the BBB are required to cross both the luminal and abluminal plasma membranes of BCECs, and thus passive transcellular diffusion is restricted to small lipophilic molecules (*e.g.* ethanol) and gases (*e.g.* O_2 and CO_2) (Abbott *et al.*, 2006).

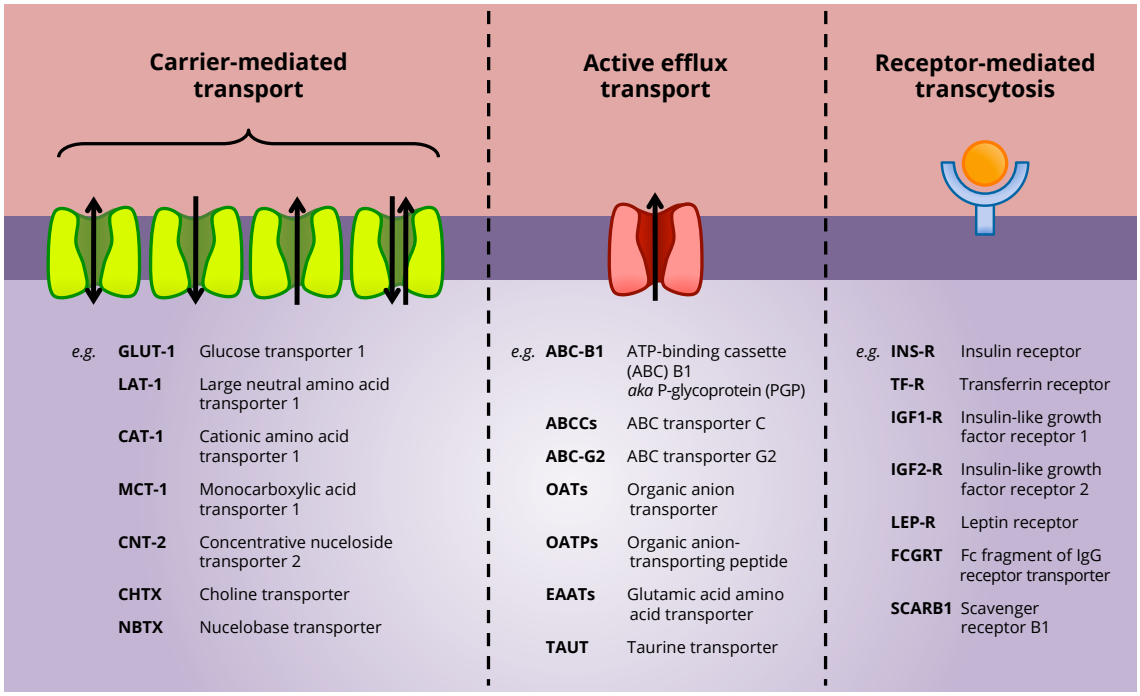

Figure 1-6: Examples of proteins involved in transport mechanisms at the BBB. The transport of many essential polar molecules such as amino acids and glucose is mediated by carrier-mediated transporters belonging to the solute carrier (SLC) transporter family. These transport mechanisms can either be facilitated (reliant on substrate concentration gradients) or secondarily active (utilising electrochemical/ion gradients), and can be bi-directional, uni-directional (influx or efflux), or exchangers. Active efflux transporters utilise ATP hydrolysis to pump substrates out of the cell. Receptor-mediated transcytosis involves the binding of substrates that are typically large proteins, such as insulin, which initiates vesicular transport across the cell. The list of proteins shown here are not exhaustive.

1.2.3 The solute carrier transporters

The result of forming a restrictive barrier between the brain and blood is that many metabolites and nutrients required for normal neuronal function (*e.g.* glucose) do not permeate the BBB and therefore rely on selective transport systems (**Figure 1-6**). Transport proteins are expressed throughout the neurovascular unit, and are not restricted to BCECs or the choroid plexus epithelium. Since the primary focus of this thesis is transport displayed by these two cell types (and their contribution to BBB and BCSFB transport respectively), the reader is referred to reviews elsewhere for transporter expression in other parts of the neurovascular unit (Neuwelt *et al.*, 2011).

Nutrient transport at the BBB is mainly mediated by the solute carrier transporters (SLCs), which constitute a super-family of 46 different sub-groups, totalling over 380 proteins in humans (Hoglund *et al.*, 2011). SLC transporters can either be facilitated transport carrier proteins or secondary active transporters. Facilitated transport involves the movement of molecules or ions across the plasma membrane through specific membrane transporters, and is an energy-independent process only enabling the movement of substances down their concentration gradient. Secondary active transporters (sometimes referred to as co-transporters or counter-transporters) utilise the electrochemical ion gradients across the membrane to transport molecules in the same (symport or co-transport) or opposite (antiport or counter-transport) direction as the ion flux. This is distinct from primary active transport, as it does not involve the direct hydrolysis of ATP.

As described in ***section 1.1.1.1A - Presence of complex tight junctions***, the existence of TJs at the BBB creates two distinct membrane domains (luminal and abluminal); facilitating the spatial segregation of functionally distinct lipids (Tewes & Galla, 2001) and proteins, including transporters (Betz & Goldstein, 1978; Betz *et al.*, 1980). SLC transporters can have either a polarised expression (either luminal or abluminal), or be expressed on both membranes (Abbott, 2002; Abbott *et al.*, 2010). The most highly expressed SLC transporter at the BBB is glucose transporter 1 (GLUT-1, encoded by the *SLC2A1* gene), no doubt reflecting the brain's requirement

for a constant supply of energy (Pardridge *et al.*, 1990). Indeed, it has recently been shown that the expression of GLUT-1 is a crucial checkpoint in the development of the BBB *in vivo* (Zheng *et al.*, 2010). GLUT-1 is expressed at both the luminal and abluminal membrane of BCECs, and has also been detected intracellularly (Harik *et al.*, 1990; Farrell & Pardridge, 1991). It is thought that intracellular GLUT-1 may be mobilised to the membranes as a response to hypoglycaemia (Simpson *et al.*, 1999). As with many of the SLC transporters, GLUT-1 displays a high-degree of substrate specificity, to the stereoisomeric level; transporting *D*-glucose, 2-deoxyglucose, 3-*O*-methyl-glucose, galactose and mannose, but not *L*-glucose (Pardridge & Oldendorf, 1975b).

While the CNS has a high demand for glucose obtained *via* GLUT-1 from the systemic circulation, it appears that glial cells and neurons have differing preferences for their energy source. Glial cells appear to be almost totally dependent on glucose for ATP production, while neurons also metabolise lactate (Pellerin & Magistretti, 2003). It is thought that after being transported across the BBB by BCECs, glucose is broken down into lactate by astrocytes, and then released into the ISF before being taken up by surrounding neurons, the so-called "lactate shuttle hypothesis" (Pellerin & Magistretti, 2003). Neurons have previously been shown to be dependent on lactate for migration during development, since the inhibition of lactate transport in neonatal mice caused extensive disorganisation of the parietal cortex attributed to irregular cortical neuronal migration and neuronal cell death (Adle-Biassette *et al.*, 2007). Lactate is transported by monocarboxylate transporters (MCTs); four of which have been detected in the brain (MCT-1, -2, -4 and -8) (Bergersen, 2007). In the process described above, the release of lactate by astrocytes into the ISF is mediated by MCT-4, and its uptake into neurons by MCT-2 (Bergersen, 2007). Transport of lactate across the BBB is mediated by MCT-1 (encoded by *SLC6A1*), which is expressed at both the luminal and abluminal membranes of BCECs (Bergersen *et al.*, 2001). MCT-8 is also expressed in BCECs, where it mediates transport of thyroid hormones (Roberts *et al.*, 2008b).

SLC transporters at the BBB that display broader substrate-specificities include the organic anion transporters (OATs) and organic anion-transporting polypeptides (OATPs). OATs belong to the SLC22 family of transporters, functioning as secondary active transporters for the movement of organic anions against chemical and ion gradients (VanWert *et al.*, 2010). OATs such as OAT-3 have been identified as key transporters involved in the transport of pharmaceutical small molecules at the BBB, (VanWert *et al.*, 2010). OATPs, are also secondary active transporters, but are sodium-independent, and typically transport large, amphipathic compounds such as bile salts, thyroid hormones and steroid conjugates (Russel *et al.*, 2002). OATP1-A4 has been detected at both the luminal and abluminal membranes of the BBB in rats, and OATP1-A5 on mainly the abluminal membrane (Roberts *et al.*, 2008b; Westholm *et al.*, 2008). In humans OATP1-A2 and –B1 are both expressed at the luminal membrane of BCECs (Bronger *et al.*, 2005). The thyroid hormone transporter, OATP1-C1 is also expressed at the human BBB, but its membrane localisation is still elusive (Eyal *et al.*, 2009).

Amino acid transporters constitute a large proportion of SLCs expressed at the BBB. These will be discussed in greater detail in ***Chapter 2***, with a particular focus on the transport of cationic amino acids across the BBB and BCSFB.

1.2.4 The ATP-binding cassette family of transporters

The ATP-binding cassette (ABC) family of transporters is made up of three sub-families:

i. **Multidrug-resistance proteins** (MDRs) – ABCB-1 to -11, including P-glycoprotein (P-gp).
ii. **Multidrug resistance-related proteins** (MRPs) – ABCC1-5.
iii. **Breast cancer-resistance proteins** (BCRPs) – ABCG1-8.

ABC transporters are multidomain integral membrane proteins that are found in all mammalian species (Jones & George, 2004). Substrates for the ABC transporters vary

from small ions to large peptides, but a common feature shared by ABC transporters is their utilisation of energy obtained through ATP hydrolysis to change the confirmation of their transmembrane domains; resulting in the transport of substrate typically against its concentration gradient (Begley, 2004). ABC transporters typically act as efflux pumps – removing substrate from cells – and thus their precise membrane localisation at the BBB is an important consideration when elucidating their function.

1.2.4.1 P-glycoprotein

One of the most important and best characterised of all ABC transporters is P-gp, which is mainly expressed at the luminal membrane of the BBB in both humans and rodents – efficiently removing a broad range of substrates that may have crossed the luminal membrane (Roberts *et al.*, 2008a; Eyal *et al.*, 2009). It has been shown that P-gp substrates can be as small as 0.3 kDa and as large as 4 kDa (Ramachandra *et al.*, 1998; Lam *et al.*, 2001), but most are hydrophobic and partition into the lipid bi-layer (Gottesman & Pastan, 1993; Gatlik-Landwojtowicz *et al.*, 2006).

P-gp, also known as MDR-1 (**Figure 1-6**) is encoded by the *ABCB1* gene in humans, and *abcb1a* and *abcb1b* genes in mice (Cordon-Cardo *et al.*, 1989; Begley, 2004). Both *abcb1a* and *abcb1b* share up to 87% sequence homology with human *ABCB1* (Ng *et al.*, 1989), and the functional significance of the two rodent isoforms is unclear, since the single MDR-1 isoform in humans appears to fulfil the functions of the two rodent isoforms (Demeule *et al.*, 2002). It should be noted that of the two rodent isoforms, only *abcb1a* is expressed in endothelial cells (Schinkel *et al.*, 1997), while *abcb1b* appears to be localised to the brain parenchyma (Regina *et al.*, 1998), with regional variation (Kwan *et al.*, 2003; Karssen *et al.*, 2004). Analysis of the mouse BBB transcriptome revealed that *abcb1a* mRNA was very highly expressed in the brain microvasculature (Linnet & Ejsing, 2008). P-gp has traditionally been recognised to be important for drug disposition and response (Silverman, 1999; Lin, 2004), and are a particularly difficult hurdle to overcome in the efficient delivery of drugs to the brain (Pardridge, 2005). However, more recent findings indicate that BCRPs may play a more significant role at the human BBB, while P-gp is more important at the murine

BBB (Uchida *et al.*, 2011). This is discussed in greater detail in ***section 1.2.4.3 - Breast cancer-resistance proteins***.

1.2.4.1A Structure and function

P-gp is a 170 kDa complex molecule, made up of 1280 amino acids in the human, and 1276 amino acids in the mouse. It is made up of two similar halves that have 43% sequence homology with each other and are joined by a flexible linker region (**Figure 1-7**) (Gottesman & Pastan, 1993). The protein contains a total of 12 hydrophobic transmembrane regions that span the membrane, and intracellular N- and C-termini (Higgins *et al.*, 1997). Two nucleotide-binding domains (one for each half of the protein) confer the ability of P-gp to bind and hydrolyse ATP and contain highly conserved amino acid sequences – the Walker motifs. The sequence of the Walker motifs are highly specific and do not tolerate mutations without completely abolishing the ATP-hydrolysing capacity and thus the overall transport function of the protein (Muller *et al.*, 1996). Similarly, mutations in the linker region between the two halves also result in a loss of transport activity (Currier *et al.*, 1989).

It has been inferred from photoaffinity probe-binding studies and site-specific mutation studies that the substrate-binding sites of P-gp are in close proximity to transmembrane regions V and VI, and XI and XII (Bruggemann *et al.*, 1989; Schurr *et al.*, 1989; Greenberger, 1993). However, a study that more recently observed that the substrate specificity and activity of P-gp can be changed by substituting specific amino acids in both transmembrane and intracellular regions outside these 4 domains – suggesting the relationship between the structure and function of P-gp is complex (Lin & Yamazaki, 2003).

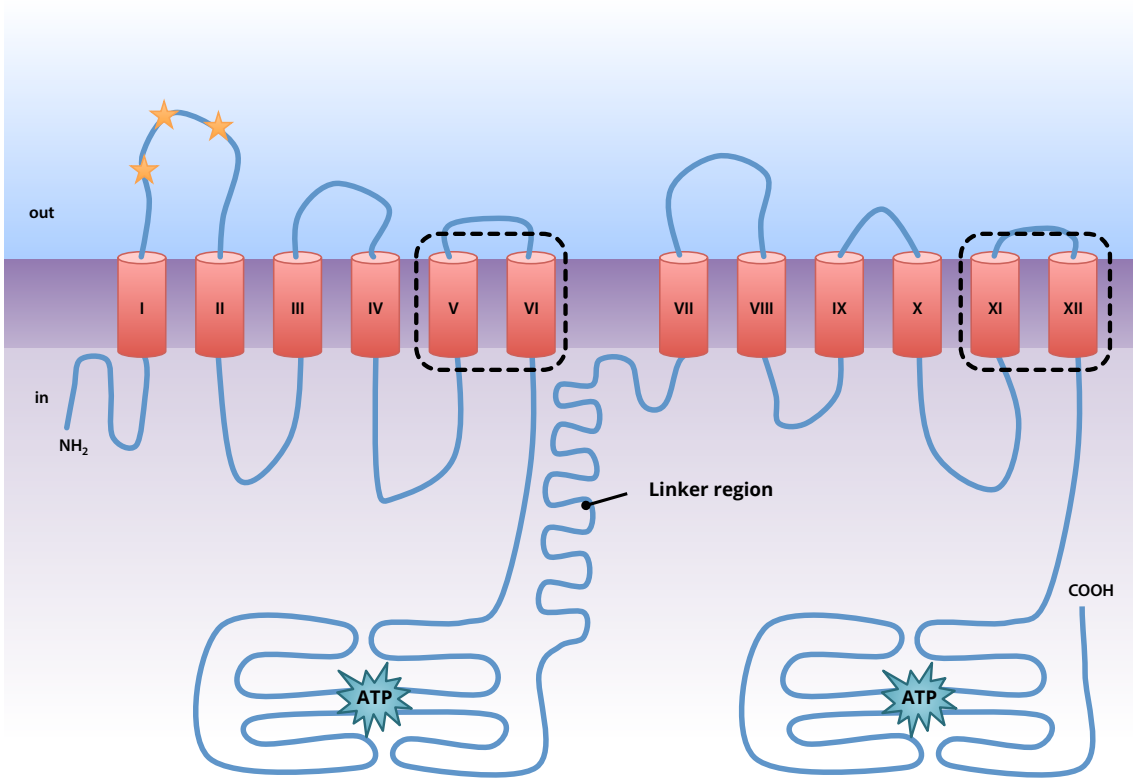

Figure 1-7: Putative structure of P-gp, with 12 predicted transmembrane regions (red cylinders). Glycosylation sites on the extracellular loop between transmembrane regions I and II are represented by orange stars. The black dotted lines represent intramembrane binding sites (domains V and VI, and XI and XII). ATP binds to two intracellular nucleotide binding domains known as the Walker motifs.

Two models have been proposed to describe the mechanism for substrate efflux from cells by P-gp – the 'hydrophobic vacuum cleaner' model and 'flippase' model (Shapiro & Ling, 1997; Aller *et al.*, 2009; Colabufo *et al.*, 2010). According to the 'hydrophobic vacuum cleaner' model, P-gp sucks in substrate from the plasma membrane and ejects it from the cell through the central pore. In the 'flippase' model, P-gp detects substrate in the inner leaflet of the plasma membrane, binds the substrate, and extrudes it from the cell by 'flipping' it orientation with respect to the phospholipids in the inner and outer leaflets of the plasma membrane. It has most recently been proposed that the reality for P-gp activity may be a combination of both models, shown in **Figure 1-8** (O'Brien *et al.*, 2012).

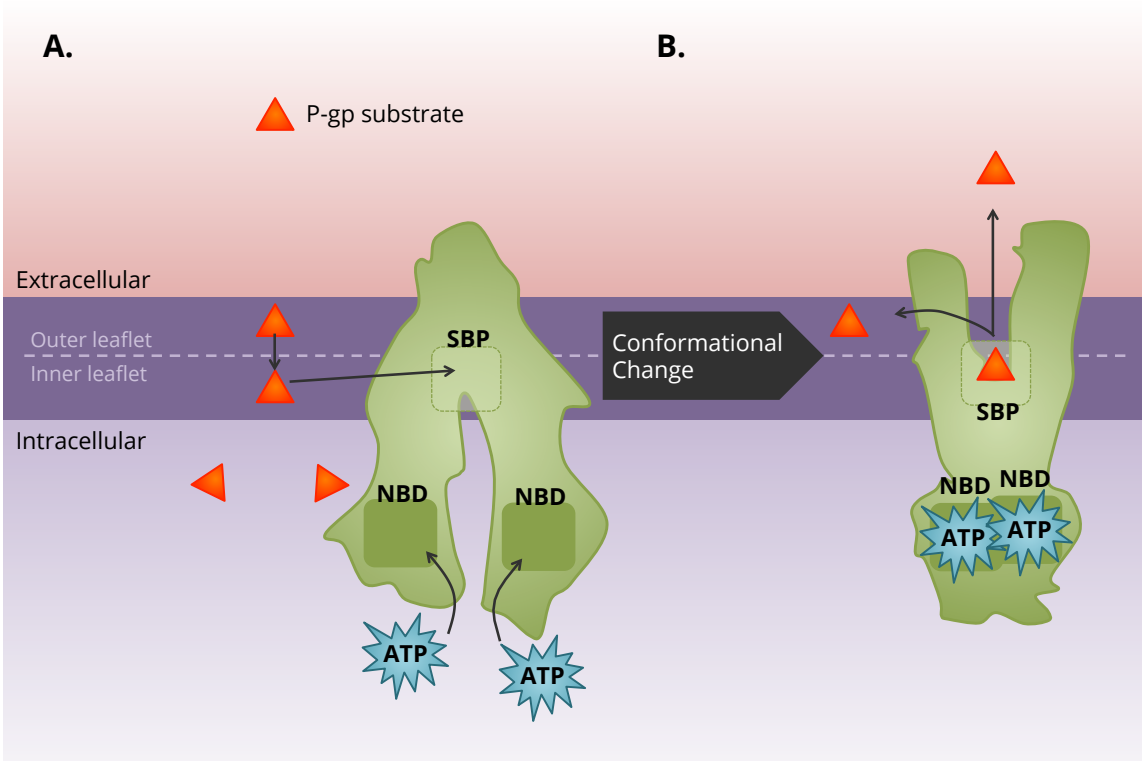

Figure 1-8: Hypothetical model of P-gp substrate transport. A). The default conformation of P-gp (primed to bind substrate) is shown. A large cavity of approximately 6000 Å^3 constitutes the substrate-binding pocket (SBP), and is lined with hydrophobic and aromatic amino acid residues. Lipid-soluble substrates for P-gp partition into the inner leaflet of the plasma membrane, before passing through pores made up of transmembrane regions V &VI or XI & XII to reach the SBP. Once the SBP has been bound, two molecules of ATP bind to the nucleotide-binding domains (NBD). **B).** ATP binding causes a conformational change in the protein that brings the NBDs together, and facilitates the release of substrate out of the cell, or back into the outer leaflet. Adapted from (O'Brien *et al.*, 2012).

While there is no clear chemical characteristic that marks a molecule out as a P-gp substrate, they are typically compounds that are hydrophobic and or amphipathic in nature (Schinkel, 1999). It has become apparent that a large number of substrates are shared between P-gp and drug-metabolising enzymes expressed at the BBB, such as the cytochrome P450 enzymes CYP2D6 (Uhr *et al.*, 2004) and CYP3A (Wacher *et al.*, 1995). Based on these observations a recent hypothesis has been proposed relating to a possible co-operation between P-gp and drug-metabolising enzymes – the 'drug transporter-metabolism alliance' hypothesis (Benet, 2009). It is thought that by preventing drug substrates from passing through the BBB in their intact form, P-gp

creates a cycle where the molecules passively diffuse into the BCEC before being ejected by P-gp. On each cycle, a portion of the drug molecules may be broken down by drug-metabolising enzymes, while intact molecules are recycled back out of the cell by P-gp (Benet, 2009).

1.2.4.2 Multi-drug resistance-related proteins

The multidrug resistance-related protein (MRP) family is made up of 9 members, encoded by the genes *ABCC1-9* in humans (Bernacki *et al.*, 2008). Of these 9 members, MRP-4, -5, -8 and -9 have a similar overall structure to P-gp, with two distinct domains comprised of 6 transmembrane regions each (12 in total). As per P-gp, these MRPs have two NBDs (Chen & Tiwari, 2011). The remaining MRPs (MRP-1, -2, -3, -6 and -7) have the same two overall domains, and a third domain made up of an additional 5 transmembrane regions (17 in total), although the function of this domain is unclear (Begley, 2004).

MRPs typically transport organic anions and neutral organic compounds, and sometimes require co-factors such as glutathione to mediate their efflux activity (Deeley & Cole, 2006; Deeley *et al.*, 2006). MRPs and P-gp have overlapping substrate specificity, and their activity is sometimes difficult to distinguish (Seelig *et al.*, 2000), although it has been noted that MRPs tend to display a preference for organic anions or drugs that are conjugated to glutathione or glucuronate in the CNS (Minn *et al.*, 2002).

The expression of MRPs in the context of the BBB is not as clearly defined as that for P-gp described in the previous section. Some authors have suggested that MRP-1 is present and active at the BBB in removing drugs from the brain (Sugiyama *et al.*, 2003), while others have detected no change in the efflux of the MRP-1 substrate fluorescein from the brain in MRP-1 knockout mice (Sun *et al.*, 2001). Since MRP-1 expression (usually apical) does not typically overlap with P-gp expression (usually basolateral) in polarised cells, it has been theorised that the same would be true at the BBB (Cisternino *et al.*, 2003). For the same study it was deemed that abluminal expression of MRP-1 would result in transport of MRP-1 substrates into the CNS, as

MRP-1, like P-gp, is an efflux transporter (removing substrates from cells). *In situ* brain perfusion with several MRP-1 substrates failed to detect MRP-1 at the mouse BBB (Cisternino *et al.*, 2003). In contrast to MRP-1, MRP-2, -4 and -5 have all been detected at the luminal membrane of BCECs (Eyal *et al.*, 2009), while MRP-3 has only been detected in the capillaries supplying brain tumours (Calatozzolo *et al.*, 2005).

1.2.4.3 Breast cancer-resistance proteins

The best-characterised transporter belonging to the breast cancer-resistance protein (BCRP) family is encoded by *ABCG2*, and was first discovered in a chemotherapy-resistant breast cancer cells line (Schinkel & Jonker, 2003). However, there is no evidence to suggest that the expression of BCRP is specific to breast cancer cells, or indeed that BCRP plays a significant role in the development of chemotherapy-resistance in breast cancer (Schinkel & Jonker, 2003). Unlike MRPs and P-gp, BCRP is made up of only one domain made up of six transmembrane regions and a single NBD; putatively functioning as a homodimer (Bernacki *et al.*, 2008).

BCRP expression has been detected mainly at the luminal surface of BCECs in pigs (Eisenblatter *et al.*, 2003), mice (Cisternino *et al.*, 2004), and humans (Cooray *et al.*, 2002). There was initially some debate surrounding the degree of expression of BCRP at the BBB, with some groups detecting greater levels of BCRP than P-gp (Eisenblatter *et al.*, 2003), and others finding that the opposite is true (Dauchy *et al.*, 2008). In any case, BCRP expression in BCECs has been found to be three times higher in P-gp deficient mice, suggesting that BCRP compensates for a lack of P-gp at the BBB (Cisternino *et al.*, 2004). Most recently, a comparison of transporter and receptor protein expression at the BBB found that BCRP is expressed at significantly higher levels than P-gp at human BBB, while the opposite is true at the murine BBB (Uchida *et al.*, 2011). The implications of this difference in expression likely indicate a disparity in the relative contributions of the transporters to drug efflux from the brain between species.

1.2.5 Endocytosis

Endocytosis is the process by which cells take up molecules by engulfing them, and in the context of endothelial cells, can be divided into three categories:

i. **Pinocytosis** – Also known as fluid- or bulk-phase endocytosis, where extracellular fluid (and any contents) is taken up by the cell in a non-specific manner following membrane invagination (downregulated in BCECs, see ***section 1.1.1.1D - Minimal pinocytotic activity***).
ii. **Adsorptive endocytosis** – Initiated when solutes bind to the cell surface and are internalised following non-specific, electrostatic interactions.
iii. **Receptor-mediated endocytosis** – Initiated where solutes bind to cognate receptors expressed in the plasma membrane *via* specific receptor-ligand interactions.

Across these categories, there are two underlying mechanisms or types of vehicles – clathrin-coated pits and caveolae. Clathrin-coated pits are vesicles with a diameter of approximately 200 nm formed by coating of the plasma membrane with the electron-dense protein, clathrin (Mousavi *et al.*, 2004). The coating of clathrin on the plasma membrane is a vital step in the recruitment of a number of accessory proteins to the plasma membrane, and the formation of vesicles (Mousavi *et al.*, 2004). The degree of plasma membrane coating with clathrin is high in BCECs, and particularly at the luminal membrane, implying that clathrin-dependent endocytosis particularly for the uptake of solutes in the blood, predominates at the BBB (Simionescu *et al.*, 1988). The coating of plasma membrane with clathrin creates an anionic microenvironment, and thus it is thought that clathrin-coated pits are primarily responsible for adsorptive endocytosis following interaction with cationic moieties in solutes (Herve *et al.*, 2008).

Caveolae are a form of lipid raft, forming an omega- (Ω-) shaped invagination of the plasma membrane typically 50-100 nm in diameter (Anderson, 1998). The scaffolds for caveolae formation are created by caveolins, a family of three integral membrane proteins – caveolin-1, -2 and -3 (Scherer *et al.*, 1996; Tang *et al.*, 1996; Williams & Lisanti, 2004). It is thought that caveolae are comparatively much fewer in number

than clathrin-coated pits at the BBB (Herve *et al.*, 2008), however this may be due to the fact that the size of caveolae make them difficult to detect by electron microscopy, particularly since BCECs *in vivo* are typically only 500 nm thick (from luminal to abluminal membranes) (Abbott *et al.*, 2010). Despite this apparent low number of caveolae at the BBB, it is known that caveolae are a crucial component in the increase in BBB permeability in pro-inflammatory conditions due to internalisation of both claudin-5 and occludin (Kirkham & Parton, 2005; Stamatovic *et al.*, 2009). It is thought that the mechanism underlying these changes in permeability may be through interactions between caveolin-1 and endothelial nitric oxide synthase (eNOS), since caveolin-1 deficient mice display increased eNOS activity (Drab *et al.*, 2001) resulting in downregulation of ZO-1 (Song *et al.*, 2007).

1.2.6 Transcytosis

Transcytosis is a form of vesicular transport that differs from endocytosis by virtue of the fact that during transcytosis vesicles are transported across the cell (from one polar side to the other). The underlying mechanisms of transcytosis initiation are identical to endocytosis, and thus it is hardly surprising that two kinds of transcytotic vesicles have been found to originate from the luminal membrane of BCECs: the caveolae and clathrin-coated pits (Herve *et al.*, 2008).

Transcytosis across the BBB *via* endocytotic/vesicular mechanisms is the main route by which macromolecules such as proteins can enter the CNS. Both specific and non-specific transcytotic mechanisms exist at the BBB – termed receptor-mediated transcytosis (RMT) and adsorptive-mediated transcytosis (AMT), respectively. RMT involves the binding of macromolecular ligands to specific receptors expressed in the plasma membrane of BCECs, resulting in the initiation of endocytosis (Abbott *et al.*, 2010). After a complex is formed between the receptor and ligand a caveolus is formed that pinches off into a vesicle, internalising both the ligand and the receptors. Vesicles are then shuttled across to the opposite pole of the cell by the cytoskeleton, before releasing the contents *via* exocytosis.

In contrast, AMT is initiated by charge interactions of strongly cationic molecules with negatively charged cell surface binding sites, rather than any receptor-ligand interactions (Sauer *et al.*, 2005).

For both mechanisms, the transcytosis of intact protein or peptide requires the avoidance of the lysosomal compartment of the cell, which would result in degradation. Routing away from lysosomes appears to be a unique feature of the BBB endothelium, where there is a stronger requirement for the transcytosis of intact macromolecules (relative to peripheral endothelia) (Mukherjee *et al.*, 1997; Nag & Begley, 2005).

1.3 Transport across the BCSFB

As discussed in ***section 1.1.2 - The blood-cerebrospinal fluid barrier (BCSFB)***, the absence of TJs between endothelial cells, 'looser' TJs that exist between epithelial cells, and increased fenestrations result in a 'leaky' BCSFB relative to the BBB, with increased paracellular permeability. This considered, other transport mechanisms do still exist at the BCSFB, with any differences to the BBB detailed below.

1.3.1 SLC transporters

The concentration of glucose in the CSF is approximately half that of glucose in plasma – creating a concentration gradient that favours transport into the CSF. Glucose transport across the BCSFB was first demonstrated in the sheep choroid plexus, and found to be Na^+-independent (Deane & Segal, 1985). GLUT-1 expression has been detected at both the apical and basolateral membranes of the choroid plexus epithelium in rats, mice and rabbits, with a much stronger presence in the basolateral membrane (Gerhart *et al.*, 1989; Harik *et al.*, 1990). Furthermore, the membrane of the choroid plexus endothelium is highly enriched with GLUT-1 (Cornford *et al.*, 1998). Data pertaining to the expression of either GLUT-2 or GLUT-3 in the choroid plexus epithelium have proved inconclusive (Fields *et al.*, 1999; Arluison *et al.*, 2004). Hexokinase-1, the high-affinity enzyme responsible for the first step of glucose metabolism, is highly expressed in the choroid plexus epithelium (Fields *et al.*, 1999). Therefore, it would appear that, while GLUT-1 expression at the BBB serves the purpose of providing the brain as a whole with its main source of energy, glucose transport at the choroid plexus is more in line with satisfying the metabolic needs of the choroid plexus itself. Interestingly, GLUT-1 does not appear to be expressed in the pineal gland (Argandona *et al.*, 2005), but is expressed in the pituitary gland in rats, at least at the mRNA level (Koehler-Stec *et al.*, 2000).

In terms of monocarboxylate transporters, the choroid plexus epithelium expresses MCT-8 at the apical surface, where it is thought it is mainly responsible for the transport of thyroid hormone (Roberts *et al.*, 2008b). MCT-1 is also expressed, with a similar non-polarised distribution between the apical and basolateral membranes (as previously described for the BBB); but at significantly lower levels relative to BCECs (Leino *et al.*, 1999). A third monocarboxylate transporter, MCT-3, is also expressed at the choroid plexus and is theorised to be involved in the regulation of lactate levels in CSF (Philp *et al.*, 2001).

The cellular localisation of OATP transporters in the choroid plexus epithelium has been determined by immunohistochemistry; revealing that OATP1-A4 is the most abundant OATP transporter at the BCSFB (Zhang *et al.*, 2010) and is expressed in the basolateral membrane (Gao *et al.*, 1999), while OATP1-A5 is expressed in the apical membrane (Kusuhara *et al.*, 2003). OATP2-B1 and OATP1-C1 have also both been detected in the choroid plexus epithelium at the mRNA and protein levels (Choudhuri *et al.*, 2003). While the precise cellular localisation of OATP2-B1 at the BCSFB is currently unknown, OATP1-C1 is known to be located mostly at the basolateral membrane, mediating thyroid hormone transport (Roberts *et al.*, 2008b).

OAT transporters are also present at the BCSFB, with OAT-1 and OAT-3 confirmed to be located apically at the choroid plexus epithelium, and OAT-2 is expressed as mRNA (Choudhuri *et al.*, 2003). Meanwhile, OCT-1, -2 and -3 have also been detected at the mRNA with unknown cellular localisations (Choudhuri *et al.*, 2003).

Amino acid transporters are also expressed at the BCSFB, and will be detailed in ***chapter 2***.

1.3.2 ABC transporters

There is some debate surrounding the expression of P-gp at the BCSFB. Some studies have detected P-gp in the human and rodent choroid plexus (Rao *et al.*, 1999; Daood *et al.*, 2008), while others have found that P-gp expression is low or even completely non-existent (Nies *et al.*, 2004; Gazzin *et al.*, 2008). Where P-gp was detected, the

localisation of expression was placed at the apical (CSF-facing) side of the choroid plexus epithelium, and in sub-apical intracellular compartments (Rao *et al.*, 1999). This implies that the direction of P-gp substrate transport favours transport back into the CSF, in contrast to the function of P-gp at the BBB as preventing blood-borne substrates from reaching the brain described in ***section 1.2.4.1 - P-glycoprotein***. Similarly, BCRP is also present at the apical membrane of the choroid plexus epithelium in mice (Tachikawa *et al.*, 2005).

In further contrast to the BBB, the most abundant efflux transporter at the BCSFB is MRP-1 (encoded by *ABCC1*), found in the basolateral membrane of the choroid plexus epithelium (Rao *et al.*, 1999). MRP-4 has also been detected at the basolateral membrane of the human choroid plexus epithelium (Nies *et al.*, 2004), while MRP-5 may also be present (at least at the transcriptional level) (Lee *et al.*, 2004).

1.3.3 Transcytosis

Transcytosis across the BCSFB was initially hypothesised to be non-existent after the observation that the endocytosis of a number of tracers at the basolateral side robustly resulted in their degradation by lysosomes (van Deurs, 1980). This reaffirmed the observations that intraventricular injection of horseradish peroxidase (at the apical side of the rat choroid plexus) overwhelmingly led to its endocytic delivery to lysosomes (van Deurs *et al.*, 1978). Since these early observations, receptor-mediated transcytosis of the peptide hormone leptin following formation of a complex with low-density lipoprotein receptor-related protein 2 (LRP2) has been detected through the choroid plexus epithelium (Dietrich *et al.*, 2008). LRP2 is also putatively involved in the clearance of β-amyloid from the CSF, as Alzheimer's patients appear to have reduced levels of LRP2 at the choroid plexus (Alvira-Botero & Carro, 2010). These most recent studies appear to indicate the existence of bi-directional transcytotic mechanisms at the BCSFB.

2

Cationic amino acid transport across the mouse blood-CNS barriers

2.1 Introduction

Despite making up only 2% of the body by mass, the human brain receives 15% of the cardiac output, 20% of total oxygen consumption, and 25% total glucose utilisation (Herculano-Houzel, 2011). In addition to obtaining the core components for cellular respiration from the blood, the brain also receives a supply of other compounds that are essential to basic anabolic and catabolic processes.

Nucleic acids are the blueprints of life, and the amino acids that they encode are the basic building blocks from which life is built. Twenty-two of these so-called "proteinogenic" or protein-building amino acids exist, and of these, twenty are directly encoded by the genetic code – the "standard" amino acids (shown in **Table 2-1**). The standard amino acids can be further categorised broadly into those that can be synthesised *de novo* by an organism (non-essential), and those that cannot (essential). Amino acids that cannot be synthesised *de novo* must therefore be obtained from the organism's external surroundings - in the case of complex organisms such as humans, the diet. Essential amino acids are dissipated through the body *via* the circulatory

system. Indeed, even non-essential amino acids can be transported from the organ of their synthetic origin, to other parts of the body. As the primary interface regulating transport between the blood and brain, the BBB contains a broad variety of specific amino acid transporters with varying characteristics and substrate specificities (Pardridge, 1998).

Table 2-1: The twenty "standard" amino acids.

Characteristics	
Non-polar, small	Glycine (Gly), Alanine (Ala)
Non-polar, hydrophobic	Valine (Val), Leucine (Leu), Isoleucine (Ile), Phenylalanine (Phe), Methionine (Met), Proline (Pro), Tryptophan (Trp)
Polar, neutral	Serine (Ser), Threonine (Thr), Tyrosine (Tyr), Cysteine (Cys), Asparagine (Asp), Glutamine (Gln)
Polar, acidic	Aspartic acid (Asp), Glutamate (Glu)
Polar, basic	Arginine (Arg), Histidine (His), Lysine (Lys)

The classical perception of diet as being solely a means of obtaining energy and building material (such as amino acids) has been challenged over the past decade. Omega-3 fatty acids, for example, are known to have positive effects on cognition and learning, and form the basis for a plethora of over-the-counter dietary supplements after they were shown to be crucial in supporting cognitive process in humans (McCann & Ames, 2005) and maintaining synaptic plasticity in rodents (Wu *et al.*, 2007). While the exact mechanisms underlying these processes are not yet clear, it is generally accepted that diet can affect behaviour and health (Gomez-Pinilla, 2008).

The transport of amino acids from blood to brain is an essential first step in several amino acid synthesis pathways. In the cases of serotonin, dopamine and other amino acid neurotransmitters synthesised from amino acid precursors, the rate-limiting enzymes responsible for their biosynthesis are generally not saturated by the intracellular concentrations for precursors typically attained in the brain (Pardridge, 1998). The consequence of this is that the biosynthesis of amino acid neurotransmitters is proportional to the availability of the precursors to the brain, which is determined by the kinetics of their transport at the BBB (Pardridge, 1977). Furthermore, and based on the same principles, the synthesis of proteins in the brain is also limited by the kinetics of amino acid transport mechanisms at the BBB.

A large number of different amino acid transport systems are known to exist at the BBB, with expression being polarised to either the luminal or abluminal membrane, or localised to both membranes of the brain capillary endothelial cells. Each transport system consists of at least one gene-product, with many systems containing several proteins. These transporters can be sufficient to transport their substrate, while others complex with other system members to function. All transport systems can be broadly categorised by their substrate specificity, transport rates, and sodium (Na^+) or chloride (Cl^-) ion dependence. Many dietary (essential) amino acids display rapid and saturable rates of brain uptake (Oldendorf, 1971); utilising a number of different transport systems that are broadly categorised as being either dependent or independent on Na^+. This chapter will focus on the transport systems with known abilities to transport cationic amino acids, however more exhaustive reviews of all amino acid transport systems at the BBB have been published elsewhere (Hawkins *et al.*, 2006).

2.1.1 Cationic amino acids (CAAs)

Among the 20 'standard' amino acids encoded by the genetic code, only three are classed as cationic, although only arginine and lysine are positively charged at pH 7.4. The structures for arginine, histidine and lysine are shown in **Figure 2-1**.

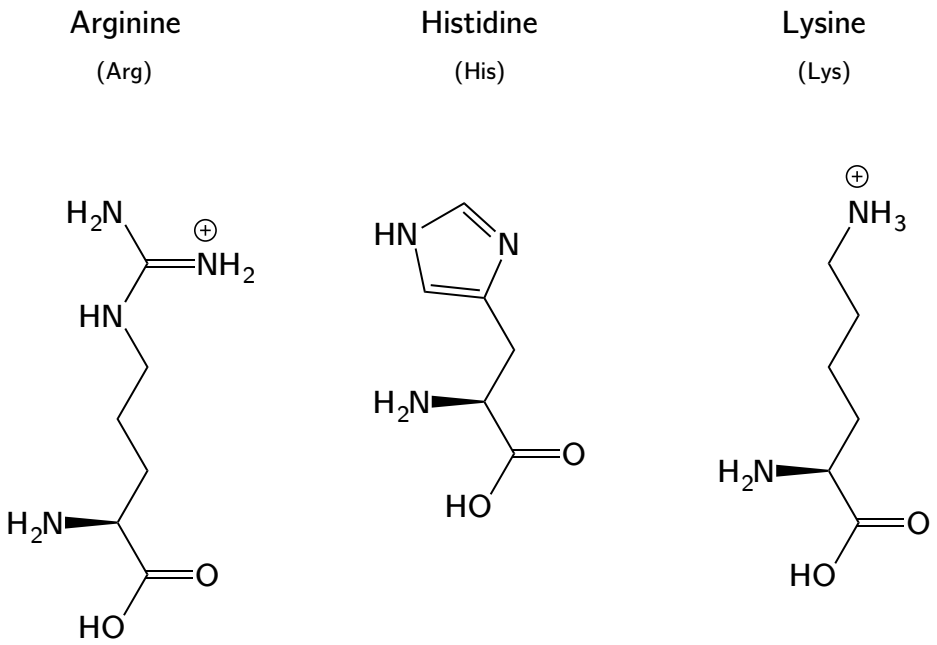

Figure 2-1: Three standard cationic amino acids and their structures.

2.1.1.1 Cationic amino acid transporters

Transport of some amino acids into the brain was shown to be a secondarily active process that is dependent on the Na^+ concentration gradient generated by (Na^+/K^+)-ATPase at the abluminal membrane (Vorbrodt, 1988). Indeed, brain capillary endothelial cells are known to have a high density of mitochondria than their counterparts in muscle tissue (Oldendorf & Brown, 1975) for generating the energy needed to drive active transport.

All transporters known to transport amino acids belong to the solute carrier (SLC) superfamily – a major group of membrane transport proteins that also include other transporters responsible for the cellular uptake and efflux of nutrients, metabolites, drugs and neurotransmitters, as described in ***chapter 1*** (Hediger *et al.*, 2004). As much as 22% of *Slc* genes expressed at high levels in brain capillary endothelial cells are amino acid transporters (Dahlin *et al.*, 2009). Within the SLC superfamily, the majority of amino acid transport at the blood-CNS barriers is thought to be mediated by the system L transporter LAT-1 (*SLC7A5*) expressed at both the abluminal and luminal membranes of the BBB (Verrey, 2003) and in the choroid plexus epithelium

(Duelli *et al.*, 2000). System L is a bi-directional transport system specific to large, neutral amino acids and is inhibited by 2-aminobicyclo-(2, 2, 1)-heptane-2-carboxylic acid (BCH) (Smith & Stoll, 1998). However, with respect to transport of CAAs across mammalian cell membranes, two families of transporters in particular are of considerable importance (O'Kane *et al.*, 2006):

i. Broad-scope Amino Acid Transporter (**BAAT**) family, consisting of systems $b^{0,+}$, y^+L, and $B^{0,+}$
ii. Cationic Amino Acid Transporter (**CAAT**) family, consisting of system y^+

A putative third transport system, b^+, has been shown to have the capacity to transport CAAs, but thus far has only been identified in mouse blastocysts, and remains an orphan transporter, with no encoding gene identified (Van Winkle & Campione, 1990). A summary of both the CAAT and BAAT family of transporters is shown in **Table 2-2** and **Table 2-3**.

Table 2-2: Summary of broad-scope amino acid transporter (BAT) family

Transport system	Protein	Gene	Expressed at BBB?	Primary substrates	Inhibitors	Na^+ dependence	Ref
$b^{0,+}$	$b^{0,+}$AT	SLC7A9	Unknown	Lysine, Arginine, NAA	Harmaline	No	(Van Winkle *et al.*, 1990b; O'Kane *et al.*, 2006)
	rBAT	SLC3A1	Yes				
y^+L	y^+LAT1	SLC7A7	Yes	Lysine, Arginine, NAA	Unknown	No for CAA, yes for NAA	(Deves & Boyd, 1998; Omidi *et al.*, 2003)
	y^+LAT2	SLC7A6					
$B^{0,+}$	$ATB^{0,+}$	SLC6A14	Yes	Lysine, Arginine, Alanine, Tryptophan, NAA	BCH, α-methyl-D,L-tryptophan	Yes	(Czeredys *et al.*, 2008; Karunakaran *et al.*, 2008)

BBB = blood-brain barrier, **BCH** = 2-amino-2-norbonane carboxylic acid, **CAA** = cationic amino acids, **NAA** = neutral amino acids

Table 2-3: Summary of cationic amino acid transporter (CAAT) family

Transport system	Protein	Gene	Expressed at BBB?	Primary substrates	Inhibitors	Na^+ dependence	Ref
y^+	CAT-1	SLC7A1	Yes	Lysine, Arginine, Ornithine, Histidine & NAA (weakly)	*L*-homoearginine & N-ethylmaleimide	No for CAA, yes for NAA	(Bogle *et al.*, 1995; Nicholson *et al.*, 1998; Closs *et al.*, 2006; Hawkins *et al.*, 2006; O'Kane *et al.*, 2006)
	CAT-2A	SLC7A2A	Yes	Lysine, Arginine, Ornithine	Unknown	Unknown	(Bogle *et al.*, 1995; Closs *et al.*, 2006; O'Kane *et al.*, 2006)
	CAT-2B	SLC7A2B			*L*-homoearginine	No	
	CAT-3	SLC7A3	Unknown	Lysine, Arginine	Unknown	No	(Huang *et al.*, 2007)
	CAT-4	SLC7A4	Unknown	Unknown	Unknown	Unknown	(Closs *et al.*, 2006; Yeramian *et al.*, 2006)

BBB = **blood-brain barrier,** CAA = **cationic amino acids,** NAA = **neutral amino acids**

2.1.1.1A Broad-scope amino acid (BAAT) transporters

Although broad-scope amino acid transporters are not prototypical cationic amino acid transporters, they do display varying abilities to transport cationic amino acids across the plasma membrane in a Na^+-independent manner, except for system $B^{0,+}$, which is dependent on Na^+ for transporting both neutral and cationic amino acids.

System $b^{0,+}$

System $b^{0,+}$, a Na^+-independent transport system, is so-called because of its ability to transport both cationic and neutral amino acids (the 0 and + exponents were given to represent neutral and cationic amino acids, respectively). System $b^{0,+}$ activity is best understood in the contexts of small intestine epithelium and renal proximal tubule, where it is mediated by two covalently-linked proteins, $b^{0,+}$AT and rBAT (*Slc7a9* and *Slc3a1*, respectively) (Wagner *et al.*, 2001). Heterologous co-expression of these two proteins facilitates the high-affinity influx of extracellular cationic amino acids and *L*-cysteine in exchange for intracellular neutral amino acids *via* an antiport mechanism (Busch *et al.*, 1994; Chillaron *et al.*, 1996; Pfeiffer *et al.*, 1999a). Mutations in either $b^{0,+}$AT and rBAT can disrupt the reabsorption of cationic amino acids and *L*-cysteine into the bloodstream, leading to cystinuria (Calonge *et al.*, 1994; Chairoungdua *et al.*, 1999; Pfeiffer *et al.*, 1999a). A recent study profiling the expression of *Slc* genes in the mouse brain revealed that rBAT is particularly highly expressed (Dahlin *et al.*, 2009). Since system $b^{0,+}$ activity requires heterodimerisation of rBAT with $b^{0,+}$AT, the fact that these proteins were not found to be expressed at the mouse BBB at equal levels raises an interesting question that is yet to be explained. The expression of system $b^{0,+}$ in the choroid plexus is currently unknown.

System y^+L

System y^+L is a high capacity transport system that transports cationic amino acids in a Na^+-independent manner and neutral amino acids in a Na^+-dependent manner (Deves *et al.*, 1992). The system was so named because of these properties, as it resembles both system y^+ and system L. System y^+L activity is mediated by the proteins y^+LAT1 and y^+LAT2, respectively encoded by *Slc7a7 and Slc7a6*, although both proteins associate with the almost constitutively expressed transmembrane protein 4F2hc,

encoded by *Slc3a2* (Deves *et al.*, 1992; Pfeiffer *et al.*, 1999b). The functional distinction of system y^+L from system y^+ is made difficult by the facts that both have a similar high affinity for cationic amino acids, but also that no specific inhibitor of system y^+L has been identified to date. Perhaps the only distinguishable difference between the two systems might be the ability of *L*-leucine (a neutral amino acid) to inhibit transport of *L*-lysine mediated by system y^+L in the presence of Na^+ - a phenomenon that is not observed with system y^+ (Estevez *et al.*, 1998; Rotmann *et al.*, 2007). The y^+LAT2 protein in particular is found to be highly expressed at the mouse choroid plexus, relative to other amino acid transporters (Dahlin *et al.*, 2009).

System $B^{0,+}$

System $B^{0,+}$ (not to be confused with $b^{0,+}$) was first discovered as displaying Na^+-dependent cationic, neutral and zwitterionic amino acid transport activity in mouse blastocysts after the observation that alanine transport was inhibited by arginine, lysine and BCH (Van Winkle *et al.*, 1985). The broad substrate specificity of the transport system led to it being given the name $B^{0,+}$. It should be noted that the inhibition of $B^{0,+}$ by BCH is believed to be competitive due to the observation that inhibition of leucine uptake by B^{0+} generates a current (Sloan & Mager, 1999). Transporter cloning has revealed a protein that is 645 amino acids long (named $ATB^{0,+}$), encoded by the *Slc6a14* gene and sharing sequence homology with glycine and proline transporters (Sloan & Mager, 1999). Human $ATB^{0,+}$ expression is greatest at the apical membrane of bronchial epithelial cells (Sloan & Mager, 1999) where it is believed to be involved in the transepithelial transport of arginine (Galietta *et al.*, 1998). In contrast, murine $ATB^{0,+}$ expression appears to be highest in the colon (Sloan & Mager, 1999). $ATB^{0,+}$ is believed to be the only cationic amino acid transporter with the ability to accumulate arginine against its concentration gradient (Deves & Boyd, 1998).

System $B^{0,+}$ was initially proposed to be one of the mediators of large neutral amino acid efflux at the abluminal side of the blood-brain barrier (O'Kane & Hawkins, 2003), however this hypothesis was later changed after further studies demonstrated a lack of cross-competition between neutral and basic amino acids (which also excluded the

transport system, y^+L) (O'Kane *et al.*, 2004). In contrast to these findings, $ATB^{0,+}$ had already been detected at the abluminal membrane of the bovine BBB *in vitro* (Sanchez del Pino *et al.*, 1995), and this observation has been confirmed more recently (Czeredys *et al.*, 2008). The exact contribution of $B^{0,+}$ to amino acid transport at the blood-brain barrier is therefore far from clear cut. Even less is known about the expression of system $B^{0,+}$ at the choroid plexus.

2.1.1.1B Cationic amino acid (CAAT) transporters

Na^+-independent bi-directional facilitated transport of cationic amino acids across plasma membranes was first attributed to system y^+ in cell culture (White, 1985), and was also later shown to be present at the rat BBB (Stoll *et al.*, 1993). System y^+ has an affinity for *L*-arginine, *L*-lysine and *L*-ornithine in the µmolar range (Stoll *et al.*, 1993), but also has a low affinity for neutral amino acids in the presence of Na^+ ions (White, 1985). Transport by system y^+ is sensitive to inhibition by *L*-homoarginine (Stoll *et al.*, 1993). The murine cationic amino acid transporter protein (CAT-1, encoded by *Slc7a1*) responsible for system y^+ activity has been cloned and expressed in *Xenopus* oocytes (Kim *et al.*, 1991), and has been found to share greater than 88% sequence homology with corresponding rat (Stoll *et al.*, 1993) and human (Yoshimoto *et al.*, 1992) genes. The putative structure of CAT-1 is depicted in **Figure 2-2**.

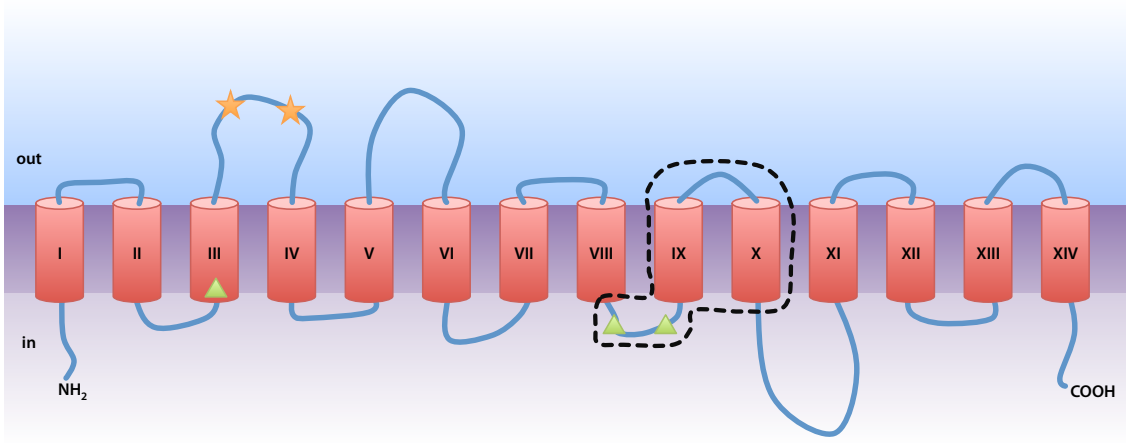

Figure 2-2: Putative structure of CAT-1, with 14 predicted transmembrane domains (red cylinders). Glycosylation sites on the extracellular loop between transmembrane domains III and IV are represented by orange stars (the number and precise position of these can vary between species). Green triangles represent residues that are critical for transport function. The black dotted line represents the region that determines differences in transport properties between different isoforms of CAT.

Three additional CAT isoforms have now been characterised, and named CAT-2, CAT-3 and CAT-4; encoded by the genes *Slc7a2, Slc7a3* and *Slc7a4*, respectively. Human CAT-2 is found as two splice variants (hCAT-2A and -2B), and both have been shown to exhibit varying degrees of voltage-dependence when *L*-arginine transport was observed after transfection into *Xenopus* oocytes (Nawrath *et al.*, 2000). CAT-3 isolated from mouse and rat brains has also been shown to exhibit system y^+ activity, however with differing substrate specificity compared to CAT-1, and also the ability to transport neutral amino acids in a Na^+-independent manner (Hosokawa *et al.*, 1997; Ito & Groudine, 1997). The final isoform identified to date, CAT-4, was isolated from human placenta and found to share approximately 40% sequence homology with other CAT proteins (Sperandeo *et al.*, 1998). However, there is currently no evidence to suggest that CAT-4 exhibits system y^+ activity (Wolf *et al.*, 2002). Despite this apparent lack of transport activity, CAT-4 has been found to be expressed at the mouse blood-CSF barrier at particularly high levels relative to all other amino acid transporters (Dahlin *et al.*, 2009).

CAT-1 has been shown to be localised at the plasma membrane of porcine aortic endothelial cells, and more specifically in caveolae-like clusters closely associated with the endothelial isoform of nitric oxide synthase, eNOS (McDonald *et al.*, 1997). As a classical system y^+ transporter, CAT-1 is bi-directional in its transport activity, however it is subject to strong stimulation by substrate at the opposite (*trans*-) side of the membrane (Kim *et al.*, 1991). This spatial and functional localisation constitutes an elegant means by which extracellular *L*-arginine can be transported into the cell and utilised in the synthesis of NO, and indicates that CAT-1 has an integral part in this process. Indeed, CAT-1 knockout mice produce pups that, when homozygous for CAT-1 deficiency, die very soon after birth (Perkins *et al.*, 1997).

CAT-1 mRNA is expressed at high levels in brain capillaries and choroid plexus (Stoll *et al.*, 1993), and the protein is found at both the luminal and abluminal membranes of brain capillary endothelial cells (Takase-Yoden & Watanabe, 2001). The half-saturation constant, $\boldsymbol{K_m}$ for arginine transport by system y^+ in the absence of competitors has previously been shown to be 56 µM, and the maximal influx rate, $\boldsymbol{V_{max}}$ 24 nmol/min/g using the rat *in situ* brain perfusion technique (Stoll *et al.*, 1993). The apparent $\boldsymbol{K_m}$ under normal physiological conditions (in the presence of other amino acids, $\boldsymbol{K_{m(app)}}$) has been calculated as 302 µM for arginine, and the rate of influx 6.7 nmol/min/g. This considered, a plasma concentration of over 100 µM would result in arginine being transported from plasma into the capillary endothelium, and then the brain as system y^+ is expressed at both the luminal and abluminal membranes of the BBB (O'Kane *et al.*, 2006).

It was originally proposed that transport of cationic amino acids across the BBB was solely due to system y^+ activity (O'Kane *et al.*, 2006), however there is more recent evidence to suggest that this may not be the case. Investigations into the transporter transcriptome of whole mouse brains and a mouse brain capillary endothelial cell line has identified transporters for systems y^+, y^+L, and $b^{0,+}$, but also system L (Dahlin *et al.*, 2009; Lyck *et al.*, 2009). One must however be weary of such data as whole-brain samples will of course contain a number of different cell types other than BCECs, and

cultured cell lines are also susceptible to culture-induced changes in gene expression. While system L does not seem to transport *L*-arginine (Tomi *et al.*, 2005), it is a transport system that warrants investigation in respect to *L*-arginine as its expression does appear to be regulated at the transcriptional level by *L*-arginine deprivation (Padbury *et al.*, 2004).

2.1.1.2 *L*-arginine, nitric oxide and its role in the brain

L-arginine is a semi-essential cationic amino acid that humans primarily obtain from the diet, although it can also be synthesised *de novo* in adults (Umbarger, 1978). *L*-arginine is the immediate precursor of nitric oxide (NO), and is also involved in the synthesis of creatine (Humm *et al.*, 1997) and growth hormone (Alba-Roth *et al.*, 1988).

Nitric oxide (NO) is a gaseous signalling molecule that is now known to act on a wide range of mammalian biological systems - an attribute which no doubt contributed to it being named 'Molecule of the Year' in 1992 by the journal Science (Culotta & Koshland, 1992). NO is synthesised from *L*-arginine by one of a family of nitric oxide synthase (NOS) enzymes. Three isoforms of NOS have been characterised in humans (Forstermann *et al.*, 1994); all of which have been classified according to the tissue or cell type of origin found when determining cDNA expression. Two of the isoforms - neuronal (nNOS) and endothelial (eNOS), have been found to be constitutively expressed, while the third isoform shown to be inducible (iNOS) (Majano *et al.*, 2001). In contrast, the nomenclature of the genes that encode the isoforms (NOS1-3) reflects the order in which the human genes were cloned, i.e. nNOS, iNOS and eNOS respectively (Moncada *et al.*, 1997).

NOS enzymes are generally accepted to function as homodimers, catalysing the conversion of *L*-arginine to *L*-citrulline and NO in the presence of the co-substrates nicotinamide adenine dinucleotide phosphate (reduced form, NADPH), O_2 and the co-factors, flavins adenine dinucleotide (FAD) and mononucleotide (FMN) (Palacios *et al.*, 1989; Bredt & Snyder, 1990; Mayer *et al.*, 1990). All three isoforms are known to require calmodulin (CaM) for efficient transfer of electrons between the oxygenase and

reductase domains of the NOS enzymes (Stuehr, 1997). However, a difference in the dependence on either CaM or Ca^{2+} provides an interesting insight into the regulation of NO production by the different isoforms. Both eNOS and nNOS have been shown to reversibly bind CaM in a Ca^{2+}-dependent manner, whereas iNOS binds CaM with high avidity regardless of intracellular Ca^{2+} concentration (Nathan & Xie, 1994). Regulation of iNOS activity is thought to vary between cell types, however regulation has been shown to occur at the transcriptional level via transcription factors such as NF-κB (Kleinert *et al.*, 2004). There is also evidence to suggest that iNOS activity is regulated by trafficking *via* calmodulin kinase II (CaMKII) in vascular smooth muscle cells (Jones *et al.*, 2007), or that is not regulated at all *e.g.* in the case of pulmonary epithelia (Guo *et al.*, 1995) and renal medulla (Morrissey *et al.*, 1994).

NO has been implicated in regulatory and mediatory roles in a variety of different physiological processes and pathological conditions involving the cardiovascular, nervous and immune systems. In the cardiovascular system, NO is known to promote smooth muscle relaxation; resulting in vasodilatation and increasing blood flow. A similar effect on smooth muscles in the gastrointestinal tract has also lead to suggestions that NO is involved in homeostasis of the gut (Lamarque *et al.*, 1996). The effect of NO in smooth muscle was first shown to involve soluble guanylate cyclase (sGC) (Katsuki *et al.*, 1977), which is known to initiate an intracellular signalling cascade through the catalytic conversion of guanosine triphosphate (GTP) to 3',5'-cyclic guanosine monophosphate (cGMP) (Arnold *et al.*, 1977). An increase in intracellular cGMP results in the activation of protein kinase G (PKG) and consequently the phosphorylation of downstream proteins involved in the regulation of intracellular Ca^{2+}; hyperpolarising smooth muscle cells via Ca^{2+}-dependent potassium channels and promoting relaxation by increasing myosin phosphatase activity (Tanaka *et al.*, 2006). It should be noted however, that NO-mediated signalling via the cGMP cascade is not restricted to smooth muscle relaxation alone, and has roles in the brain in neurotransmission and synaptic plasticity.

A significant role for NO in the brain was first described in neurotransmission when it was shown to be produced as the result of stimulation N-methyl-D-aspartate (NMDA) receptors by glutamate (Garthwaite *et al.*, 1988), a known prerequisite for long term potentiation - a form of synaptic plasticity in the brain implicated in memory. Since then, NO has been implicated in the release of other neurotransmitters such as dopamine and serotonin in the rat medial pre-optic area (Lorrain & Hull, 1993) by a process that requires both sGC and cGMP (Kaehler *et al.*, 1999).

An additional role of NO in the brain is in the regulation of cerebral blood flow. This was first discovered *via* the cranial window method, whereby the competitive NOS inhibitor N^G-monomethyl-*L*-arginine (*L*-NMMA) was topically applied to the basilar artery, which then constricted (Faraci, 1990). Since these early experiments, NO has been implicated in cerebral autoregulation (White *et al.*, 2000), and the chemoregulation of cerebral blood flow in humans (Lavi *et al.*, 2003). A very comprehensive review of the current understanding of the cornucopia of roles NO has in the regulation of cerebral blood flow has been recently published (Toda *et al.*, 2009). However, it suffices to say that the role of NO in the brain is both complex and far reaching, and any disruption to the delicately balanced processes that control its production can be expected to have severe consequences in the brain, for example in ischaemic stroke (Terpolilli *et al.*, 2012).

One such molecule that is known to inhibit NO production is N^G,N^G-dimethyl-*L*-arginine (asymmetric dimethylarginine or ADMA) – an endogenously occurring analogue of *L*-arginine.

2.1.1.3 ADMA

ADMA was first found to be a biologically significant inhibitor of nitric oxide production in 1992 (Vallance *et al.*, 1992a; Vallance *et al.*, 1992b). It is believed that the inhibition of NOS by ADMA stems from the inability of NOS to utilise ADMA as a substrate (Vallance *et al.*, 1992a). Since these initial observations there has been an

explosion of interest in ADMA, as evidenced by the exponential increase in the number of publications relating to "asymmetric dimethylarginine" (**Figure 2-3**).

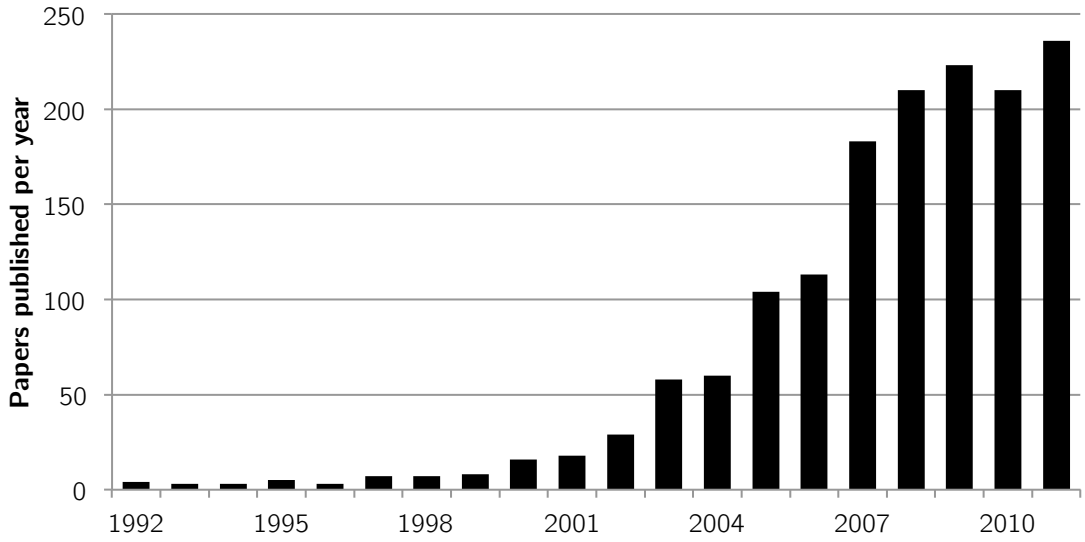

Figure 2-3: Number of scientific publications (including reviews) per year relating to "asymmetric dimethylarginine" (PubMed searches, November 2012).

The K_i (dissociation constant for inhibitor binding) for ADMA's inhibition of nNOS has been calculated to be 0.7 µM (Cardounel & Zweier, 2002) and the K_i of eNOS to be 0.9 µM (Cardounel *et al.*, 2007), however ADMA appears to have a preference for nNOS as demonstrated by the IC_{50} (half the maximal inhibitory concentration) for nNOS being almost 10-fold lower than that for eNOS (1.5µM *vs* 12 µM) (Tsikas *et al.*, 2000). With these values taken into account, one may expect that the ADMA concentration is sufficient to tonically inhibit nNOS, however when considering that the $\boldsymbol{K_m}$ of arginine for nNOS is as low as 2.4 µM (Cardounel & Zweier, 2002) the effects of arginine will predominate under normal, physiological conditions.

However, much of the interest in ADMA surrounds its involvement in disease as an endogenous inhibitor of NOS. It has become apparent that abnormally high levels of ADMA circulating in plasma are often detected in a number of pathological conditions associated with cardiovascular or endothelial dysfunction. A summary of cardiovascular conditions linked to ADMA, and the observed increase in ADMA levels relative to

control conditions is shown in **Table 2-4**. **Table 2-5** shows a number of cerebrovascular diseases and others relating to the brain where altered ratios of arginine:ADMA are found.

Table 2-4: Some clinical conditions associated with elevated levels of ADMA in human plasma relative to health humans (control). Modified from (Bode-Boger et al., 2007)

Condition	**ADMA plasma concentration (Increase *vs* healthy)**	**Ref**
Hypercholestrolemia	≈ 200%	(Boger *et al.*, 1998a)
Chronic heart failure	≈ 200%	(Usui *et al.*, 1998)
Impaired renal function	200-700%	(Kielstein *et al.*, 1999; Zoccali *et al.*, 2001)
Hypertension	≈ 200%	(Goonasekera *et al.*, 1997; Surdacki *et al.*, 1999)
Peripheral arterial disease	200-300%	(Boger *et al.*, 1997; Boger *et al.*, 1998b)
Heart failure	200-300%	(Valkonen *et al.*, 2001)
Diabetes mellitus	200-300%	(Abbasi *et al.*, 2001)
Pre-eclampsia	200-300%	(Pettersson *et al.*, 1998)
Hyperhomocysteinemia	≈ 200%	(Sydow *et al.*, 2003)

Table 2-5: Some cerebrovascular conditions associated with altered arginine:ADMA ratios.

Condition	**Arginine:ADMA *vs* control**	**Ref**
Microangiopathy-related cerebral damage	Decrease	(Notsu *et al.*, 2009)
Cerebral small vessel disease	Decrease	(Khan *et al.*, 2007)
Ischemic stroke	Decrease	(Yoo & Lee, 2001; Wanby *et al.*, 2003; Wanby *et al.*, 2006; Xu *et al.*, 2007; Nishiyama *et al.*, 2010)
Parkinson's disease	Decrease	(Dorszewska *et al.*, 2007)
Alzheimer's disease	[ADMA] in CSF **decreases,** [ADMA] in plasma **increases**, [Arginine] not measured	(Abe *et al.*, 2001; Selley, 2003; Arlt *et al.*, 2008)
Sucarachnoid haemorrhage	Decrease	(Pluta, 2008)
Cerebral autosomal dominant arteriopathy with subcortical infarct and leukoencephalopathy	Decrease	(Rufa *et al.*, 2008)
Depression	[ADMA] in plasma **increases**	(Selley, 2004)
Schizophrenia	[ADMA] in plasma **increases**	(Das *et al.*, 1996; Sydow *et al.*, 2003)

2.1.1.3A ADMA synthesis from L-arginine

Protein methylation is a common mechanism of post-translational modification utilised in the regulation of many different cellular processes in both prokaryotes and eukaryotes. Methylation of amino acids (specifically arginine, lysine and histidine) provides a useful means of expanding the functional repertoire of the cellular proteome. Arginine methylation is mediated by protein arginine methyltransferase (PRMT) enzymes, which specifically methylate the guanidino group of arginine residues incorporated into proteins (Rawal *et al.*, 1995). PRMT activity was first characterised and attributed to 'protein methylase I' over 40 years ago (Paik & Kim, 1968). Two types of PRMT have been classified to date - type I and type II (Gary & Clarke, 1998). Both subtypes catalyse the formation of *L*-NMMA as the first step of methylation, however the second step of methylation is where the difference between PRMT subtypes is seen. Type I PRMT enzymes catalyse the formation of ADMA, whereas type II PRMT enzymes catalyse the formation of symmetric dimethylarginine (SDMA) (Gary & Clarke, 1998) (shown in **Figure 2-4**). Proteomic analysis of HeLa cells revealed that approximately 200 proteins contain putatively methylated arginine residues, preferentially in arginine-glycine rich sequences (Boisvert *et al.*, 2003), and it has also been demonstrated that in some cases, arginine methylation is required as a signal for localisation within the nucleus of the cell (Smith *et al.*, 2004). Interestingly, approximately 65% of all intracellular protein-incorporated ADMA is found in heterogenous nuclear ribonuclear proteins (hnRNPs), which are involved in the regulation of mRNA maturation (Boffa *et al.*, 1977).

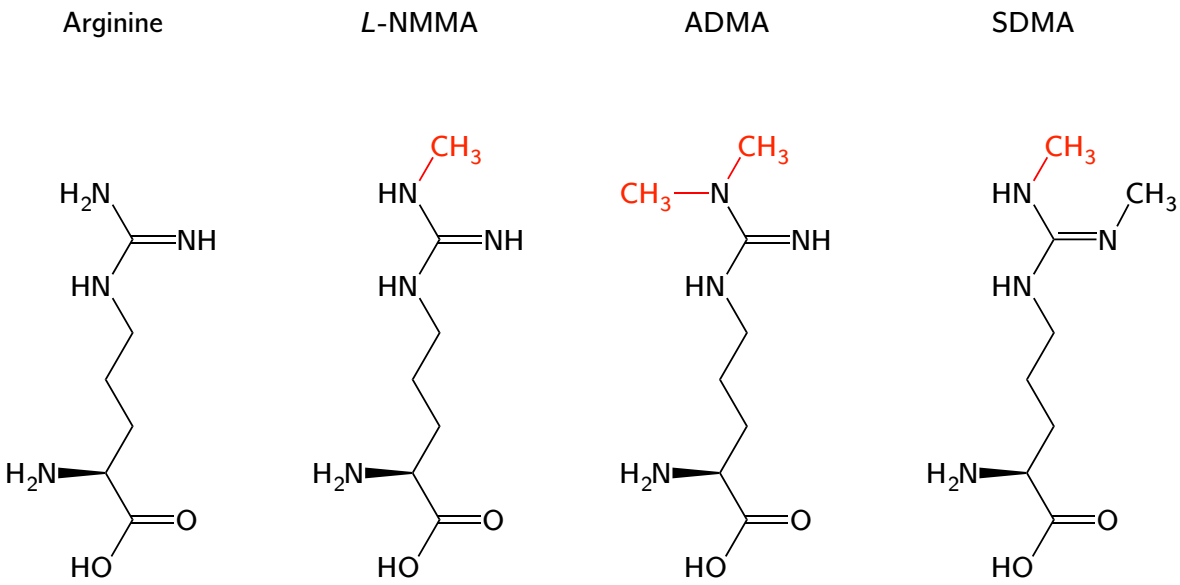

Figure 2-4: Arginine and its methylated derivatives.

As direct methylation of free *L*-arginine is yet to be demonstrated (Vallance & Leiper, 2004) cytosolic methylated arginine derivatives are believed to occur only through the proteolysis of proteins containing methylated arginine. Proteolysis is a complex and multi-step process, and thus the rate determining factor for plasma levels of ADMA are yet to be determined, although it has been suggested that there is a correlation between PRMT expression and the amount of ADMA produced (Boger *et al.*, 2000b).

The high expression and activity of type I PRMT enzymes in the lungs designate them as the major source of ADMA (4.23 µmol per gram of protein) in interstitial fluid and plasma (Bulau *et al.*, 2007), however an early study in rat brains showed that the ADMA concentration is typically 1.10 µmol per gram of protein (similar to that found in the heart, and higher than that found in the liver), while separation of whole brain into nuclear, myelin and mitochondria-synaptosome fractions demonstrated the concentrations of free ADMA to be 2.12, 0.44 and 0.07 µmol per gram of dry weight, respectively (Nakajima *et al.*, 1971). Soon after this initial data was published, the arginine concentration in rabbit brain was found to be almost 300-fold greater than that of ADMA (McDermott, 1976). More recently, quantification of arginine and

ADMA in rat brain slices revealed concentrations of approximately 95 and 5 µM, respectively (Cardounel & Zweier, 2002).

2.1.1.3B ADMA clearance

After the detection of substantial amounts of both SDMA and ADMA in human urine, it was generally accepted that free methylarginines were cleared from the body by renal excretion (Kakimoto & Akazawa, 1970). This notion was challenged when the amount of SDMA in rabbit urine was found to be 30-fold higher than that of ADMA, and it was proposed that some catabolic pathway must exist for both ADMA and also **L**-NMMA (McDermott, 1976). Support for this theory came from studies involving radio-labelled ADMA and SDMA in rat (Ogawa *et al.*, 1987b), in which it was seen that radio-labelled methylarginine metabolites were present in tissue and plasma samples of rats that were injected with [^{14}C]-ADMA, but not [^{14}C]-SDMA. Further investigation revealed that more than 90% of all ADMA generated was metabolised as opposed to being excreted (Ogawa *et al.*, 1987a), and the enzyme responsible was later purified and termed N^G,N^G-dimethylarginine dimethylaminohydrolase (DDAH) (Ogawa *et al.*, 1989). In humans, approximately 300 µmol of ADMA is produced each day, of which approximately 250 µmol (80%) is metabolised by DDAH (Achan *et al.*, 2003).

DDAH enzymes are highly conserved throughout evolution and have been identified in prokaryotes (Tran *et al.*, 2000). Two isoforms (DDAH-1 & -2) exist in higher vertebrates and are thought to be the result of a gene duplication event that occurred some time before the evolution of bony fish (Tran *et al.*, 2000). Both DDAH isoforms catalyse the conversion of ADMA to citrulline and dimethylamine, with a Michaelis affinity constant ($\boldsymbol{K_m}$) of approximately 180 µM (Ogawa *et al.*, 1989). DDAH-mediated metabolism of ADMA is thought to occur *via* nucleophilic attack of the methylated guanidino group of ADMA by a cysteine residue (Cys-249) in the tertiary structure of the activated DDAH enzyme (Murray-Rust *et al.*, 2001), although this is yet to be definitively shown. It is known however, that substitution of the cysteine residue for serine renders the DDAH enzyme inactive, and thus Cys-249 does have some critical role in DDAH function (Murray-Rust *et al.*, 2001). As yet, no co-factors have been

conclusively identified, and it has been shown that Zn^{2+}, Cu^{2+} and Cd^{2+} are inhibitory (Ogawa *et al.*, 1989), although this may be species specific (Bogumil *et al.*, 1998). Closer analysis of DDAH-2 has revealed many hallmarks of a 'house-keeping' gene within the promoter region (Jones *et al.*, 2003), and although it is expressed constitutively, it does also appear to be subject to some form of regulation at the transcriptional level (Achan *et al.*, 2002).

DDAH enzymes were initially shown to co-localise with NOS enzymes in the rat (Tojo *et al.*, 1997) and this was later confirmed in humans (Leiper *et al.*, 1999). Studies on the pattern of expression of both DDAH-1 and -2 have shown that they are frequently associated respectively to nNOS and eNOS (Tran *et al.*, 2000), although not exclusively confined to tissues expressing NOS. As a consequence, DDAH is able to indirectly activate NOS by clearing ADMA. However, in conditions of elevated levels of ADMA, it has been shown that the resulting inhibition of eNOS can result in the complete uncoupling of the enzyme, leading to a switch from NO production to the production of superoxide radicals (Boger *et al.*, 2000a). The sulfhydryl group present on the cysteine residue in the active site of DDAH renders it extremely sensitive to oxidative stress (Murray-Rust *et al.*, 2001), and as ADMA can itself induce oxidative stress, the DDAH-ADMA-NOS system can easily slip into a vicious cycle if ADMA levels are not tightly regulated. This is particularly important in inflammation and diabetes, where excessive NO produced by iNOS and oxidative stress can respectively result in the nitrosylation (Leiper *et al.*, 2002) or oxidation (Lin *et al.*, 2002) of the critical cysteine in DDAH, and ultimately the inactivation of the enzyme.

At this stage it is unclear if ADMA has any biological significance in a regulatory role, or whether it is merely a by-product of product of normal protein turnover in the cell. However, it should be noted that ADMA is also subject to metabolic conversion to α-keto valeric acid by the enzyme alanine:glyoxylate aminotransferase (Ogawa *et al.*, 1990), although the overall contribution of this route to overall ADMA metabolism is undetermined thus far.

2.1.1.4 The *L*-arginine paradox

Prior to the discovery of ADMA, it was shown that dietary supplementation with *L*-arginine was sufficient to alleviate endothelial dysfunctions caused by impaired nitric oxide synthesis associated with conditions such as hypercholestrolemia (Cooke *et al.*, 1991). In contrast, characterisation of the enzyme kinetics of nitric oxide synthesis showed that levels of endogenous *L*-arginine (the nitric oxide precursor) were already above the saturation threshold in these conditions (Schmidt *et al.*, 1991). Quantification of the intracellular concentration of *L*-arginine revealed it to be approximately 0.3-0.8 mM in bovine endothelial cells (Gold *et al.*, 1989), which is easily sufficient to saturate eNOS when considering the $\boldsymbol{K_m}$ (substrate concentration that produces half-maximal velocity in the presence of an inhibitor) is approximately 2.9 µM (Bredt & Snyder, 1990). Plasma concentrations of *L*-arginine in both healthy humans and patients suffering from cardiovascular disease are typically between 45-100 µM (Boger & Bode-Boger, 2001), and slightly higher (140 µM) in mice (Hallemeesch *et al.*, 2004). Therefore, the observation that dietary (Bode-Boger *et al.*, 1998) or intravenous (Drexler *et al.*, 1991; Creager *et al.*, 1992; Bode-Boger *et al.*, 1996; Bode-Boger *et al.*, 1998) supplementation with *L*-arginine was sufficient to increase NO production in humans (healthy or otherwise), and in animal models of cardiovascular disease (Girerd *et al.*, 1990; Rossitch *et al.*, 1991) was somewhat puzzling at first. As such, this phenomenon became known as the '*L*-arginine paradox'.

Plasma concentrations of ADMA are often measured at between 0.3-0.5 µM in healthy humans (Martens-Lobenhoffer *et al.*, 2004), and can reach 3 µM in certain disease states (Cakir *et al.*, 2005; Bode-Boger *et al.*, 2007). It has been shown that ADMA produced by one cell (e.g. an endothelial cell) can inhibit nitric oxide synthesis in a neighbouring cell (e.g. a macrophage) (Fickling *et al.*, 1999).

Taking into consideration that ADMA appears to be able to exit and enter cells, exploring the *L*-arginine paradox with respect to ADMA and *L*-arginine transport is a sensible step to understanding the pathway for NO generation. The route by which ADMA crosses the cell membrane is yet to be formally identified, however it has been

shown that ADMA can be a substrate for transport by the y^+ cationic amino acid transport system, albeit at concentrations that are far greater than those seen in physiological or even pathological conditions (Bogle *et al.*, 1995). The archetypal system y^+ transporter CAT-1 and eNOS are sub-cellularly located in close proximity to each other in caveolae in the plasma membrane (McDonald *et al.*, 1997); ensuring that eNOS receives a plentiful supply of *L*-arginine in *via* CAT-1 transport. Indeed, *L*-arginine transport by CAT-1 is a pre-requisite of NO production by the endothelium *in vivo* (Zani & Bohlen, 2005).

Two possible explanations have been put forward to explain the *L*-arginine paradox:

2.1.1.4A Competition hypothesis

Pathological concentrations of ADMA in plasma could compete with *L*-arginine for transport into endothelial cells; thus reducing the intracellular bioavailability of *L*-arginine for the synthesis of NO by eNOS. Increasing plasma concentrations of *L*-arginine with dietary supplementation could then 'tip' transport mediated by system y^+ back in favour of transporting *L*-arginine into the cell; as the proportion of ADMA present in plasma would be reduced, and the degree of competition for transport exerted by ADMA also reduced. Therefore, it is conceivable that increased competition for *L*-arginine transport into the cell with extracellular ADMA would result in NO deficiency, both due to reduced intracellular *L*-arginine, and due to the fact that extracellular ADMA would have a direct route for inhibiting eNOS *via* CAT-1. In this case NO deficiency could be alleviated with *L*-arginine supplementation, and reduced competition for *L*-arginine transport into the cell. A schematic representation of the competition hypothesis is shown in **Figure 2-5**.

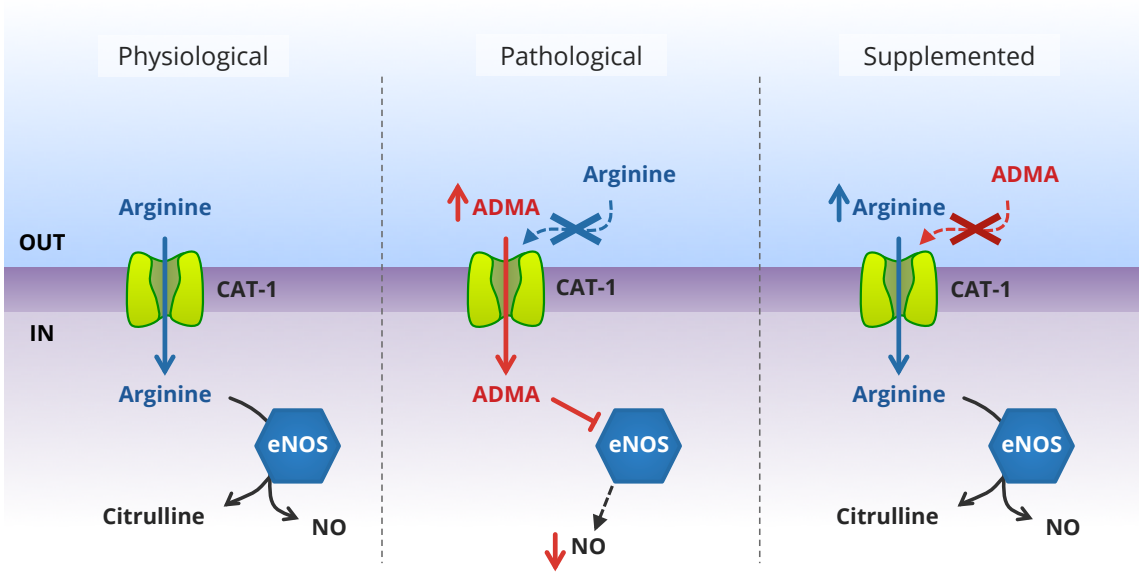

Figure 2-5: The competition hypothesis to explain the *L*-arginine paradox. **Left panel:** Under physiological conditions, *L*-arginine is transported into the cell by the CAT-1 transporter and converted to *L*-citrulline and nitric oxide (NO) by endothelial nitric oxide synthase (eNOS). **Centre panel:** Increases in extracellular ADMA observed under pathological conditions out-compete *L*-arginine for transport into the cell. Once inside the cell, ADMA inhibits eNOS, with the net result being a drop in NO production. **Right panel**: Following dietary supplementation with *L*-arginine, the concentration of extracellular *L*-arginine increases. This tips the balance of transport into the cell back into the favour of *L*-arginine ahead of ADMA, and restores NO production.

2.1.1.4B Trans-stimulation hypothesis

Since ADMA is produced intracellularly (see ***section 2.1.1.3A - ADMA synthesis from L-arginine***), inhibition of NOS may be due directly to free ADMA released by the proteolysis of proteins containing methylated *L*-arginine residues. An alternative model to explain the *L*-arginine paradox has been proposed, stating that increasing plasma concentrations of *L*-arginine following dietary supplementation could promote efflux of intracellular ADMA from the cell *via trans*-stimulation of CAT-1 (Teerlink *et al.*, 2009). The simultaneous removal of ADMA from the cell with increased influx of *L*-arginine into the cell could conceivably simultaneously relieve inhibition of NOS by ADMA while also providing *L*-arginine substrate for NO production.

CAT-2B is also known to have the capacity to transport ADMA (in addition to other methylarginines) and it has been shown that the presence of some methylarginines such as ADMA can inhibit *L*-arginine uptake into the brain (Closs *et al.*, 1997). While CAT-2B and CAT-3 are both expressed in the brain, have strong affinity for cationic amino acids, and also demonstrate *trans*-activation activity, they are both less sensitive to *trans*-stimulation relative to CAT-1 (Closs *et al.*, 1997; Vekony *et al.*, 2001). A schematic representation of the trans-stimulation hypothesis is shown in **Figure 2-6**.

The facts that y^+ transporters at the abluminal membrane would be directly subject to changes in ADMA production in the brain, and similarly luminal y^+ transporters to ADMA in plasma, make ADMA and *L*-arginine transport an interesting subject for investigation in the context of the blood-CNS barriers.

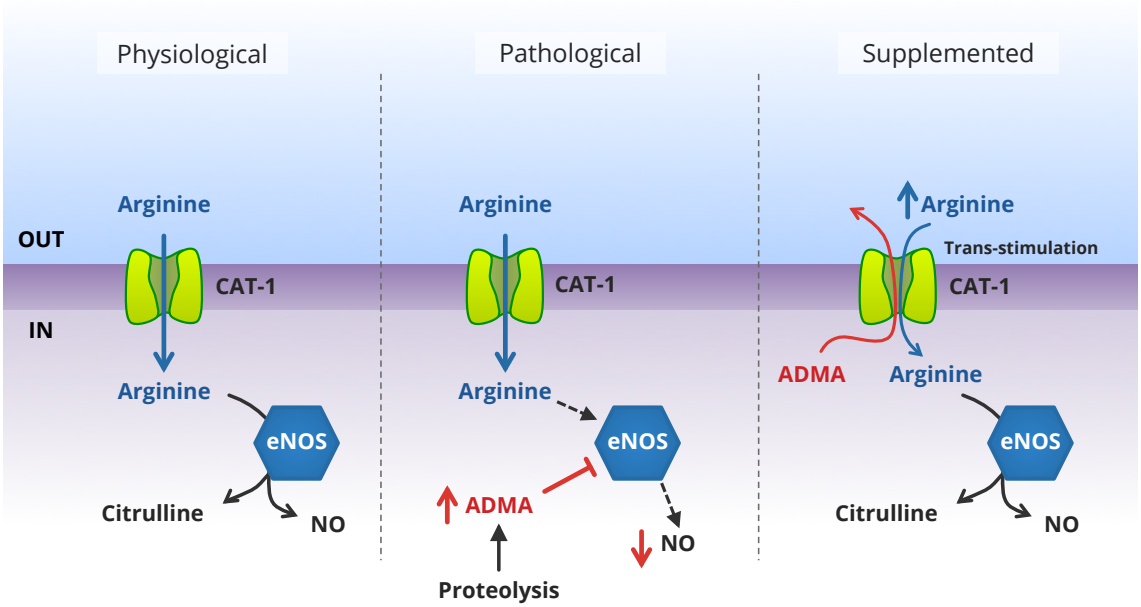

Figure 2-6: The trans-stimulation hypothesis to explain the *L*-arginine paradox. **Left panel:** Under physiological conditions, *L*-arginine is transported into the cell by the CAT-1 transporter and converted to *L*-citrulline and nitric oxide (NO) by endothelial nitric oxide synthase (eNOS). **Centre panel:** Increases in intracellular ADMA observed under pathological conditions result from the proteolysis of proteins containing methylated arginine residues. Intracellular ADMA inhibits eNOS, with the net result being a drop in NO production. **Right panel**: Dietary supplementation with *L*-arginine trans-stimulates the CAT-1 transporter to increase the rate of removal of ADMA from the cell while allowing *L*-arginine into the cell and restoring NO production.

2.2 Aims

The aims of this chapter of the thesis are to:

i. Elucidate the transport mechanism(s) utilised by ADMA at the murine blood-brain and blood-CSF barriers, and compare them to those used by *L*-arginine.

ii. Determine the effects (if any) of ADMA on *L*-arginine transport at the murine blood-brain and blood-CSF barriers.

iii. Determine the effects (if any) of *L*-arginine on ADMA transport at the murine blood-brain and blood-CSF barriers.

iv. Investigate the aforementioned two hypotheses (competition and trans-stimulation) to explain the *L*-arginine paradox in the context of the murine blood-brain and blood-CSF barriers.

2.3 Methods

2.3.1 Blood-CNS barrier model & accessory methodologies

2.3.1.1 Animals & anaesthesia

All experiments requiring the use of animals were performed in accordance with the Animal (Scientific Procedures) Act, 1986. All animals used in procedures were adult male BALB/c mice (between 23 g and 25 g) sourced from Harlan Laboratories, Oxon, UK, unless otherwise stated. Free access to water and food was provided *ad libitum*.

Domitor® (medetomidine hydrochloride) and Vetalar® (ketamine) were both purchased from Harlan Laboratories; Cambridge, UK. All animals were anaesthetised (2 mg/kg Domitor® and 150 mg/kg Vetalar® injected intraperitoneally), and a lack of self-righting and paw-withdrawal reflexes (as surrogate indicators of consciousness) thoroughly checked prior to carrying out all procedures. Animals were heparinised with 100 units heparin (in 0.9% m/v $NaCl_{(aq)}$, Harlan Laboratories; Oxon, UK), administered *via* the intraperitoneal route prior to surgery.

2.3.1.2 *In situ* brain/choroid plexus perfusion

The *in situ* brain/choroid plexus perfusion method is designed to directly infuse the brain with artificial plasma *via* a cannula placed in the heart. Artificial plasma is prepared to mimic the ionic composition of blood, and any solutes and transport inhibitors of interest can be added in known concentrations and delivered to the brain for defined periods of time. There are a number of advantages associated with using the *in situ* brain/choroid plexus perfusion technique over other methods (e.g. brain uptake index (BUI) method) to study blood-brain and blood-CSF barrier transport:

i. Perfusions can be carried out over a long period of time (up to 30 minutes), allowing accurate measurements of brain uptake with respect to time for slowly permeating molecules, and the kinetics of transport calculated accordingly.

ii. The solute of interest is delivered to the CNS at a known concentration with a constant flow that does not vary with time.

iii. The concentration of solutes, potential competitors, transport inhibitors and ions can easily be manipulated in the perfusate in order to measure saturable transport across the BBB and identify the transport systems involved.

iv. The solute is exposed to the brain microcirculation before any peripheral organs involved in metabolism (*e.g.* liver, kidneys or lungs) and thus one can be confident that the compound is intact when interacting with transporters at the blood-brain and blood-CSF barriers.

2.3.1.2A Surgical preparation

The experimental procedure followed a previously outlined protocol (Sanderson *et al.*, 2007). Following anaesthesia and heparinisation of the mouse (as described in ***section 2.3.1.1 - Animals & anaesthesia***), a low transverse incision was made with scissors just above the pubic region, which was then extended up on both sides up to just under the forelimbs. This exposed the entire peritoneal cavity, enabling the movement of the liver to expose the diaphragm. An incision in the diaphragm was then made, and the ribcage also cut and held open with a haemostat.

2.3.1.2B Experimental procedure

The pericardium was then carefully cut, and the left ventricle of the heart cannulated with a 25G x 10mm butterfly-winged needle, before making an incision in the right atrium. The butterfly-winged needle was connected to a perfusion circuit as detailed in **Figure 2-7**.

2.3.1.2C Perfusion circuit

The artificial plasma was infused into the heart *via* this circuit and could thus enter the body and reach the vasculature of the head. The right atrium of the heart was sectioned to allow outflow of the artificial plasma. Thus, an open circuit is created and the artificial plasma only passes through the circulation once.

The artificial plasma was kept at physiological temperature (37 °C) and oxygenated by 95% O_2 / 5% CO_2 gas being bubbled through the solution, before being pumped through the tubing circuit by means of a peristaltic pump. Radiolabelled and unlabelled test molecules, substrates and inhibitors were infused into the inflowing artificial plasma via the slow drive syringe pump. The speed of the peristaltic pump and syringe plunger pressure was fine-tuned to give a pre-determined and constant flow rate of 5 mL/minute. On its route, the artificial plasma was passed through a bubble trap to ensure that any bubbles that could compromise the integrity of the blood-CNS interfaces were removed.

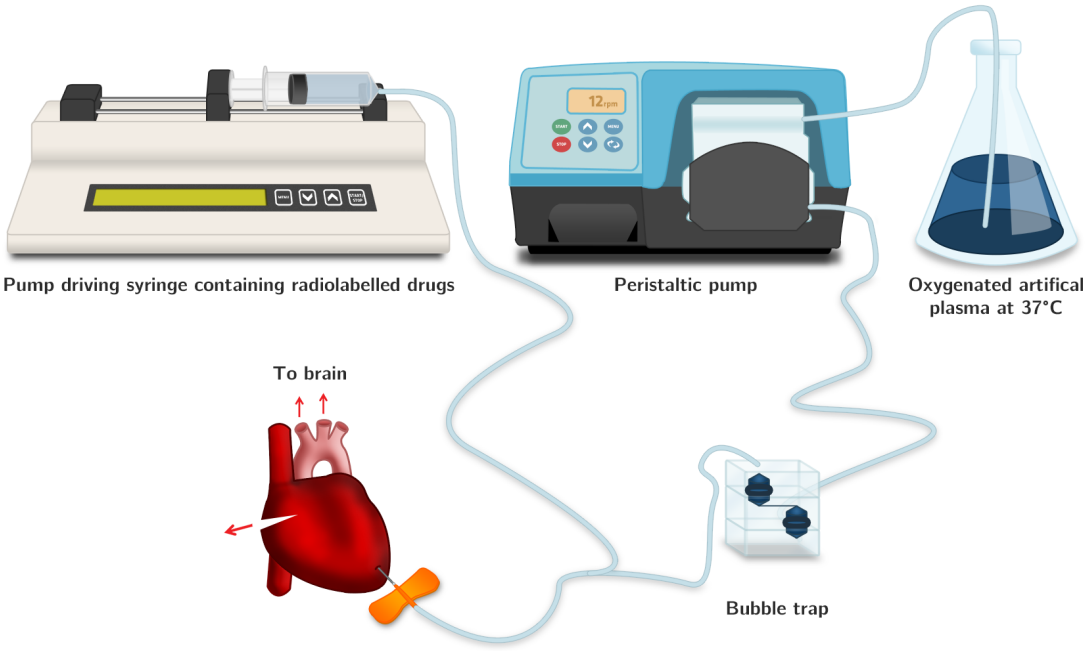

Figure 2-7: Schematic representation of experimental setup for *in situ* brain/choroid plexus perfusion. The heart is drawn in isolation for simplicity, but in reality is still *in situ* and provides access to the vascular bed after cannulation of the left ventricle with a 25G x 10mm butterfly-winged needle (shown with orange wings). The oxygenated artificial plasma is passed through the system of tubing by a peristaltic pump at a flow rate of 5 mL/minute, and bubbles removed by a bubble trap. The perfusate is then infused with the solute of interest, which is radiolabelled. After one full circulation of the entire circulatory system the perfusate exits the body *via* an incision made in the right atrium.

2.3.1.2D Composition of artificial plasma

A full breakdown of the contents of artificial plasma is shown in ***Appendix 1***.

2.3.1.2E Radiolabelled solutes of interest

Sucrose (non-metabolisable baseline)

[^{14}C]-sucrose (mol. wt., 342.3 g/mol; specific activity, 0.412 Ci/mmol; 99% radiochemical purity; Moravek Biochemicals, Brea, CA), was present in the artificial plasma for all perfusion experiments. First and foremost, it should be noted that the molecular weight of [^{14}C]-sucrose is comparable to that of the other radiolabelled solutes of interest (*e.g.* [^{3}H]-arginine = 174.2 g/mol, [^{3}H]-ADMA = 276.7 g/mol). Thus, based on the molecular weight alone, it would not be un-reasonable to expect that the three compounds would have similar transport characteristics. However, molecular weight is only one determinant of a compound's transport characteristics, and indeed [^{14}C]-sucrose is frequently used as a measure of BBB permeability due to its poor penetrance through the brain microvasculature as a polar molecule with no specific transport system.

In these experiments, [^{14}C]-sucrose was used both as an internal control of blood-brain barrier integrity, but also as a quantitative measure of cerebrovascular space. All values for uptake of [^{3}H]-arginine or [^{3}H]-ADMA in brain regions were corrected for [^{14}C]-sucrose vascular space to normalise uptake and reduce regional discrepancies due to differences in vascularity. Thus, any regional differences in brain uptake of radiolabelled solutes of interests are likely to be due to differences in transporter expression, rather than due to differences in blood supply.

By comparison to vascular space in brain regions, [^{14}C]-sucrose distribution in the pineal and pituitary gland samples is also an indicator of vascular space but represents the ability of [^{14}C]-sucrose to cross between capillary endothelial cells in the absence of tight junctions (paracellular permeability). By contrast, [^{14}C]-sucrose distribution in choroid plexus samples represents the vascular space and extracellular space formed between choroid plexus capillary endothelium and epithelium (Sanderson *et al.*, 2009).

Arginine

[^{3}H]-arginine (mol. wt., 174.2 g/mol; specific activity, 43 Ci/mmol; >97% radiochemical purity) was purchased from Amersham Radiochemicals, Buckinghamshire, UK.

The inclusion of [^{3}H]-arginine as a radiolabelled solute of interest in the artificial plasma thus facilitated the measurement of its penetration into the CNS after *in situ* brain/choroid plexus perfusion.

ADMA

[^{3}H]-ADMA (mol. wt., 276.7 g/mol; specific activity, 8 Ci/mmol; 96.4% radiochemical purity) was synthesised and tritiated by Amersham Radiochemicals, Cardiff, UK.

The inclusion of [^{3}H]-ADMA as a radiolabelled solute of interest in the artificial plasma thus facilitated the measurement of its penetration into the CNS after *in situ* brain/choroid plexus perfusion.

2.3.1.2F CNS sampling

After the perfusion time had elapsed the butterfly-winged needle was removed, and a sample of the artificial plasma taken. A sample of CSF was then taken from the *cisterna magna* (a subarachnoid compartment where CSF accumulates, and most convenient site for CSF sampling from small animals) using a pre-prepared micro-needle made from borosilicate glass capillaries, the animal decapitated and the brain removed. Samples were taken using micro-forceps and a Leica S4E L2 stereo-microscope (Leica; Buckinghamshire, UK), and are outlined in **Table 2-6**.

Table 2-6: Brain regions and circumventricular organs (CVOs) sampled for the *in situ* brain perfusion technique.

Brain regions	Circumventricular organs (CVOs)
Frontal cortex (FC)	Pineal gland (Pin)
Caudate nucleus (CN)	Choroid plexus (CP)
Occipital cortex (OC)	Pituitary gland (Pit)
Hippocampus (H)	
Hypothalamus (Hy)	
Thalamus (Th)	
Pons (P)	
Cerebellum (C)	

Cut-off values for vascular space were used for all brain perfusion experiments based on [^{14}C]-sucrose distribution (**Table 2-7**). These were in accordance with previously published values using the same method and in the same strain of mouse (Sanderson *et al.*, 2007). In the infrequent event that [^{14}C]-sucrose distribution in a CNS sample exceeded this maximum value, the sample was not utilised in any further analyses, as excess [^{14}C]-sucrose in a CNS sample indicates loss of brain barrier integrity, due to the poor penetrance of sucrose through the brain barriers under normal healthy conditions.

Table 2-7: Cut-off values for [^{14}C]-sucrose distribution in the mouse CNS at 2.5, 10, 20 and 30 minutes. The success rate for [^{14}C]-sucrose distribution being lower than values shown here was above 97%.

	Maximum [^{14}C]-sucrose distribution (mL·100 g^{-1})			
CNS region	**2.5 min**	**10 min**	**20 min**	**30 min**
Choroid plexus	15.0	25.0	35.0	45.0
Majority of brain regions	2.5	4.0	6.0	8.0
Cerebellum	3.0	5.0	8.0	10.0

2.3.1.2G Capillary depletion analysis

The microvasculature within a sample of brain tissue can be separated from the brain parenchyma using capillary depletion analysis (Triguero *et al.*, 1990). This method was previously validated by assaying the separated fractions for γ-glutamyl transpeptidase and alkaline phosphatase activity (two vascular enzyme markers). Separation was found to be approximately 95% efficient, and thus merely enriches the pellet resulting from centrifugation with brain capillary endothelial cells. This facilitates the broad examination of respective uptake into both the brain parenchyma fraction and the cerebral capillaries.

Following perfusion, the remaining brain tissue after microdissection of the regions described above (typically 200-300 mg) underwent capillary depletion following a method slightly modified for mouse (Sanderson *et al.*, 2007). A whole-brain homogenate was prepared using physiological capillary depletion buffer (defined in ***Appendix 1***) and a manual homogeniser, before adding 26% m/v dextran (final concentration 13% m/v, 60-90kDa, MP Biomedicals Europe, France) and homogenising again. Both the physiological capillary depletion buffer and dextran solution were maintained at 4 °C both to halt any cell metabolism and transport processes, and to reducing any cellular or protein damage due to heat generated from the homogenisation process. The homogenate (***Hom***) was centrifuged at 5400 r.c.f and 4 °C to produce an endothelial cell-enriched pellet (***Pel***) and supernatant containing brain parenchyma (***Sup***). A schematic depiction of this process is shown in **Figure 2-8**.

An important limitation of the capillary depletion technique is that the capillary-enriched pellet fraction is also likely to be contaminated with a number of other cells, such as smooth muscle cells and pericytes. Furthermore, while steps are taken to reduce cell damage it is likely some cells rupture during the process due to the shear forces generated by the homogenisation, and their contents may leak out to contaminate the supernatant fraction. As such, capillary depletion data should not be used to make firm conclusions but merely to better inform further studies.

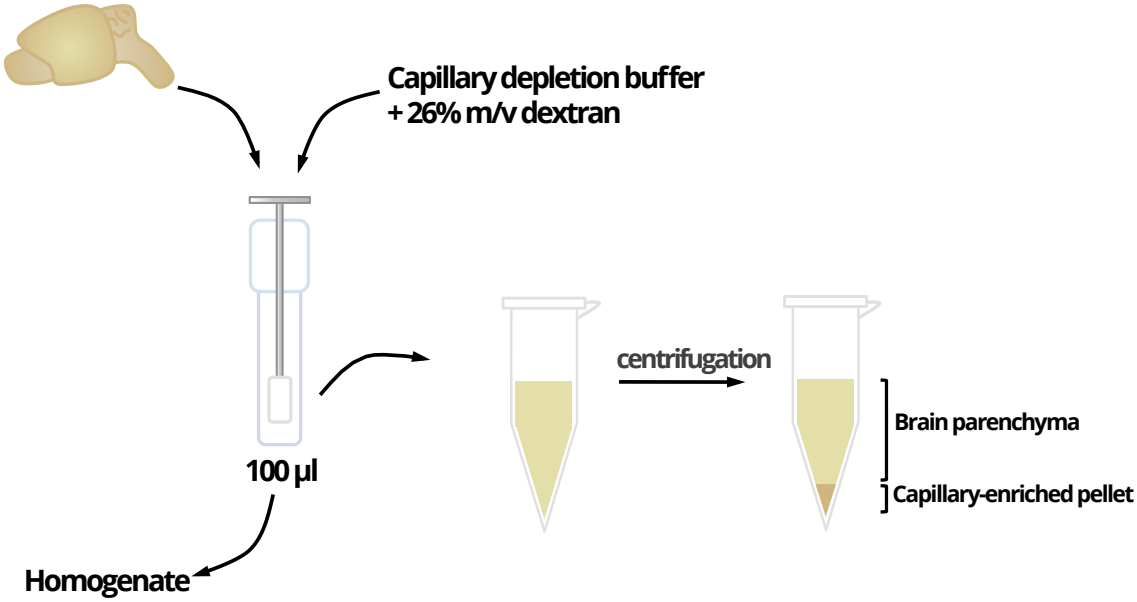

Figure 2-8: Capillary depletion assay. The remainder of the dissected brain is weighed and then homogenised in physiological capillary depletion buffer (3-fold volume of brain mass) and dextran added (4-fold volume of brain mass). Centrifugation of the homogenate at 5400 x r.c.f. for 15 minutes at 4 °C results in an endothelial cell enriched pellet and a supernatant consisting of brain parenchyma and interstitial fluid.

2.3.1.2H Liquid scintillation analysis

All samples (brain regions, capillary depletion brain homogenate, pellet and supernatant, CVOs, CSF and plasma samples) were solubilised in 0.5 mL tissue solubiliser (Solvable; Perkin-Elmer; Boston, MA, USA). After incubating the samples at room temperature for 48 h, 4 mL scintillation fluid (Lumasafe®; Perkin-Elmer; Boston, MA, USA) was added to each before vigorous vortexing. The amounts of [^{3}H] and [^{14}C] radioactivity in each sample were then quantified using a Packard Tri-Carb 2900TR counter (Perkin-Elmer; Boston, MA, USA). Counts per minute were then converted to disintegrations per minute (dpm) by the counter using internally stored quench curves from standards.

2.3.1.2I Expression of results

The distribution of radioactivity in the brain regions, CVOs and CSF is expressed as a percentage of that in the artificial plasma and termed R_{BRAIN}, R_{CVO} or R_{CSF}, respectively:

$$\begin{aligned} R_{BRAIN} &= \frac{\text{amount of radioactivity in tissue (dpm/g)}}{\text{amount of radioactivity in plasma (dpm/mL)}} \\ &= \frac{dpm\,/\,g}{dpm\,/\,mL} = \frac{dpm}{g} \times \frac{mL}{dpm} \\ &\therefore R_{BRAIN} = mL \cdot 100g^{-1} \end{aligned} \qquad [2.1]$$

Correcting for vascular space involved subtracting the R_{BRAIN} value obtained for [^{14}C]-sucrose in each sample from the R_{BRAIN} value concurrently obtained for the [^{3}H]-labelled solute of interest.

2.3.1.2J Perfusion time

As described in ***section 2.3.1.2 - In situ brain/choroid plexus perfusion***, one of the advantages of the *in situ* brain/choroid plexus perfusion technique utilised in these studies is the ability to easily vary perfusion time and determine uptake into the CNS at these different time points. Multiple-time (2.5, 10, 20 and 30 minute) uptake studies were performed in order to measure the respective uptake of [^{3}H]-arginine and [^{3}H]-ADMA into the mouse CNS over time. For these experiments both the radiolabelled

solute of interest and [^{14}C]-sucrose were included in the artificial plasma, and the perfusion stopped at the relevant time-points.

After perfusion the CNS samples were taken and prepared for liquid scintillation sampling as described in ***section 2.3.1.2F - CNS sampling***.

Using these data, the influx of the radiolabelled solutes of interest into the CNS can be calculated as the unidirectional transfer constant ($\boldsymbol{K_{in}}$). There are two methods to determine the $\boldsymbol{K_{in}}$ value of solutes into the CNS:

i. Single-time point analysis method, described by equation [2.3]
ii. Multiple-time point analysis method, described by equation [2.5]

The first method (i) is defined below (Collins & Dedrick, 1983; Smith & Rapoport, 1986):

$$K_{in} = \frac{C_{tissue}(T)}{\int_0^T C_{plasma}\, dt} \qquad [2.2]$$

Where $C_{tissue}(T)$ is radioactivity (dpm) per g of tissue at time-point T (perfusion time in minutes), and C_{plasma} is radioactivity (dpm) per mL of artificial plasma.

This equation assumes that the entry of the radiolabelled solute of interest into the CNS is proportional to, but less than, its concentration in the artificial plasma. Efflux of the solute from the CNS is therefore ignored (Collins & Dedrick, 1983; Smith & Rapoport, 1986; Zlokovic *et al.*, 1986; Williams *et al.*, 1996). Since the concentration of the radiolabelled solute of interest was kept constant during these experiments, $\int_0^T C_{plasma}\, dt = C_{plasma}(T)$, and thus equation [2.2] can be re-written as follows:

$$K_{in} = \frac{C_{tissue}(T)}{C_{plasma}(T)} \qquad [2.3]$$

It should however be noted that calculating the unidirectional rate constant from blood to CNS using this method requires that R_{tissue} *at time* T is first corrected for vascular

space by subtracting the concurrent R_{tissue} accumulation value for [^{14}C[-sucrose at that time-point.

The second method (ii) for calculating the unidirectional rate constant from blood to CNS requires multiple-time uptake data, shown in equation [2.4]:

$$\frac{C_{tissue}(T)}{C_{plasma}(T)} = K_{in}\frac{\int_0^T C_{plasma}\,dt}{C_{plasma}} + V_i \qquad [2.4]$$

Where $C_{tissue}(T)$ and $C_{plasma}(T)$ are amounts of radioactivity (dpm) per g of tissue and per mL of plasma, respectively; and $\boldsymbol{V_i}$ is the initial volume of distribution (Gjedde, 1981; Gjedde, 1982; Patlak et al., 1983; Zlokovic et al., 1986).

The following assumptions are made under this model (Williams *et al.*, 1996):

a. Within the system, artificial plasma is the only source of the solute of interest.
b. Concentration of the solute of interest may vary over time
c. The solute of interest does not alter the system

However, since the concentration of the radiolabelled solute of interest remains constant during these experimental conditions, $\frac{\int_0^T C_{plasma}\,dt}{C_{plasma}} = T$ and so equation [2.4] can be re-written as:

$$\frac{C_{tissue}(T)}{C_{plasma}(T)} = K_{in}T + V_i \qquad [2.5]$$

Thus, plotting the data points resulting from equation [2.5] at each time point defines a straight line ($y=mx+c$), where $\boldsymbol{K_{in}}$ is the slope, and $\boldsymbol{V_i}$ is the ordinate intercept. The goodness of fit (R^2) and p-value for deviation of slope from zero (p) were used to determine the suitability of this method for calculating the $\boldsymbol{K_{in}}$ and $\boldsymbol{V_i}$ values for each brain region and sample. Any transport of the radiolabelled solute of interest back from

the brain to the blood can be detected by a loss of linearity of the experimental points and could more easily be detected in the later time points (Zlokovic *et al.*, 1986).

2.3.1.2K Self-inhibition experiments

In situ brain perfusion self-inhibition experiments were performed with a ten-minute perfusion time, and each treatment group had N=5, unless otherwise stated. As a point of comparison to all other treatments, each set of experiments contained a 'control' group containing only the radiolabelled solute of interest and [^{14}C]-sucrose as a baseline measure.

The inclusion of solute of interest in its non-radiolabelled form in the artificial plasma provides an opportunity to quantify the competition for transport between the radiolabelled solute (detectable by liquid scintillation counting) and non-radiolabelled solute (undetectable), if any. Since uptake of only radiolabelled solute can be detected in the brain, a decrease in the uptake of radiolabelled solute in the presence of an excess of non-radiolabelled solute is indicative of a saturable influx transport system. Conversely, an increase in the uptake of radiolabelled solute in the presence of an excess of non-radiolabelled solute is indicative of a saturable efflux transport system.

Based on these principles, the uptake of [^{3}H]-arginine was measured in the presence of un-labelled *L*-arginine (Sigma Aldrich; Dorset, UK), and the uptake of [^{3}H]-ADMA measured in the presence of un-labelled N^{G},N^{G}-dimethylarginine dihydrochloride (ADMA, Sigma Aldrich; Dorset, UK). A breakdown of the experimental conditions used for self-inhibition experiments are shown in **Table 2-8** and **Table 2-9**.

Table 2-8: Summary of self-inhibition experiments for [^{3}H]-arginine uptake into the CNS as measured by *in situ* brain perfusion. Experiments were performed in the either the presence or absence of un-labelled arginine.

Radiolabelled compound	Added compound
[^{3}H]-Arginine (11.6 nM)	-
[^{3}H]-Arginine (11.6 nM)	Un-labelled *L*-arginine (100.0 µM)

Table 2-9: Summary of self-inhibition experiments for [^{3}H]-ADMA uptake into the CNS as measured by *in situ* brain perfusion.

Radiolabelled compound	Added compound
[^{3}H]-ADMA (62.5 nM)	-
[^{3}H]-ADMA (62.5 nM)	Un-labelled ADMA (0.5 µM)
[^{3}H]-ADMA (62.5 nM)	Un-labelled ADMA (3.0 µM)
[^{3}H]-ADMA (62.5 nM)	Un-labelled ADMA (10.0 µM)
[^{3}H]-ADMA (62.5 nM)	Un-labelled ADMA (100.0 µM)
[^{3}H]-ADMA (62.5 nM)	Un-labelled ADMA (500.0 µM)

These concentrations were selected as the plasma concentration for ADMA under normal physiological conditions is typically found to be approximately 0.5 µM in humans and a number of mammalian species, including mouse (Martens-Lobenhoffer *et al.*, 2004; Lajer *et al.*, 2008; Wang *et al.*, 2008; Wang *et al.*, 2009). Plasma concentrations for ADMA under pathological conditions are typically in the range of 3.0 µM (Cakir *et al.*, 2005; Bode-Boger *et al.*, 2007). Concentrations above 10 µM can be considered as supraphysiological as ADMA would not ordinarily be found at concentrations that high in the body in health or disease.

After co-perfusion with the relevant radiolabelled solute of interest, the CNS was sampled and prepared for liquid scintillation counting as described earlier (***section 2.3.1.2F - CNS sampling***).

The perfusion of [^{3}H]-ADMA with a range of un-lablled ADMA concentrations presented an opportunity for the calculation of $\boldsymbol{K_m}$ (half-saturation constant) and $\boldsymbol{V_{max}}$ (maximal velocity of transport). These were calculated for every sample obtained from ADMA self-inhibition studies, as follows:

1. Divide $\boldsymbol{R_{BRAIN}}$ values for [^{3}H]-ADMA (sucrose-corrected where applicable, mL.100g^1) by the length of perfusion time (in this case 10 minutes) to obtain $\boldsymbol{K_{in}}$ (mL.min^{-1} g^{-1})
2. Multiply $\boldsymbol{K_{in}}$ values by the total concentration of ADMA (radiolabelled + un-labelled, in mM) in the perfusate for each experimental group to obtain total flux values (µmol.min^{-1} g^{-1})
3. Plot total flux values (*y*-axis) against concentration (*x*-axis) and perform Michaelis-Menten kinetics analysis
4. Determine $\boldsymbol{K_d}$ (diffusion constant, mL.min^{-1} g^{-1}) by calculating the slope of flux *vs.* concentration for values after saturation using linear regression analysis. Saturation can be determined by performing multiple un-paired two-tailed t-tests comparing the values. The saturation point is the point at which the values do not significantly differ from each other.
5. Multiply $\boldsymbol{K_d}$ values by the range of total ADMA concentrations used for each experimental group (in mM).
6. Subtract these values from the total flux values for each treatment group to obtain the saturable component of total flux
7. Plot values for saturable component of total (*y*-axis) against concentration (*x*-axis) and perform Michaelis-Menten kinetics analysis to obtain $\boldsymbol{K_m}$ and $\boldsymbol{V}$

2.3.1.2L Cross-competition experiments

Based on a similar principle to that explained above (see ***section 2.3.1.2K - Self-inhibition experiments***), cross-competition experiments involve the inclusion of un-labelled potential competitors or inhibitors of transport. ADMA and arginine cross-competition experiments followed the following experimental designs:

i. Transporter inhibitor experiments
ii. Direct competition between ADMA & *L*-arginine
iii. Pre-loading / trans-stimulation experiments

After confirming the existence of a saturable transport system *via* self-inhibition studies one can measure the uptake of radiolabelled solutes of interest in the presence of these potential competitors or inhibitors. In the event that uptake of the solute of interest in the presence of a potential competitor *decreases* relative to control one can conclude that the potential competitor does indeed compete for transport into the brain. Conversely, if the uptake of the radiolabelled solute of interest *increases* this would be indicative of competition for efflux from the CNS to the blood.

Transporter inhibitor experiments

To examine the involvement of transporters in the uptake of both *L*-arginine and ADMA into the CNS, specific inhibitors of transport were added to the artificial plasma. The inclusion of transport inhibitors can correlate with either an increase or decrease in the uptake of the solute of interest; which is respectively indicative of an efflux from, or influx into the CNS. All experimental groups involved a perfusion time of 10 minutes. All transport inhibitors used were purchased from Sigma Aldrich; Dorset, UK and were readily soluble in the artificial plasma – requiring no extra steps for dissolution beyond standard mechanical stirring and heating to physiological temperature (37 °C). A breakdown of the experimental conditions used for transport inhibitor experiments are shown in **Table 2-10**. After co-perfusion with the relevant radiolabelled solute of interest, the CNS was sampled and prepared for liquid scintillation counting as described earlier.

Table 2-10: Summary of transport inhibitor experiments for [^{3}H]-arginine and [^{3}H]-ADMA uptake into the CNS as measured by *in situ* brain perfusion.

[^{3}H]-Arginine

Inhibitor and molar concentration	**Transporters inhibited**	**Ref**
L-homoarginine (20 mM)	CAT-1	(White, 1985)
BCH (4mM)	$ATB^{0,+}$, LAT-1	(Van Winkle *et al.*, 1990a)
α-methyl-*D,L*-tryptophan (500 μM)	$ATB^{0,+}$	(Karunakaran *et al.*, 2008)

[^{3}H]-ADMA

L-homoarginine (20 mM)	CAT-1	(White, 1985)
BCH (4mM)	$ATB^{0,+}$, LAT-1	(Van Winkle *et al.*, 1990a)
α-methyl-*D,L*-tryptophan (500 μM)	$ATB^{0,+}$	(Karunakaran *et al.*, 2008)
L-phenylalanine (200 μM)	LAT-1	(Smith *et al.*, 1987)
L-leucine (5 mM)	y^+LAT-1, -2?	(Deves *et al.*, 1992)
Harmaline (2 mM)	$b^{0,+}$AT, rBAT	(O'Kane *et al.*, 2006)

Direct competition between ADMA & *L*-arginine

Uptake of [^{3}H]-arginine was also measured in the presence of un-labelled ADMA, and the uptake of [^{3}H]-ADMA measured in the presence of un-labelled *L*-arginine. A breakdown of the experimental conditions used for cross-competition experiments are shown in **Table 2-11** and **Table 2-12.**

Table 2-11: Summary of cross-competition experiments for [^{3}H]-arginine uptake into the CNS as measured by *in situ* brain perfusion.

Radiolabelled compound	Added compound
[^{3}H]-Arginine (11.6 nM)	-
[^{3}H]-Arginine (11.6 nM)	Un-labelled ADMA (0.5 μM)
[^{3}H]-Arginine (11.6 nM)	Un-labelled ADMA (3.0 μM)
[^{3}H]-Arginine (11.6 nM)	Un-labelled ADMA (10.0 μM)
[^{3}H]-Arginine (11.6 nM)	Un-labelled ADMA (100.0 μM)
[^{3}H]-Arginine (11.6 nM)	Un-labelled ADMA (500.0 μM)

Table 2-12: Summary of cross-competition experiments for [^{3}H]-ADMA uptake into the CNS as measured by *in situ* brain perfusion.

Radiolabelled compound	Added compound
[^{3}H]-ADMA (62.5 nM)	-
[^{3}H]-ADMA (62.5 nM)	Un-labelled *L*-arginine (100.0 μM)

As described previously, ADMA concentrations were selected at 0.5 and 3.0 μM to represent plasma concentrations seen in health and disease, respectively, whereas the higher concentrations of ADMA were deliberately selected to recreate conditions of excess ADMA. After co-perfusion with the relevant radiolabelled solute of interest, the

CNS was sampled and prepared for liquid scintillation counting as described earlier (***section 2.3.1.2F - CNS sampling***).

Pre-loading / trans-stimulation experiments

As described in ***section 2.1.1.4B - Trans-stimulation hypothesis***, trans-stimulation is the stimulation of transport of a substrate, by the presence of substrate on the opposite side of the membrane.

To investigate trans-stimulation of ADMA and *L*-arginine transport at the mouse blood-brain barrier, a series of trans-stimulation experiments were designed to investigate the influence of supplemental amounts of *L*-arginine (200 µM *L*-arginine) on the efflux of preloaded ADMA (either radiolabelled or un-labelled), or the effect of increasing concentrations of intracellular ADMA on the influx of extracellular [^{3}H]-arginine into the CNS. The basic premise for these experiments was to pre-load the CNS and CNS microvasculature with ADMA to re-create conditions of high ADMA concentrations seen in disease, to measure what effect this had on consequent [^{3}H]-arginine influx into the CNS and [^{3}H]-ADMA efflux from the CNS.

Based on the previously observed uptake of [^{3}H]-ADMA into the CNS in experiments described in ***section 2.3.1.2J - Perfusion time***, the concentration of ADMA pre-loaded with or without [^{3}H]-ADMA (and [^{14}C]-sucrose) was 500 µM – an excess concentration to ensure ADMA accumulated within the brain capillary endothelium and CNS. Transport of only one radiolabelled solute of interest was investigated at a time per experimental group (*i.e.* efflux of [^{3}H]-ADMA first in one set of animals, and then influx of [^{3}H]-arginine into the CNS in a separate set of animals). [^{14}C]-sucrose was included in all experiments as an internal control of blood-CNS barrier integrity, measure of vascular space in brain regions and choroid plexus, and extracellular space in pineal and pituitary glands, as described in ***section 2.3.1.2E - Radiolabelled solutes of interest***. The use of 200 µM un-labelled *L*-arginine was following the observation that the plasma concentration of *L*-arginine attained after dietary

supplementation of *L*-arginine in patients is 200 µM (Clarkson *et al.*, 1996; Adams *et al.*, 1997).

Pre-loading was achieved by perfusion for 20 minutes with one solution, and then switching to a second solution for the remaining 10-minute perfusion. The total perfusion time was 30 minutes. Since artificial plasma exits circulation *via* an incision made in the right atrium of the heart, one can be reasonably sure that solutes in the perfusate are only exposed to transporters in the circulation once – with a 'single-pass'. As an extension of this concept, changing to a new solution of artificial plasma during the perfusion should expose the circulation only to the solutes in the new artificial plasma, rather than any left behind from the pre-load perfusion.

A breakdown of the experimental conditions used for trans-stimulation experiments are shown in **Table 2-13**. After the full 30-minute perfusion with the relevant radiolabelled solute of interest had elapsed, the CNS was sampled and prepared for liquid scintillation counting as described earlier.

Table 2-13: Summary of trans-stimulation experiments for [^{3}H]-arginine and [^{3}H]-ADMA uptake into the CNS as measured by *in situ* brain perfusion.

Pre-perfusion (pre-load, 20 minutes)	**Post-perfusion (10 minutes)**
No additives (control)	[^{3}H]-arginine
Un-labelled ADMA (500 µM)	[^{3}H]-arginine
Un-labelled ADMA (500 µM)	[^{3}H]-arginine + un-labelled *L*-arginine (200 µM)
[^{3}H]-ADMA	No additives (control)
[^{3}H]-ADMA	Un-labelled *L*-arginine (200 µM)

2.3.1.3 Octanol-saline partition coefficient

0.75 mL phosphate buffered saline (pH 7.4) containing 1 µCi (0.037 MBq) of either [^{14}C]-sucrose (2.5 µM), [^{3}H]-ADMA (542.8 nM) [^{3}H]-arginine (101.0 nM) was added to an Eppendorf centrifuge tube containing 0.75 mL octanol (Sigma Aldrich; Dorset, UK) before vortexing for 5 seconds. This was then centrifuged (2634 *r.c.f* for 5 mins) and 100 µL samples taken from both the hydrophobic (octanol) phase and hydrophilic (saline) phase in triplicate for radioactive scintillation counting. The following equation was used to calculate the octanol-saline partition coeffecient of the respective drugs and expressed as mean±SEM:

$$\frac{\text{mean radioactivity in octanol (dpm/mL)}}{\text{mean radioactivity in saline (dpm/mL)}} \qquad [2.6]$$

2.3.2 Statistics

Data from all experiments are presented as mean ± standard error of the mean (SEM). Due to the broad range of experimental design and methods, specific details of statistical analyses performed on individual data sets will be presented in the context of the data in results chapters. Statistical significance was taken as follows: not significant (ns) $p > 0.05$, $^{*}p < 0.05$, $^{**}p < 0.01$, $^{***}p < 0.001$. All statistical analyses were performed using GraphPad Prism v5.0c graphing and statistics package for Mac.

2.4 Results

2.4.1 Solute uptake using the *in situ* brain/choroid plexus perfusion method

2.4.1.1 Sucrose baseline

Since [^{14}C]-Sucrose can only enter the brain and CSF by simple diffusion it is a useful molecule to use as an internal control for BBB and BCSFB integrity in each experiment. It can also provide an approximation of cerebrovascular space in brain regions, and extracellular space formed between choroid plexus capillary endothelium and epithelium, and thus is a measure of variation between animals (Sanderson *et al.*, 2009). [^{14}C]-Sucrose values for all control experiments in all regions were concurrently compared to [^{14}C]-sucrose values for treatment experiments (one-way ANOVA with Dunnett's post-hoc test comparing means for each region), and found to be not significant in any cases ($p > 0.05$, example of comparison shown in **Figure 2-9**). Thus, none of the experimental conditions affected vascular space or barrier integrity.

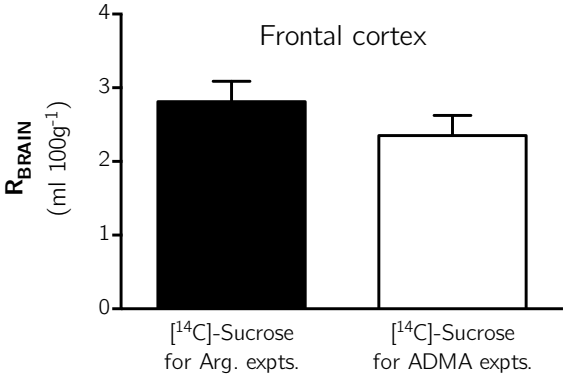

Figure 2-9: Example of the distribution of [^{14}C]-Sucrose in the frontal cortex following co-perfusion with either [^{3}H]-arginine alone or [^{3}H]-ADMA alone for 10 minutes. Each bar represents the mean ± SEM of 4-7 animals. Distribution is expressed as the percentage ratio of tissue to plasma (mL.100 g^{-1}). Means ± SEM values were compared and found to not differ (one-way ANOVA with Dunnett's post hoc test, $p > 0.05$).

Figure 2-10 shows multiple-time uptake plots for [^{14}C]-sucrose distribution in the eight brain regions (frontal cortex, caudate nucleus, occipital cortex, hippocampus, hypothalamus, thalamus, pons and cerebellum). As demonstrated in all plots, the distribution of [^{14}C]-sucrose in all regions of the brain after perfusion is very low. A time-dependent increase in the distribution (% R_{Brain}) of [^{14}C]-sucrose was observed in all regions (*e.g.* 2.34±0.23% after 2.5 minutes to 5.86±0.92% after 30 minutes in the frontal cortex), however no regional differences were observed ($p > 0.05$, two-way ANOVA with Tukey's multiple comparison test for each brain region compared to all others within each time point). The unidirectional transfer constants ($\boldsymbol{K_{in}}$) and initial volumes of distribution ($\boldsymbol{V_i}$) for [^{14}C]-sucrose in these regions were respectively determined as the slope and ordinate intercept from the plots in **Figure 2-10**, and are shown in **Table 2-14**.

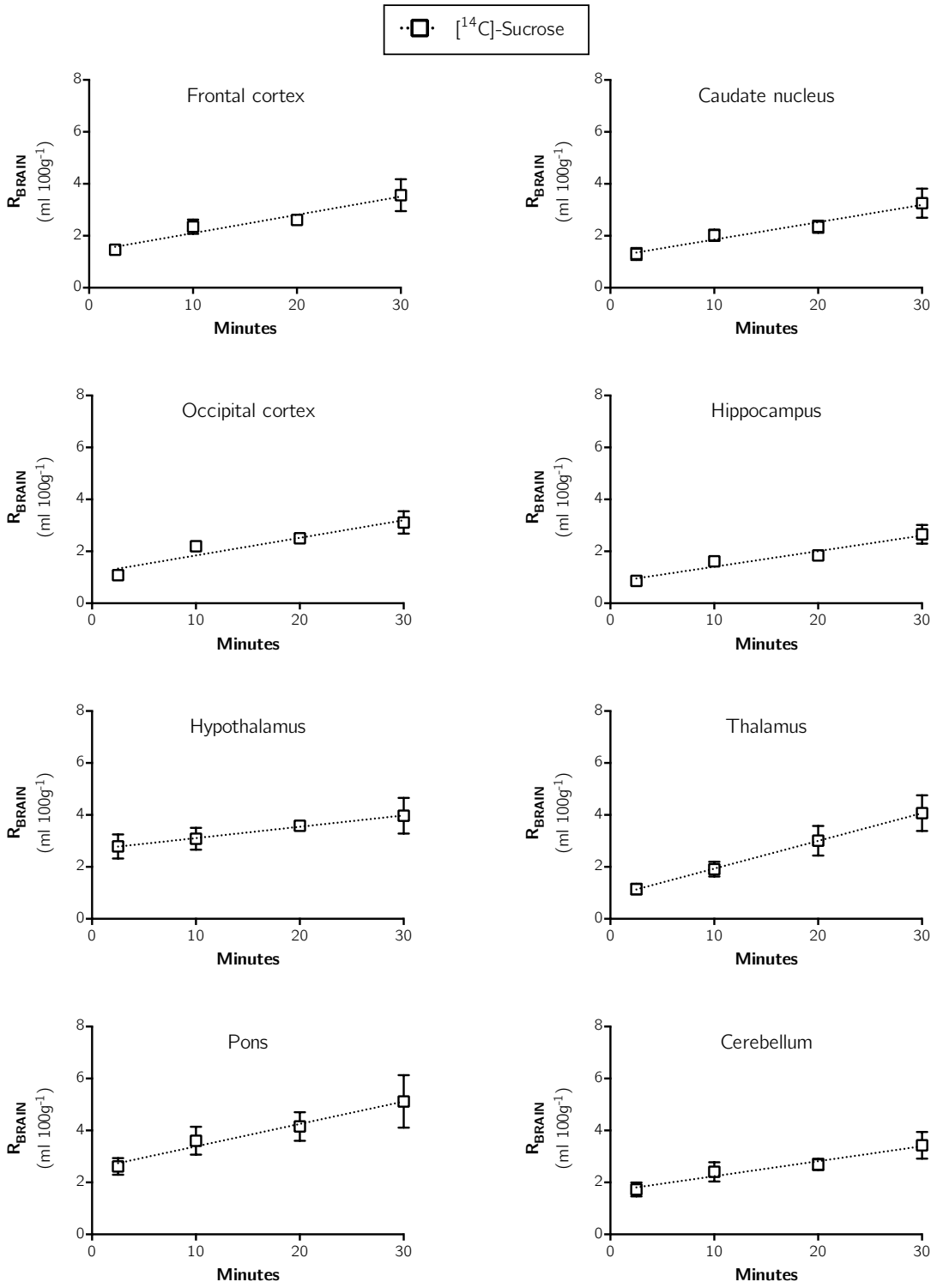

Figure 2-10: The brain distribution of [^{14}C]-Sucrose as a function of time. Distribution is expressed as the percentage ratio of tissue to plasma (mL.100 g^{-1}). Each point represents the mean ± SEM of 4-7 animals. K_{in} and V_i values were determined as the slope and ordinate intercept of the computed regression lines where appropriate (GraphPad Prism 6.0 for Mac).

Figure 2-11 shows multiple-time uptake plots for [^{14}C]-sucrose distribution in capillary depletion samples. While a time-dependent increase in sucrose distribution was observed in whole-brain homogenate, and its components after separation (brain parenchyma-containing supernatant and endothelial cell-enriched pellet), only the endothelial cell-enriched pellet was found to significantly differ from the other capillary depletion samples, and brain regions sampled ($p < 0.01$, two-way ANOVA with Tukey's multiple comparison test for each brain region compared to all others within each time point). The unidirectional transfer constants ($\boldsymbol{K_{in}}$) and initial volumes of distribution ($\boldsymbol{V_i}$) for [^{14}C]-sucrose in these regions were respectively determined as the slope and ordinate intercept from the plots in **Figure 2-11**, and are shown in **Table 2-14**.

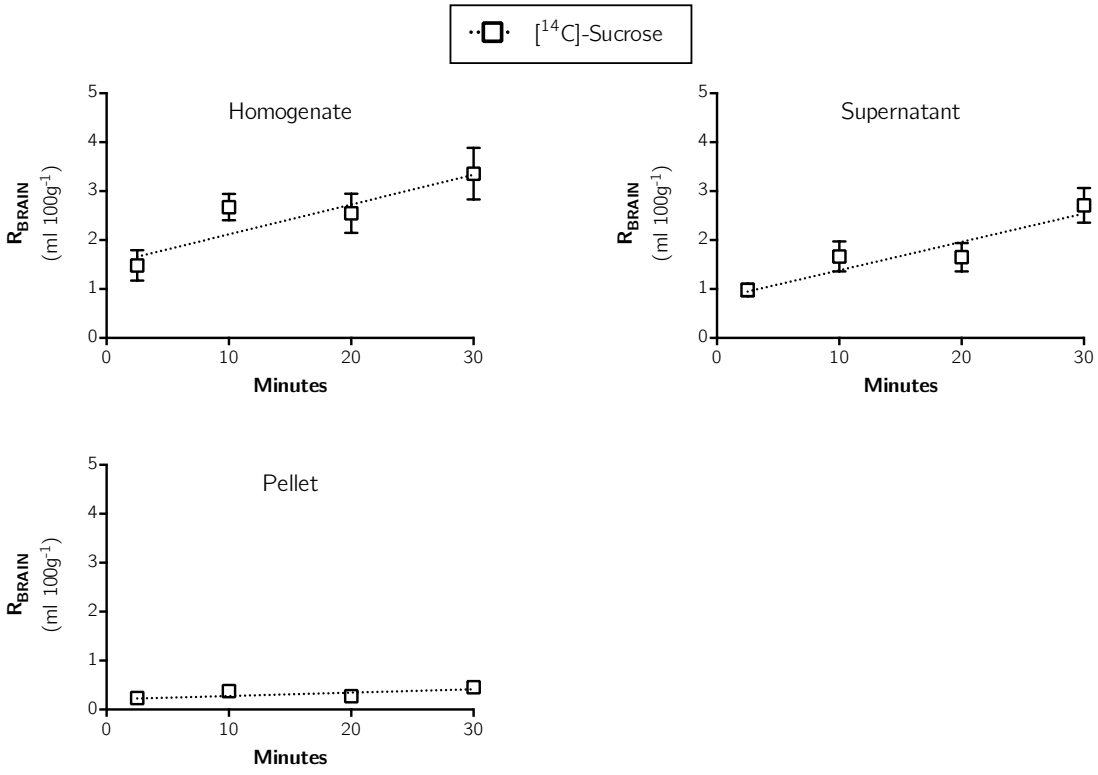

Figure 2-11: Distribution of [^{14}C]-Sucrose in capillary depletion samples following *in* situ brain perfusion as a function of time. Uptake is expressed as the percentage ratio of tissue to plasma (mL.100 g^{-1}). Each point represents the mean ± SEM of 4-7 animals. $\boldsymbol{K_{in}}$ and $\boldsymbol{V_i}$ values were determined as the slope and ordinate intercept of the computed regression lines (GraphPad Prism 6.0 for Mac).

Multiple-time uptake plots for [^{14}C]-sucrose distribution in the CSF, pineal gland, choroid plexus and pituitary gland are shown in **Figure 2-12**. Maximum values for [^{14}C]-sucrose accumulation in the CSF (10.14±0.11% at 30 minutes) are lower than in the pineal gland (38.47±3.12% at 10 minutes), choroid plexus (22.30±3.57% at 30 minutes) or pituitary gland (21.49±2.31% at 20 minutes). This is expected, as CSF accumulation values only represent diffusion through the paracellular pathways of the choroid plexus. Since the slope of the linear regression line fitted to the multiple-time uptake values for [^{14}C]-sucrose in the pineal gland, choroid plexus and pituitary gland did not significantly deviate from zero ($p > 0.05$), calculation of $\boldsymbol{K_{in}}$ and $\boldsymbol{V_i}$ by the multiple-time uptake method was deemed inappropriate. $\boldsymbol{K_{in}}$ was therefore calculated using the single time point method, and shown in **Table 2-15**.

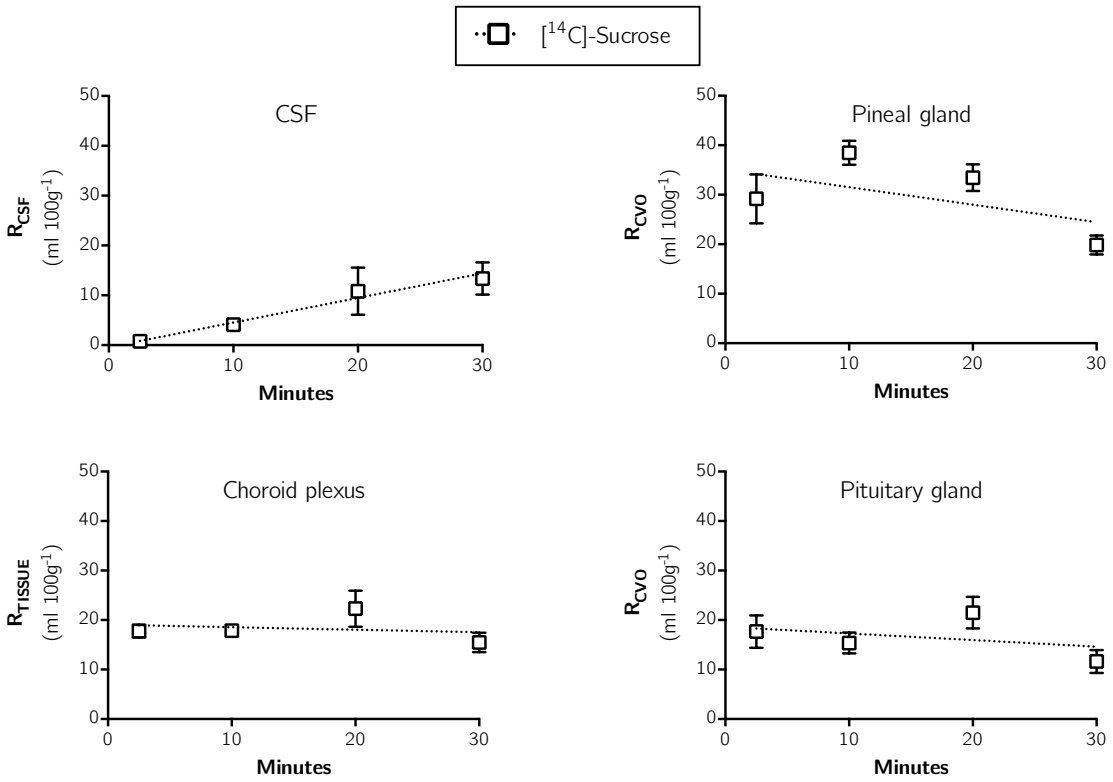

Figure 2-12: Distribution of [^{14}C]-Sucrose in the CSF, pineal gland, choroid plexus and pituitary gland following *in* situ brain perfusion as a function of time. Distribution is expressed as the %age ratio of tissue or CSF to plasma (mL.100 g^{-1}). Each point represents the mean±SEM of 4-7 animals. $\boldsymbol{K_{in}}$ and $\boldsymbol{V_i}$ values were determined where appropriate as the slope and ordinate intercept of computed regression lines (GraphPad Prism 6.0 for Mac).

Table 2-14: [^{14}C]-Sucrose K_{in} values in different brain regions, capillary depletion samples, choroid plexus, and circumventricular organs, calculated from 2.5, 10, 20 & 30 minute co-perfusions with [^{3}H]-Arginine (multiple-time uptake equation). *P* values calculated using linear regression analysis to determine slope deviation from zero.

	Brain sample	p	R^2	K_{in} ($\mu L.min^{-1}\ g^{-1}$)	V_i ($mL.100\ g^{-1}$)
Brain regions	Front cortex	0.0004	0.5071	0.0704 ± 0.0164	1.3981 ± 0.3068
	Caudate nucleus	0.0005	0.4951	0.0667 ± 0.0159	1.1892 ± 0.2978
	Occipital cortex	< 0.0001	0.6130	0.0678 ± 0.0127	1.1650 ± 0.2380
	Hippocampus	< 0.0001	0.6579	0.0600 ± 0.0102	0.8076 ± 0.1913
	Hypothalamus	0.0491	0.8221	0.0437 ± 0.0227	2.6721 ± 0.4302
	Thalamus	0.0001	0.5714	0.1067 ± 0.0218	0.8664 ± 0.4085
	Pons	0.0074	0.3524	0.0864 ± 0.0284	2.5244 ± 0.5102
	Cerebellum	0.0026	0.4027	0.0577 ± 0.0166	1.6639 ± 0.3105
Capillary depletion	Homogenate	0.0061	0.3835	0.0609 ± 0.0193	1.5081 ± 0.3761
	Supernatant	0.0006	0.5540	0.0580 ± 0.0134	0.8038 ± 0.2672
	Pellet	0.0151	0.3539	0.0069 ± 0.0025	0.2079 ± 0.0506
BCSFB	CSF	0.0026	0.6121	0.4937 ± 0.1243	0.1578 ± 0.3937
	Pineal gland	n.s.	0.1700	-	-
	Choroid plexus	n.s.	0.0134	-	-
	Pituitary gland	n.s.	0.0439	-	-

Table 2-15: [^{14}C]-Sucrose K_{in} values in the pineal gland, choroid plexus and pituitary gland samples, calculated from 10 minute co-perfusions with [^{3}H]-Arginine (single time point equation).

	Time point	**K_{in}** ($\mu L.min^{-1}\ g^{-1}$)	**n**
Pineal gland	10 minutes	6.2182 ± 1.5222	7
Choroid plexus	10 minutes	2.7214 ± 0.6443	7
Pituitary gland	10 minutes	1.5373 ± 0.2123	7

$\boldsymbol{K_{in}}$ values shown in **Table 2-14** and **Table 2-15** were analysed by one-way ANOVA with Tukey's multiple comparisons test. Samples within the group of eight brain regions analysed were not found to be significantly different from each other ($p > 0.05$). Within the group of samples obtained from capillary depletion analysis, only the $\boldsymbol{K_{in}}$ value for whole-brain homogenate was found to be significantly greater than that for the capillary-enriched pellet. Within the group of CVO samples, only the $\boldsymbol{K_{in}}$ value for the pineal gland was found to be significantly higher than that for the pituitary gland.

$\boldsymbol{V_i}$ values shown in **Table 2-14** and **Table 2-15** were also analysed by one-way ANOVA with Tukey's multiple comparisons test. Samples within the group of eight brain regions analysed were not found to be significantly different from each other ($p > 0.05$). Within the group of samples obtained from capillary depletion analysis, only the $\boldsymbol{V_i}$ value for whole-brain homogenate was found to be significantly greater than that for the capillary-enriched pellet.

2.4.1.2 Arginine: The NO precursor

As previously mentioned in ***section 2.3.1.2E - Radiolabelled solutes of interest***, the molecular weights of [^{14}C]-sucrose and [^{3}H]-arginine are comparable. Furthermore, the two compounds are similarly polar; as octanol saline analysis of [^{14}C]-sucrose and [^{3}H]-arginine revealed octanol partition coefficients of 0.00105±0.00022 and 0.00149±0.00016 respectively.

Figure 2-13 shows the progressive increase in the distribution (% R_{Brain}) of [^{3}H]-arginine over time (relative to [^{14}C]-sucrose) in the frontal cortex, caudate nucleus, occipital cortex, hippocampus, pons and cerebellum. Uptake of [^{3}H]-arginine is significantly greater than [^{14}C]-sucrose in all brain regions, at all time points (multiple Student's paired t-tests, $p < 0.05$ in all cases).

A time-dependent increase in the distribution of [^{3}H]-arginine (corrected for [^{14}C]-sucrose) was observed in all regions (*e.g.* 28.96±4.03% after 2.5 minutes to 176.78±31.60% after 30 minutes in the frontal cortex, **Figure 2-13**), however no regional differences were observed ($p > 0.05$, two-way ANOVA with Tukey's multiple comparison test for each brain region compared to all others within each time point).

Figure 2-15 shows a time-dependent increase in the distribution of [^{3}H]-arginine in all three capillary depletion samples. No differences in the distribution of [^{3}H]-arginine between the homogenate and supernatant (containing brain parenchyma) were observed, however both of these samples contained a higher distribution than that observed in the endothelial cell-enriched pellet ($p < 0.01$, two-way ANOVA with Tukey's multiple comparison test for each sample compared to all others).

A similar time-dependent increase in the distribution of [^{3}H]-arginine (un-corrected data) was observed in the CSF (4.41±1.41% after 2.5 minutes to 120.44±25.08% after 30 minutes, **Figure 2-16**). A comparison of the mean [^{3}H]-arginine distributions between the pineal gland, choroid plexus and pituitary gland revealed that a significant difference is observed between the pineal gland and pituitary gland, but only after a 30

minute perfusion ($p < 0.001$, two-way ANOVA with Tukey's multiple comparison test for each sample compared to all others within each time point).

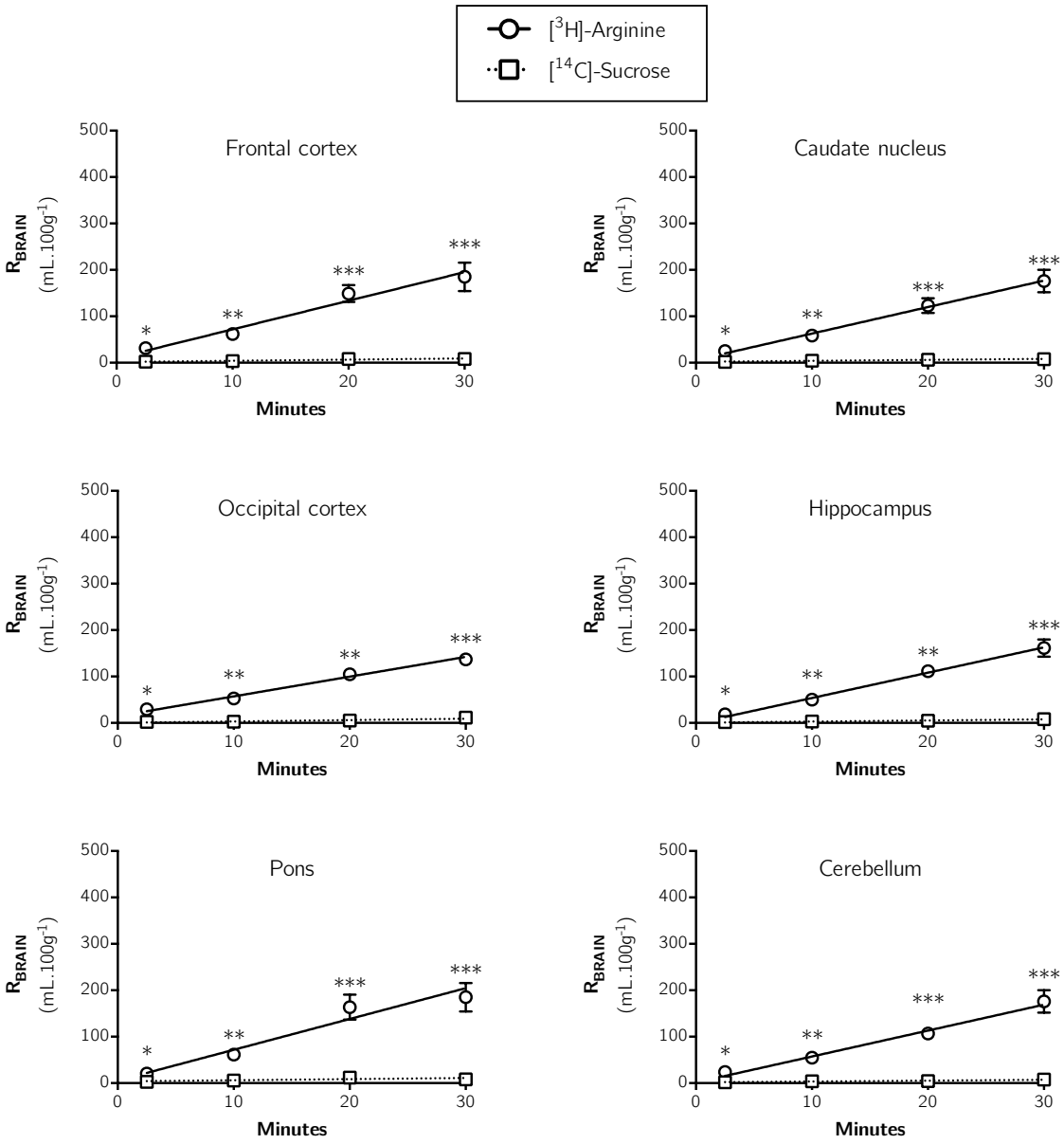

Figure 2-13: The brain distribution of [^{3}H]-arginine and [^{14}C]-sucrose as a function of time. Uptake is expressed as the percentage ratio of tissue to plasma (mL.100 g^{-1}). Each point represents the mean ± SEM of 4-7 animals. K_{in} and V_i values were determined as the slope and ordinate intercept of the computed regression lines where appropriate. Asterisks represent one-tailed, paired student's t-tests comparing mean±SEM at each time point, *$p < 0.05$, **$p < 0.01$, ***$p < 0.001$ (GraphPad Prism 6.0 for Mac).

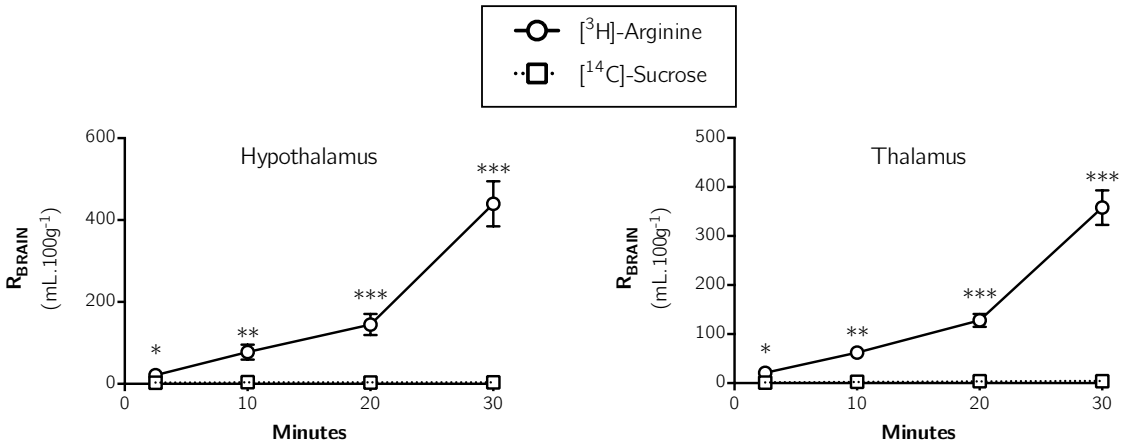

Figure 2-14: The distribution of [^{3}H]-arginine and [^{14}C]-sucrose into the mouse hypothalamus and thalamus as a function of time. Uptake is expressed as the percentage ratio of tissue to plasma (mL.100 g^{-1}). Each point represents the mean ± SEM of 4-7 animals. K_{in} and V_i values could not be determined as the slope and ordinate intercept of the computed regression lines for [^{3}H]-arginine, since the ordinate intercept in both analyses were negative, and thus these data points are shown with connecting lines (GraphPad Prism 6.0 for Mac). K_{in} values for [^{3}H]-arginine were therefore calculated using the single-time uptake method. Asterisks represent one-tailed, paired student's t-tests comparing mean±SEM at each time point, *$p < 0.05$, **$p < 0.01$, ***$p < 0.001$.

A time-dependent increase in the distribution of [^{3}H]-arginine (corrected for [^{14}C]-sucrose) was observed in both the hypothalamus and thalamus (shown in **Figure 2-14**). These brain regions are shown separately from the others, as the R_{BRAIN} values for 30-minute perfusions were both so high that linear regression analysis produced negative V_i values. Since this is impossible it was not deemed appropriate to analyse these samples in the same way. K_{in} values were therefore calculated using the single-time uptake method, and shown in **Table 2-17**.

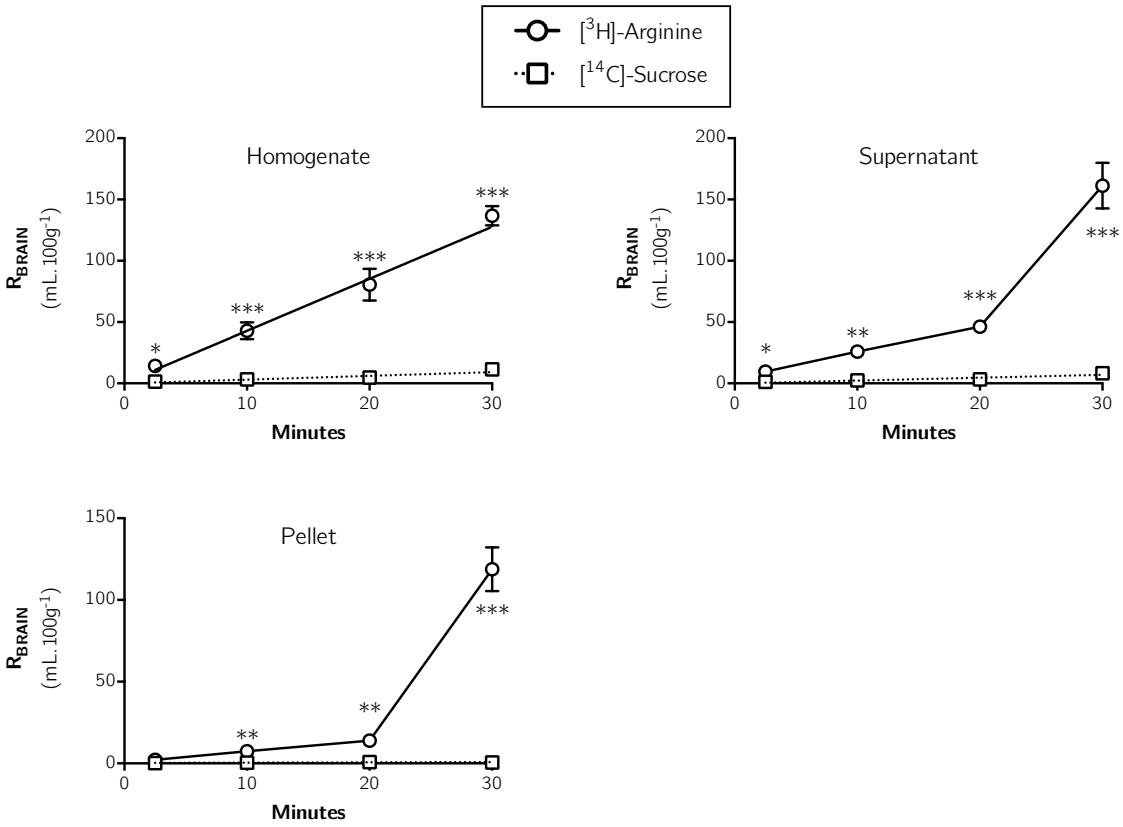

Figure 2-15: Distribution of [^{3}H]-arginine and [^{14}C]-sucrose in capillary depletion samples following *in* situ brain perfusion as a function of time. Uptake is expressed as the percentage ratio of tissue to plasma (mL.100 g^{-1}). Each point represents the mean ± SEM of 4-7 animals. K_{in} and V_i values were determined as the slope and ordinate intercept of the computed regression lines (GraphPad Prism 6.0 for Mac). K_{in} and V_i values could not be determined as the slope and ordinate intercept of the computed regression lines for [^{3}H]-arginine distribution in the supernatant and pellet samples, since the ordinate intercept in both analyses were negative, and thus these data points are shown with connecting lines (GraphPad Prism 6.0 for Mac). K_{in} values for [^{3}H]-arginine were therefore calculated using the single-time uptake method. Asterisks represent one-tailed, paired student's t-tests comparing mean±SEM at each time point, *$p < 0.05$, **$p < 0.01$, ***$p < 0.001$.

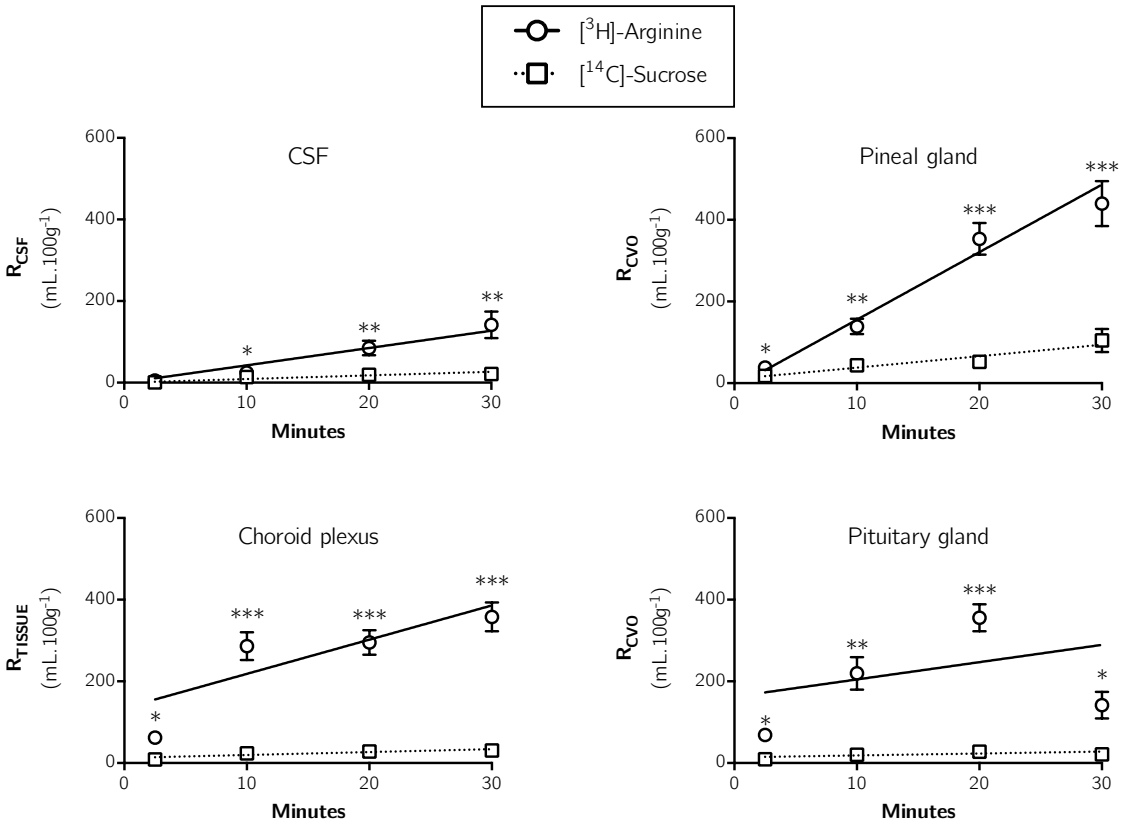

Figure 2-16: Distribution of [^{3}H]-arginine and [^{14}C]-sucrose in the CSF, pineal gland, choroid plexus and pituitary gland following *in* situ brain perfusion as a function of time. Uptake is expressed as the percentage ratio of tissue or CSF to plasma (mL.100 g^{-1}). Each point represents the mean ± SEM of 4-7 animals. K_{in} and V_i values were determined as the slope and ordinate intercept of the computed regression lines. Asterisks represent one-tailed, paired student's t-tests comparing mean±SEM at each time point, $*p < 0.05$, $**p < 0.01$, $***p < 0.001$ (GraphPad Prism 6.0 for Mac).

$\boldsymbol{K_{in}}$ and $\boldsymbol{V_i}$ values for [^{3}H]-arginine in brain regions were respectively determined as the slope and ordinate intercept from the plots shown in **Figure 2-13**, **Figure 2-14**, **Figure 2-15** and **Figure 2-16**, and are shown in **Table 2-16**. Linear regression analysis on these plots produced R-square (R^2) for goodness of fit, and p-values relating to the deviation of the line slope from 0. P-values were found to be significant for all samples ($p < 0.05$) except for the pituitary gland, and thus it was deemed inappropriate to calculate $\boldsymbol{K_{in}}$ or $\boldsymbol{V_i}$ using the multiple-time uptake method.

For all remaining samples, the goodness of fit for the linear regression analysis was found within acceptable limits ($R^2 < 0.4$). However, $\boldsymbol{V_i}$ values for [^{3}H]-arginine in the all samples except for the occipital cortex and choroid plexus were calculated to be negative either outright (*e.g.* -9.82 ± 37.40 mL.100 g^{-1} for the pineal gland), or when considering SEM (*e.g.* 10.28 ± 17.37 mL.100 g^{-1} for the frontal cortex). Negative $\boldsymbol{V_i}$ values are of course a technical impossibility, and the values shown in **Table 2-16** more likely represent a limitation of this analysis. However, this fact in itself pulls into question the credibility of the $\boldsymbol{K_{in}}$ values calculated by the same multiple-time uptake method. Thus the multiple-time uptake method for calculating $\boldsymbol{K_{in}}$ for these data was deemed inappropriate, and values shown in **Table 2-16** are therefore more as a point of reference to demonstrate how this conclusion was reached. It was therefore deemed more appropriate to calculate the $\boldsymbol{K_{in}}$ value for these regions using the single-uptake method – shown in **Table 2-17**.

No significant difference was observed for $\boldsymbol{K_{in}}$ values for [^{3}H]-arginine between any of the brain regions, the CSF, or capillary depletion samples ($p > 0.05$, one-way ANOVA with Dunnett's multiple comparisons test). The $\boldsymbol{K_{in}}$ values for [^{3}H]-arginine in the pineal gland, choroid plexus and pituitary gland were however significantly greater than those observed for the brain regions, CSF and capillary depletion samples ($p < 0.01$, one-way ANOVA with Dunnett's multiple comparisons test), and were also found to be significantly different from each other ($p < 0.05$, one-way ANOVA with Dunnett's multiple comparisons test).

Table 2-16: [^{3}H]-Arginine K_{in} values in different brain regions, capillary depletion samples, choroid plexus, and circumventricular organs, calculated from 2.5, 10, 20 & 30 minute co-perfusions with [^{14}C]-sucrose (multiple-time uptake equation). *P* values calculated using linear regression analysis to determine slope deviation from zero.

	Brain sample	**p**	**R^2**	**K_{in}** ($\mu L.min^{-1}\ g^{-1}$)	**V_i** ($mL.100\ g^{-1}$)
Brain regions	Front cortex	< 0.0001	0.7015	6.162 ± 0.9475	10.28 ± 17.37
	Caudate nucleus	< 0.0001	0.7589	5.707 ± 0.7582	5.786 ± 13.90
	Occipital cortex	< 0.0001	0.8395	4.253 ± 0.4650	14.69 ± 7.686
	Hippocampus	< 0.0001	0.8339	5.453 ± 0.5901	-0.8139 ± 11.09
	Hypothalamus	< 0.0001	0.6826	13.15 ± 2.315	-
	Thalamus	< 0.0001	0.7875	11.78 ± 1.530	-
	Pons	< 0.0001	0.6296	6.630 ± 1.200	5.386 ± 22.00
	Cerebellum	< 0.0001	0.8018	5.584 ± 0.6544	1.478 ± 11.99
Capillary depletion	Homogenate	< 0.0001	0.7506	4.246 ± 0.6120	0.3592 ± 10.12
	Supernatant	< 0.0001	0.7300	5.247 ± 0.7523	-
	Pellet	0.0004	0.5543	3.160 ± 0.7085	-
BCSFB	CSF	< 0.0001	0.6944	5.258 ± 0.8459	-20.56 ± 14.80
	Pineal gland	< 0.0001	0.7901	16.53 ± 2.200	-9.82 ± 37.40
	Choroid plexus	0.0025	0.4453	8.377 ± 2.337	134.6 ± 41.66
	Pituitary gland	0.2200	0.0871	-	-

Table 2-17: [^{3}H]-Arginine K_{in} values in all samples, calculated from 10-minute co-perfusions with [^{14}C]-sucrose (single time point equation).

	Time point	K_{in} ($\mu L.min^{-1}\ g^{-1}$)	n
Frontal cortex	10 minutes	5.8375 ± 0.8632	7
Caudate nucleus	10 minutes	5.4000 ± 0.6725	7
Occipital cortex	10 minutes	4.9813 ± 0.7216	7
Hippocampus	10 minutes	4.7148 ± 0.5615	7
Hypothalamus	10 minutes	7.2549 ± 1.7620	7
Thalamus	10 minutes	5.8701 ± 1.0730	7
Pons	10 minutes	5.5758 ± 0.9683	7
Cerebellum	10 minutes	5.1004 ± 0.5000	7
Homogenate	10 minutes	3.9714 ± 0.6697	7
Supernatant	10 minutes	2.3470 ± 0.4174	7
Pellet	10 minutes	0.6959 ± 0.0990	7
CSF	10 minutes	1.0813 ± 0.2413	5
Pineal gland	10 minutes	9.5071 ± 2.0215	7
Choroid plexus	10 minutes	28.8541 ± 4.1542	7
Pituitary gland	10 minutes	19.9429 ± 3.7577	7

The above three groups of samples were analysed using three separate one-way ANOVA with Tukey's post-hoc multiple comparisons tests comparing the K_{in} values ± SEM. No statistically significant differences were found between the eight brain regions sampled ($p > 0.05$). The K_{in} value for the homogenate sample was found to be significantly higher than that for the capillary-enriched pellet sample ($p < 0.001$). The K_{in} value for the CSF sample was found to be significantly less than those for the choroid plexus and pituitary gland ($p < 0.001$ and 0.01 respectively). The K_{in} value for the choroid plexus was also found to be significantly higher than that for the pineal gland ($p < 0.01$). K_{in} values were only compared using 10-minute perfusions as these were found to be the most reproducible and reliable.

2.4.1.3 ADMA: The NOS inhibitor

The molecular weights of [^{14}C]-sucrose and [^{3}H]-ADMA are also comparable and the two compounds are similarly polar; as octanol saline analysis of [^{14}C]-sucrose and [^{3}H]-ADMA revealed octanol partition coefficients of 0.00105±0.00022 and 0.00226±0.00006 respectively.

Figure 2-17 shows the progressive increase in the distribution (% R_{Brain}) of [^{3}H]-ADMA over time (relative to [^{14}C]-sucrose) in the frontal cortex, caudate nucleus, occipital cortex, hippocampus, hypothalamus, thalamus, pons and cerebellum. Uptake of [^{3}H]-ADMA is significantly greater than [^{14}C]-sucrose in all brain regions, at all time points (multiple Student's paired t-tests, $p < 0.05$ in all cases).

A time-dependent increase in the distribution of [^{3}H]-ADMA (corrected for [^{14}C]-sucrose) was observed in all regions up to 20 minutes (*e.g.* 9.86±1.43% after 2.5 minutes to 27.64±4.30% after 20 minutes in the frontal cortex), however this was followed by a decrease in the distribution of [^{3}H]-ADMA at 30 minutes in all regions (*e.g.* 10.41±2.77%). No regional differences were observed ($p > 0.05$, two-way ANOVA with Tukey's multiple comparison test for each brain region compared to all others within each time point).

A very similar pattern of a time-dependent peak in the distribution of [^{3}H]-ADMA after perfusing for 20 minutes was observed in whole brain homogenate and brain parenchyma (supernatant) following capillary depletion (**Figure 2-18**). By contrast, the peak in [^{3}H]-ADMA distribution in the endothelial cell-enriched pellet following capillary depletion was observed earlier, after only 10 minutes of perfusion.

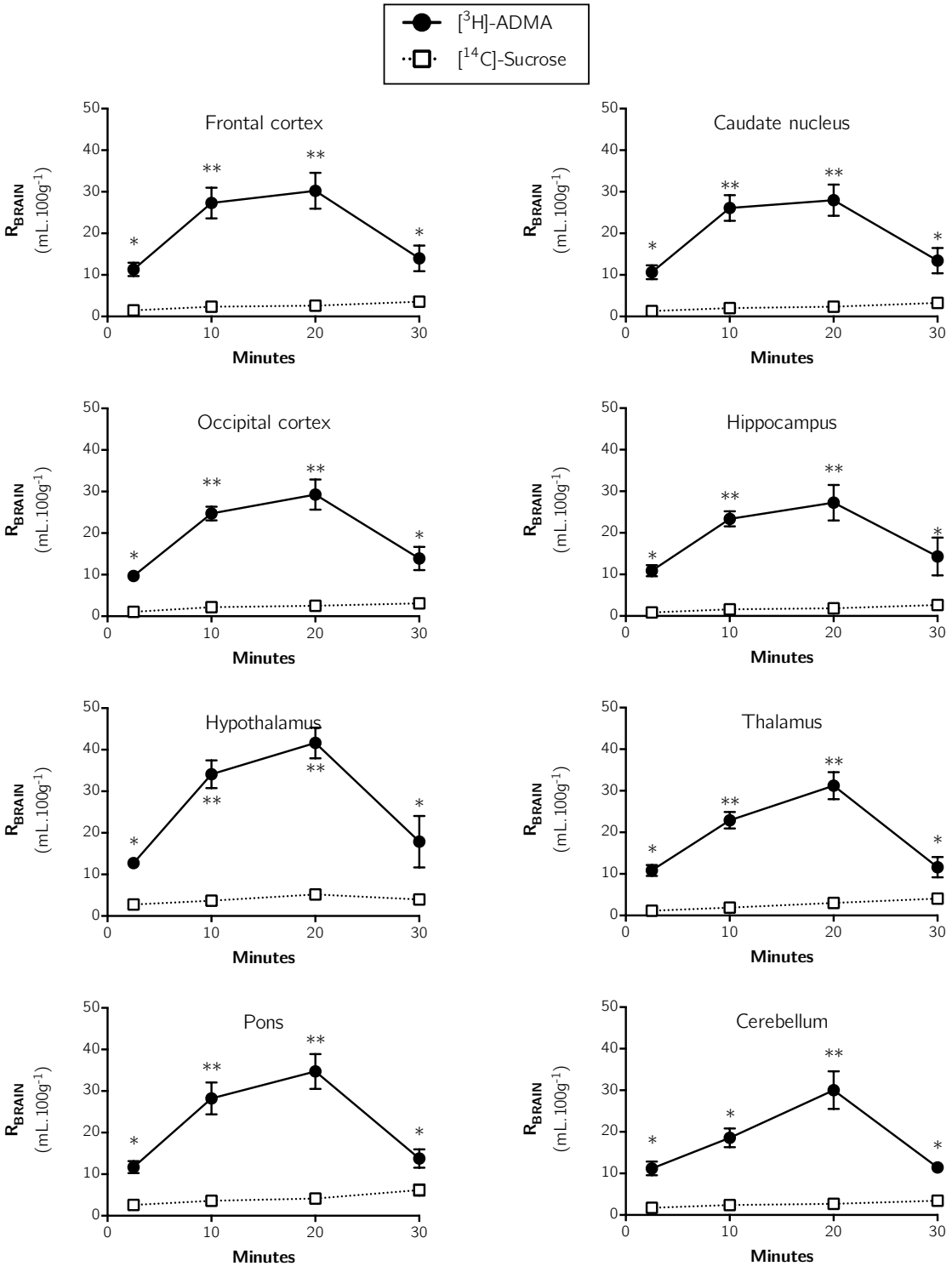

Figure 2-17: Brain distribution of [^{3}H]-ADMA and [^{14}C]-sucrose as a function of time. Uptake is expressed as the percentage ratio of tissue to plasma (mL.100 g^{-1}). Each point represents the mean ± SEM of 5 animals. One-tailed, paired student's t-tests comparing mean±SEM at each time point, *$p < 0.05$, **$p < 0.01$ (GraphPad Prism 6.0 for Mac).

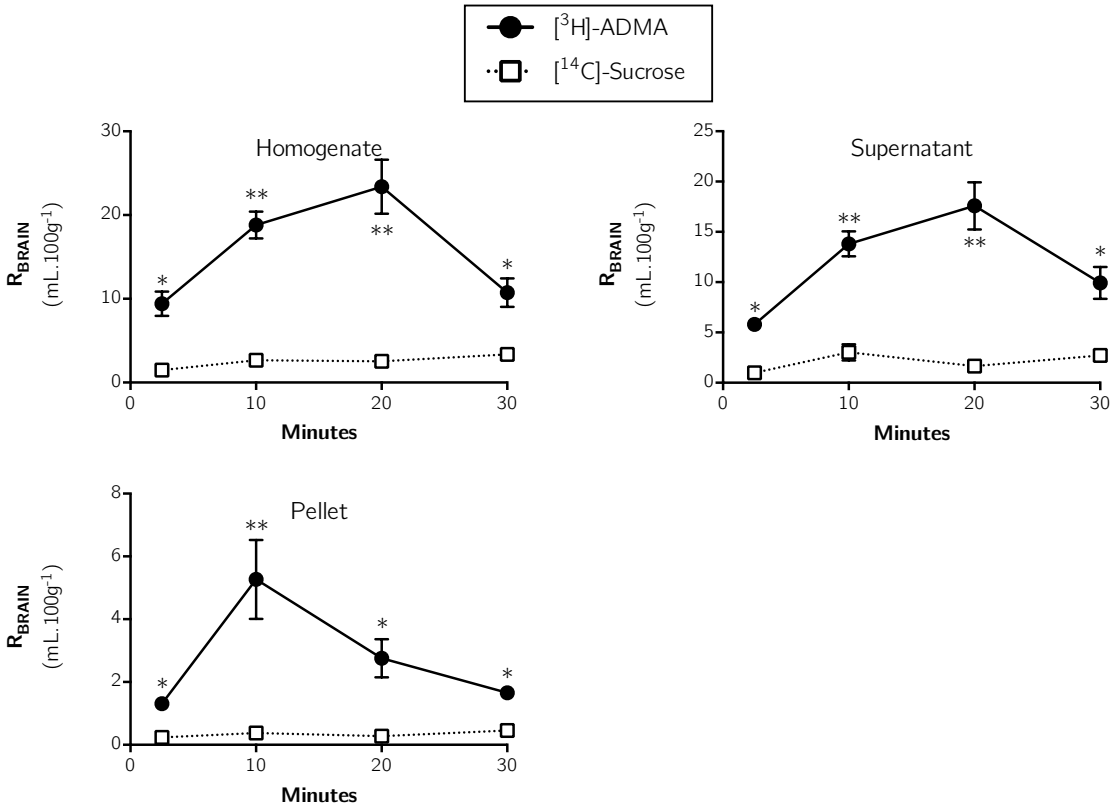

Figure 2-18: Distribution of [^{3}H]-ADMA and [^{14}C]-sucrose in capillary depletion samples as a function of time. Uptake is expressed as the percentage ratio of tissue to plasma (mL.100 g^{-1}). Each point represents the mean ± SEM of 5 animals. One-tailed, paired student's t-tests comparing mean±SEM at each time point, *$p < 0.05$, **$p < 0.01$ (GraphPad Prism 6.0 for Mac).

A similar time-dependent increase and then decrease in the distribution of [^{3}H]-ADMA was observed in the pineal gland, choroid plexus and pituitary gland, however distribution peaked at 10 minutes (**Figure 2-19**). The mean [^{3}H]-ADMA distribution in the choroid plexus, pineal gland and pituitary gland was not significantly different at any time point (uncorrected values, two-way ANOVA with Tukey's multiple comparison test for each sample compared to all others within each time point). The mean [^{3}H]-ADMA distribution in the CSF was significantly lower than all brain regions at all time points (uncorrected values, two-way ANOVA with Tukey's multiple comparison test for each sample compared to all others within each time point).

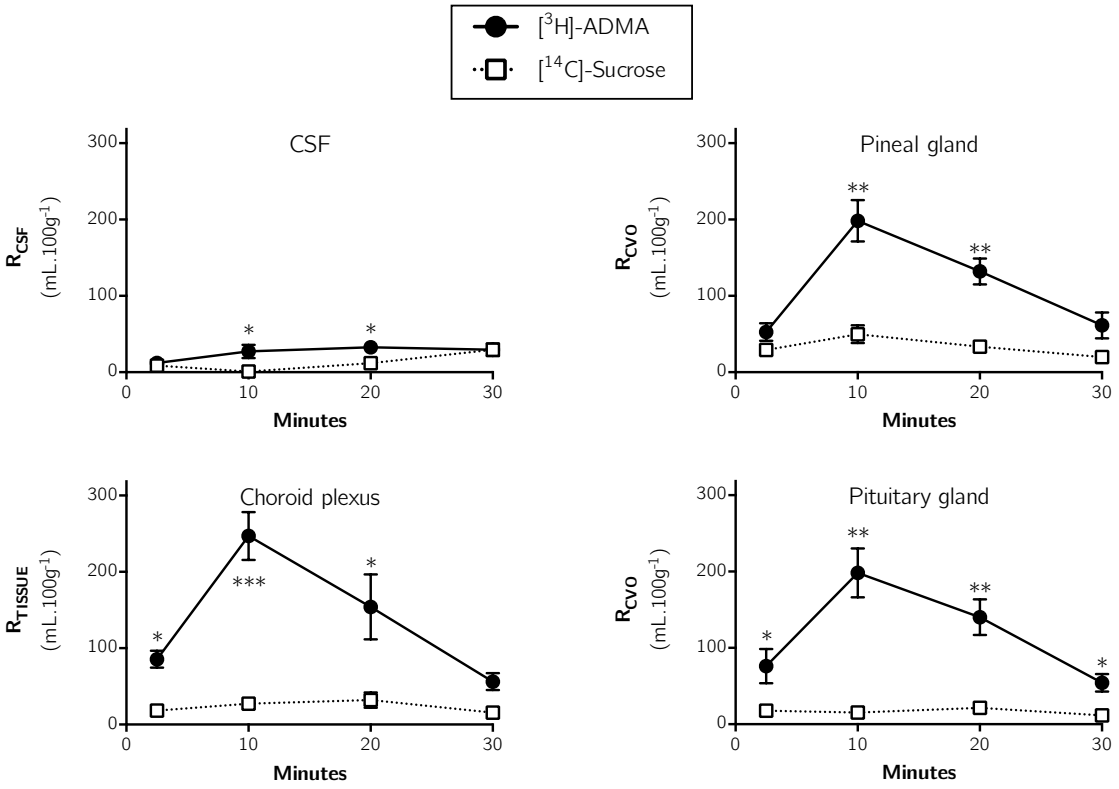

Figure 2-19: Distribution of [^{3}H]-ADMA and [^{14}C]-sucrose in the CSF, pineal gland, choroid plexus and pituitary gland following *in* situ brain perfusion as a function of time. Uptake is expressed as the percentage ratio of tissue or CSF to plasma (mL.100 g^{-1}). Each point represents the mean±SEM of 5 animals. One-tailed, paired student's t-tests comparing mean±SEM at each time point, *$p < 0.05$, **$p < 0.01$, ***$p < 0.001$ (GraphPad Prism 6.0 for Mac).

$\boldsymbol{K_{in}}$ and $\boldsymbol{V_i}$ values for [^{3}H]-ADMA in brain regions were respectively calculated as the slope and ordinate intercept from the plots in **Figure 2-17**, **Figure 2-18** and **Figure 2-19**. Linear regression analysis on these plots produced R-square (R^2, for goodness of fit) and p-values (relating to the deviation of the line slope from 0). No p-values were found to be significant for any of the brain regions sampled ($p > 0.05$) and goodness of fit was outside acceptable limits ($R^2 < 0.4$), as shown in **Table 2-18**. It was therefore deemed more appropriate to calculate the $\boldsymbol{K_{in}}$ value for [^{3}H]-ADMA in all regions using the single-uptake method – shown in **Table 2-19**.

$\boldsymbol{K_{in}}$ values calculated using the single-uptake method after 10 minutes of perfusion revealed no significant difference between the eight brain regions sampled (one-way ANOVA with Dunnett's multiple comparisons of means, $p > 0.05$). The same analysis also revealed that the $\boldsymbol{K_{in}}$ value for [^{3}H]-ADMA in the CSF was not significantly different from any of the eight brain regions sampled. By comparison, $\boldsymbol{K_{in}}$ values for the pineal gland, choroid plexus and pituitary gland were significantly higher than all other samples (*i.e.* brain regions and CSF, one-way ANOVA with Dunnett's multiple comparisons of means, $p < 0.05$), but not significantly different from each other.

All regional differences observed in $\boldsymbol{K_{in}}$ for [^{3}H]-ADMA after 10-minute perfusions were not observed after a 30-minute perfusion (one-way ANOVA with Tukey's multiple comparisons of means, $p > 0.05$, data not shown). A paired, two-tailed Student's t-test comparing $\boldsymbol{K_{in}}$ values in each region at 10 and 30 minutes revealed that values were significantly lower at all time points in animals at the later time points ($p < 0.05$).

Table 2-18: [^{3}H]-ADMA K_{in} values in different brain regions, capillary depletion samples, choroid plexus, and circumventricular organs, calculated from 2.5, 10, 20 & 30 minute co-perfusions with [^{14}C]-sucrose (multiple-time uptake equation). *P* values calculated using linear regression analysis to determine slope deviation from zero.

	Brain sample	**p**	**R^2**	**K_{in}** ($\mu L.min^{-1}\ g^{-1}$)	**V_i** ($mL.100\ g^{-1}$)
Brain regions	Front cortex	0.7652	0.0051	-	-
	Caudate nucleus	0.7625	0.0052	-	-
	Occipital cortex	0.5033	0.0253	-	-
	Hippocampus	0.5869	0.0167	-	-
	Hypothalamus	0.5659	0.0187	-	-
	Thalamus	0.5409	0.0224	-	-
	Pons	0.5633	0.0200	-	-
	Cerebellum	0.4724	0.0308	-	-
Capillary depletion	Homogenate	0.5059	0.0281	-	-
	Supernatant	0.2254	0.0852	-	-
	Pellet	0.5959	0.0159	-	-
BCSFB	CSF	0.0968	0.1845	-	-
	Pineal gland	0.7104	0.0083	-	-
	Choroid plexus	0.2689	0.0758	-	-
	Pituitary gland	0.3153	0.0560	-	-

Table 2-19: [^{3}H]-ADMA K_{in} values in all samples, calculated from 10-minute co-perfusions with [^{14}C]-sucrose (single time point equation).

	K_{in} (μL.min^{-1} g^{-1})	n
Frontal cortex	2.4944 ± 0.3502	5
Caudate nucleus	2.4073 ± 0.2924	5
Occipital cortex	2.2517 ± 0.1652	5
Hippocampus	2.1742 ± 0.1750	5
Hypothalamus	3.0424 ± 0.2981	5
Thalamus	2.1000 ± 0.1742	5
Pons	2.4639 ± 0.3435	5
Cerebellum	1.6150 ± 0.1907	5
Homogenate	1.2702 ± 0.5550	5
Supernatant	0.8620 ± 0.1629	5
Pellet	0.0783 ± 0.1960	5
CSF	2.6954 ± 0.9020	5
Pineal gland	19.4057 ± 4.8466	5
Choroid plexus	26.0860 ± 4.2447	5
Pituitary gland	18.2856 ± 3.2278	5

The above three groups of samples were analysed using three separate one-way ANOVA with Tukey's post-hoc multiple comparisons tests comparing the K_{in} values ± SEM. Among the eight brain regions sampled, the only statistically significant difference in the K_{in} values was between the hypothalamus and cerebellum ($p > 0.05$). The K_{in} value for the homogenate sample was found to be significantly higher than that for the capillary-enriched pellet sample ($p < 0.001$). The K_{in} value for the CSF sample was found to be significantly less than those for the pineal gland, choroid plexus and pituitary gland ($p < 0.05$, 0.01 and 0.05 respectively).

2.4.1.4 Comparative amino acid uptake: Arginine *vs.* ADMA

Figure 2-20 shows a comparison between the progressive distributions of [^{3}H]-ADMA and [^{3}H]-arginine (and [^{14}C]-sucrose from each experiment) in the eight brain regions sampled; plotting results from previous figures (**Figure 2-10** and **Figure 2-17**) on the same graph.

In this section, multiple Student's unpaired, two-tailed t-tests were used for the comparison of two means. At the time points of 2.5, 10, 20 and 30 minutes, the uptake of [^{3}H]-arginine into all eight brain regions was significantly higher than that of [^{3}H]-ADMA into the same tissue ($p < 0.05$). In the case of the CSF, pineal gland, choroid plexus and pituitary gland, [^{3}H]-arginine distribution was significantly higher than [^{3}H]-ADMA at 20 and 30 minute time points ($p < 0.05$).

In the whole brain homogenate, and resulting supernatant following capillary depletion, [^{3}H]-arginine distribution was significantly higher than [^{3}H]-ADMA at 10-, 20- and 30-minute time points ($p < 0.05$). In the endothelial cell-enriched pellet resulting from capillary depletion, [^{3}H]-arginine distribution was only significantly higher than [^{3}H]-ADMA for 20- and 30-minute time points ($p < 0.01$).

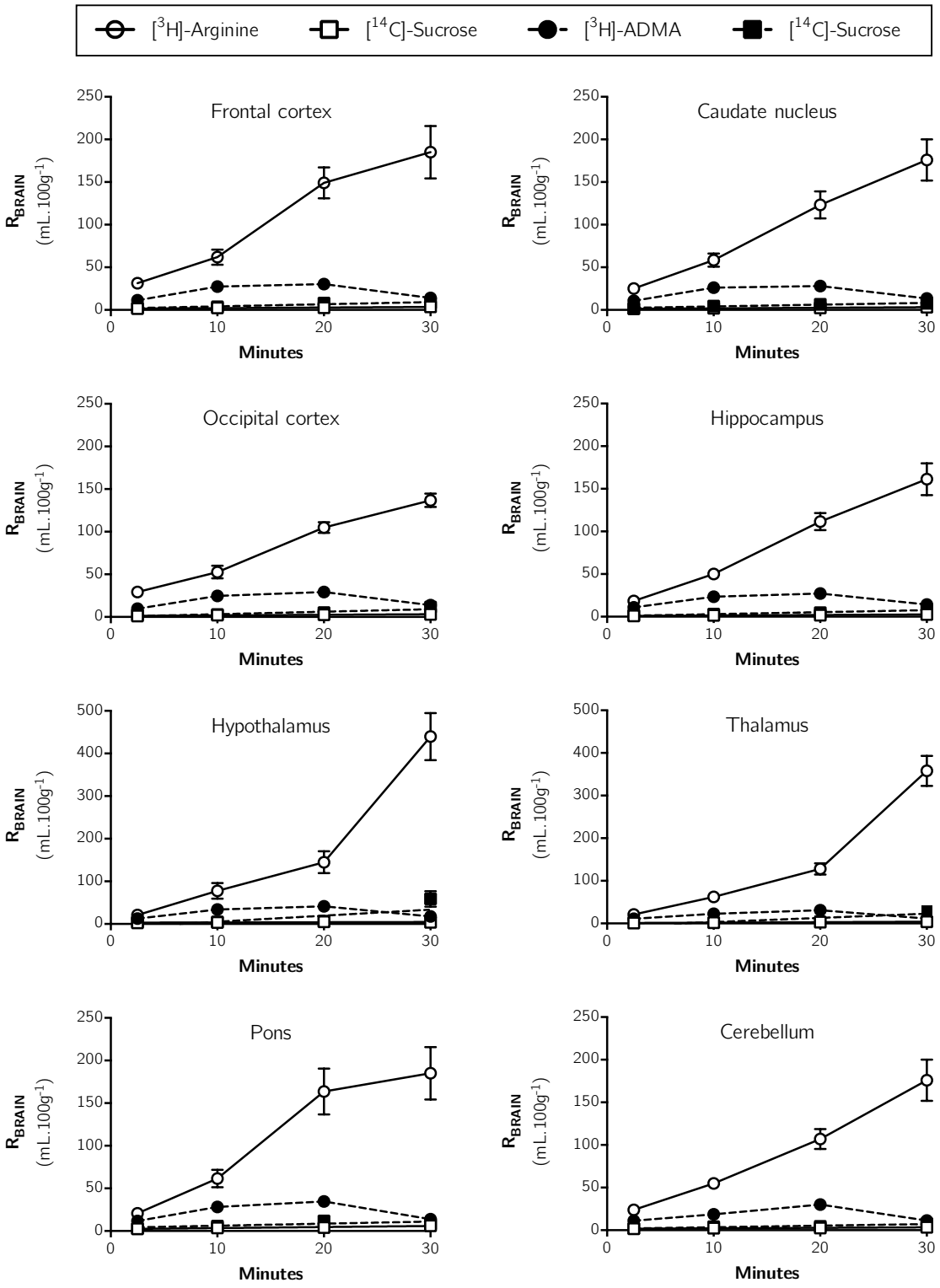

Figure 2-20: Comparative uptake of [^{3}H]-arginine, [^{3}H]-ADMA and [^{14}C]-sucrose as a function of time. Uptake is expressed as the percentage ratio of tissue to plasma (mL.100 g^{-1}). Each point represents the mean ± SEM of 4-7 animals (GraphPad Prism 6.0 for Mac).

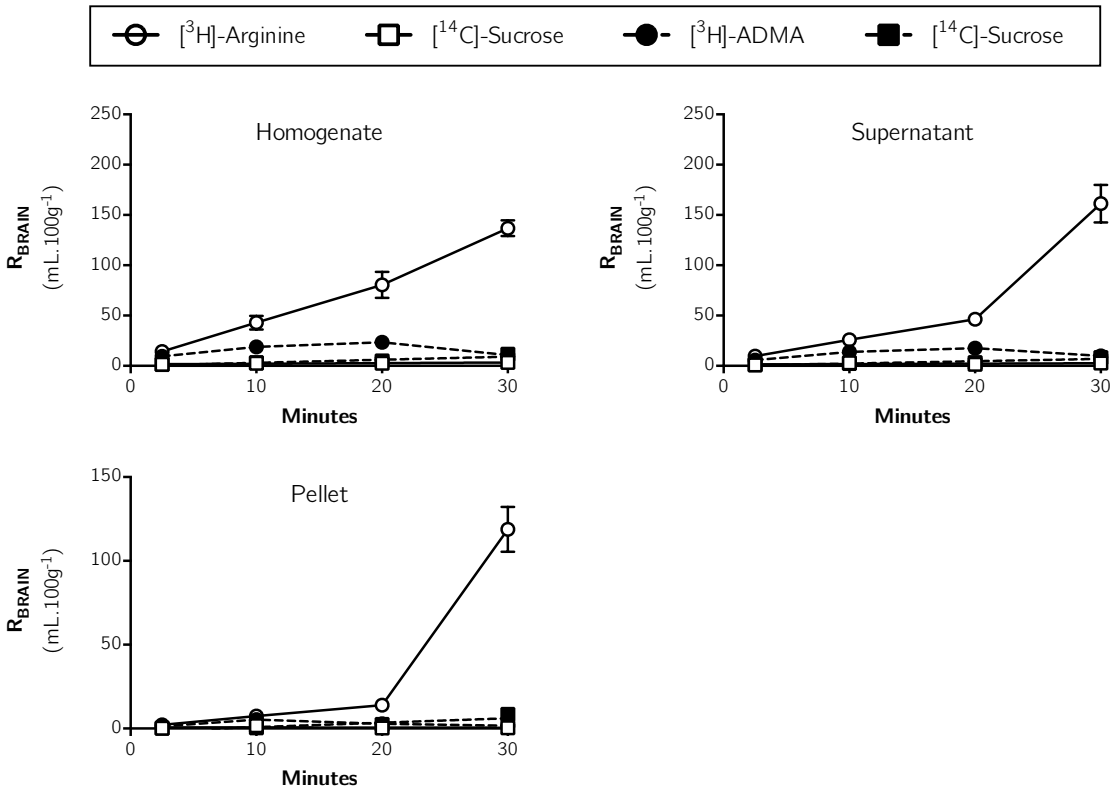

Figure 2-21: Distribution of [^{3}H]-arginine, [^{3}H]-ADMA and [^{14}C]-sucrose in capillary depletion samples as a function of time. Uptake is expressed as the percentage ratio of tissue to plasma (mL.100 g^{-1}). Each point represents the mean ± SEM of 5 animals. K_{in} and V_i values were determined as the slope and ordinate intercept of the computed regression lines (GraphPad Prism 6.0 for Mac).

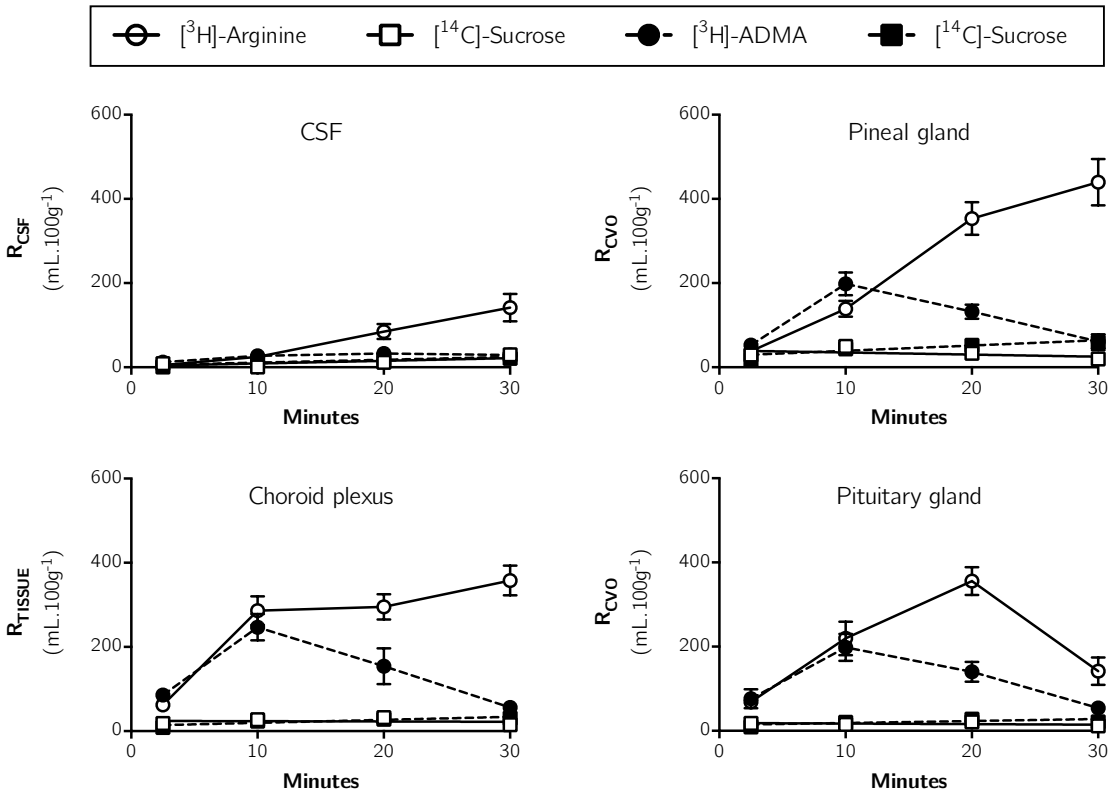

Figure 2-22: Comparative distribution of [^{3}H]-arginine, [^{3}H]-ADMA and [^{14}C]-Sucrose in the CSF, pineal gland, choroid plexus and pituitary gland following *in situ* brain perfusion as a function of time. Uptake is expressed as the percentage ratio of tissue or CSF to plasma (mL.100 g^{-1}). Each point represents the mean ± SEM of 4-7 animals (GraphPad Prism 6.0 for Mac).

2.4.2 Self-inhibition

2.4.2.1 Self-inhibition of Arginine transport

Figure 2-23 shows the effect of an excess of un-labelled arginine on the uptake of [^{3}H]-arginine into all brain regions. These data indicate that [^{3}H]-arginine uptake into all eight brain regions is markedly self-inhibited by an average of approximately 67% ($p < 0.05$, unpaired, one-tailed Student's t-test comparing means, **Table 2-20**).

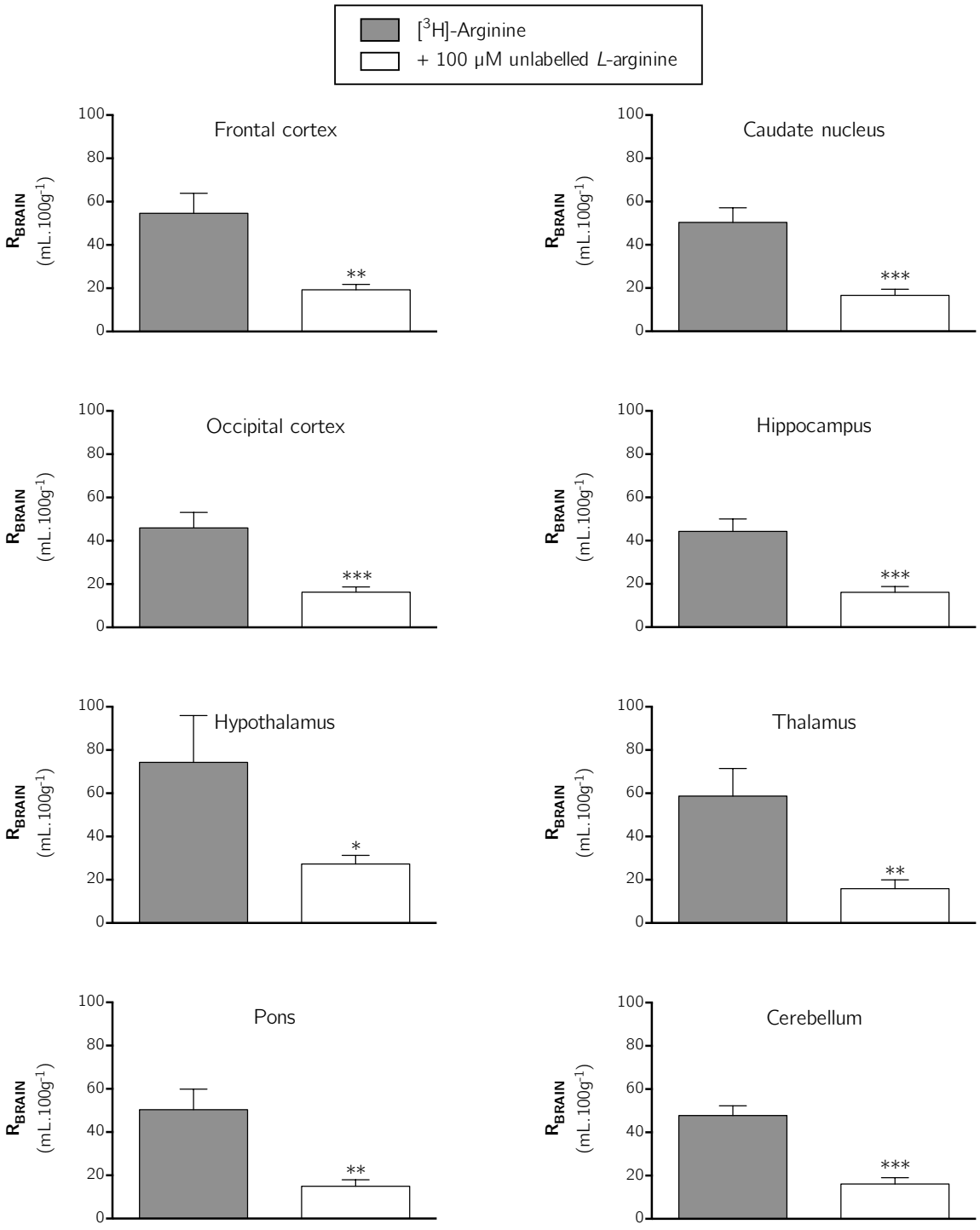

Figure 2-23: The effect of 100µM un-labelled *L*-arginine on the uptake of [^{3}H]-arginine in the brain. Uptake is expressed as the percentage ratio of tissue to plasma (mL.100 g^{-1}) and is corrected for [^{14}C]-sucrose (vascular space). Perfusion time is 10 minutes. Each bar represents the mean ± SEM of 6-7 animals (GraphPad Prism 6.0 for Mac). *$p < 0.05$, **$p < 0.01$, ***$p < 0.001$.

Table 2-20: Results obtained from self-inhibition studies for [^{3}H]-arginine. Unpaired, one-tailed Student's t-test was used to compare two means, with statistical significance taken as $p < 0.05$. n = number of experiments.

Tissue	n	R_{BRAIN} (mL.100g^{-1})		% inhibition	*p*
Frontal cortex					
[^{3}H]-arginine alone	6	54.65 ± 9.21	-	-	
+ 100 µM un-labelled arginine	7	-	19.30 ± 2.53	64.7	$p < 0.01$
Caudate nucleus					
[^{3}H]-arginine alone	6	50.38 ± 6.71	-	-	
+ 100 µM un-labelled arginine	7	-	16.52 ± 2.89	67.2	$p < 0.001$
Occipital cortex					
[^{3}H]-arginine alone	6	45.93 ± 7.19	-	-	
+ 100 µM un-labelled arginine	7	-	16.29 ± 2.45	64.5	$p < 0.001$
Hippocampus					
[^{3}H]-arginine alone	6	44.32 ± 5.74	-	-	
+ 100 µM un-labelled arginine	7	-	16.10 ± 2.73	63.7	$p < 0.001$
Hypothalamus					
[^{3}H]-arginine alone	5	74.29 ± 21.67	-	-	
+ 100 µM un-labelled arginine	7	-	27.31 ± 3.94	63.2	$p < 0.05$
Thalamus					
[^{3}H]-arginine alone	6	58.74 ± 12.70	-	-	
+ 100 µM un-labelled arginine	7	-	15.84 ± 4.13	73.0	$p < 0.01$
Pons					
[^{3}H]-arginine alone	6	50.38 ± 9.53	-	-	
+ 100 µM un-labelled arginine	7	-	14.98 ± 3.00	70.3	$p < 0.001$
Cerebellum					
[^{3}H]-arginine alone	6	47.77 ± 4.52	-	-	
+ 100 µM un-labelled arginine	7	-	16.09 ± 2.99	66.3	$p < 0.001$

Figure 2-24 shows the effect of an excess of un-labelled arginine on the distribution of [^{3}H]-arginine into capillary depletion samples. These data indicate that [^{3}H]-arginine uptake is markedly inhibited by an average of approximately 56% ($p < 0.05$, unpaired, one-tailed Student's t-test comparing means, **Table 2-21**).

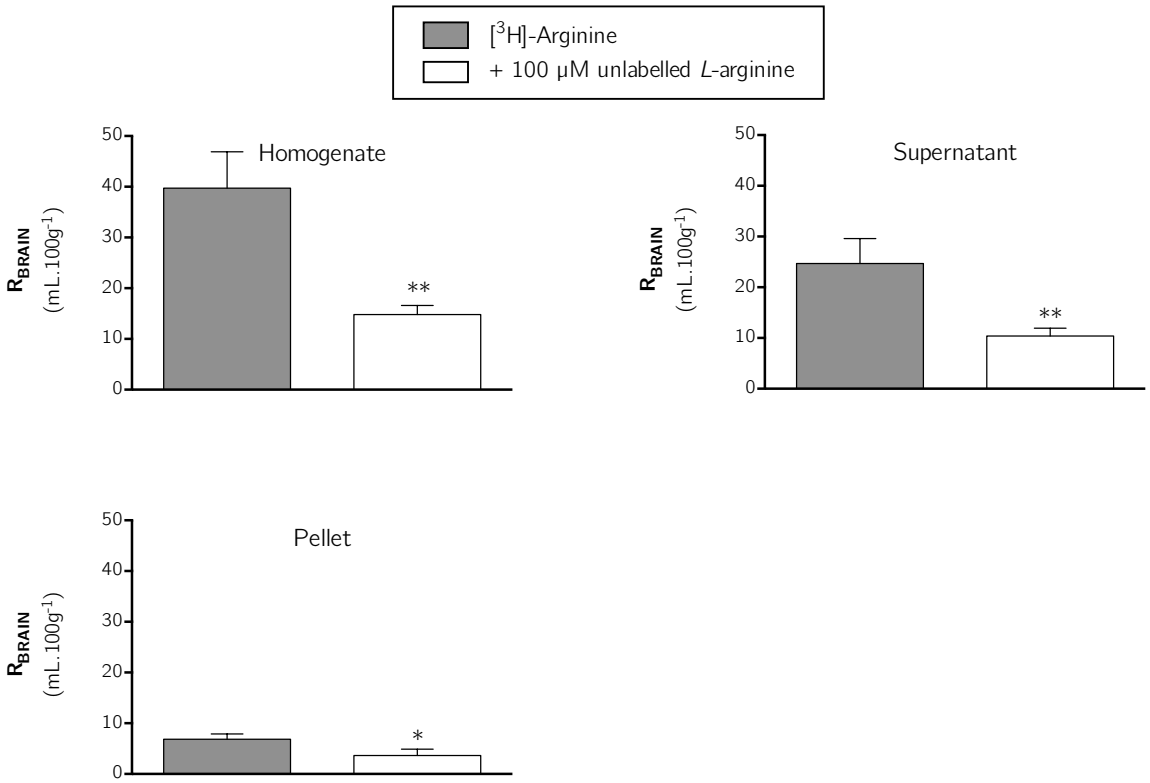

Figure 2-24: The effect of 100µM un-labelled *L*-arginine on the distribution of [^{3}H]-arginine in capillary depletion samples. Uptake is expressed as the percentage ratio of tissue to plasma (mL.100 g^{-1}) and is corrected for [^{14}C]-sucrose (vascular space). Perfusion time is 10 minutes. Each bar represents the mean ± SEM of 6-7 animals (GraphPad Prism 6.0 for Mac). *$p < 0.05$, **$p < 0.01$.

Table 2-21: Results obtained from self-inhibition studies for [^{3}H]-arginine in capillary depletion samples. Unpaired, one-tailed Student's t-test was used to compare two means, with statistical significance taken as $p < 0.05$. n = number of experiments.

Tissue	n	R_{BRAIN} (mL.100g^{-1})		% inhibition	*p*
Homogenate					
[^{3}H]-arginine alone	6	39.71 ± 7.19	-	-	
+ 100 µM un-labelled arginine	7	-	14.83 ± 1.78	62.7	$p < 0.01$
Supernatant					
[^{3}H]-arginine alone	6	24.70 ± 4.91	-	-	
+ 100 µM un-labelled arginine	7	-	10.41 ± 1.54	57.9	$p < 0.01$
Pellet					
[^{3}H]-arginine alone	6	6.87 ± 1.02	-	-	
+ 100 µM un-labelled arginine	6	-	3.64 ± 1.25	47.0	$p < 0.05$

Figure 2-25 shows the effect of an excess of un-labelled arginine on the distribution of [^{3}H]-arginine into the CSF, pineal gland, choroid plexus and pituitary gland. These data indicate that [^{3}H]-arginine uptake is markedly inhibited by an average of approximately 52% ($p < 0.05$, unpaired, one-tailed Student's t-test comparing means, **Table 2-22**).

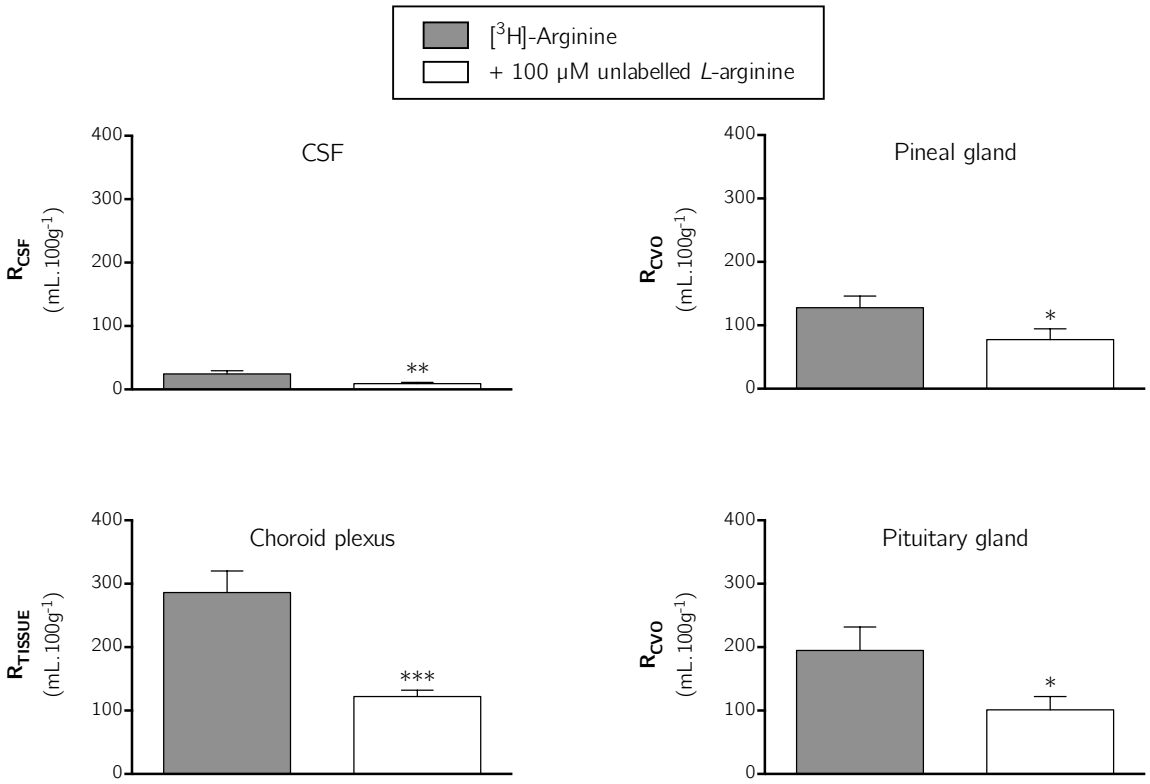

Figure 2-25: The effect of 100µM un-labelled *L*-arginine on the distribution of [^{3}H]-arginine in the CSF, choroid plexus and circumventricular organs. Uptake is expressed as the percentage ratio of tissue or CSF to plasma (mL.100 g^{-1}). Perfusion time is 10 minutes. Each bar represents the mean ± SEM of 6-7 animals (GraphPad Prism 6.0 for Mac). *$p < 0.05$, **$p < 0.01$, ***$p < 0.001$.

Table 2-22: Results obtained from self-inhibition studies for [^{3}H]-arginine in CSF, choroid plexus & CVOs. Unpaired, one-tailed Student's t-test was used to compare two means, with statistical significance taken as $p < 0.05$. n = number of experiments.

Tissue	n	R_{BRAIN} (mL.100g^{-1})		% inhibition	*p*
CSF					
[^{3}H]-arginine alone	7	24.51 ± 5.10	-	-	
+ 100 µM un-labelled arginine	7	-	9.25 ± 1.78	62.2	$p < 0.01$
Pineal gland					
[^{3}H]-arginine alone	6	128.0 ± 18.11	-	-	
+ 100 µM un-labelled arginine	7	-	77.63 ± 16.85	39.4	$p < 0.05$
Choroid plexus					
[^{3}H]-arginine alone	6	286.1 ± 33.92	-	-	
+ 100 µM un-labelled arginine	7	-	122.1 ± 9.96	57.3	$p < 0.001$
Pituitary gland					
[^{3}H]-arginine alone	6	194.9 ± 36.90	-	-	
+ 100 µM un-labelled arginine	6	-	101.2 ± 20.85	48.1	$p < 0.05$

2.4.2.2 Self-inhibition of ADMA transport

The uptake of [^{3}H]-ADMA is also significantly self-inhibited by 0.5, 3.0, 10, 100 and 500 µM un-labelled ADMA in all brain regions (**Figure 2-26**). **Table 2-23** shows the percentage inhibition and p values for each concentration of ADMA in each brain region. The same phenomenon was observed in capillary depletion samples (**Figure 2-27** and **Table 2-24**). Distribution of [^{3}H]-ADMA into the CSF was inhibited at all concentrations of un-labelled ADMA except for 0.5 µM (**Figure 2-28** and **Table 2-25**). Distribution of [^{3}H]-ADMA into the pineal gland, choroid plexus and pituitary gland was significantly self-inhibited by all concentrations of un-labelled ADMA.

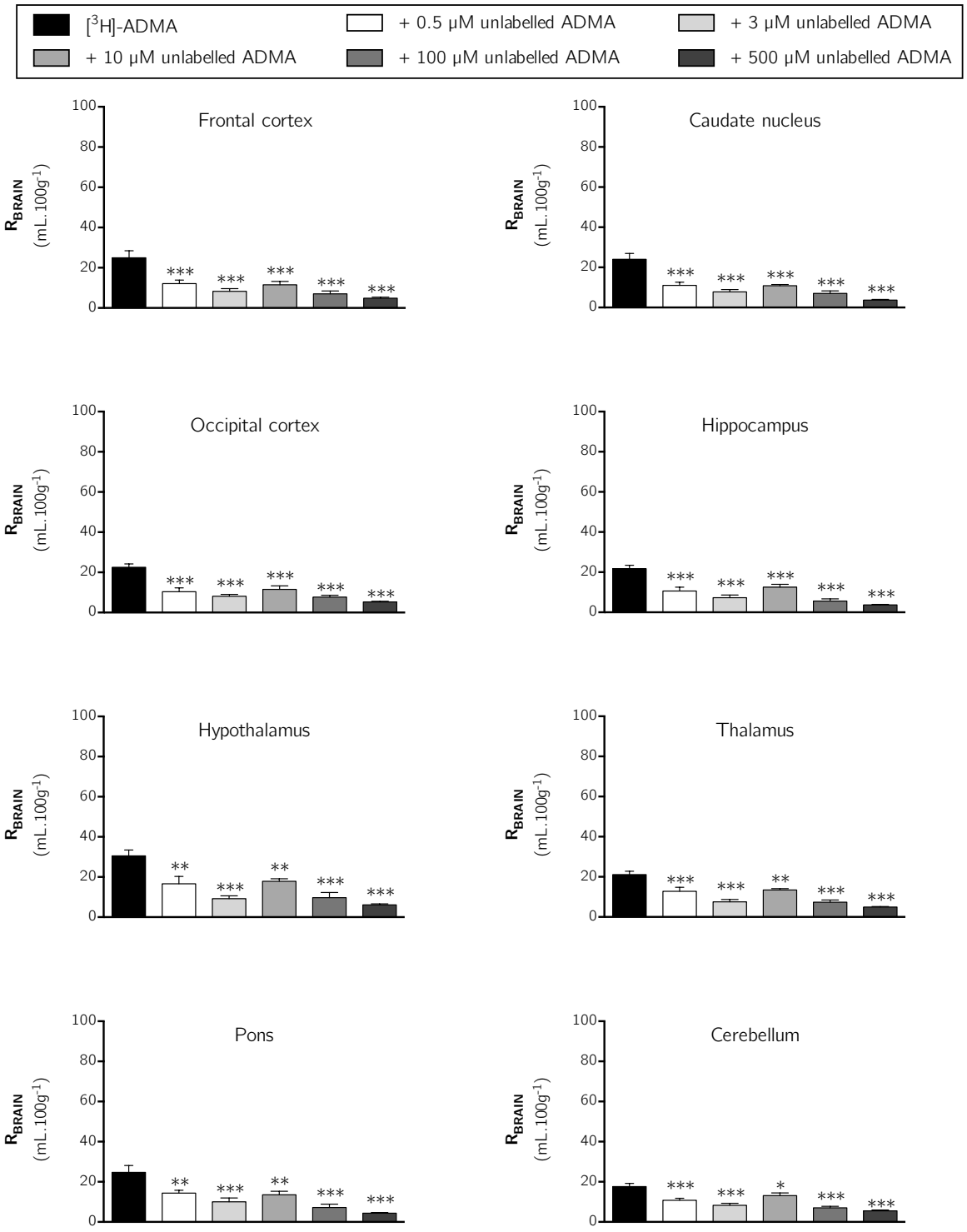

Figure 2-26: The effect of 0.5, 3, 10, 100 and 500 µM un-labelled ADMA on the uptake of [^{3}H]-ADMA in the brain. Uptake is expressed as the percentage ratio of tissue to plasma (mL.100 g^{-1}) and is corrected for [^{14}C]-sucrose (vascular space). Perfusion time is 10 minutes. Each bar represents the mean ± SEM of 5 animals. Asterisks represent one-way ANOVA with Dunnett's post-hoc tests comparing mean±SEM to control, *$p < 0.05$, **$p < 0.01$, ***$p < 0.001$ (GraphPad Prism 6.0 for Mac).

Table 2-23: Results obtained from self-inhibition studies for [^{3}H]-ADMA in the brain. One-way ANOVA with Dunnett's post-hoc test was used to compare means to control ([^{3}H]-ADMA alone), with statistical significance taken as $p < 0.05$. n = number of experiments.

Tissue	n	R_{BRAIN} (mL.100g^{-1})		% inhibition	*p*
Frontal cortex					
[^{3}H]-ADMA alone	5	24.94 ± 3.50	-	-	
+ 0.5 µM un-labelled ADMA	5	-	12.14 ± 1.76	51.3	$p < 0.001$
+ 3.0 µM un-labelled ADMA	5	-	8.32 ± 1.30	66.7	$p < 0.001$
+ 10 µM un-labelled ADMA	5	-	11.56 ± 1.65	53.6	$p < 0.001$
+ 100 µM un-labelled ADMA	5	-	6.96 ± 1.39	72.1	$p < 0.001$
+ 500 µM un-labelled ADMA	5	-	4.91 ± 0.43	80.3	$p < 0.001$
Caudate nucleus					
[^{3}H]-ADMA alone	5	24.07 ± 2.92	-	-	
+ 0.5 µM un-labelled ADMA	5	-	11.05 ± 1.60	54.1	$p < 0.001$
+ 3.0 µM un-labelled ADMA	5	-	7.78 ± 1.22	67.7	$p < 0.001$
+ 10 µM un-labelled ADMA	4	-	10.76 ± 0.63	55.3	$p < 0.001$
+ 100 µM un-labelled ADMA	4	-	7.071 ± 1.22	70.6	$p < 0.001$
+ 500 µM un-labelled ADMA	5	-	3.67 ± 0.39	84.7	$p < 0.001$
Occipital cortex					
[^{3}H]-ADMA alone	5	22.52 ± 1.65	-	-	
+ 0.5 µM un-labelled ADMA	5	-	10.34 ± 1.92	54.1	$p < 0.001$
+ 3.0 µM un-labelled ADMA	5	-	8.16 ± 0.87	63.8	$p < 0.001$
+ 10 µM un-labelled ADMA	4	-	11.56 ± 1.77	48.7	$p < 0.001$
+ 100 µM un-labelled ADMA	4	-	7.67 ± 0.97	65.9	$p < 0.001$
+ 500 µM un-labelled ADMA	5	-	5.26 ± 0.38	76.7	$p < 0.001$
Hippocampus					
[^{3}H]-ADMA alone	5	21.74 ± 1.75	-	-	
+ 0.5 µM un-labelled ADMA	5	-	10.66 ± 1.88	51.0	$p < 0.001$
+ 3.0 µM un-labelled ADMA	5	-	7.32 ± 1.32	66.4	$p < 0.001$
+ 10 µM un-labelled ADMA	5	-	12.57 ± 1.37	42.2	$p < 0.001$
+ 100 µM un-labelled ADMA	4	-	5.60 ± 1.08	74.3	$p < 0.001$
+ 500 µM un-labelled ADMA	5	-	3.70 ± 0.24	83.0	$p < 0.001$
Hypothalamus					
[^{3}H]-ADMA alone	5	30.42 ± 2.98	-	-	
+ 0.5 µM un-labelled ADMA	5	-	16.63 ± 3.69	45.3	$p < 0.01$
+ 3.0 µM un-labelled ADMA	5	-	9.23 ± 1.40	69.7	$p < 0.001$
+ 10 µM un-labelled ADMA	4	-	17.88 ± 1.24	41.2	$p < 0.01$
+ 100 µM un-labelled ADMA	4	-	9.72 ± 2.61	68.0	$p < 0.001$
+ 500 µM un-labelled ADMA	5	-	6.09 ± 0.55	80.0	$p < 0.001$

Table 2-23 continued...

Tissue	n	R_{BRAIN} (mL.100g^{-1})		% inhibition	*p*
Thalamus					
[^{3}H]-ADMA alone	5	21.00 ± 1.74	-	-	
+ 0.5 µM un-labelled ADMA	5	-	12.78 ± 2.01	39.1	$p < 0.001$
+ 3.0 µM un-labelled ADMA	5	-	7.55 ± 1.13	64.1	$p < 0.001$
+ 10 µM un-labelled ADMA	4	-	13.41 ± 0.67	36.1	$p < 0.01$
+ 100 µM un-labelled ADMA	4	-	7.27 ± 1.10	65.4	$p < 0.001$
+ 500 µM un-labelled ADMA	5	-	4.92 ± 0.28	76.6	$p < 0.001$
Pons					
[^{3}H]-ADMA alone	5	24.64 ± 3.44	-	-	
+ 0.5 µM un-labelled ADMA	5	-	14.41 ± 1.42	41.5	$p < 0.01$
+ 3.0 µM un-labelled ADMA	5	-	10.06 ± 1.94	59.2	$p < 0.001$
+ 10 µM un-labelled ADMA	5	-	13.53 ± 1.77	45.1	$p < 0.01$
+ 100 µM un-labelled ADMA	4	-	7.24 ± 1.61	70.6	$p < 0.001$
+ 500 µM un-labelled ADMA	5	-	4.35 ± 0.33	82.4	$p < 0.001$
Cerebellum					
[^{3}H]-ADMA alone	5	17.65 ± 1.52	-	-	
+ 0.5 µM un-labelled ADMA	5	-	10.79 ± 1.01	38.9	$p < 0.001$
+ 3.0 µM un-labelled ADMA	5	-	8.28 ± 1.04	53.1	$p < 0.001$
+ 10 µM un-labelled ADMA	4	-	13.15 ± 1.31	25.5	$p < 0.05$
+ 100 µM un-labelled ADMA	4	-	7.01 ± 0.79	60.3	$p < 0.001$
+ 500 µM un-labelled ADMA	5	-	5.56 ± 0.41	68.5	$p < 0.001$

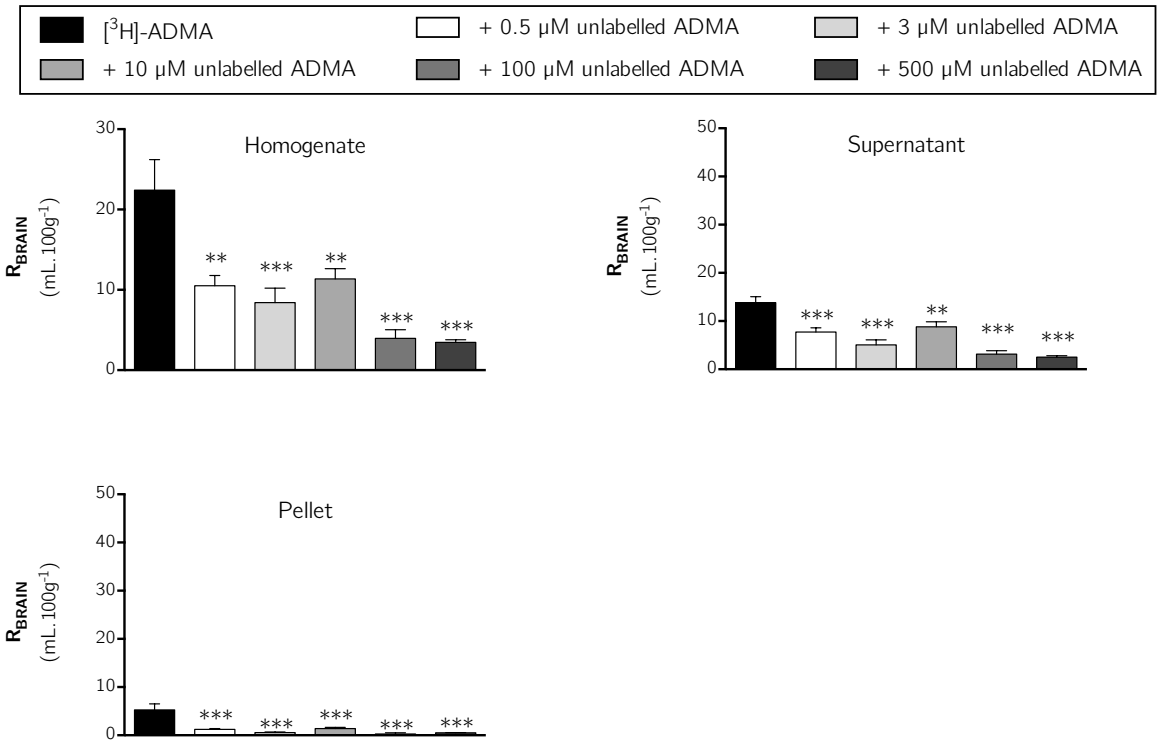

Figure 2-27: The effect of 0.5, 3, 10, 100 and 500 µM un-labelled ADMA on the distribution of [^{3}H]-ADMA in capillary depletion samples. Uptake is expressed as the percentage ratio of tissue to plasma (mL.100 g^{-1}) and is corrected for [^{14}C]-sucrose (vascular space). Perfusion time is 10 minutes. Each bar represents the mean ± SEM of 6-7 animals. Asterisks represent one-way ANOVA with Dunnett's post-hoc tests comparing mean±SEM to control, $^{**}p < 0.01$, $^{***}p < 0.001$ (GraphPad Prism 6.0 for Mac).

Table 2-24: Results obtained from self-inhibition studies for [^{3}H]-ADMA in capillary depletion samples. One-way ANOVA with Dunnett's post-hoc test was used to compare means to control ([^{3}H]-ADMA alone), with statistical significance taken as $p < 0.05$. n = number of experiments.

Tissue	n	R_{BRAIN} (mL.100g^{-1})		% inhibition	*p*
Homogenate					
[^{3}H]-ADMA alone	5	22.41 ± 3.81	-	-	
+ 0.5 µM un-labelled ADMA	5	-	10.52 ± 1.28	53.1	$p < 0.01$
+ 3.0 µM un-labelled ADMA	5	-	8.41 ± 1.80	62.5	$p < 0.001$
+ 10 µM un-labelled ADMA	5	-	11.37 ± 1.27	49.3	$p < 0.01$
+ 100 µM un-labelled ADMA	4	-	3.96 ± 1.07	82.3	$p < 0.001$
+ 500 µM un-labelled ADMA	5	-	3.47 ± 0.32	84.5	$p < 0.001$
Supernatant					
[^{3}H]-ADMA alone	5	13.81 ± 1.24	-	-	
+ 0.5 µM un-labelled ADMA	5	-	7.73 ± 0.877	44.0	$p < 0.001$
+ 3.0 µM un-labelled ADMA	5	-	5.08 ± 1.04	63.2	$p < 0.001$
+ 10 µM un-labelled ADMA	5	-	8.79 ± 1.07	36.3	$p < 0.01$
+ 100 µM un-labelled ADMA	4	-	3.16 ± 0.679	77.1	$p < 0.001$
+ 500 µM un-labelled ADMA	5	-	2.51 ± 0.305	81.8	$p < 0.001$
Pellet					
[^{3}H]-ADMA alone	5	5.27 ± 1.26	-	-	
+ 0.5 µM un-labelled ADMA	5	-	1.23 ± 0.158	76.6	$p < 0.001$
+ 3.0 µM un-labelled ADMA	5	-	0.576 ± 0.108	89.1	$p < 0.001$
+ 10 µM un-labelled ADMA	4	-	1.41 ± 0.245	73.3	$p < 0.001$
+ 100 µM un-labelled ADMA	4	-	0.251 ± 0.251	95.2	$p < 0.001$
+ 500 µM un-labelled ADMA	5	-	0.505 ± 0.077	90.4	$p < 0.001$

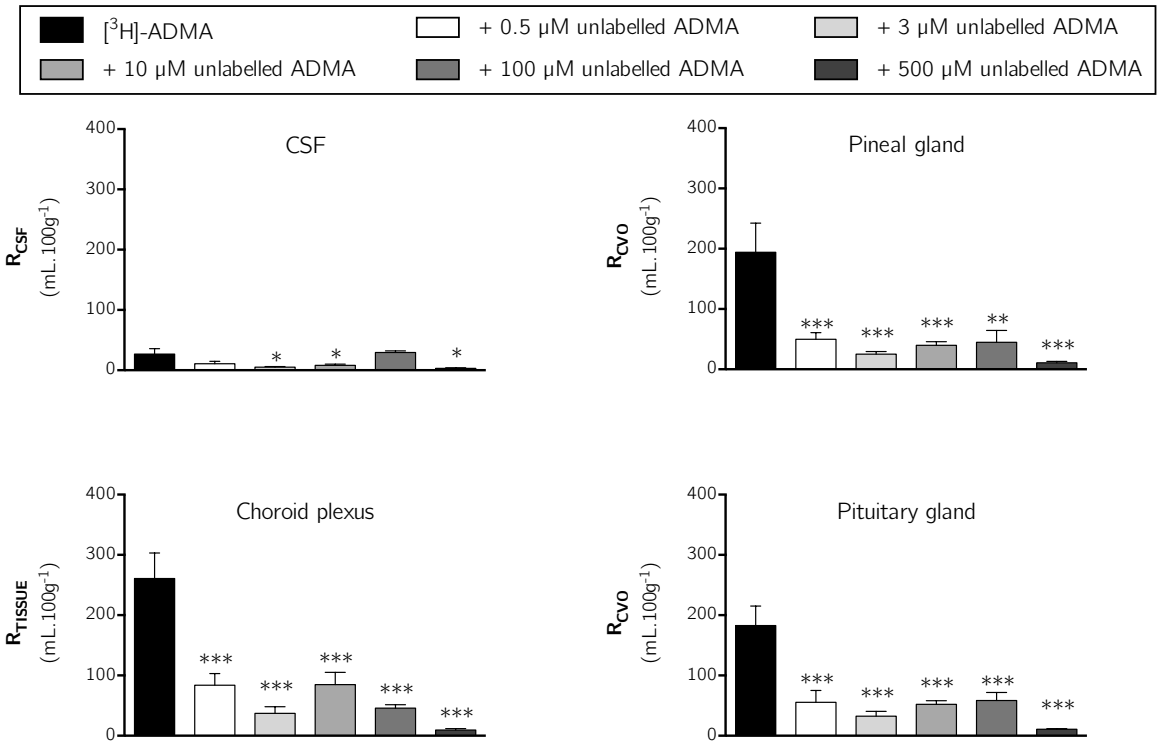

Figure 2-28: The effect of 0.5, 3, 10, 100 and 500 µM un-labelled ADMA on the distribution of [^{3}H]-ADMA in the CSF and circumventricular organs. Uptake is expressed as the percentage ratio of tissue or CSF to plasma (mL.100 g^{-1}). Perfusion time is 10 minutes. Each bar represents the mean ± SEM of 5 animals. Asterisks represent one-way ANOVA with Dunnett's post-hoc tests comparing mean±SEM to control, *p < 0.05, **p < 0.01, ***p < 0.001 (GraphPad Prism 6.0 for Mac).

Table 2-25: Results obtained from self-inhibition studies for [^{3}H]-ADMA in CSF, choroid plexus and CVOs. One-way ANOVA with Dunnett's post-hoc test was used to compare means to control ([^{3}H]-ADMA alone), with statistical significance taken as $p < 0.05$. n = number of experiments.

Tissue	n	R_{BRAIN} (mL.100g^{-1})		% inhibition	*p*
CSF					
[^{3}H]-ADMA alone	5	26.95 ± 9.02	-	-	
+ 0.5 µM un-labelled ADMA	5	-	10.7 ± 4.05	-	n.s.
+ 3.0 µM un-labelled ADMA	5	-	4.77 ± 1.00	82.3	$p < 0.05$
+ 10 µM un-labelled ADMA	4	-	7.73 ± 2.13	71.3	$p < 0.05$
+ 100 µM un-labelled ADMA	2	-	2.99 ± 0.03	89.1	$p < 0.05$
+ 500 µM un-labelled ADMA	4	-	3.06 ± 1.21	88.7	$p < 0.05$
Pineal gland					
[^{3}H]-ADMA alone	5	194.1 ± 48.47	-	-	
+ 0.5 µM un-labelled ADMA	5	-	49.78 ± 11.08	74.4	$p < 0.001$
+ 3.0 µM un-labelled ADMA	5	-	25.01 ± 4.47	87.1	$p < 0.001$
+ 10 µM un-labelled ADMA	5	-	39.65 ± 6.00	79.6	$p < 0.001$
+ 100 µM un-labelled ADMA	5	-	44.67 ± 19.81	77.0	$p < 0.01$
+ 500 µM un-labelled ADMA	5	-	10.92 ± 2.31	94.4	$p < 0.001$
Choroid plexus					
[^{3}H]-ADMA alone	5	260.9 ± 42.45	-	-	
+ 0.5 µM un-labelled ADMA	5	-	83.97 ± 19.11	67.8	$p < 0.001$
+ 3.0 µM un-labelled ADMA	5	-	37.17 ± 11.04	85.8	$p < 0.001$
+ 10 µM un-labelled ADMA	4	-	84.74 ± 20.27	67.5	$p < 0.001$
+ 100 µM un-labelled ADMA	4	-	45.79 ± 5.56	82.4	$p < 0.001$
+ 500 µM un-labelled ADMA	5	-	9.43 ± 2.50	96.4	$p < 0.001$
Pituitary gland					
[^{3}H]-ADMA alone	5	182.9 ± 32.28	-	-	
+ 0.5 µM un-labelled ADMA	5	-	55.42 ± 19.82	69.7	$p < 0.001$
+ 3.0 µM un-labelled ADMA	5	-	32.45 ± 7.89	82.3	$p < 0.001$
+ 10 µM un-labelled ADMA	5	-	52.02 ± 6.24	71.6	$p < 0.001$
+ 100 µM un-labelled ADMA	4	-	58.58 ± 13.38	68.0	$p < 0.001$
+ 500 µM un-labelled ADMA	5	-	10.81 ± 0.92	94.1	$p < 0.001$

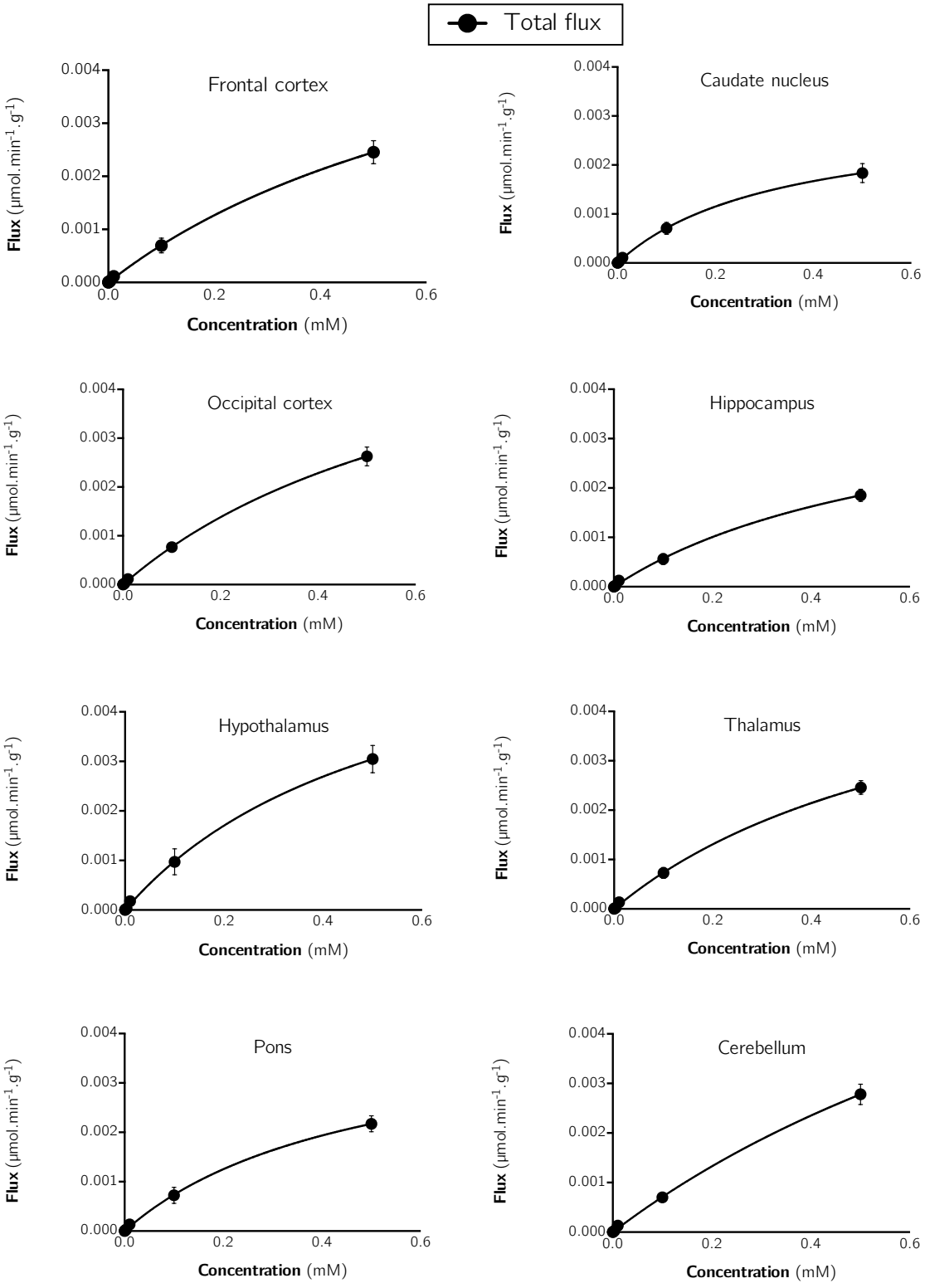

Figure 2-29: Total brain [^{3}H]-ADMA flux is plotted against unlabelled ADMA concentration. Measured values are mean±SEM for 4-5 animals at 5 unlabelled ADMA concentrations.

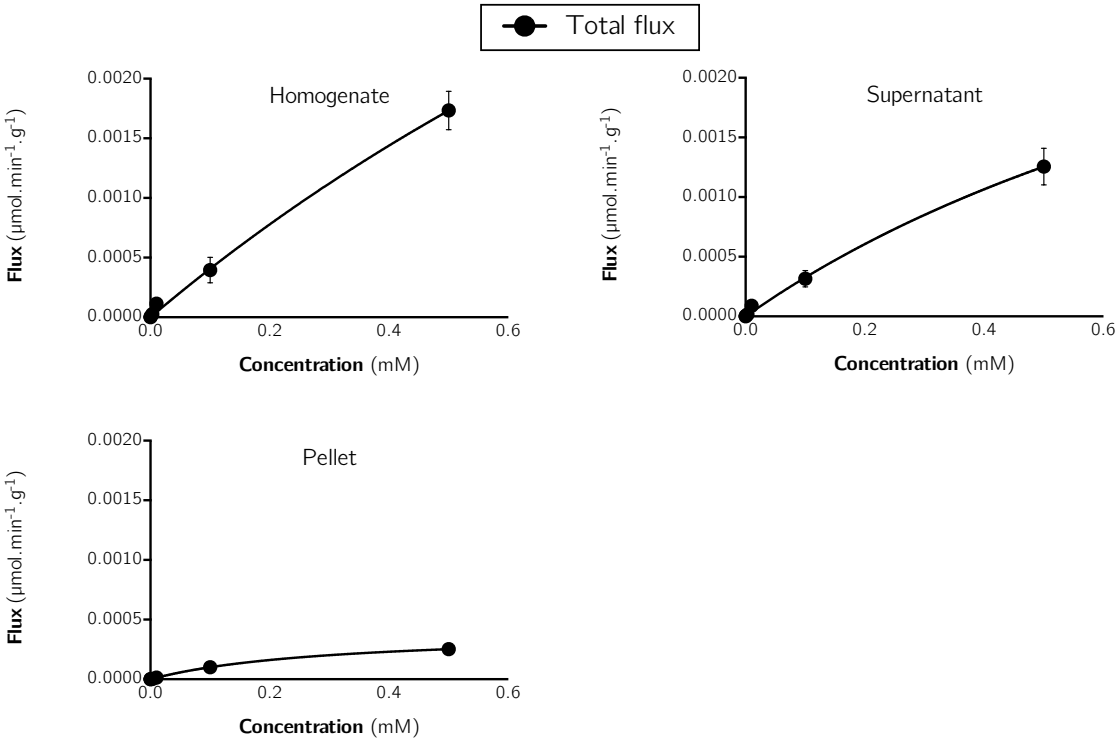

Figure 2-30: Total [^{3}H]-ADMA flux in capillary depletion samples is plotted against unlabelled ADMA concentration. Measured values are mean±SEM for 4-5 animals at 5 unlabelled ADMA concentrations.

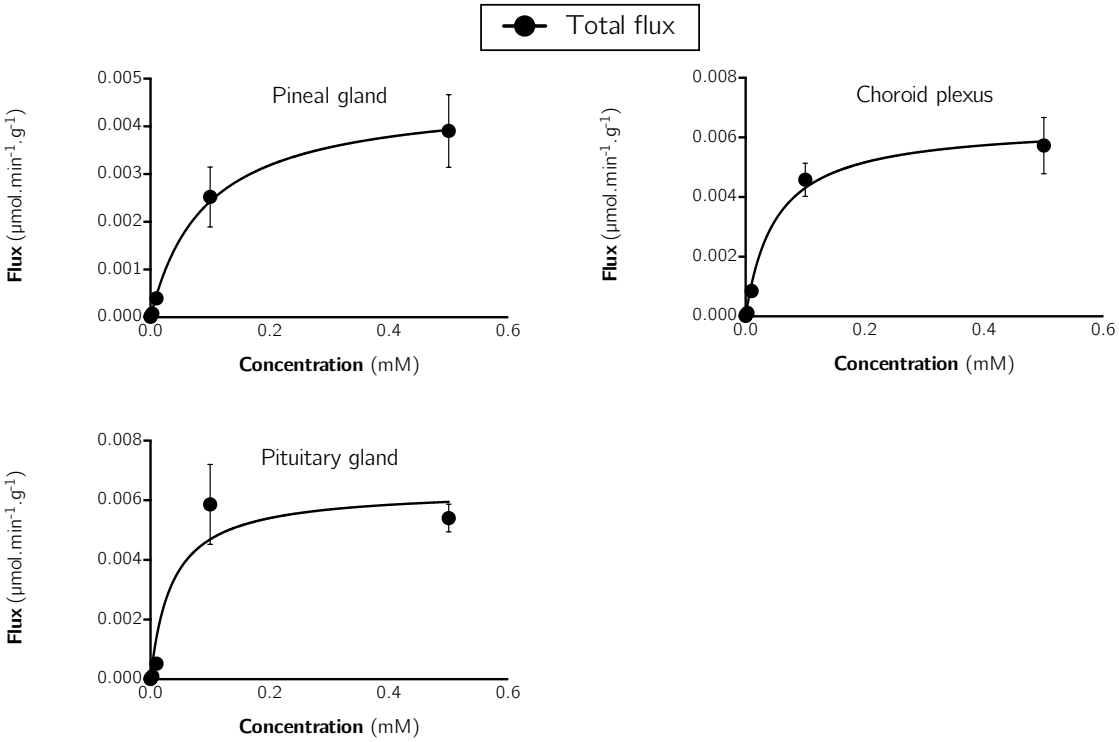

Figure 2-31: Total [^{3}H]-ADMA flux in pineal gland, choroid plexus and pituitary gland is plotted against unlabelled ADMA concentration. Measured values are mean±SEM for 4-5 animals at 5 unlabelled ADMA concentrations.

Table 2-26 shows the values for K_m (half saturation constant) and V_{max} (maximal transport rate), which were derived using non-linear regression analysis (Enzyme kinetics – Michaelis-Menten, GraphPad Prism 6.0 for Mac) of the data shown in **Figure 2-29**, **Figure 2-30** and **Figure 2-31**.

Table 2-26: The kinetic constants for [^{3}H]-ADMA influx into all brain samples.

Tissue	K_m (μM)	V_{max} (nmol.min^{-1}.g^{-1})
Frontal cortex	831.4 ± 479.3	6.534 ± 2.428
Caudate nucleus	327.9 ± 121.9	3.040 ± 0.511
Occipital cortex	752.8 ± 321.1	6.583 ± 1.750
Hippocampus	632.7 ± 241.4	4.192 ± 0.0938
Hypothalamus	552.2 ± 268.4	6.410 ± 1.735
Thalamus	706.6 ± 242.9	5.932 ± 1.244
Pons	478.5 ± 176.1	4.250 ± 0.0824
Cerebellum	1352 ± 946.0	10.30 ± 5.343
Homogenate	2225 ± 319.9	9.442 ± 1.117
Supernatant	1249 ± 129.6	4.392 ± 3.312
Pellet	301.4 ± 25.72	4.045 ± 1.367
Pineal gland	281.0 ± 166.7	9.711 ± 2.336
Choroid plexus	49.96 ± 17.41	6.455 ± 0.555
Pituitary gland	51.41 ± 16.42	6.160 ± 0.439

K_m and V_{max} values for the three groups of samples shown in **Table 2-26** were analysed by one-way ANOVA with Tukey's post-hoc multiple comparisons tests. There were no statistically significant differences between the K_m values for the eight brain regions sampled. The K_m values for capillary depletion samples were all significantly

different from each other ($p < 0.05$). Among the CVOs, the $\boldsymbol{K_m}$ for the pineal gland was found to differ from the $\boldsymbol{K_m}$ values for the choroid plexus and pituitary gland ($p < 0.05$).

With regards to $\boldsymbol{V_{max}}$ values for ADMA in the eight brain regions sampled, no statistically significant differences were found. Similarly among the capillary depletion samples and the CVO samples respectively there were no statistically significant differences ($p > 0.05$ in both cases).

2.4.3 Cross-competition studies

Cross-competition studies were broken down into the following (see ***section 2.3.1.2L - Cross-competition experiments***):

i. Specific transport inhibition studies based on known inhibitors of transport systems
ii. Direct competition of ADMA on arginine transport
iii. Direct competition of arginine on ADMA transport
iv. Pre-loading/trans-stimulation experiments

2.4.3.1 Identification of specific transport system

2.4.3.1A Arginine

The transport of [^{3}H]-arginine across the blood-brain and blood-CSF barriers was examined in the presence of specific transport inhibitors (previously described with the transporters they inhibit in **Table 2-10**). All inhibitors were used at previously published concentrations known to maximally inhibit the relevant transport systems. In this section, one-way ANOVA with Dunnett's multiple comparisons tests were used to compare means to each other within each sample/region.

The uptake of [^{3}H]-arginine is almost totally inhibited (up to 99.7%, **Table 2-27**) by 20 mM *L*-homoarginine in all brain regions (**Figure 2-32**, $p < 0.001$ in all regions except thalamus ($p < 0.01$), and pons and hypothalamus ($p < 0.05$)). While the inclusion of 4 mM BCH in artificial plasma caused slight increases in [^{3}H]-arginine uptake, these differences did not attain statistical significance in any of the brain regions sampled. Inclusion of 500 µM α-methyl-*D*,*L*-tryptophan in artificial plasma conversely had a tendency to decrease [^{3}H]-arginine uptake, but only attained statistical significance in the hippocampus (47.5% inhibition, **Table 2-27**). These trends were also mirrored in whole brain homogenate, supernatant containing brain parenchyma, and endothelial cell-enriched pellets following capillary depletion (**Figure 2-33**).

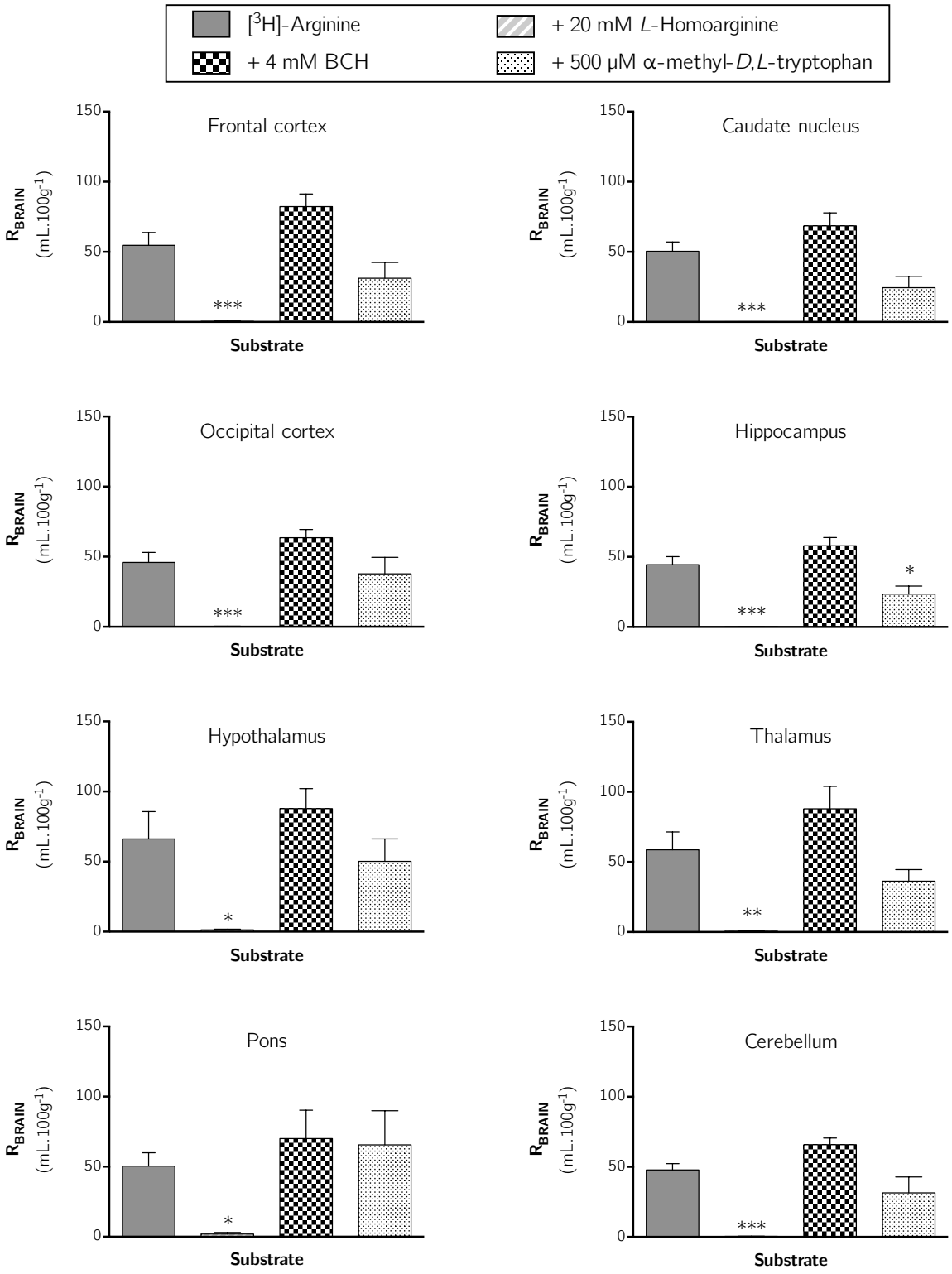

Figure 2-32: The effect of *L*-homoarginine, BCH and α-methyl-*D,L*-tryptophan on the regional brain uptake of [^{3}H]-arginine (10 minute perfusion). Uptake is expressed as the percentage ratio of tissue to plasma (mL.100 g^{-1}) and is corrected for [^{14}C]-sucrose (vascular space). Perfusion time is 10 minutes. Each bar represents the mean ± SEM of 4-6 animals. Asterisks represent one-way ANOVA with Dunnett's post-hoc tests comparing mean±SEM to control, *$p < 0.05$, **$p < 0.01$, ***$p < 0.001$ (GraphPad Prism 6.0 for Mac).

Table 2-27: Results obtained from specific transport-inhibition studies for [^{3}H]-arginine in the brain. One-way ANOVA with Dunnett's post-hoc test was used to compare means to control ([^{3}H]-arginine alone), with statistical significance taken as $p < 0.05$. n = number of experiments. All values corrected for [^{14}C]-sucrose vascular space.

Tissue	n	R_{BRAIN} (mL.100g^{-1})		% inhibition	*p*
Frontal cortex					
[^{3}H]-arginine alone	6	54.65 ± 9.12	-	-	
+ 20 mM *L*-homoarginine	5	-	0.46 ± 0.25	99.2	$p < 0.001$
+ 4 mM BCH	5	-	82.36 ± 8.99	-	n.s.
+ 500 µM α-methyl-*D*,*L*-tryptophan	4	-	31.16 ± 11.2	-	n.s.
Caudate nucleus					
[^{3}H]-arginine alone	6	50.38 ± 6.71	-	-	
+ 20 mM *L*-homoarginine	5	-	0.13 ± 0.07	99.7	$p < 0.001$
+ 4 mM BCH	5	-	68.57 ± 9.24	-	n.s.
+ 500 µM α-methyl-*D*,*L*-tryptophan	4	-	24.47 ± 8.11	-	n.s.
Occipital cortex					
[^{3}H]-arginine alone	6	45.93 ± 7.19	-	-	
+ 20 mM *L*-homoarginine	5	-	0.30 ± 0.11	99.4	$p < 0.001$
+ 4 mM BCH	5	-	63.57 ± 5.83	-	n.s.
+ 500 µM α-methyl-*D*,*L*-tryptophan	4	-	37.83 ± 11.8	-	n.s.
Hippocampus					
[^{3}H]-arginine alone	6	44.32 ± 5.74	-	-	
+ 20 mM *L*-homoarginine	5	-	0.18 ± 0.11	99.6	$p < 0.001$
+ 4 mM BCH	5	-	57.92 ± 5.88	-	n.s.
+ 500 µM α-methyl-*D*,*L*-tryptophan	4	-	23.32 ± 5.71	47.5	$p < 0.05$
Hypothalamus					
[^{3}H]-arginine alone	6	66.20 ± 19.5	-	-	
+ 20 mM *L*-homoarginine	4	-	1.31 ± 0.56	98.0	$p < 0.05$
+ 4 mM BCH	5	-	87.83 ± 14.3	-	n.s.
+ 500 µM α-methyl-*D*,*L*-tryptophan	4	-	50.19 ± 16.0	-	n.s.
Thalamus					
[^{3}H]-arginine alone	6	58.74 ± 12.7	-	-	
+ 20 mM *L*-homoarginine	5	-	0.53 ± 0.35	99.1	$p < 0.01$
+ 4 mM BCH	5	-	87.90 ± 16.0	-	n.s.
+ 500 µM α-methyl-*D*,*L*-tryptophan	4	-	36.34 ± 8.20	-	n.s.
Pons					
[^{3}H]-arginine alone	6	50.38 ± 9.53	-	-	
+ 20 mM *L*-homoarginine	5	-	1.91 ± 1.11	96.2	$p < 0.05$
+ 4 mM BCH	5	-	70.09 ± 20.2	-	n.s.
+ 500 µM α-methyl-*D*,*L*-tryptophan	4	-	65.60 ± 24.3	-	n.s.

Table 2-27 continued...

Tissue	n	R_{BRAIN} (mL.100g^{-1})		% inhibition	*p*
Cerebellum					
[^{3}H]-arginine alone	6	47.77 ± 4.52	-		
+ 20 mM *L*-homoarginine	5	-	0.4411 ± 0.14	99.1	$p < 0.001$
+ 4 mM BCH	5	-	65.84 ± 4.77	-	n.s.
+ 500 µM α-methyl-*D*,*L*-tryptophan	4	-	31.45 ± 11.4	-	n.s.

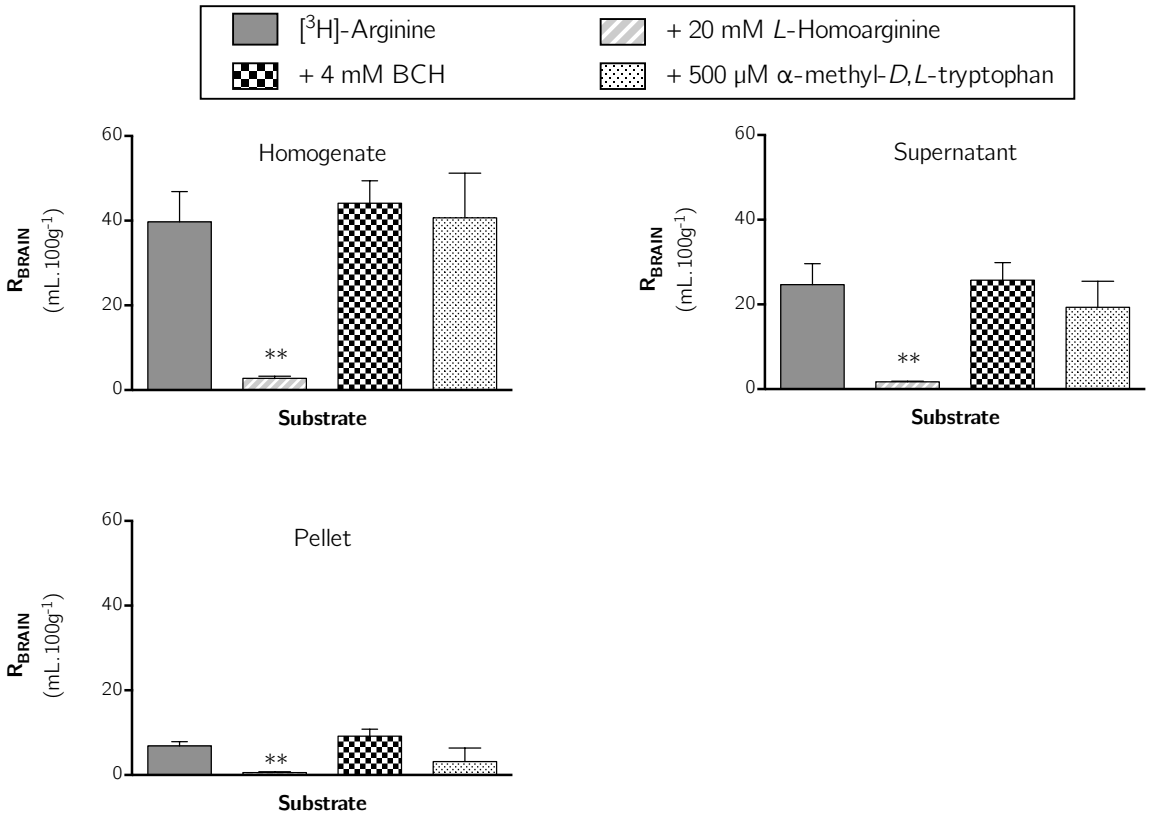

Figure 2-33: The effect of *L*-homoarginine, BCH and α-methyl-*D*,*L*-tryptophan on the distribution of [^{3}H]-arginine in capillary depletion samples (10 minute perfusion). Uptake is expressed as the percentage ratio of tissue to plasma (mL.100 g^{-1}) and is corrected for [^{14}C]-sucrose (vascular space). Perfusion time is 10 minutes. Each bar represents the mean ± SEM of 4-6 animals. Asterisks represent one-way ANOVA with Dunnett's post-hoc tests comparing mean±SEM to control, $^{**}p < 0.01$ (GraphPad Prism 6.0 for Mac).

Table 2-28: Results obtained from specific transport-inhibition studies for [^{3}H]-arginine in capillary depletion samples. One-way ANOVA with Dunnett's post-hoc test was used to compare means to control ([^{3}H]-arginine alone), with statistical significance taken as $p < 0.05$. n = number of experiments.

Tissue	n	R_{BRAIN} (mL.100g^{-1})		% inhibition	*p*
Homogenate					
[^{3}H]-arginine alone	6	39.71 ± 7.19	-	-	
+ 20 mM *L*-homoarginine	5	-	2.80 ± 0.47	93.0	$p < 0.01$
+ 4 mM BCH	5	-	44.13 ± 5.30	-	n.s.
+ 500 µM α-methyl-*D,L*-tryptophan	4	-	40.66 ± 10.57	-	n.s.
Supernatant					
[^{3}H]-arginine alone	6	24.7 ± 4.91	-	-	
+ 20 mM *L*-homoarginine	5	-	1.75 ± 0.14	92.9	$p < 0.01$
+ 4 mM BCH	5	-	25.71 ± 4.14	-	n.s.
+ 500 µM α-methyl-*D,L*-tryptophan	4	-	19.3 ± 6.16	-	n.s.
Pellet					
[^{3}H]-arginine alone	6	6.871 ± 1.02	-	-	
+ 20 mM *L*-homoarginine	5	-	0.58 ± 0.20	91.5	$p < 0.01$
+ 4 mM BCH	5	-	9.16 ± 1.68	-	n.s.
+ 500 µM α-methyl-*D,L*-tryptophan	4	-	3.18 ± 3.10	-	n.s.

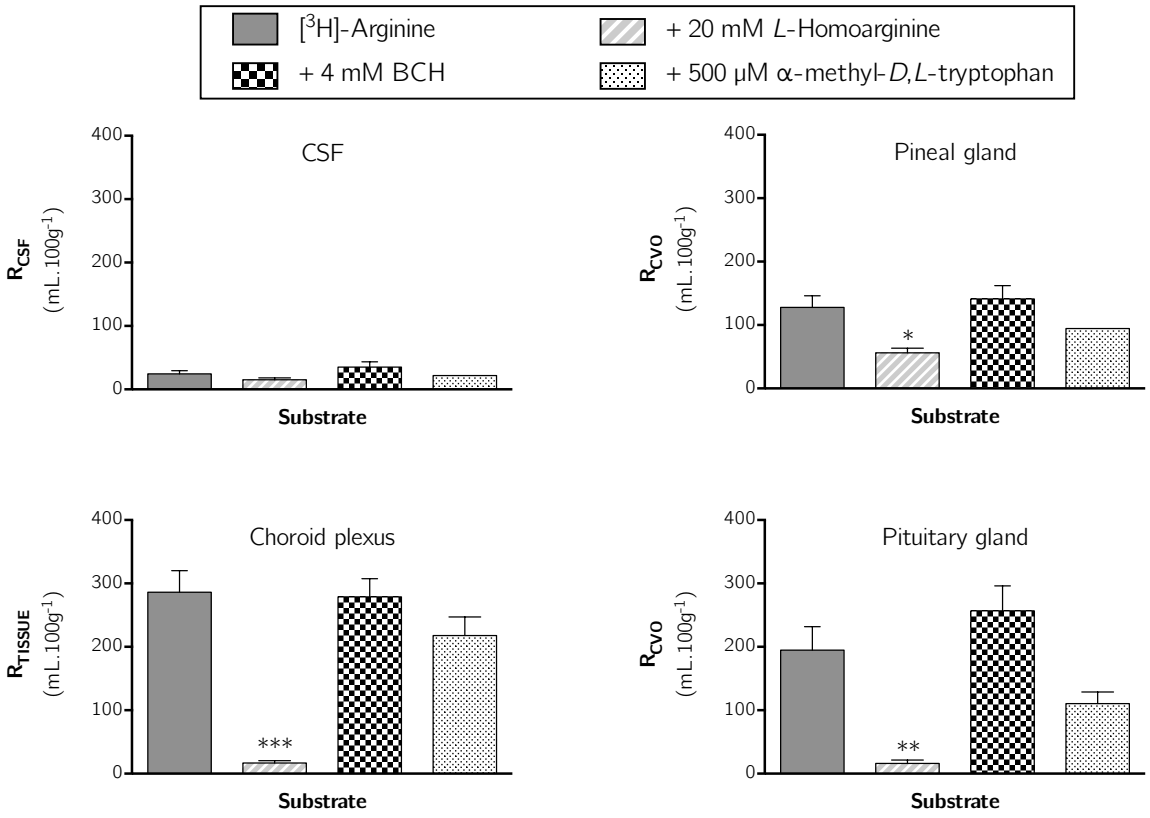

Figure 2-34: The effect of *L*-homoarginine, BCH and α-methyl-*D,L*-tryptophan on the distribution of [^{3}H]-arginine in CSF, choroid plexus and CVOs (10 minute perfusion). Uptake is expressed as the percentage ratio of tissue or CSF to plasma (mL.100 g^{-1}). Perfusion time is 10 minutes. Each bar represents the mean ± SEM of 4-6 animals. Asterisks represent one-way ANOVA with Dunnett's post-hoc tests comparing mean±SEM to control, *$p < 0.05$, **$p < 0.01$, ***$p < 0.001$ (GraphPad Prism 6.0 for Mac).

The distribution of [^{3}H]-arginine in the pineal gland, choroid plexus and pituitary gland was significantly inhibited by 20 mM *L*-homoarginine, (**Figure 2-34** and **Table 2-29**, $p < 0.05$), however no effect was observed in the CSF ($p > 0.05$). In line with observations in all other samples, the inclusion of either 4 mM BCH or 500 µM α-methyl-*D,L*-tryptophan in artificial plasma had no statistically significant effect on the distribution of [^{3}H]-arginine ($p > 0.05$).

Table 2-29: Results obtained from specific transport-inhibition studies for [^{3}H]-arginine in the CSF, choroid plexus and CVOs. One-way ANOVA with Dunnett's post-hoc test was used to compare means to control ([^{3}H]-arginine alone), with statistical significance taken as $p < 0.05$. n = number of experiments.

Tissue	n	R_{BRAIN} (mL.100g^{-1})		% inhibition	*p*
CSF					
[^{3}H]-arginine alone	6	24.51 ± 5.01	-	-	
+ 20 mM *L*-homoarginine	5	-	15.09 ± 2.95	-	n.s.
+ 4 mM BCH	5	-	35.16 ± 8.34	-	n.s.
+ 500 µM α-methyl-*D*,*L*-tryptophan	4	-	21.93 ± 0.05	-	n.s.
Pineal gland					
[^{3}H]-arginine alone	6	128.0 ± 18.11	-	-	
+ 20 mM *L*-homoarginine	5	-	56.07 ± 7.45	56.2	$p < 0.05$
+ 4 mM BCH	5	-	141.3 ± 20.9	-	n.s.
+ 500 µM α-methyl-*D*,*L*-tryptophan	4	-	94.54 ± 0.31	-	n.s.
Choroid plexus					
[^{3}H]-arginine alone	6	286.1 ± 33.92	-	-	
+ 20 mM *L*-homoarginine	5	-	17.00 ± 3.34	94.1	$p < 0.001$
+ 4 mM BCH	5	-	278.8 ± 28.8	-	n.s.
+ 500 µM α-methyl-*D*,*L*-tryptophan	4	-	217.8 ± 29.6	-	n.s.
Pituitary gland					
[^{3}H]-arginine alone	6	194.9 ± 36.9	-	-	
+ 20 mM *L*-homoarginine	5	-	16.21 ± 5.45	91.7	$p < 0.001$
+ 4 mM BCH	5	-	256.7 ± 39.6	-	n.s.
+ 500 µM α-methyl-*D*,*L*-tryptophan	4	-	110.5 ± 18.3	-	n.s.

2.4.3.1B ADMA

The transport of [^{3}H]-ADMA across the blood-brain and blood-CSF barriers was also examined in the presence of specific transport inhibitors (previously described with the transporters they inhibit in **Table 2-10**). All inhibitors were used at previously published concentrations known to maximally inhibit the relevant transport systems. In this section, one-way ANOVA with Dunnett's multiple comparisons tests were used to compare means to each other within each sample/region.

The uptake of [^{3}H]-ADMA is almost totally inhibited by 20 mM *L*-homoarginine in all brain regions (**Figure 2-35** and **Table 2-30**, $p < 0.001$). Meanwhile, the inclusion of either 4 mM BCH, 500 µM α-methyl-*D*,*L*-tryptophan, 200 µM *L*-phenylalanine, 5 mM *L*-leucine, or 2 mM harmaline in artificial plasma also appeared to inhibit [^{3}H]-ADMA uptake in brain regions, but to a much lesser degree, and only attaining statistical significance in some regions (**Figure 2-35** and **Table 2-30**).

L-homoarginine also inhibited uptake of [^{3}H]-ADMA in whole brain homogenate and brain parenchyma (supernatant) following capillary depletion (**Figure 2-36** and **Table 2-31**, $p < 0.05$). *L*-phenylalanine and *L*-leucine inhibited [^{3}H]-ADMA in whole brain homogenate, but not brain parenchyma (supernatant) following capillary depletion (**Table 2-31**, $p < 0.05$). None of the inhibitors inhibited uptake in the endothelial cell-enriched pellet (**Figure 2-36** and **Table 2-31**).

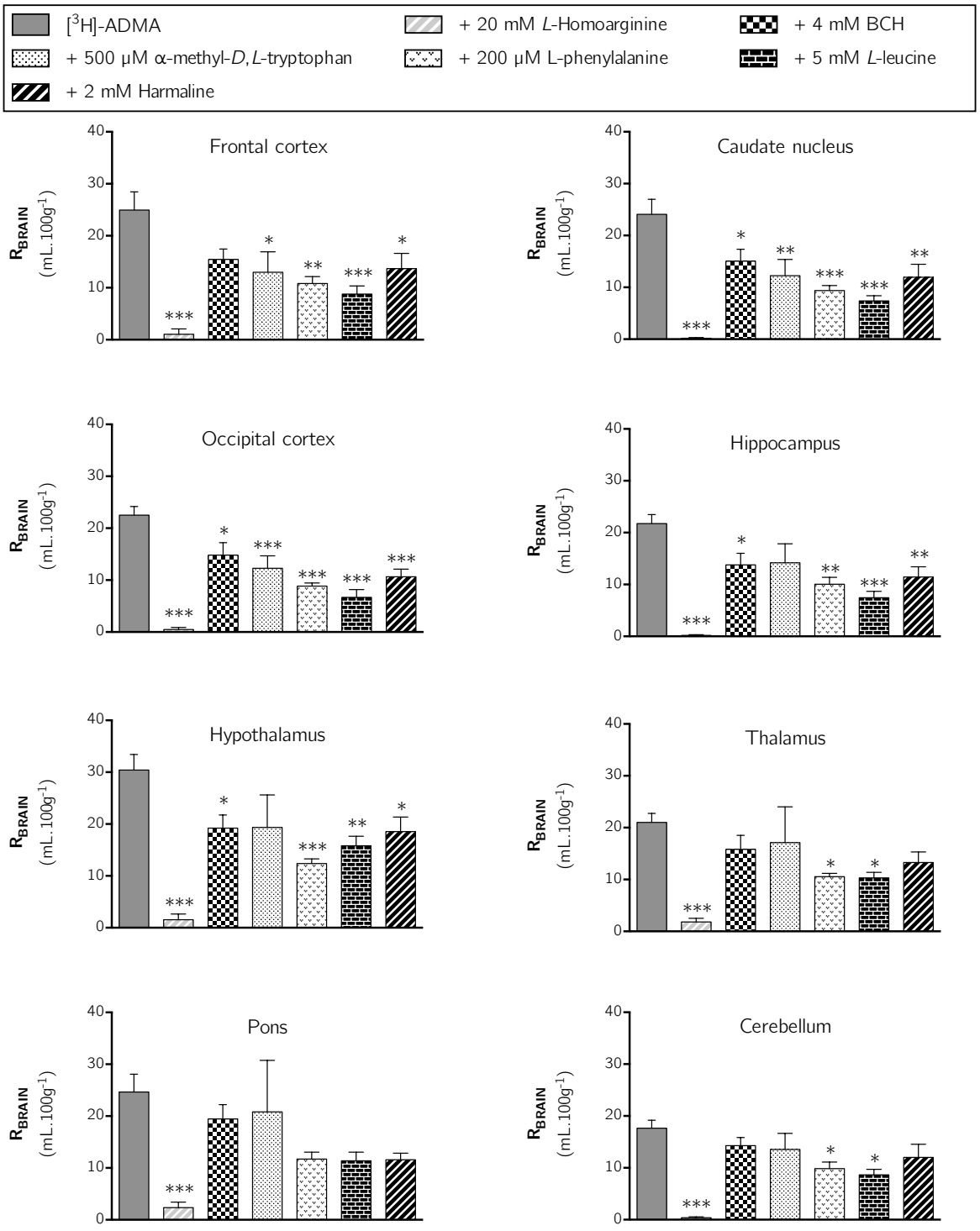

Figure 2-35: The effect of *L*-homoarginine, BCH, α-methyl-*D*,*L*-tryptophan, *L*-phenylalanine, *L*-leucine and harmaline on the regional brain uptake of [^{3}H]-ADMA (10 minute perfusion). Uptake is expressed as the percentage ratio of tissue to plasma (mL.100 g^{-1}) and is corrected for [^{14}C]-sucrose (vascular space). Perfusion time is 10 minutes. Each bar represents the mean ± SEM of 4-5 animals. Asterisks represent one-way ANOVA with Dunnett's post-hoc tests comparing mean±SEM to control, *$p < 0.05$, **$p < 0.01$, ***$p < 0.001$ (GraphPad Prism 6.0 for Mac).

Table 2-30: Results obtained from specific transport-inhibition studies for [^{3}H]-ADMA in the brain. One-way ANOVA with Dunnett's post-hoc test was used to compare means to control ([^{3}H]-ADMA alone), with statistical significance taken as $p < 0.05$. n = number of experiments.

Tissue	n	R_{BRAIN} (mL.100g^{-1})		% inhibition	*p*
Frontal cortex					
[^{3}H]-ADMA alone	5	24.94 ± 3.50	-		
+ 20 mM *L*-homoarginine	5	-	1.06 ± 1.02	95.7	$p < 0.001$
+ 4 mM BCH	5	-	15.45 ± 1.98	-	n.s.
+ 500 µM α-methyl-*D,L*-tryptophan	5	-	12.97 ± 3.94	48.0	$p < 0.05$
+ 200 µM *L*-phenylalanine	5	-	10.8 ± 1.35	56.7	$p < 0.01$
+ 5 mM *L*-leucine	5	-	8.785 ± 1.56	64.8	$p < 0.001$
+ 2 mM Harmaline	5	-	13.68 ± 2.95	45.1	$p < 0.05$
Caudate nucleus					
[^{3}H]-ADMA alone	5	24.07 ± 2.92	-		
+ 20 mM *L*-homoarginine	5	-	0.18 ± 0.13	99.2	$p < 0.001$
+ 4 mM BCH	5	-	15.04 ± 2.31	37.5	$p < 0.05$
+ 500 µM α-methyl-*D,L*-tryptophan	5	-	12.24 ± 3.14	49.1	$p < 0.01$
+ 200 µM *L*-phenylalanine	5	-	9.39 ± 0.96	61.0	$p < 0.001$
+ 5 mM *L*-leucine	5	-	7.38 ± 0.99	69.3	$p < 0.001$
+ 2 mM Harmaline	5	-	11.94 ± 2.51	50.4	$p < 0.01$
Occipital cortex					
[^{3}H]-ADMA alone	5	22.52 ± 1.65	-		
+ 20 mM *L*-homoarginine	5	-	0.49 ± 0.40	97.8	$p < 0.001$
+ 4 mM BCH	5	-	14.82 ± 2.41	34.2	$p < 0.05$
+ 500 µM α-methyl-*D,L*-tryptophan	5	-	12.28 ± 2.41	45.5	$p < 0.001$
+ 200 µM *L*-phenylalanine	5	-	8.86 ± 0.59	60.7	$p < 0.001$
+ 5 mM *L*-leucine	5	-	6.69 ± 1.50	70.3	$p < 0.001$
+ 2 mM Harmaline	5	-	10.65 ± 1.49	52.7	$p < 0.001$
Hippocampus					
[^{3}H]-ADMA alone	5	21.74 ± 1.75	-		
+ 20 mM *L*-homoarginine	5	-	0.20 ± 0.13	99.1	$p < 0.001$
+ 4 mM BCH	5	-	13.79 ± 2.21	36.6	$p < 0.05$
+ 500 µM α-methyl-*D,L*-tryptophan	5	-	14.17 ± 3.69	-	n.s.
+ 200 µM *L*-phenylalanine	5	-	10.05 ± 1.32	53.8	$p < 0.01$
+ 5 mM *L*-leucine	5	-	7.45 ± 1.24	65.7	$p < 0.001$
+ 2 mM Harmaline	5	-	11.45 ± 1.97	47.3	$p < 0.01$
Hypothalamus					
[^{3}H]-ADMA alone	5	30.42 ± 2.98	-		
+ 20 mM *L*-homoarginine	5	-	1.54 ± 1.12	94.9	$p < 0.001$
+ 4 mM BCH	4	-	19.23 ± 2.51	36.8	$p < 0.05$
+ 500 µM α-methyl-*D,L*-tryptophan	3	-	19.34 ± 6.28	-	n.s.
+ 200 µM *L*-phenylalanine	5	-	12.38 ± 0.89	59.3	$p < 0.001$
+ 5 mM *L*-leucine	5	-	15.81 ± 1.84	48.0	$p < 0.01$
+ 2 mM Harmaline	5	-	18.56 ± 2.79	39.0	$p < 0.05$

Table 2-30 continued...

Tissue	n	R_{BRAIN} (mL.100g^{-1})		% inhibition	*p*
Thalamus					
[^{3}H]-ADMA alone	5	21.09 ± 1.74	-		
+ 20 mM *L*-homoarginine	5	-	1.81 ± 0.71	91.4	$p < 0.001$
+ 4 mM BCH	5	-	15.82 ± 2.69	-	n.s.
+ 500 µM α-methyl-*D*,*L*-tryptophan	4	-	17.12 ± 6.91	-	n.s.
+ 200 µM *L*-phenylalanine	5	-	10.54 ± 0.65	49.8	$p < 0.05$
+ 5 mM *L*-leucine	5	-	10.31 ± 1.06	50.9	$p < 0.05$
+ 2 mM Harmaline	5	-	13.29 ± 2.03	36.7	n.s.
Pons					
[^{3}H]-ADMA alone	5	24.64 ± 3.44	-		
+ 20 mM *L*-homoarginine	5	-	2.36 ± 1.06	90.4	$p < 0.001$
+ 4 mM BCH	5	-	19.44 ± 2.80	-	n.s.
+ 500 µM α-methyl-*D*,*L*-tryptophan	4	-	20.83 ± 9.92	-	n.s.
+ 200 µM *L*-phenylalanine	5	-	11.71 ± 1.35	-	n.s.
+ 5 mM *L*-leucine	5	-	11.38 ± 1.67	-	n.s.
+ 2 mM Harmaline	5	-	11.57 ± 1.29	-	n.s.
Cerebellum					
[^{3}H]-ADMA alone	4	17.65 ± 1.52	-		
+ 20 mM *L*-homoarginine	5	-	0.37 ± 0.19	97.9	$p < 0.001$
+ 4 mM BCH	5	-	14.29 ± 1.56	-	n.s.
+ 500 µM α-methyl-*D*,*L*-tryptophan	5	-	13.55 ± 3.09	-	n.s.
+ 200 µM *L*-phenylalanine	5	-	9.84 ± 1.27	44.3	$p < 0.05$
+ 5 mM *L*-leucine	5	-	8.66 ± 1.07	51.0	$p < 0.05$
+ 2 mM Harmaline	5	-	12.02 ± 2.52	-	n.s.

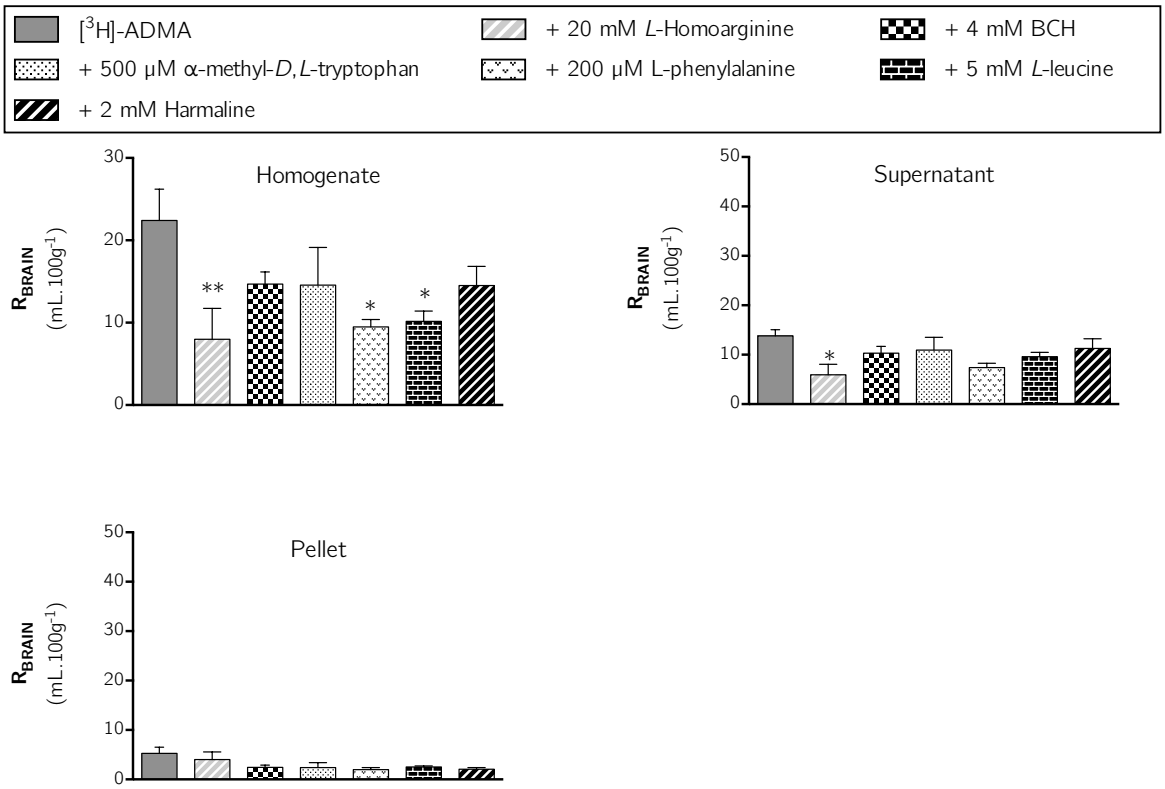

Figure 2-36: The effect of *L*-homoarginine, BCH, α-methyl-*D*,*L*-tryptophan, *L*-phenylalanine, *L*-leucine and harmaline on the distribution of [^{3}H]-ADMA in capillary depletion samples (10 minute perfusion). Uptake is expressed as the percentage ratio of tissue to plasma (mL.100 g^{-1}) and is corrected for [^{14}C]-sucrose (vascular space). Perfusion time is 10 minutes. Each bar represents the mean ± SEM of 4-5 animals. Asterisks represent one-way ANOVA with Dunnett's post-hoc tests comparing mean±SEM to control, *$p < 0.05$, **$p < 0.01$ (GraphPad Prism 6.0 for Mac).

Table 2-31: Results obtained from specific transport-inhibition studies for [^{3}H]-ADMA in capillary depletion samples. One-way ANOVA with Dunnett's post-hoc test was used to compare means to control ([^{3}H]-ADMA alone), with statistical significance taken as $p < 0.05$. n = number of experiments.

Tissue	n	R_{BRAIN} (mL.100g^{-1})		% inhibition	*p*
Homogenate					
[^{3}H]-ADMA alone	5	22.41 ± 3.81	-		
+ 20 mM *L*-homoarginine	5	-	8.00 ± 3.74	64.3	$p < 0.001$
+ 4 mM BCH	5	-	14.71 ± 1.46	-	n.s.
+ 500 µM α-methyl-*D,L*-tryptophan	4	-	14.57 ± 4.58	-	n.s.
+ 200 µM *L*-phenylalanine	5	-	9.48 ± 0.90	57.7	$p < 0.05$
+ 5 mM *L*-leucine	5	-	10.15 ± 1.25	54.7	$p < 0.05$
+ 2 mM Harmaline	5	-	14.49 ± 2.33	-	n.s.
Supernatant					
[^{3}H]-ADMA alone	5	13.81 ± 1.24	-		
+ 20 mM *L*-homoarginine	5	-	5.96 ± 2.11	56.9	$p < 0.05$
+ 4 mM BCH	5	-	10.31 ± 1.39	-	n.s.
+ 500 µM α-methyl-*D,L*-tryptophan	5	-	10.88 ± 2.59	-	n.s.
+ 200 µM *L*-phenylalanine	5	-	7.41 ± 0.86	-	n.s.
+ 5 mM *L*-leucine	4	-	9.60 ± 0.86	-	n.s.
+ 2 mM Harmaline	5	-	11.28 ± 1.96	-	n.s.
Pellet					
[^{3}H]-ADMA alone	5	5.27 ± 1.26	-		
+ 20 mM *L*-homoarginine	5	-	4.03 ± 1.53	-	n.s.
+ 4 mM BCH	5	-	2.38 ± 0.48	-	n.s.
+ 500 µM α-methyl-*D,L*-tryptophan	5	-	2.39 ± 0.99	-	n.s.
+ 200 µM *L*-phenylalanine	5	-	1.98 ± 0.40	-	n.s.
+ 5 mM *L*-leucine	4	-	2.53 ± 0.19	-	n.s.
+ 2 mM Harmaline	5	-	2.07 ± 0.32	-	n.s.

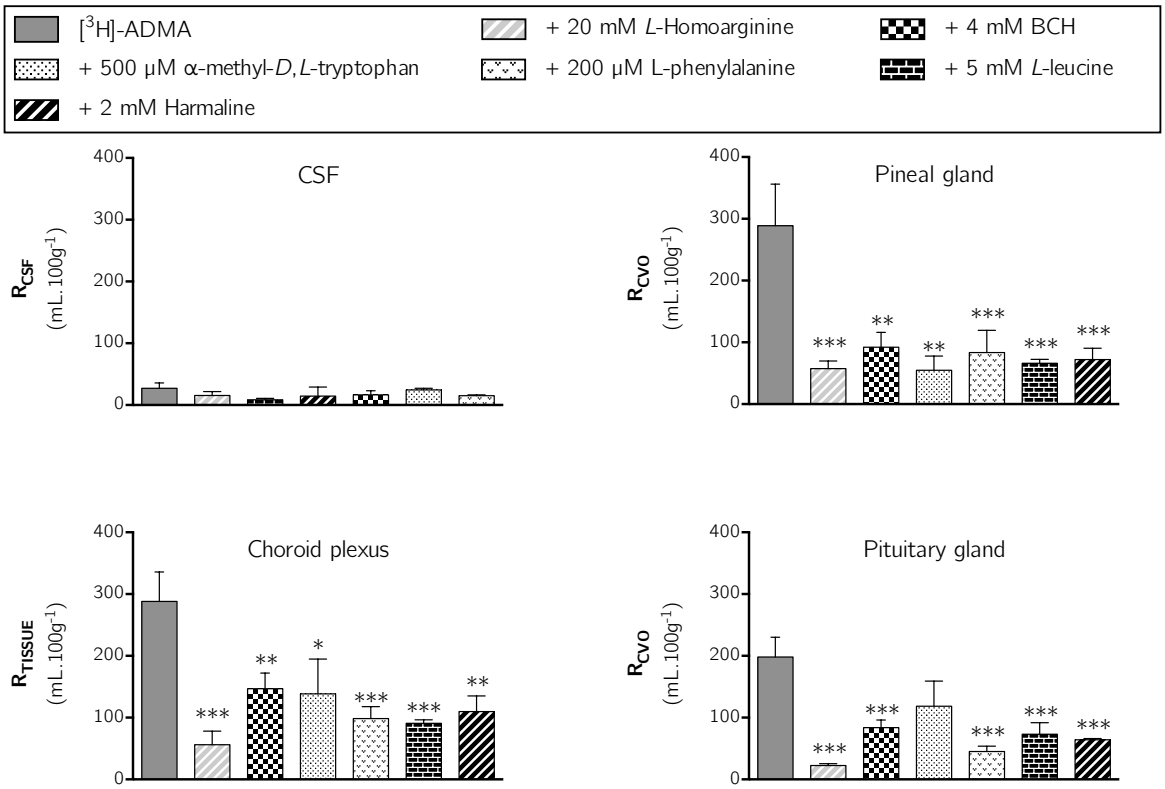

Figure 2-37: The effect of *L*-homoarginine, BCH, α-methyl-*D*,*L*-tryptophan, *L*-phenylalanine, *L*-leucine and harmaline on the distribution of [^{3}H]-ADMA in CSF, choroid plexus and CVOs (10 minute perfusion). Uptake is expressed as the percentage ratio of tissue or CSF to plasma (mL.100 g^{-1}). Perfusion time is 10 minutes. Each bar represents the mean ± SEM of 4-5 animals. Asterisks represent one-way ANOVA with Dunnett's post-hoc tests comparing mean±SEM to control, *$p < 0.05$, **$p < 0.01$, ***$p < 0.001$ (GraphPad Prism 6.0 for Mac).

None of the inhibitors affected the distribution of [^{3}H]-ADMA in CSF (**Figure 2-37**). All inhibitors inhibited the distribution of [^{3}H]-ADMA in the pineal gland and choroid plexus (**Figure 2-37** and **Table 2-32**, $p < 0.05$). The distribution of [^{3}H]-ADMA in the pituitary gland was inhibited by all inhibitors except for 500 µM α-methyl-*D*,*L*-tryptophan.

Table 2-32: Results obtained from specific transport-inhibition studies for [^{3}H]-ADMA in the CSF, choroid plexus and CVOs. One-way ANOVA with Dunnett's post-hoc test was used to compare means to control ([^{3}H]-ADMA alone), with statistical significance taken as $p < 0.05$. n = number of experiments.

Tissue	n	R_{BRAIN} (mL.100g^{-1})		% inhibition	*p*
CSF					
[^{3}H]-ADMA alone	5	27.26 ± 8.69	-		
+ 20 mM *L*-homoarginine	5	-	15.44 ± 6.47	-	n.s.
+ 4 mM BCH	5	-	8.45 ± 2.36	-	n.s.
+ 500 µM α-methyl-*D,L*-tryptophan	4	-	14.60 ± 14.53	-	n.s.
+ 200 µM *L*-phenylalanine	4	-	16.51 ± 6.79	-	n.s.
+ 5 mM *L*-leucine	5	-	24.54 ± 2.48	-	n.s.
+ 2 mM Harmaline	5	-	15.18 ± 1.341	-	n.s.
Pineal gland					
[^{3}H]-ADMA alone	4	288.7 ± 67.54	-		
+ 20 mM *L*-homoarginine	5	-	57.42 ± 12.34	80.1	$p < 0.001$
+ 4 mM BCH	5	-	92.29 ± 23.82	68.0	$p < 0.01$
+ 500 µM α-methyl-*D,L*-tryptophan	4	-	54.40 ± 23.25	81.2	$p < 0.01$
+ 200 µM *L*-phenylalanine	5	-	83.42 ± 36.06	71.1	$p < 0.001$
+ 5 mM *L*-leucine	5	-	66.28 ± 6.28	77.0	$p < 0.001$
+ 2 mM Harmaline	4	-	72.20 ± 18.18	75.0	$p < 0.001$
Choroid plexus					
[^{3}H]-ADMA alone	5	288.1 ± 47.73	-		
+ 20 mM *L*-homoarginine	5	-	56.01 ± 22.01	80.6	$p < 0.001$
+ 4 mM BCH	5	-	146.8 ± 25.52	49.0	$p < 0.01$
+ 500 µM α-methyl-*D,L*-tryptophan	4	-	138.2 ± 56.18	52.0	$p < 0.05$
+ 200 µM *L*-phenylalanine	5	-	98.36 ± 19.53	65.9	$p < 0.001$
+ 5 mM *L*-leucine	5	-	90.75 ± 5.89	68.5	$p < 0.001$
+ 2 mM Harmaline	4	-	109.8 ± 25.53	61.9	$p < 0.01$
Pituitary gland					
[^{3}H]-ADMA alone	5	198.2 ± 31.93	-		
+ 20 mM *L*-homoarginine	5	-	22.61 ± 2.81	88.6	$p < 0.001$
+ 4 mM BCH	5	-	83.80 ± 12.44	57.7	$p < 0.001$
+ 500 µM α-methyl-*D,L*-tryptophan	4	-	118.4 ± 40.81	-	n.s.
+ 200 µM *L*-phenylalanine	5	-	45.22 ± 8.45	77.2	$p < 0.001$
+ 5 mM *L*-leucine	5	-	73.04 ± 18.77	63.1	$p < 0.001$
+ 2 mM Harmaline	5	-	64.27 ± 1.78	67.6	$p < 0.001$

2.4.3.2 Effect of ADMA on *L*-arginine transport

In order to determine the effect of ADMA on the transport of *L*-arginine across the blood-brain and blood-CSF barriers, [^{3}H]-arginine was co-perfused with escalating concentrations of un-labelled ADMA. Concentrations of ADMA were specifically selected to mimic plasma concentrations under normal conditions (0.5 µM), pathophysiological conditions (3.0 µM), and then supraphysiological concentrations (10, 100 and 500 µM); see ***section 2.3.1.2L - Cross-competition experiments (Direct competition between ADMA & L-arginine)***.

Figure 2-38 shows the effect of an excess of unlabelled ADMA on the uptake of [^{3}H]-arginine into all brain regions. These data indicate that [^{3}H]-arginine uptake is only inhibited by 500 µM unlabelled ADMA by an average of approximately 70% (**Table 2-33**, one-way ANOVA with Dunnett's post-hoc test comparing means to control, $p < 0.05$). Capillary depletion analysis of remaining whole brain tissue revealed that distribution of [^{3}H]-arginine in only the whole brain homogenate and resulting supernatant (brain parenchyma) was inhibited by 500 µM unlabelled ADMA by 65.1% and 72.0%, respectively (**Figure 2-39** and **Table 2-34**, $p < 0.05$).

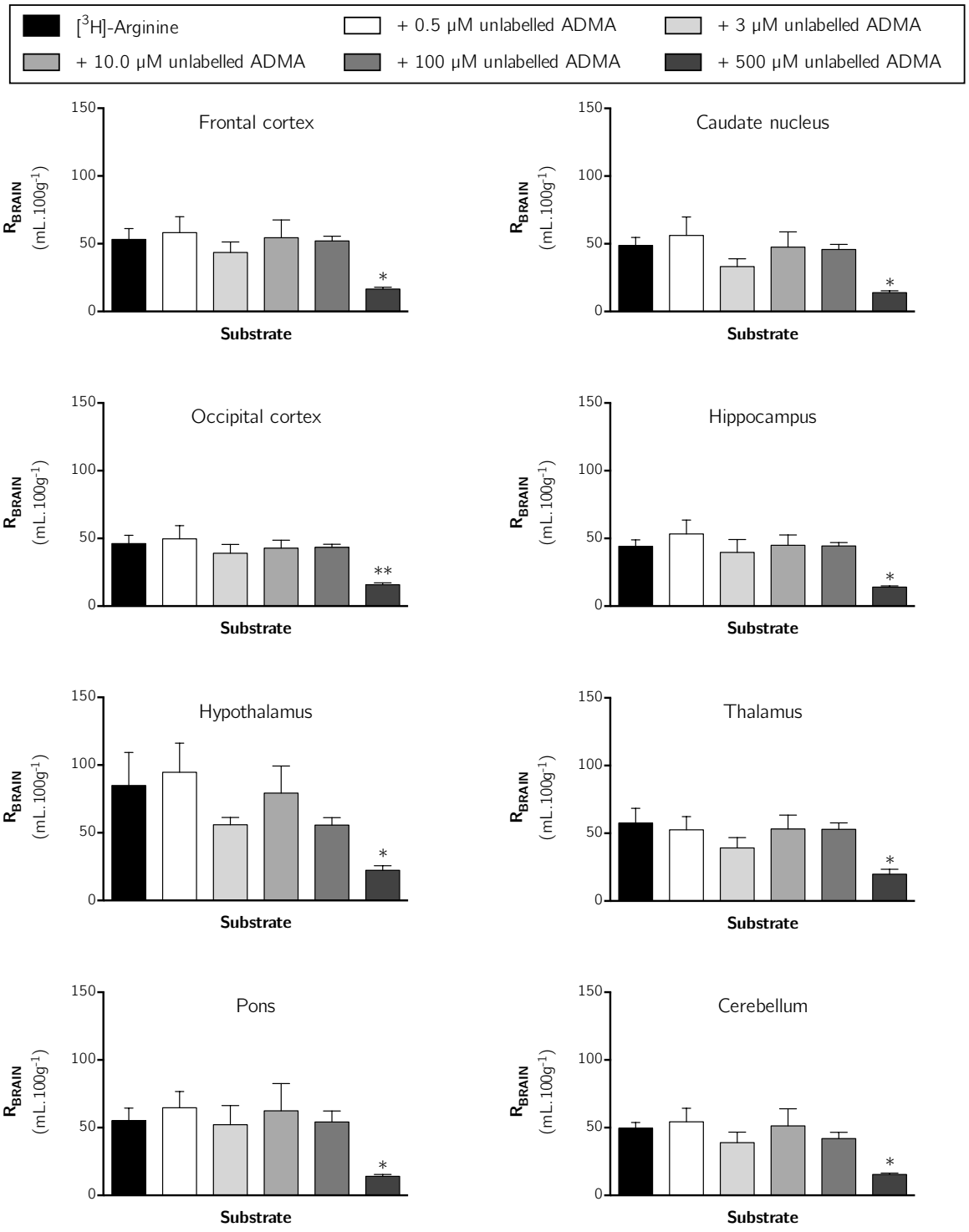

Figure 2-38: The effect of unlabelled ADMA on the regional brain uptake of [^{3}H]-arginine (10 minute perfusion). Uptake is expressed as the percentage ratio of tissue to plasma (mL.100 g^{-1}) and is corrected for [^{14}C]-sucrose (vascular space). Perfusion time is 10 minutes. Each bar represents the mean ± SEM of 4-7 animals. Asterisks represent one-way ANOVA with Dunnett's post-hoc tests comparing mean±SEM to control, *p < 0.05, **p < 0.01 (GraphPad Prism 6.0 for Mac).

Table 2-33: Results obtained from cross-competition studies for [^{3}H]-arginine and un-labelled ADMA in the brain. One-way ANOVA with Dunnett's post-hoc test was used to compare means to control ([^{3}H]-ADMA alone), with statistical significance taken as $p < 0.05$. n = number of experiments.

Tissue	n	R_{BRAIN} (mL.100g^{-1})		% inhibition	*p*
Frontal cortex					
[^{3}H]-arginine alone	7	53.21 ± 7.92	-		
+ 0.5 µM un-labelled ADMA	5	-	58.20 ± 11.79	-	n.s.
+ 3.0 µM un-labelled ADMA	5	-	43.57 ± 7.75	-	n.s.
+ 10 µM un-labelled ADMA	4	-	54.48 ± 13.07	-	n.s.
+ 100 µM un-labelled ADMA	5	-	52.10 ± 3.45	-	n.s.
+ 500 µM un-labelled ADMA	4	-	16.61 ± 1.33	68.8	$p < 0.05$
Caudate nucleus					
[^{3}H]-arginine alone	7	48.85 ± 5.87	-		
+ 0.5 µM un-labelled ADMA	5	-	56.13 ± 13.66	-	n.s.
+ 3.0 µM un-labelled ADMA	5	-	33.18 ± 5.81	-	n.s.
+ 10 µM un-labelled ADMA	4	-	47.53 ± 11.24	-	n.s.
+ 100 µM un-labelled ADMA	5	-	45.84 ± 3.67	-	n.s.
+ 500 µM un-labelled ADMA	4	-	13.98 ± 1.36	71.4	$p < 0.05$
Occipital cortex					
[^{3}H]-arginine alone	7	46.20 ± 6.09	-		
+ 0.5 µM un-labelled ADMA	5	-	49.74 ± 9.69	-	n.s.
+ 3.0 µM un-labelled ADMA	5	-	39.06 ± 6.48	-	n.s.
+ 10 µM un-labelled ADMA	4	-	42.77 ± 5.88	-	n.s.
+ 100 µM un-labelled ADMA	5	-	43.43 ± 2.22	-	n.s.
+ 500 µM un-labelled ADMA	4	-	15.79 ± 1.39	65.8	$p < 0.01$
Hippocampus					
[^{3}H]-arginine alone	7	44.13 ± 4.85	-		
+ 0.5 µM un-labelled ADMA	5	-	53.32 ± 10.27	-	n.s.
+ 3.0 µM un-labelled ADMA	5	-	39.66 ± 9.53	-	n.s.
+ 10 µM un-labelled ADMA	4	-	44.99 ± 7.51	-	n.s.
+ 100 µM un-labelled ADMA	5	-	44.46 ± 2.53	-	n.s.
+ 500 µM un-labelled ADMA	4	-	14.04 ± 0.95	68.2	$p < 0.05$
Hypothalamus					
[^{3}H]-arginine alone	7	84.99 ± 24.32	-		
+ 0.5 µM un-labelled ADMA	5	-	94.63 ± 21.58	-	n.s.
+ 3.0 µM un-labelled ADMA	5	-	55.98 ± 5.30	-	n.s.
+ 10 µM un-labelled ADMA	4	-	79.37 ± 20.00	-	n.s.
+ 100 µM un-labelled ADMA	5	-	55.70 ± 5.46	-	n.s.
+ 500 µM un-labelled ADMA	4	-	22.26 ± 3.43	73.8	$p < 0.05$

Table 2-33 continued...

Tissue	n	R_{BRAIN} (mL.100g^{-1})		% inhibition	*p*
Thalamus					
[^{3}H]-arginine alone	7	57.62 ± 10.79	-		
+ 0.5 µM un-labelled ADMA	5	-	52.52 ± 9.79	-	n.s.
+ 3.0 µM un-labelled ADMA	5	-	39.20 ± 7.60	-	n.s.
+ 10 µM un-labelled ADMA	4	-	53.25 ± 10.14	-	n.s.
+ 100 µM un-labelled ADMA	5	-	52.89 ± 4.77	-	n.s.
+ 500 µM un-labelled ADMA	4	-	19.79 ± 3.66	65.7	$p < 0.05$
Pons					
[^{3}H]-arginine alone	7	55.14 ± 9.35	-		
+ 0.5 µM un-labelled ADMA	5	-	64.64 ± 12.04	-	n.s.
+ 3.0 µM un-labelled ADMA	5	-	52.20 ± 14.12	-	n.s.
+ 10 µM un-labelled ADMA	4	-	62.40 ± 20.13	-	n.s.
+ 100 µM un-labelled ADMA	5	-	54.23 ± 8.06	-	n.s.
+ 500 µM un-labelled ADMA	4	-	14.03 ± 1.39	74.6	$p < 0.05$
Cerebellum					
[^{3}H]-arginine alone	7	49.58 ± 4.22	-		
+ 0.5 µM un-labelled ADMA	5	-	54.26 ± 10.09	-	n.s.
+ 3.0 µM un-labelled ADMA	5	-	38.99 ± 7.67	-	n.s.
+ 10 µM un-labelled ADMA	4	-	51.31 ± 12.62	-	n.s.
+ 100 µM un-labelled ADMA	5	-	41.96 ± 4.64	-	n.s.
+ 500 µM un-labelled ADMA	4	-	15.41 ± 1.022	68.9	$p < 0.05$

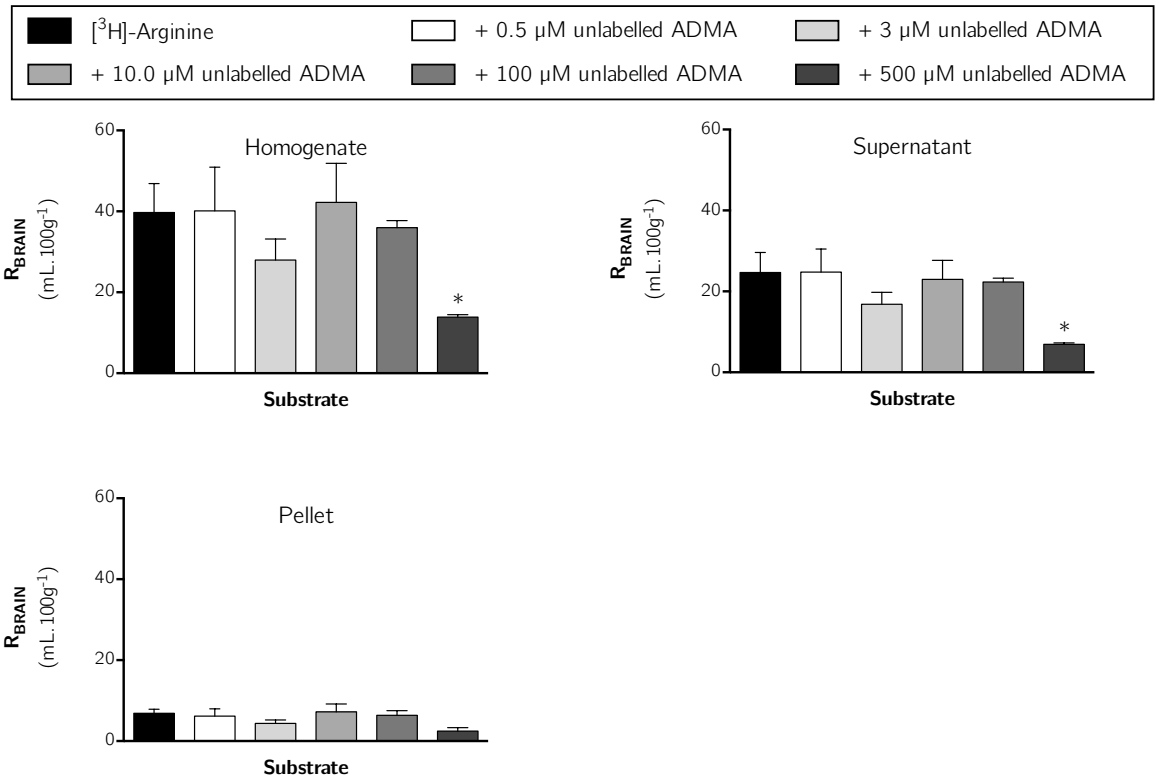

Figure 2-39: The effect of unlabelled ADMA on the distribution of [^{3}H]-arginine in capillary depletion samples (10 minute perfusion). Uptake is expressed as the percentage ratio of tissue to plasma (mL.100 g^{-1}) and is corrected for [^{14}C]-sucrose (vascular space). Perfusion time is 10 minutes. Each bar represents the mean ± SEM of 4-7 animals. Asterisks represent one-way ANOVA with Dunnett's post-hoc tests comparing mean±SEM to control, *$p < 0.05$ (GraphPad Prism 6.0 for Mac).

Table 2-34: Results obtained from cross-competition studies for [^{3}H]-arginine and unlabelled ADMA in capillary depletion samples. One-way ANOVA with Dunnett's post-hoc test was used to compare means to control ([^{3}H]-arginine alone), with statistical significance taken as $p < 0.05$. n = number of experiments.

Tissue	n	R_{BRAIN} (mL.100g^{-1})		% inhibition	*p*
Homogenate					
[^{3}H]-arginine alone	6	39.71 ± 7.19	-		
+ 0.5 µM un-labelled ADMA	5	-	40.11 ± 10.81	-	n.s.
+ 3.0 µM un-labelled ADMA	5	-	27.95 ± 5.24	-	n.s.
+ 10 µM un-labelled ADMA	4	-	42.20 ± 9.68	-	n.s.
+ 100 µM un-labelled ADMA	5	-	35.96 ± 1.79	-	n.s.
+ 500 µM un-labelled ADMA	4	-	13.85 ± 0.64	65.1	$p < 0.05$
Supernatant					
[^{3}H]-arginine alone	6	24.70 ± 4.91	-		
+ 0.5 µM un-labelled ADMA	5	-	24.80 ± 5.66	-	n.s.
+ 3.0 µM un-labelled ADMA	5	-	16.83 ± 2.92	-	n.s.
+ 10 µM un-labelled ADMA	4	-	22.99 ± 4.68	-	n.s.
+ 100 µM un-labelled ADMA	5	-	22.29 ± 0.94	-	n.s.
+ 500 µM un-labelled ADMA	4	-	6.92 ± 0.32	72.0	$p < 0.05$
Pellet					
[^{3}H]-arginine alone	6	6.87 ± 1.02	-		
+ 0.5 µM un-labelled ADMA	5	-	6.17 ± 1.81	-	n.s.
+ 3.0 µM un-labelled ADMA	5	-	4.40 ± 0.81	-	n.s.
+ 10 µM un-labelled ADMA	4	-	7.24 ± 1.95	-	n.s.
+ 100 µM un-labelled ADMA	5	-	6.39 ± 1.14	-	n.s.
+ 500 µM un-labelled ADMA	4	-	2.47 ± 0.87	-	n.s.

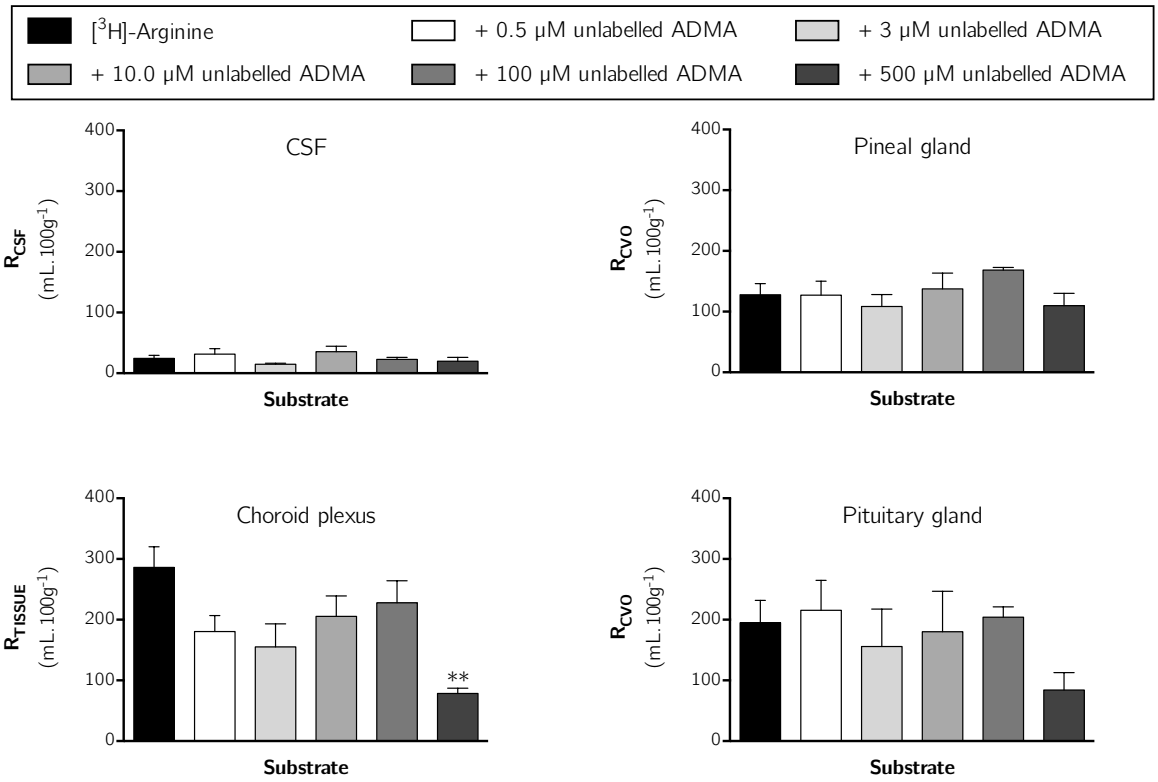

Figure 2-40: The effect of unlabelled ADMA on the distribution of [^{3}H]-arginine in CSF, choroid plexus and CVOs (10 minute perfusion). Uptake is expressed as the percentage ratio of tissue or CSF to plasma (mL.100 g^{-1}). Perfusion time is 10 minutes. Each bar represents the mean ± SEM of 4-7 animals. Asterisks represent one-way ANOVA with Dunnett's post-hoc tests comparing mean±SEM to control, $^{**}p < 0.01$ (GraphPad Prism 6.0 for Mac).

Distribution of [^{3}H]-arginine in the CSF, pineal gland and pituitary gland was not affected by any of the concentrations of unlabelled ADMA included in artificial plasma (**Figure 2-40**). However, 500 µM unlabelled ADMA inhibited the distribution of [^{3}H]-arginine in the choroid plexus by 72.6% (**Table 2-35**, $p < 0.01$).

Table 2-35: Results obtained from cross-competition studies for [^{3}H]-arginine and unlabelled ADMA in the CSF, choroid plexus and CVOs. One-way ANOVA with Dunnett's post-hoc test was used to compare means to control ([^{3}H]-arginine alone), with statistical significance taken as $p < 0.05$. n = number of experiments.

Tissue	n	R_{BRAIN} (mL.100g^{-1})	% inhibition	*p*
CSF				
[^{3}H]-arginine alone	7	24.51 ± 5.10		
+ 0.5 µM un-labelled ADMA	5	31.47 ± 9.16	-	n.s.
+ 3.0 µM un-labelled ADMA	4	14.68 ± 1.74	-	n.s.
+ 10 µM un-labelled ADMA	5	35.63 ± 8.98	-	n.s.
+ 100 µM un-labelled ADMA	5	22.8 ± 3.44	-	n.s.
+ 500 µM un-labelled ADMA	4	19.75 ± 6.47	-	n.s.
Pineal gland				
[^{3}H]-arginine alone	6	128.0 ± 18.11		
+ 0.5 µM un-labelled ADMA	4	127.3 ± 22.82	-	n.s.
+ 3.0 µM un-labelled ADMA	5	108.6 ± 19.69	-	n.s.
+ 10 µM un-labelled ADMA	4	137.4 ± 25.97	-	n.s.
+ 100 µM un-labelled ADMA	4	168.6 ± 4.32	-	n.s.
+ 500 µM un-labelled ADMA	4	109.8 ± 20.36	-	n.s.
Choroid plexus				
[^{3}H]-arginine alone	6	286.1 ± 33.92		
+ 0.5 µM un-labelled ADMA	5	180.6 ± 26.14	-	n.s.
+ 3.0 µM un-labelled ADMA	4	155.1 ± 38.01	-	n.s.
+ 10 µM un-labelled ADMA	5	205.5 ± 33.67	-	n.s.
+ 100 µM un-labelled ADMA	5	227.7 ± 36.44	-	n.s.
+ 500 µM un-labelled ADMA	4	78.39 ± 8.84	72.6	$p < 0.01$
Pituitary gland				
[^{3}H]-arginine alone	7	194.9 ± 36.90		
+ 0.5 µM un-labelled ADMA	5	215.5 ± 49.53	-	n.s.
+ 3.0 µM un-labelled ADMA	4	155.8 ± 61.71	-	n.s.
+ 10 µM un-labelled ADMA	5	180.3 ± 66.64	-	n.s.
+ 100 µM un-labelled ADMA	5	204.2 ± 17.10	-	n.s.
+ 500 µM un-labelled ADMA	4	84.24 ± 28.48	-	n.s.

While 100 µM unlabelled ADMA did not inhibit the distribution of [^{3}H]-arginine in any of the samples analysed, 100 µM *L*-arginine was sufficient to significantly inhibit distribution of [^{3}H]-arginine. This is demonstrated in **Figure 2-41** by combining data from self-inhibition experiments for [^{3}H]-arginine (see ***section 2.4.2.1 - Self-inhibition of Arginine transport***) with data in this section in the frontal cortex and choroid plexus. In both samples, 100 µM unlabelled *L*-arginine was sufficient to inhibit [^{3}H]-arginine uptake into the frontal cortex and distribution in the choroid plexus, while 100 µM unlabelled ADMA had no effect.

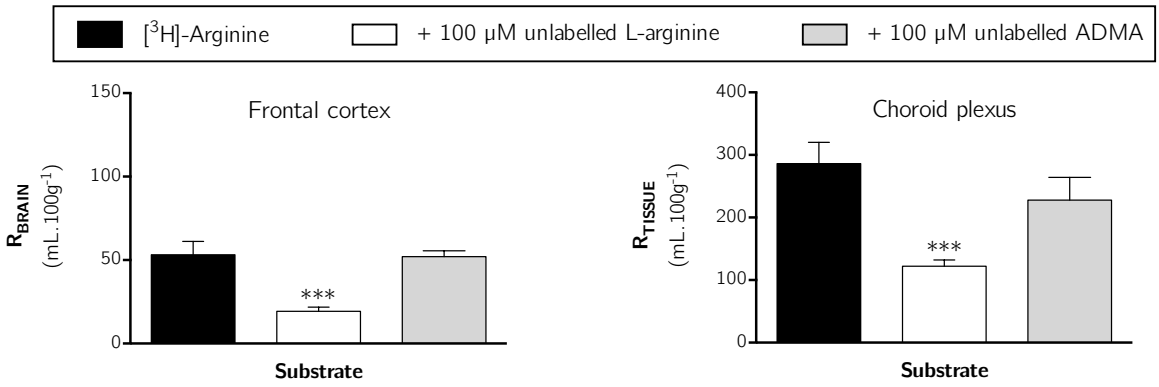

Figure 2-41: Effect of either 100 µM unlabelled *L*-arginine or 100 µM unlabelled ADMA on the respective uptake and distribution of [^{3}H]-arginine in frontal cortex and choroid plexus. Uptake is expressed as the percentage ratio of tissue or CSF to plasma (mL.100 g^{-1}). Perfusion time is 10 minutes. Each bar represents the mean ± SEM of 4-7 animals (GraphPad Prism 6.0 for Mac). One-way ANOVA with Dunnett's post-hoc test comparing means to control ([^{3}H]-arginine only), ***$p < 0.001$).

2.4.3.3 Effect of *L*-arginine of ADMA transport

In order to determine the effect of *L*-arginine on the transport of ADMA across the blood-brain and blood-CSF barriers, [^{3}H]-ADMA was co-perfused with 100 µM *L*-arginine.

Figure 2-42 shows the effect of an excess of unlabelled *L*-arginine on the uptake of [^{3}H]-ADMA into all brain regions. These data indicate that [^{3}H]-ADMA uptake is inhibited by 100 µM unlabelled *L*-arginine by up to 80.4% (**Table 2-36**, one-tailed unpaired Student's t-test comparing means, $p < 0.001$). This trend was also mirrored in samples from capillary depletion analysis where 100 µM *L*-arginine inhibited [^{3}H]-ADMA distribution in all samples by up to 80.0% (**Figure 2-43** and **Table 2-37**, $p < 0.01$).

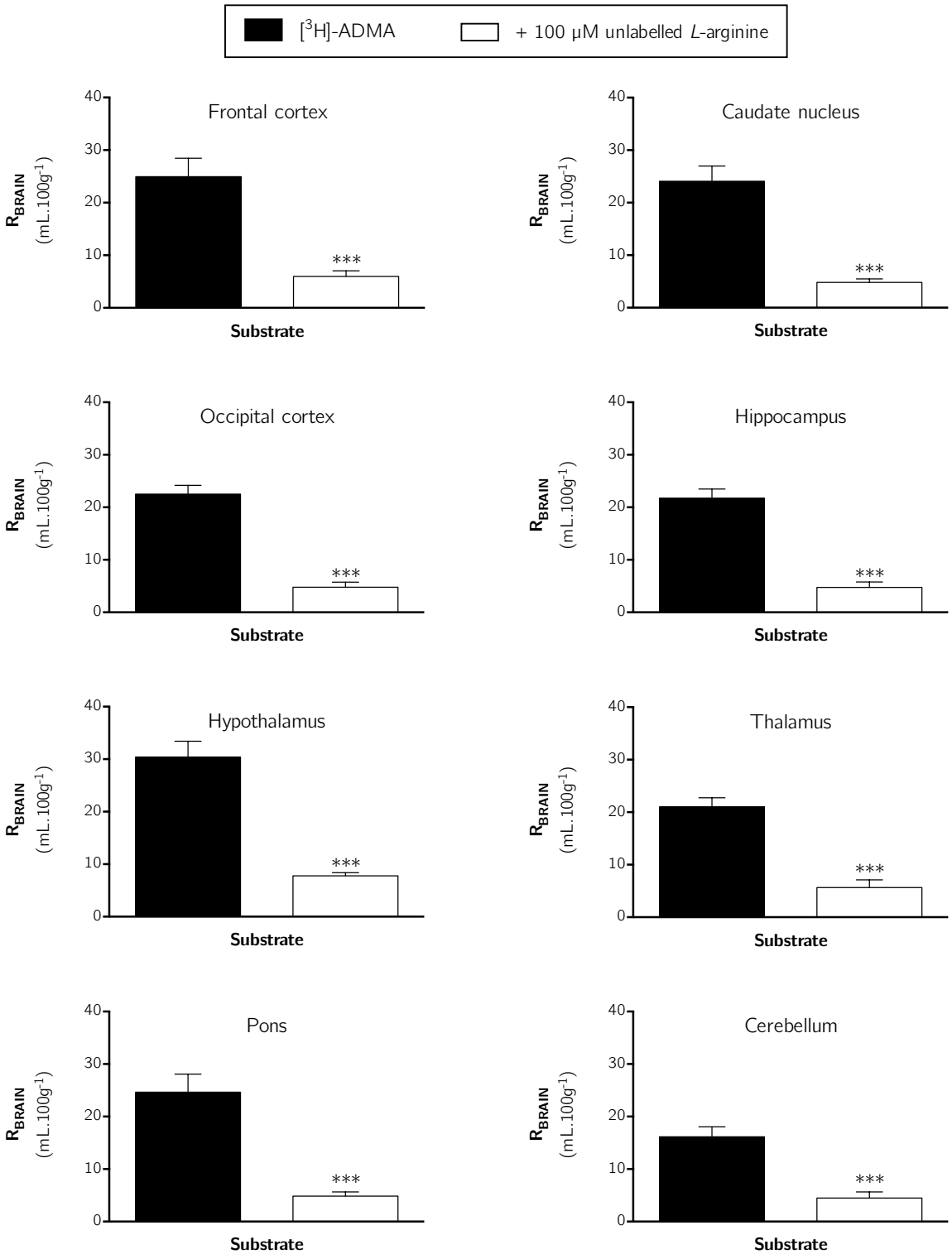

Figure 2-42: The effect of unlabelled *L*-arginine on the regional brain uptake of [^{3}H]-ADMA (10 minute perfusion). Uptake is expressed as the percentage ratio of tissue to plasma (mL.100 g^{-1}) and is corrected for [^{14}C]-sucrose (vascular space). Perfusion time is 10 minutes. Each bar represents the mean ± SEM of 5 animals. Asterisks represent unpaired, one-tailed Student's t-tests comparing mean±SEM, *p < 0.05, **p < 0.01, ***p < 0.001 (GraphPad Prism 6.0 for Mac).

Table 2-36: Results obtained from cross-competition studies for [^{3}H]-ADMA and unlabelled *L*-arginine in the brain. Unpaired, one-tailed Student's t-test was used to compare two means, with statistical significance taken as $p < 0.05$. n = number of experiments.

Tissue	n	R_{BRAIN} (mL.100g^{-1})		% inhibition	*p*
Frontal cortex					
[^{3}H]-ADMA alone	5	24.94 ± 3.50	-	-	
+ 100 µM un-labelled arginine	4	-	5.98 ± 10.6	76.0	$p < 0.001$
Caudate nucleus					
[^{3}H]-ADMA alone	5	24.07 ± 2.92	-	-	
+ 100 µM un-labelled arginine	4	-	4.81 ± 0.67	80.0	$p < 0.001$
Occipital cortex					
[^{3}H]-ADMA alone	5	22.52 ± 1.65	-	-	
+ 100 µM un-labelled arginine	4	-	4.80 ± 0.95	78.7	$p < 0.001$
Hippocampus					
[^{3}H]-ADMA alone	5	21.74 ± 1.75	-	-	
+ 100 µM un-labelled arginine	4	-	4.75 ± 1.04	78.2	$p < 0.001$
Hypothalamus					
[^{3}H]-ADMA alone	5	30.42 ± 2.98	-	-	
+ 100 µM un-labelled arginine	4	-	7.77 ± 0.61	74.5	$p < 0.001$
Thalamus					
[^{3}H]-ADMA alone	5	21.09 ± 1.74	-	-	
+ 100 µM un-labelled arginine	4	-	5.66 ± 1.47	73.2	$p < 0.001$
Pons					
[^{3}H]-ADMA alone	5	24.64 ± 3.44	-	-	
+ 100 µM un-labelled arginine	4		4.83 ± 0.77	80.4	$p < 0.001$
Cerebellum					
[^{3}H]-ADMA alone	5	17.65 ± 1.52	-	-	
+ 100 µM un-labelled arginine	4	-	4.45 ± 1.16	74.8	$p < 0.001$

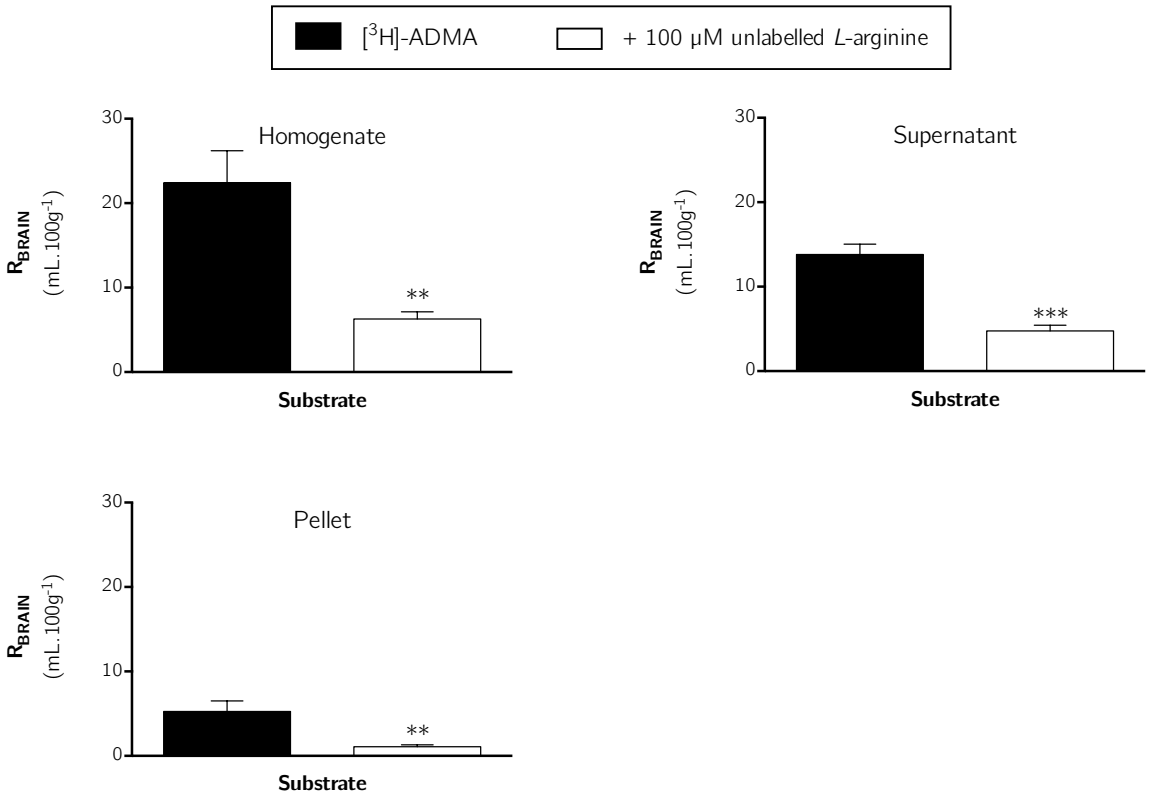

Figure 2-43: The effect of unlabelled *L*-arginine on the distribution of [^{3}H]-ADMA in capillary depletion samples (10 minute perfusion). Uptake is expressed as the percentage ratio of tissue to plasma (mL.100 g^{-1}) and is corrected for [^{14}C]-sucrose (vascular space). Perfusion time is 10 minutes. Each bar represents the mean ± SEM of 5 animals. Asterisks represent unpaired, one-tailed Student's t-tests comparing mean±SEM, $^{**}p < 0.01$, $^{***}p < 0.001$ (GraphPad Prism 6.0 for Mac).

Table 2-37: Results obtained from cross-competition studies for [^{3}H]-ADMA and unlabelled *L*-arginine in capillary depletion samples. Unpaired, one-tailed Student's t-test was used to compare two means, with statistical significance taken as $p < 0.05$. n = number of experiments.

Tissue	n	R_{BRAIN} (mL.100g^{-1})		% inhibition	*p*
Homogenate					
[^{3}H]-ADMA alone	5	22.41 ± 3.81	-	-	
+ 100 µM un-labelled arginine	4	-	6.30 ± 0.84	71.9	$p < 0.001$
Supernatant					
[^{3}H]-ADMA alone	5	13.81 ± 1.24	-	-	
+ 100 µM un-labelled arginine	4	-	4.76 ± 0.67	65.5	$p < 0.001$
Pellet					
[^{3}H]-ADMA alone	5	5.27 ± 1.26	-	-	
+ 100 µM un-labelled arginine	4	-	1.01 ± 0.21	80.8	$p < 0.01$

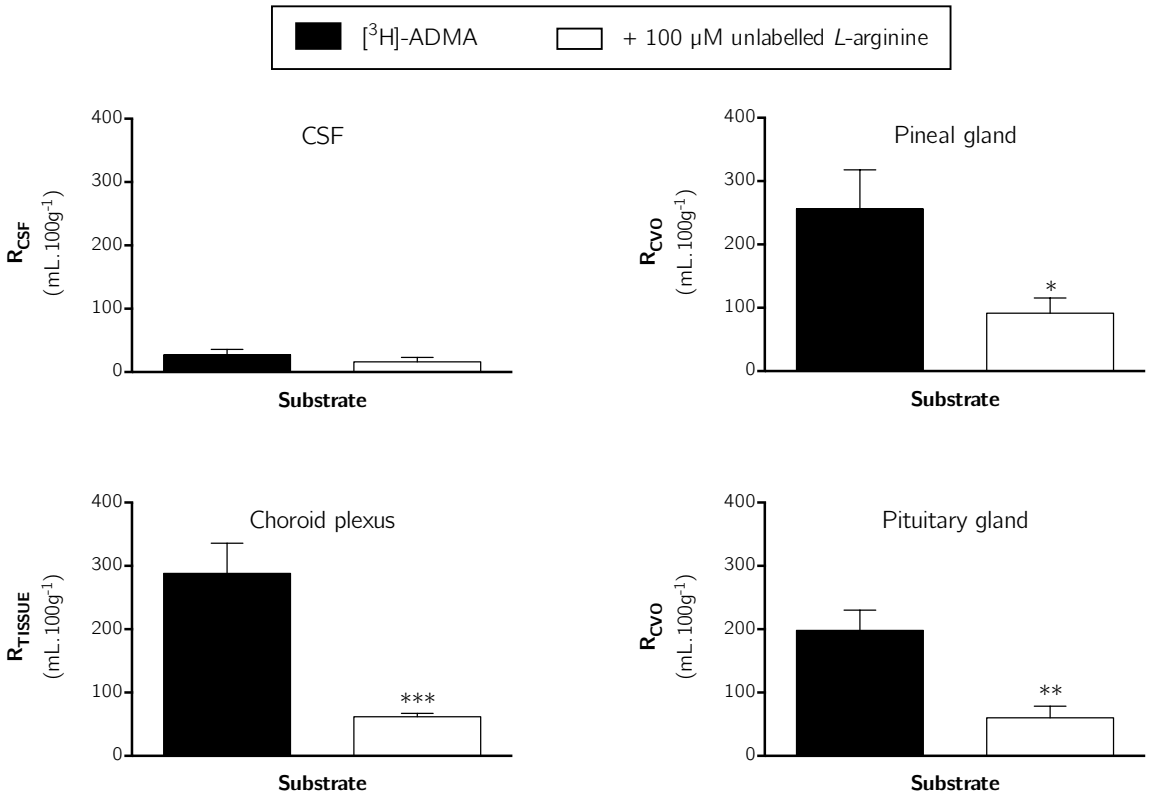

Figure 2-44: The effect of unlabelled *L*-arginine on the distribution of [^{3}H]-ADMA in CSF, choroid plexus and CVOs (10 minute perfusion). Uptake is expressed as the percentage ratio of tissue or CSF to plasma (mL.100 g^{-1}). Perfusion time is 10 minutes. Each bar represents the mean ± SEM of 5 animals. Asterisks represent unpaired, one-tailed Student's t-tests comparing mean±SEM, *$p < 0.05$, **$p < 0.01$, ***$p < 0.001$ (GraphPad Prism 6.0 for Mac).

Figure 2-44 shows the effect of an excess of un-labelled *L*-arginine on the distribution of [^{3}H]-ADMA into the CSF, pineal gland, choroid plexus and pituitary gland. These data indicate that [^{3}H]-ADMA uptake is markedly inhibited by up to 78.6% and ($p < 0.05$, unpaired, one-tailed Student's t-test comparing means, **Table 2-38**). The inclusion of unlabelled *L*-arginine however had no effect on the distribution of [^{3}H]-ADMA in the CSF.

Table 2-38: Results obtained from cross-competition studies for [^{3}H]-ADMA and unlabelled *L*-arginine in the brain. Unpaired, one-tailed Student's t-test was used to compare two means, with statistical significance taken as $p < 0.05$. n = number of experiments.

Tissue	n	R_{BRAIN} (mL.100g^{-1})		% inhibition	*p*
CSF					
[^{3}H]-ADMA alone	5	27.26 ± 8.69	-	-	
+ 100 µM un-labelled arginine	4	-	16.24 ± 6.77	-	n.s.
Pineal gland					
[^{3}H]-ADMA alone	5	256.2 ± 61.56	-	-	
+ 100 µM un-labelled arginine	4	-	91.51 ± 24.05	64.3	$p < 0.05$
Choroid plexus					
[^{3}H]-ADMA alone	5	288.1 ± 47.73	-	-	
+ 100 µM un-labelled arginine	4	-	61.57 ± 5.26	78.6	$p < 0.001$
Pituitary gland					
[^{3}H]-ADMA alone	5	198.2 ± 31.93	-	-	
+ 100 µM un-labelled arginine	4	-	60.03 ± 18.48	69.7	$p < 0.01$

The degree of inhibition of [^{3}H]-ADMA distribution respectively exerted by the inclusion of either 100 µM unlabelled *L*-arginine (cross-competition) and 100 µM unlabelled ADMA (self-inhibition) appears to be identical. This is demonstrated in **Figure 2-45** by combining data from self-inhibition experiments for [^{3}H]-ADMA (see ***section 2.4.2.2 - Self-inhibition of ADMA transport***) with data in this section in the frontal cortex and choroid plexus. Both 100 µM unlabelled *L*-arginine and 100 µM unlabelled ADMA significantly inhibited [^{3}H]-ADMA uptake into the frontal cortex and distribution in the choroid plexus ($p < 0.001$, one-way ANOVA with Dunnett's post-hoc test comparing means to control). [^{3}H]-ADMA distribution in the presence of either 100 µM unlabelled ADMA or *L*-arginine were found to not be significantly different (unpaired, two-tailed Student's t-test comparing means, $p > 0.05$).

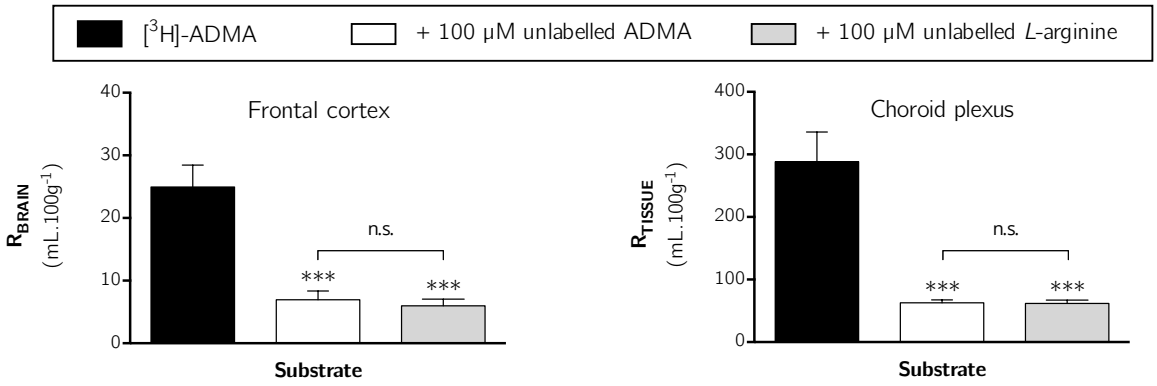

Figure 2-45: Effect of either 100 µM unlabelled ADMA or 100 µM unlabelled *L*-arginine on the respective uptake and distribution of [^{3}H]-ADMA in frontal cortex and choroid plexus. Uptake is expressed as the percentage ratio of tissue or CSF to plasma (mL.100 g^{-1}). Perfusion time is 10 minutes. Each bar represents the mean ± SEM of 4-5 animals (GraphPad Prism 6.0 for Mac). One-way ANOVA with Dunnett's post-hoc test comparing means to control ([^{3}H]-ADMA only), ***$p < 0.001$).

2.4.3.4 Trans-stimulation of *L*-arginine influx by ADMA

In order to determine if *L*-arginine transport across the blood-brain and blood-CSF barriers is subject to trans-stimulation by ADMA, experiments were designed to mimic pre-loading with ADMA. Following pre-perfusion with 500 µM unlabelled ADMA for 20 minutes, mice were perfused with [^{3}H]-arginine (with or without 200 µM unlabelled *L*-arginine). As mentioned in ***section 2.3.1.2L - Cross-competition experiments (Pre-loading / trans-stimulation experiments)*** a concentration of 200 µM unlabelled *L*-arginine was selected to mimic the concentration of *L*-arginine achieved in plasma following oral supplementation in human patients (Clarkson *et al.*, 1996; Adams *et al.*, 1997).

The 'control' comparison for this set of experiments involved a 20-minute pre-perfusion with artificial plasma containing no additives followed by a 10-minute perfusion with artificial plasma containing [^{3}H]-arginine alone. All comparisons made in this section are relative to the [^{3}H]-arginine distribution in samples under these 'control' conditions. A reminder of the overall experimental design for this group of experiments is shown schematically in **Figure 2-46**.

Pre-load (20 min)	'Empty' plasma	500µM ADMA	500µM ADMA
Post-perfusion (10 min)	[^{3}H]-Arginine	[^{3}H]-Arginine	[^{3}H]-Arginine + 200µM *L*-Arginine

Figure 2-46: Schematic representation of experiments designed to investigate the possible trans-stimulation effect of ADMA on [^{3}H]-arginine flux into the brain.

Figure 2-47 shows that [^{3}H]-arginine distribution is increased in all regions except for hypothalamus and thalamus when pre-loading with 500 µM unlabelled ADMA and then perfusing with [^{3}H]-arginine and 200 µM unlabelled *L*-arginine (one-way ANOVA with Dunnett's post-hoc test comparing means to control, $p < 0.05$). Interestingly, this

was not observed if the artificial plasma for 'post-perfusion' did not contain 200 µM unlabelled *L*-arginine in addition to [^{3}H]-arginine. The comparative increase in [^{3}H]-arginine uptake when combined with 200 µM unlabelled *L*-arginine (relative to the control, where neither 500 µM unlabelled ADMA is pre-perfused, nor 200 µM unlabelled *L*-arginine included in the post-perfusion) can be compared to the self-inhibition experiments for [^{3}H]-arginine described in ***section 2.4.2.1 - Self-inhibition of Arginine transport***. Following from these experiments one would expect the 200 µM unlabelled *L*-arginine would compete for transport with radiolabelled [^{3}H]-arginine, resulting in a decrease in [^{3}H]-arginine uptake.

Interestingly, this trend was mirrored in whole-brain homogenate and particularly endothelial cell-enriched pellet samples from capillary depletion analysis ($p < 0.01$), but not brain parenchyma-containing supernatant ($p > 0.05$, one-way ANOVA with Dunnett's post-hoc test comparing means to control). These data are shown in **Figure 2-48**.

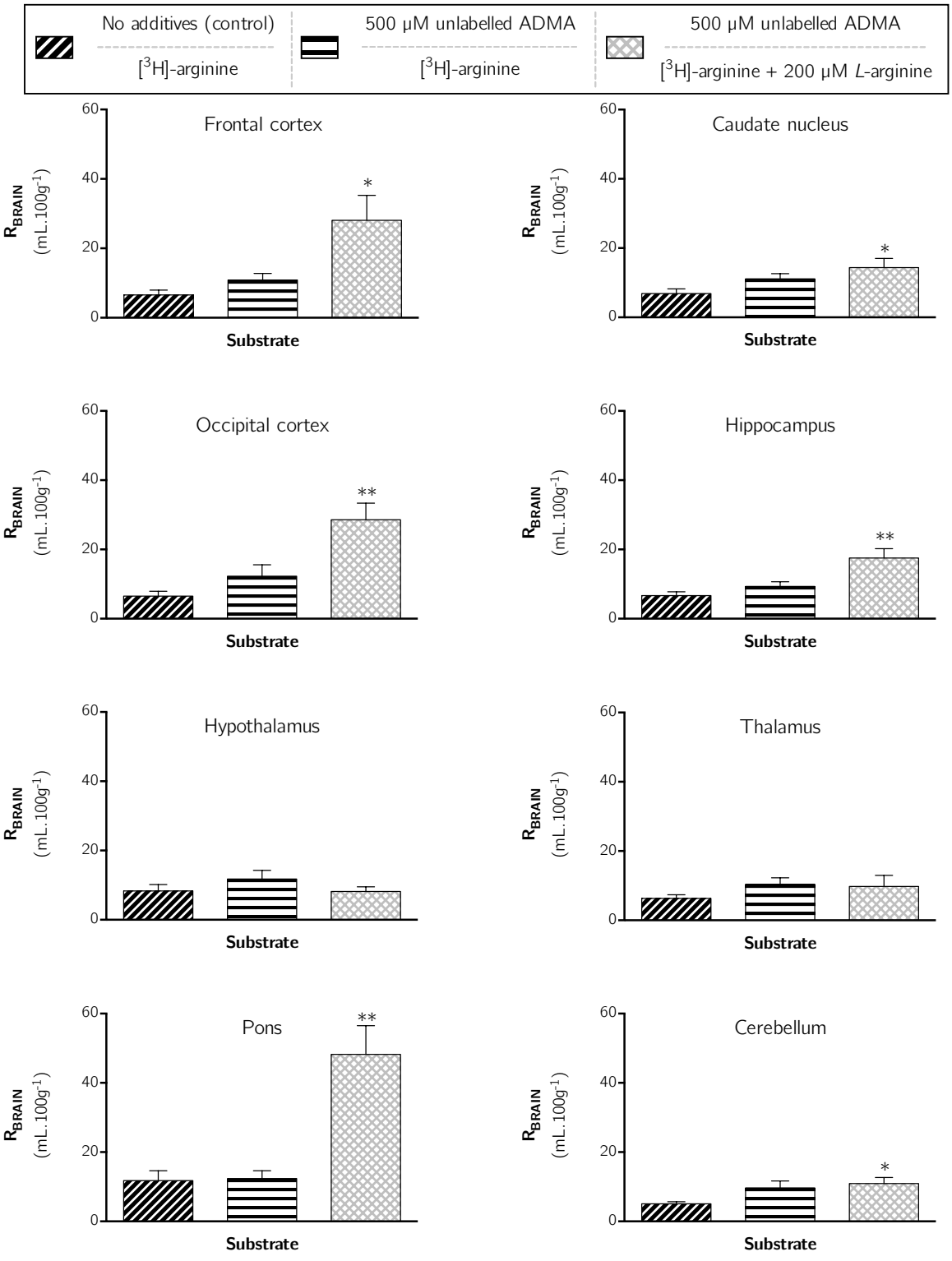

Figure 2-47: Effect of pre-perfusion with 500 µM ADMA on [^{3}H]-arginine uptake in brain regions. Uptake is expressed as the percentage ratio of tissue to plasma (mL.100 g^{-1}) and is corrected for [^{14}C]-sucrose (vascular space). Each bar represents the mean ± SEM of 5 animals. Asterisks represent one-way ANOVA with Dunnett's post-hoc tests comparing mean±SEM to control, *$p < 0.05$, **$p < 0.01$ (GraphPad Prism 6.0 for Mac).

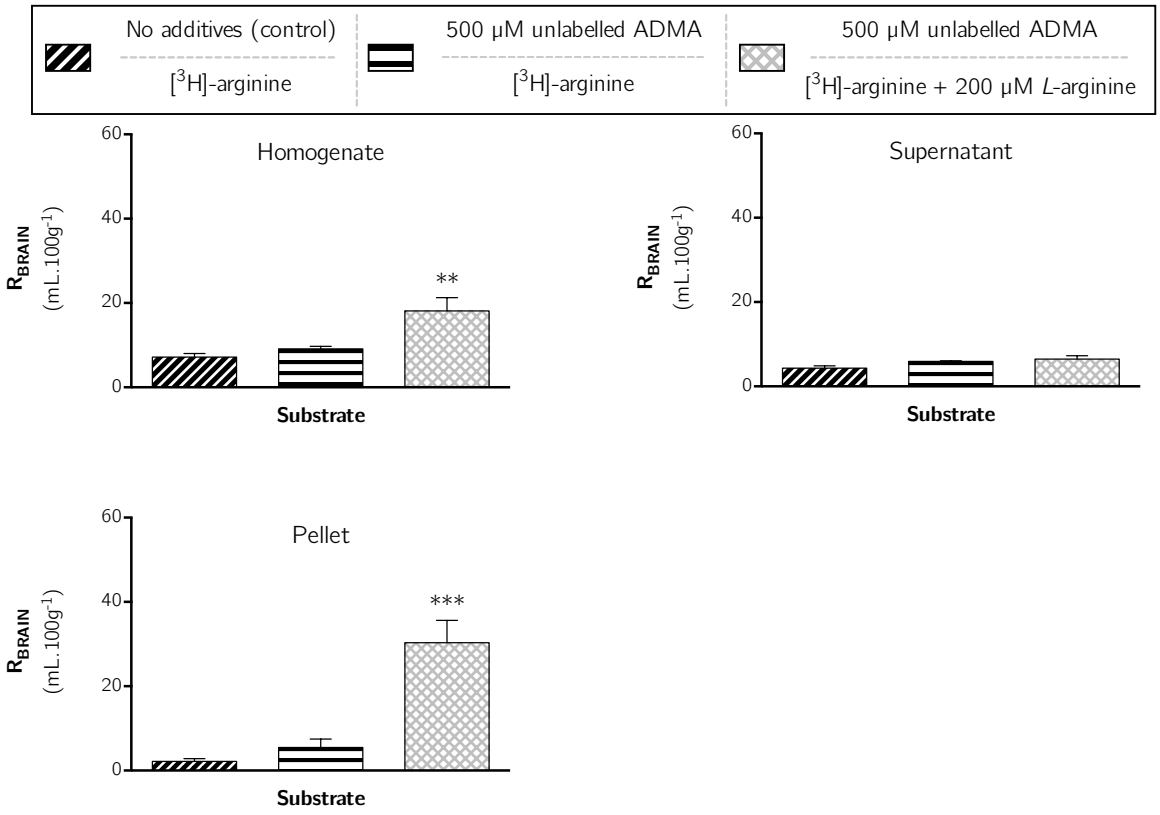

Figure 2-48: Effect of pre-perfusion with 500 µM ADMA on [^{3}H]-arginine distribution in capillary depletion samples. Uptake is expressed as the percentage ratio of tissue to plasma (mL.100 g^{-1}) and is corrected for [^{14}C]-sucrose (vascular space). Each bar represents the mean ± SEM of 5 animals. Asterisks represent one-way ANOVA with Dunnett's post-hoc tests comparing mean±SEM to control, $^{**}p < 0.01$, $^{***}p < 0.001$ (GraphPad Prism 6.0 for Mac).

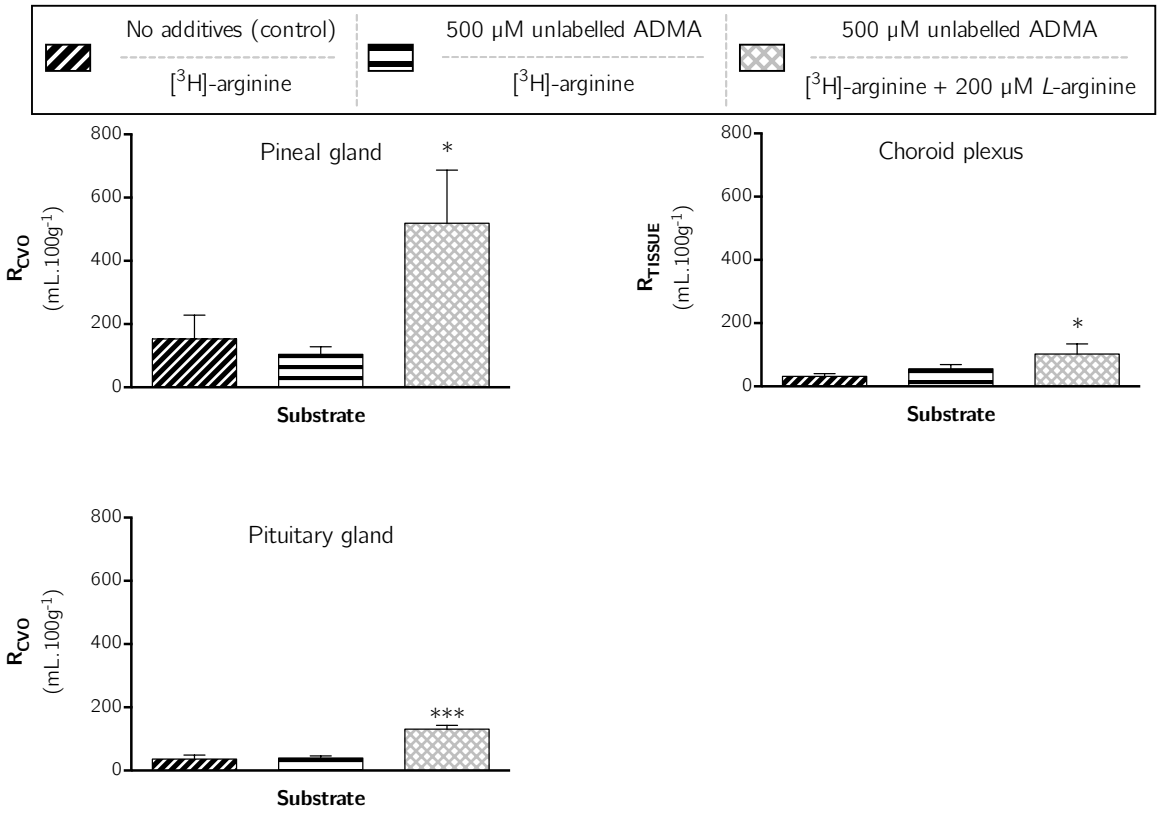

Figure 2-49: Effect of pre-perfusion with 500 µM ADMA on [^{3}H]-arginine distribution in choroid plexus and CVOs. Uptake is expressed as the percentage ratio of tissue to plasma (mL.100 g^{-1}). Each bar represents the mean ± SEM of 5 animals. Asterisks represent one-way ANOVA with Dunnett's post-hoc tests comparing mean±SEM to control, *$p < 0.05$, ***$p < 0.001$ (GraphPad Prism 6.0 for Mac).

Pre-perfusing with 500 µM unlabelled ADMA followed by [^{3}H]-arginine and 200 µM unlabelled *L*-arginine significantly increased the distribution of [^{3}H]-arginine in the pineal gland, choroid plexus and pituitary gland (**Figure 2-49**, $p < 0.05$, one-way ANOVA with Dunnett's post-hoc test comparing means to control).

2.4.3.5 Effect of *L*-arginine on ADMA efflux

In order to determine if ADMA transport across the blood-brain and blood-CSF barriers is subject to trans-stimulation by *L*-arginine, experiments were designed to mimic pre-loading with [^{3}H]-ADMA and then measuring its efflux from the brain after perfusing with artificial plasma containing 200 µM unlabelled *L*-arginine. Following pre-perfusion with [^{3}H]-ADMA for 20 minutes, mice were perfused for 10 minutes with either artificial plasma alone, or artificial plasma containing 200 µM unlabelled *L*-arginine (***section 2.3.1.2L - Cross-competition experiments (Pre-loading / trans-stimulation experiments)***).

The 'control' comparison for this set of experiments involved a 20-minute perfusion with artificial plasma containing [^{3}H]-ADMA alone (taken from multiple-time uptake experiments for [^{3}H]-ADMA, see ***section 2.4.1.3 - ADMA: The NOS inhibitor***). All comparisons made in this section are relative to the [^{3}H]-ADMA distribution in samples under these 'control' conditions. A reminder of the overall experimental design for this group of experiments is shown schematically in **Figure 2-50**. Multiple individual student's t-tests comparing means±SEM under each experimental condition were performed per sample for all comparisons made in this section.

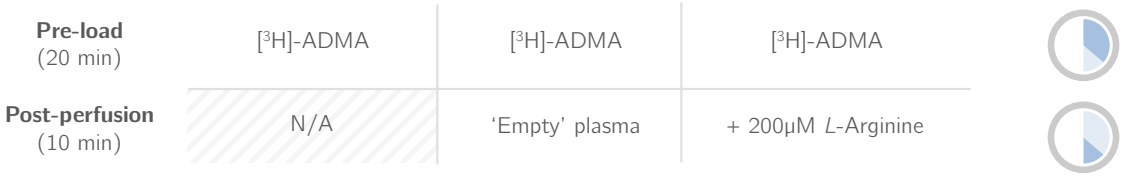

Figure 2-50: Schematic representation of experiments designed to investigate the possible trans-stimulation effect of *L*-arginine on [^{3}H]-ADMA flux from the brain.

Figure 2-51 shows that [^{3}H]-ADMA distribution in all brain regions is significantly decreased following 20 minutes of pre-perfusion with [^{3}H]-ADMA followed by post-perfusion with artificial plasma with no additives relative to control (no post-perfusion, $p < 0.01$). In contrast, including 200 µM unlabelled *L*-arginine in the post-perfusion

artificial plasma only significantly reduces the distribution of [^{3}H]-ADMA relative to control in the thalamus ($p < 0.05$, significance not shown on graph). When comparing the effect of including 200 µM unlabelled *L*-arginine in the post-perfusion artificial plasma to post-perfusion with artificial plasma alone, it is clear that [^{3}H]-ADMA distribution is significantly increased ($p < 0.05$).

In the case of capillary depletion samples, shown in **Figure 2-52**, the 'wash-out' effect of reducing [^{3}H]-ADMA distribution following post-perfusion with artificial plasma that contained no additives was only observed in whole-brain homogenate ($p < 0.05$). No statistically significant differences in [^{3}H]-ADMA distribution were found in the parenchyma-containing supernatant or capillary endothelial cell-enriched pellet samples.

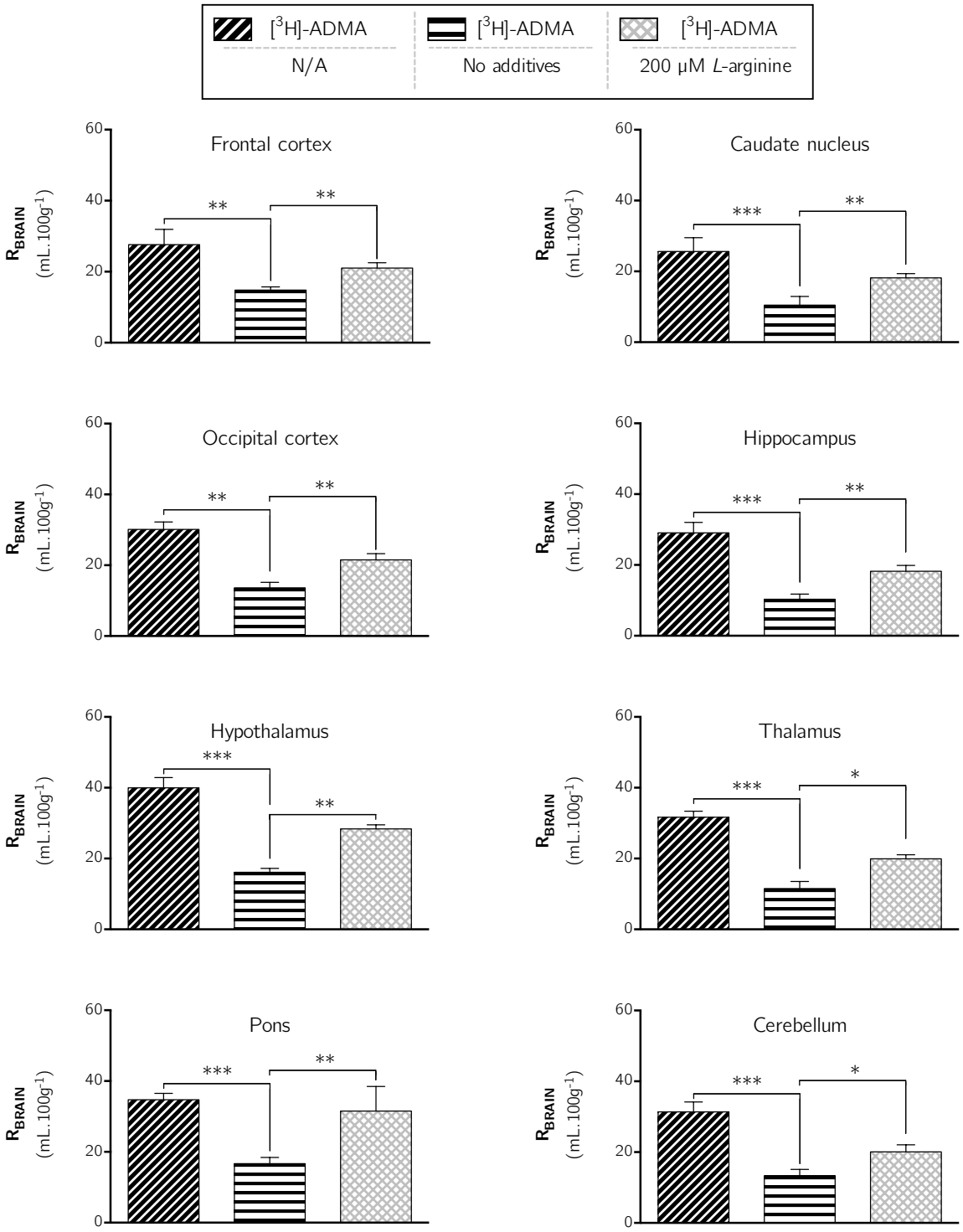

Figure 2-51: Effect of post-perfusion with 200 µM *L*-arginine on [^{3}H]-ADMA uptake in brain regions. Uptake is expressed as the percentage ratio of tissue to plasma (mL.100 g^{-1}) and is corrected for [^{14}C]-sucrose (vascular space). Each bar represents the mean ± SEM of 5 animals, multiple individual student's T-tests for each region, ***p < 0.001, **p < 0.01, *p < 0.05 (GraphPad Prism 6.0 for Mac). Experiments performed to detect efflux of pre-loaded [^{3}H]-ADMA under conditions designed to re-create supplementation of *L*-arginine in pathologies relating to the *L*-arginine paradox.

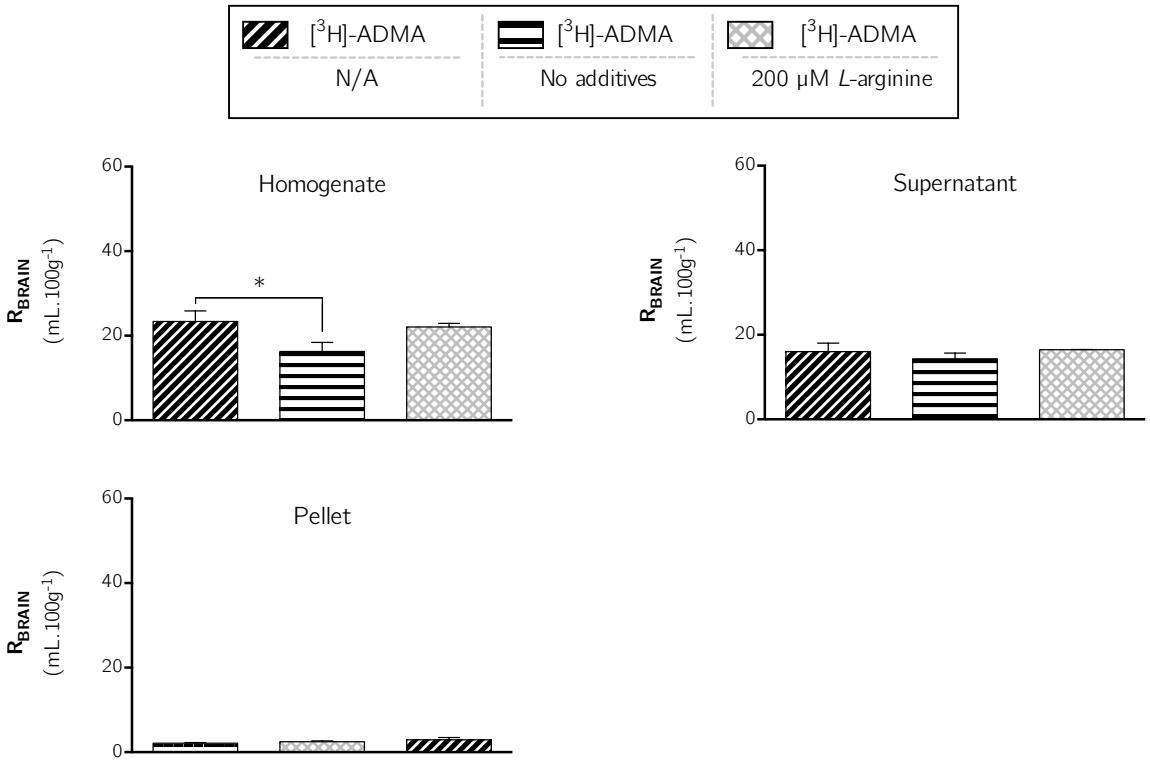

Figure 2-52: Effect of post-perfusion with 200 µM *L*-arginine on [^{3}H]-ADMA distribution in capillary depletion samples. Uptake is expressed as the percentage ratio of tissue to plasma (mL.100 g^{-1}) and is corrected for [^{14}C]-sucrose (vascular space). Each bar represents the mean ± SEM of 5 animals, multiple individual student's T-tests for each region, $*p < 0.05$ (GraphPad Prism 6.0 for Mac). Experiments performed to detect efflux of pre-loaded [^{3}H]-ADMA under conditions designed to re-create supplementation of *L*-arginine in pathologies relating to the *L*-arginine paradox.

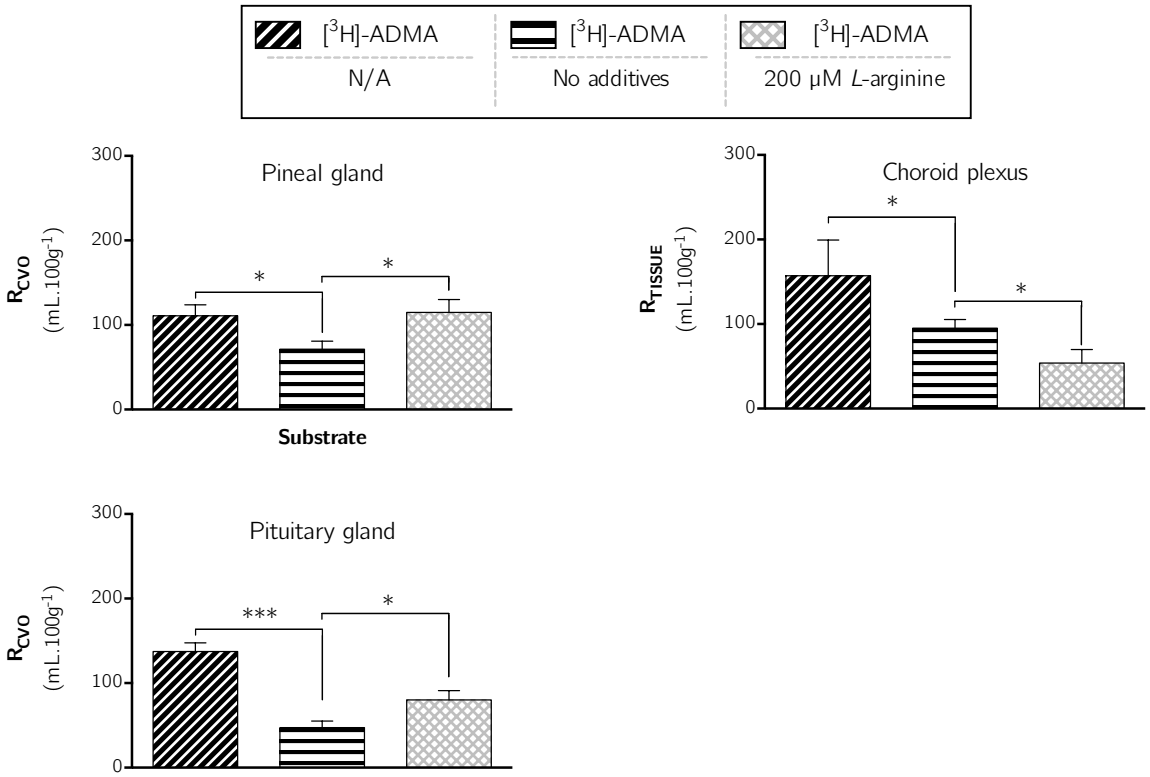

Figure 2-53: Effect of post-perfusion with 200 µM *L*-arginine on [^{3}H]-ADMA distribution in choroid plexus and CVOs. Uptake is expressed as the percentage ratio of tissue to plasma (mL.100 g^{-1}). Each bar represents the mean ± SEM of 5 animals, multiple individual student's T-tests for each region, ***$p < 0.001$, *$p < 0.05$ (GraphPad Prism 6.0 for Mac). Experiments performed to detect efflux of pre-loaded [^{3}H]-ADMA under conditions designed to re-create supplementation of *L*-arginine in pathologies relating to the *L*-arginine paradox.

As was observed in the brain regions sampled, [^{3}H]-ADMA distribution in the pineal gland, choroid plexus and pituitary gland was decreased by post-perfusing for 10 minutes with artificial plasma containing no additives ($p < 0.05$, shown in **Figure 2-53**). The distribution of [^{3}H]-ADMA was then increased by the inclusion of 200 µM unlabelled *L*-arginine in the post-perfusion artificial plasma in the case of the pineal and pituitary glands relative to post-perfusing with artificial plasma with no additives ($p < 0.05$). In the choroid plexus, the inclusion of 200 µM unlabelled *L*-arginine results in a significant decrease ($p < 0.05$) in the distribution of [^{3}H]-ADMA relative to post-perfusing with artificial plasma with no additives.

2.5 Discussion

This chapter has examined the transport of two, structurally related cationic amino acids across the blood-CNS barriers using an *in vivo* mouse model of *in situ* brain and choroid plexus perfusion. Results indicate that [^{3}H]-arginine and [^{3}H]-ADMA have differing abilities to accumulate in the brain and CSF, and that transporters play a significant role in their transfer between the blood and CNS. Further interpretation of the data suggest that [^{3}H]-arginine uses only one transport system for transport across the blood-CNS barriers, while [^{3}H]-ADMA may interact with multiple transport systems with varying directions of transport, leading to more complex kinetics. The transport systems used by ADMA and *L*-arginine at the blood-CNS barriers also appear to be shared to some degree, as they each affect the others' transport, but to a different extent. Attempts to dissect these subtleties have been made with the experiments contained in this chapter, also extending to probing the possibility of the transport of ADMA and *L*-arginine in explaining the *L*-arginine paradox.

These findings will be discussed in greater detail in the sections that follow.

2.5.1 Sucrose as a marker molecule

[^{14}C]-sucrose was used to assess the integrity of the brain barriers and as a measure of vascular space in brain regions and extracellular space in the choroid plexus/CVOs. As described previously, the poor penetration of sucrose into the CNS (Levin *et al.*, 1976), as well as its similarities to both ADMA and *L*-arginine in both size and charge, make [^{14}C]-sucrose a particularly suitable marker molecule for these studies.

Furthermore, the use of [^{14}C]-sucrose in the protocol for *in situ* brain/choroid plexus perfusion *via* the heart used in the assimilation of these data provides a useful comparison to other validated methods for measuring brain accumulation of solutes *in vivo*. For the majority of brain regions sampled in this study, and under all treatment conditions, the [^{14}C]-sucrose (vascular) space was found to be approximately 2 mL.100g^{-1}, which is very similar to the value of 1.5 ± 0.2 mL.100g^{-1} published previously using this technique (Sanderson *et al.*, 2007), and indeed the value of 1.3 ± 0.2 mL.100g^{-1}

typically observed after perfusing the CNS *via* the carotid artery in mice (Dagenais *et al.*, 2000).

With respect to the blood-CSF barrier, the physiology of choroid plexus capillaries (as described in ***chapter 1***) allows sucrose to penetrate into the stromal space, but sucrose does not gain access to the cellular compartment of the choroid plexus (Quinton *et al.*, 1973). Thus the use of [^{14}C]-sucrose in this work represents the vascular and interstitial fluid spaces within the choroid plexus and CVOs. The movement of sucrose through the apical membrane of the choroid plexus into the CSF is limited by TJs situated towards the apical surface of the choroid plexus epithelium (Quinton *et al.*, 1973), and thus CSF accumulation of [^{14}C]-sucrose represents slow paracellular diffusion through these TJs.

An interesting high-level observation of [^{14}C]-sucrose permeability across the blood-brain and blood-CSF barriers measured in this study is the difference in accumulation over time between so-called 'tight' and 'leaky' tissues. A steady, linear time-dependent increase in [^{14}C]-sucrose accumulation was observed in all brain regions sampled and CSF, but not in the pineal gland, choroid plexus and pituitary glands. One possible explanation for this observation could be that a higher degree of non-specific, non-saturable transport of [^{14}C]-sucrose into the CVOs (relative to other regions) allows for more rapid equilibration across the membranes involved (*e.g.* basolateral membrane of the choroid plexus epithelial cells), which does not occur within 30 minutes in brain regions where the BBB is present. Another possibility is that low-level pinocytosis in BCECs provides a route for time-dependent increases in [^{14}C]-sucrose accumulation into those regions where TJs do not allow paracellular flux.

The poor permeability of [^{14}C]-sucrose through the BBB and BCSFB is shown in **Figure 2-10**, **Figure 2-11** and **Figure 2-12**, but also demonstrated by the very low $\boldsymbol{K_{in}}$ values shown in **Table 2-14** and **Table 2-15**.

2.5.2 [^{3}H]-Arginine transport across the BBB and BCSFB is predominantly mediated by system y^+

This study investigated the ability of [^{3}H]-arginine to cross the mouse blood-CNS barriers and accumulate within the CNS. ***Section 2.5.2.1*** provides a brief summary of the results from this part of the study, while their biological relevance will be interpreted in depth in the ensuing sections.

2.5.2.1 Summary of results

Multiple-time uptake studies (**Figure 2-13**, **Figure 2-14** and **Figure 2-16**) measured substantial [^{3}H]-arginine uptake into all brain regions, CSF, choroid plexus and CVOs (significantly higher than [^{14}C]-sucrose at all time points). Capillary depletion analysis (**Figure 2-15**) suggests that [^{3}H]-arginine could cross the endothelial cell luminal membrane (as measured by the pellet sample) and could accumulate in the brain parenchyma (as measured by the supernatant sample) following perfusion. A departure from a linear rate of [^{3}H]-arginine uptake was observed between 20 and 30 minutes in the hypothalamus and thalamus, also observed in the brain parenchyma and capillary endothelial cells following capillary depletion analysis, but not in whole-brain homogenate.

2.5.2.2 [^{3}H]-Arginine uptake into the CNS

2.5.2.2A Brain regions

Of the two radiolabelled cationic amino acids of interest studied, [^{3}H]-arginine demonstrated the greatest ability (more than two-fold in most cases) to cross the BBB and accumulate within all eight brain regions sampled (**Figure 2-13**). While *in situ* brain/choroid plexus perfusion has previously been used to study [^{3}H]-arginine uptake into the rat brain (Stoll *et al.*, 1993), no absolute values were published, and thus there is no previously published comparison to make to the results described here.

After 30 minutes, brain uptake of [^{3}H]-arginine as a percentage of perfused plasma levels reached a maximum of 185.1 ± 30.7% in the pons, but was similarly high in the majority of other brain regions, including the frontal cortex, caudate nucleus, occipital

cortex, hippocampus, and cerebellum (**Figure 2-13**). An interesting observation for these data is the very high [^{3}H]-arginine uptake in the hypothalamus and thalamus at 30 minutes relative to the earlier time-points (**Figure 2-14**). The biological relevance of this is not immediately clear, although the prototypical cationic amino acid transporter CAT-1 was very recently shown to be expressed at particularly high levels in the hypothalamus and thalamus (Jager *et al.*, 2013). Furthermore, the increased uptake of [^{3}H]-arginine observed in these two regions could be due to a difference in transporter expression at the abluminal membrane, as afforded by the presence of TJs (described in ***section 1.1.1.1A - Presence of complex tight junctions***). Transport systems such as system y^+ have previously been detected at both luminal and abluminal membranes, however not necessarily in a symmetric expression pattern (O'Kane *et al.*, 2006). Capillary depletion analysis confirmed that [^{3}H]-arginine could cross the BBB to accumulate in the brain parenchyma, whilst negligible levels of drug remained trapped in BCECs until 30 minutes (**Figure 2-15**). After 30 minutes it appears that [^{3}H]-arginine accumulates within the brain parenchyma and BCECs at levels greater than plasma levels ($R_{Brain} > 100\%$). One may predict that this would create a concentration gradient favouring flux of [^{3}H]-arginine from the brain and endothelial cells back into the plasma, at least under the experimental conditions presented here ([^{3}H]-arginine plasma concentration of 11.6 nM). However, this is unlikely to occur *in vivo* under normal conditions as the concentration of *L*-arginine in plasma is typically 100 µM in humans (Boger & Bode-Boger, 2001) and 140 µM in mice (Hallemeesch *et al.*, 2004), while brain concentrations in both mice and humans are typically much lower at approximately 0.2-0.3 µM (Leypoldt *et al.*, 2009; Jung *et al.*, 2012). This creates a concentration gradient that overwhelmingly favours facilitated transport of *L*-arginine from plasma into the brain.

2.5.2.2B CSF

[^{3}H]-arginine was also able to cross the blood-CSF barrier, and levels in the CSF reached approximately 120% of plasma levels after 30 minutes (**Figure 2-16**). While the transport of *L*-arginine from plasma to CSF in any species has not previously been published to provide a direct comparison, saturable *L*-arginine transport that was

sensitive to inhibition by *L*-NMMA has been reported at the rat choroid plexus (Stuhlmiller & Boje, 1995). The accumulation of [^{3}H]-arginine in the CSF over time is not an unexpected observation, since the presence of *L*-arginine in the extracellular CSF is known to be a requirement for the production of inducible NO by brain astrocytes following transport of *L*-arginine into the cell by CAT-2 (Stevens *et al.*, 1996).

2.5.2.2C Pineal gland, choroid plexus and pituitary gland

[^{3}H]-arginine uptake into the pineal gland and choroid plexus was substantial (**Figure 2-16**); respectively reaching 634.2 ± 153.2% and 379.1 ± 63.1% of plasma levels after 30 minutes. [^{3}H]-Arginine uptake into the pituitary gland was also significant, however a peak in the accumulation of [^{3}H]-arginine was observed at 20 minutes (327.7 ± 32.5% of plasma levels), which then fell to 141.7 ± 10.2% of plasma levels after 30 minutes. This would imply the existence of [^{3}H]-arginine efflux (passive or otherwise) from the pituitary gland and that the rate of [^{3}H]-arginine efflux begins to override the rate of influx at 30 minutes, after initial accumulation. The biological relevance of this could possibly be revealed when considering the role of *L*-arginine in the physiological functions and processes of the pituitary gland, relative to the pineal gland and choroid plexus. Beyond the dependence on *L*-arginine for the normal physiological processes of the cell (such as protein synthesis), *L*-arginine has an active role in promoting the release of growth hormone by the pituitary gland, likely by blocking somatostatin activity *via* NO signalling (Valverde *et al.*, 2001; Adriao *et al.*, 2004). It is therefore possible, that an efflux transport system for *L*-arginine exists at the pituitary gland to regulate the release of growth hormone – an excess of which leads to acromegaly (chronic body tissue growth) and tumours.

2.5.2.3 [^{3}H]-Arginine transporter identification

Saturable transport of *L*-arginine, *L*-lysine and *L*-ornithine across rat BBB has previously been observed using *in situ* brain/choroid plexus perfusion (Kavanaugh, 1993; Stoll *et al.*, 1993). These studies found that the $\boldsymbol{K_m}$ (half-saturation constant) for these amino acids was 56-110 µM, with a $\boldsymbol{V_{max}}$ (maximal influx rate) of 24 nmol.min^{-1}.g^{-1} and attributed the transport to system y$^+$. Subsequent to these initial observations, system y$^+$ was proposed to be the only transport system responsible for cationic amino acid transport across the BBB (O'Kane *et al.*, 2006). Saturable transport of *L*-arginine was also identified at the ovine blood-CSF barrier and attributed to system y$^+$ (Segal *et al.*, 1990; Preston & Segal, 1992). Experiments designed to identify the transport systems involved in *L*-arginine transport at the murine BBB and BCSFB are described below.

2.5.2.3A Summary of results

Self-inhibition studies with 100 µM unlabelled *L*-arginine (**Figure 2-23** and **Figure 2-25**) were utilised to assess the involvement of transporters in [^{3}H]-arginine movement across the blood-CNS barriers. It was found that [^{3}H]-arginine uptake into all brain regions, CSF, choroid plexus and CVOs (including the pituitary gland) was reduced in the presence of unlabelled *L*-arginine, implying that [^{3}H]-arginine influx into the brain, choroid plexus and CVOs involves at least one saturable transport system. Capillary depletion analysis (**Figure 2-24**) revealed that the inhibition of [^{3}H]-arginine uptake into BCECs by unlabelled *L*-arginine results in reduced influx of [^{3}H]-arginine into the brain parenchyma.

Specific transport inhibitor studies (**Figure 2-32**) revealed the transporter(s) for [^{3}H]-arginine influx into the brain regions sampled is sensitive to inhibition by *L*-homoarginine, which almost completely prevented the entry of [^{3}H]-arginine into the brain regions sampled. Capillary depletion analysis (**Figure 2-33**) revealed that the inhibition of [^{3}H]-arginine uptake into BCECs by *L*-homoarginine results in reduced influx of [^{3}H]-arginine into the brain parenchyma – a phenomenon observable on the scale of whole-brain homogenate. The transport inhibitors BCH and α-methyl-*D*,*L*-

tryptophan did not significantly alter the uptake of [^{3}H]-arginine in any of the brain regions sampled, except for in the hippocampus; where α-methyl-*D*,*L*-tryptophan significantly inhibited [^{3}H]-arginine uptake, albeit to a much lesser degree than the inhibitory effect of *L*-homoarginine (47.5% *vs.* 99.6% inhibition, respectively). None of the transport inhibitors utilised in this group of experiments affected the accumulation of [^{3}H]-arginine in the CSF. However, of the three transport inhibitors utilised, only *L*-homoarginine significantly inhibited the accumulation of [^{3}H]-arginine in the pineal gland, choroid plexus and pituitary gland (**Figure 2-34**).

2.5.2.3B BBB

It has been known for some time that *L*-arginine transport across the rat BBB is saturable at concentrations as low as 100 µM (Pardridge & Oldendorf, 1975a). Results from self-inhibition experiments carried out in this present study (**Figure 2-23**) demonstrated that unlabelled 100 µM *L*-arginine had a significant inhibitory effect on [^{3}H]-arginine uptake into all brain regions sampled at 10 minutes. The degree of inhibition exerted by unlabelled 100 µM *L*-arginine was very similar in all brain regions, but highest (73.0% inhibition) in the thalamus (**Table 2-20**). This effect was also observed in BCECs following capillary depletion analysis, and translated to significant inhibition of [^{3}H]-arginine accumulation in the brain parenchyma (**Table 2-21**).

Further investigation was undertaken to establish the identity of the saturable transport system for [^{3}H]-arginine at the BBB. Since the primary transport system identified for *L*-arginine identified at the BBB of other species is system y^+ (described above), [^{3}H]-arginine uptake into brain regions was measured in the presence of the system y^+ specific inhibitor, *L*-homoarginine (**Figure 2-32**). [^{3}H]-arginine uptake in all brain regions and capillary depletion samples was highly sensitive to inhibition by 20 mM *L*-homoarginine, with almost 100% inhibition in some samples (**Table 2-27**). This suggests that [^{3}H]-arginine transport into the brain *via* the BBB is almost entirely mediated by system y^+. While there was a tendency for [^{3}H]-arginine uptake to increase in the presence of the system L and system $B^{0,+}$ inhibitor BCH, and decrease in the presence of the system $B^{0,+}$ specific inhibitor α-methyl-*D*,*L*-tryptophan, a lack of

statistical significance makes it difficult to rule out inherent experimental variability. It should be noted, however, that [^{14}C]-sucrose space for all samples in these did not differ (one-way ANOVA with Dunnett's multiple comparisons test, $p > 0.05$, graphs not shown).

While the specificity of specific transport inhibitors can always be questioned, as can the possibility of compensation by other transporters, in this specific case, *L*-lysine transport at BBB is known not to be affected by BCH at concentrations up to 10 mM (O'Kane & Hawkins, 2003). The observed slight effects on [^{3}H]-arginine uptake by 4 mM BCH can therefore be attributed to experimental variability, rather than a real effect.

2.5.2.3C BCSFB and CVOs

Accumulation of [^{3}H]-arginine in the CSF, pineal gland, choroid plexus and pituitary gland was sensitive to inhibition by unlabelled 100 µM *L*-arginine – indicative of a saturable transport system at the blood-CSF barrier (**Figure 2-25**). However, transport inhibitor studies revealed that accumulation of [^{3}H]-arginine in the CSF was not affected by any of the three specific transport inhibitors used in these studies (**Figure 2-34**, *L*-homoarginine, BCH and α-methyl-*D*,*L*-tryptophan). The reason for this is not entirely clear, as the accumulation of [^{3}H]-arginine in the CSF appears to be susceptible to self-inhibition by 100 µM *L*-arginine (**Figure 2-25**). One possible explanation for this observation may be that *L*-arginine is able to access transporters in a location (such as the apical membrane of the choroid plexus epithelium), that the transport inhibitors used in this study are unable to. It would not be possible to confirm this hypothesis without knowing whether the transport inhibitors in question can themselves be transported. In the cases of the pineal gland, choroid plexus and pituitary gland, the only specific inhibitor to significantly inhibit the uptake of [^{3}H]-arginine was *L*-homoarginine – suggesting that [^{3}H]-arginine uptake into these organs is mediated only by system y^{+}.

While the available data on amino acid concentrations in the CSF is inconsistent, it is clear that CSF to plasma ratios are typically much less than 1, creating a concentration

gradient that favours influx of amino acids from the blood to the CSF (Abbott *et al.*, 2010). While a saturable transport system for [^{3}H]-arginine has been identified in the studies discussed in this section, the fact that *L*-homoarginine does not inhibit [^{3}H]-arginine accumulation in the CSF presents something of a puzzle. Despite the fact that [^{3}H]-arginine is similar in size and charge to [^{14}C]-sucrose (octanol-saline partition coefficients of 0.00149±0.00016 and 0.00105±0.00022 respectively), it is clear from the multiple-time uptake studies shown in **Figure 2-16** that the difference between [^{3}H]-arginine and [^{14}C]-sucrose accumulation in the CSF after a 10 minute perfusion ($p < 0.05$) is greater at 30 minutes ($p < 0.001$). The existence of tight-junctions at the apical membrane between epithelial cells of the choroid plexus means that the passage of a polar molecule such as [^{3}H]-arginine from the plasma into the CSF *via* the BCSFB is likely to require transport systems at both the basolateral and apical membranes of the choroid plexus epithelium working in concert. System y^+ has thus far been identified at the basolateral (blood-facing) side of the ovine choroid plexus (Segal *et al.*, 1990; Preston & Segal, 1992), and the system y^+ activity demonstrated by these experiments is also likely to be due to transporters at the basolateral membrane, since this is the first choroid plexus membrane encountered by [^{3}H]-arginine during *in situ* brain/choroid plexus perfusion. A better technique to detect apical transport at the choroid plexus is the isolated incubated choroid plexus technique, as it would involve the introduction of [^{3}H]-arginine on the apical side of the choroid plexus before measuring transport through this membrane.

Since the observed efflux of [^{3}H]-arginine from the pituitary gland in multiple-time uptake experiments (**Figure 2-16**) did not manifest until 30 minutes, one would expect that identification of the transport system responsible for this would be improved by extending the perfusion time for the transport inhibitor experiments from 10 to 30 minutes.

2.5.3 [^{3}H]-ADMA transport across the BBB and BCSFB mainly involves system y^+ but also a number of additional transport systems

This study investigated the ability of [^{3}H]-ADMA to cross the mouse blood-CNS barriers and accumulate within the CNS. ***Section 2.5.3.1*** provides a brief summary of the results from this part of the study, while their biological relevance will be interpreted in depth in the ensuing sections.

2.5.3.1 Summary of results

Multiple-time uptake studies (**Figure 2-17** and **Figure 2-19**) measured substantial [^{3}H]-ADMA uptake into all brain regions, choroid plexus and CVOs (significantly higher than [^{14}C]-sucrose at all time points, one-tailed, paired student's t-test, $p < 0.05$). However, transport of [^{3}H]-ADMA appears to be bi-phasic in nature, with a peak in accumulation being reached at 20 minutes before decreasing at 30 minutes brain regions. Capillary depletion analysis (**Figure 2-18**) confirmed that [^{3}H]-ADMA accumulates in the brain parenchyma following perfusion in the same manner. However, rather than accumulation peaking at 20 minutes in BCECs, the peak accumulation of [^{3}H]-ADMA in the capillary endothelial cell-enriched pellet was observed after 10 minutes. This pattern of peak accumulation of [^{3}H]-ADMA after 10 minutes was also observed in the pineal gland, choroid plexus and pituitary gland (**Figure 2-19**).

2.5.3.2 [^{3}H]-ADMA uptake into the CNS

2.5.3.2A Brain regions

While the accumulation of [^{3}H]-ADMA within the brain regions sampled was found typically to be 50% or less of the accumulation of [^{3}H]-arginine (**Figure 2-20**), [^{3}H]-ADMA accumulation in the brain regions sampled did reach significantly higher levels than values observed for [^{14}C]-sucrose ($p < 0.05$, **Figure 2-17**). The data presented here represent the first study to ever investigate the transport of ADMA across any

biological membrane *in vivo*, and certainly the first to investigate the movement of ADMA from plasma into the brain.

The observed decrease in [^{3}H]-ADMA accumulation in brain regions after 30 minutes (**Figure 2-17**) implies the existence of an efflux mechanism that removes accumulating ADMA. The fact that his effect is mirrored exactly in the brain parenchyma following capillary depletion analysis (**Figure 2-18**), but occurs 10 minutes earlier (after 20 minutes) in BCECs suggests this is a real effect whereby efflux is occurring at the level of capillaries supplying the brain regions, and contributing to removal from the brain back into plasma. These data alone are insufficient to predict whether the candidate efflux transport system utilises active processes, or if it merely reflects transport mediated by one or more facilitative transport systems after [^{3}H]-ADMA has accumulated in the brain parenchyma and BCECs above the concentration of [^{3}H]-ADMA in artificial plasma (62.5 nM). The identity of the system(s) mediating ADMA transport across the BBB will be discussed in ***section 2.5.3.3 - Transporter identification***. It is also possible that ADMA may be broken down by DDAH, the enzyme responsible for ADMA metabolism described in ***section 2.1.1.3B - ADMA clearance***. The expression of DDAH in the brain approximately mirrors the expression profile for NOS, with DDAH-1 often being expressed in neuronal tissue with nNOS, and DDAH-2 being expressed in the capillary endothelium, along with eNOS (Leiper *et al.*, 1999; Palm *et al.*, 2007). Metabolism of [^{3}H]-ADMA at the BBB cannot entirely be ruled out in this instance without performing HPLC with radiodetector analysis of capillary depletion samples (brain parenchyma and BCECs). While several attempts were made to carry out these aforementioned HPLC analyses (data not shown), the structural similarity of *L*-arginine, ADMA and its metabolite *L*-citrulline meant that co-elution was a significant problem, and distinguishing between the three in our samples impossible.

2.5.3.2B CSF

[^{3}H]-ADMA was also able to cross the blood-CSF barrier, and levels in the CSF reached approximately 30% of plasma levels after 10 minutes (**Figure 2-16**). This study represents the first investigation into the movement of ADMA from plasma to CSF and thus no data has previously been published to provide a direct comparison. It should be noted that [^{3}H]-ADMA accumulation in the CSF was only significantly higher ($p < 0.05$) from [^{14}C]-sucrose at 10- and 20- minute time-points (**Figure 2-16**). This re-affirms the efflux of [^{3}H]-ADMA observed at the BBB, described above.

2.5.3.2C Pineal gland, choroid plexus and pituitary gland

[^{3}H]-ADMA accumulation in the pineal gland, choroid plexus and pituitary gland was highest after 10 minutes (**Figure 2-19**); respectively reaching 194.1 ± 48.5%, 260.9 ± 42.5% and 182.9 ± 32.3% of plasma levels. In all three organs the accumulation of [^{3}H]-ADMA declines after 20 and then 30 minutes, returning to levels observed after just 2.5 minutes of perfusion. This would imply the existence of an efflux transport system for ADMA at the pineal gland, choroid plexus and pituitary gland, and that the rate of [^{3}H]-ADMA efflux begins to override the rate of influx at some point between 10 and 20 minutes, following initial accumulation.

Taking into consideration that [^{3}H]-ADMA efflux exists in all of the samples investigated in this study, it is clear that efflux mechanisms for ADMA at the BBB and BCSFB may be an evolutionary adaptation to prevent the CNS-accumulation of ADMA circulating in the plasma.

2.5.3.3 Transporter identification

Following the observations that [^{3}H]-ADMA in artificial plasma can accumulate and then be removed from the murine brain, experiments were designed to identify the transport system(s) responsible.

2.5.3.3A Summary of results

Self-inhibition studies with a range of concentrations of unlabelled ADMA from 0.5 – 500 µM (**Figure 2-26** and **Figure 2-28**) were utilised to assess the involvement of transporters in [^{3}H]-ADMA movement across the blood-CNS barriers at 10 minutes. It was found that [^{3}H]-ADMA uptake into all brain regions, choroid plexus and CVOs was reduced in the presence of unlabelled ADMA at all concentrations, implying that [^{3}H]-ADMA influx into the brain, choroid plexus and CVOs involves at least one saturable transport system. Capillary depletion analysis (**Figure 2-27**) suggests that the inhibition of [^{3}H]-ADMA uptake into BCECs by unlabelled ADMA results in reduced influx of [^{3}H]-ADMA into the brain parenchyma, however the previously discussed susceptibility of the capillary depletion technique to contamination means that further analysis would be required to be sure of this.

The utilisation of a range of unlabelled ADMA concentrations enabled the calculation of the half saturation constant, $\boldsymbol{K_m}$, for ADMA flux into the brain regions sampled, which varied from 327.9 ± 121.9 µM in the caudate nucleus to 1352 ± 946.0 µM in the cerebellum. The $\boldsymbol{K_m}$ values for ADMA accumulation into the pineal gland, choroid plexus and pituitary gland was comparatively lower, at 281.0 ± 166.7 µM, 49.96 ± 17.41 µM and 51.41 ± 16.42 µM respectively.

[^{3}H]-ADMA uptake into brain regions during 10-minute perfusions was sensitive to inhibition by all specific inhibitors utilised in this study to varying degrees, but with no obvious consistency or pattern between the different brain regions sampled (**Figure 2-35**). The complexity of interactions between [^{3}H]-ADMA and different transport systems at the BBB was reaffirmed by capillary depletion analysis, where [^{3}H]-ADMA was found to be sensitive to 20 mM *L*-homoarginine, 200 µM *L*-phenylalanine and 5 mM *L*-leucine in the whole-brain homogenate, but only to 20 mM *L*-homoarginine in

the parenchyma, and completely insensitive in BCECs (**Figure 2-36**). [^{3}H]-ADMA accumulation in the CSF was also completely insensitive to inhibition by any of the inhibitors utilised, while seemingly sensitive to all inhibitors in the pineal gland and choroid plexus, and all bar 500 µM α-methyl-*D*,*L*-tryptophan in the pituitary gland.

2.5.3.3B BBB

Self-inhibition studies revealed that [^{3}H]-ADMA influx into brain regions after 10 minutes is sensitive to inhibition by unlabelled ADMA at concentrations as low as 0.5 µM (**Figure 2-26**). Capillary depletion analysis revealed that this phenomenon appears to also be robustly observed in whole-brain homogenate, BCECs, and brain parenchyma, assuming there is no fraction-to-fraction contamination (**Figure 2-27**). Half-saturation constant ($\boldsymbol{K}_m$) values for [^{3}H]-ADMA at the BBB calculated from these experiments and described above are higher than previously published $\boldsymbol{K}_m$ values of 50-100 µM for influx of the other cationic amino acids, *L*-lysine, *L*-arginine and *L*-ornithine at the rat BBB (Stoll *et al.*, 1993). While not a direct species comparison, the larger $\boldsymbol{K}_m$ observed for BBB uptake of [^{3}H]-ADMA in the present study would suggest that the transport system(s) responsible (if shared) have a higher affinity for these cationic amino acids over ADMA.

Taken alone, the almost complete inhibition of [^{3}H]-ADMA uptake in all brain regions sampled in the presence of 20 mM *L*-homoarginine would suggest that ADMA transport at the BBB, as with [^{3}H]-arginine, is almost exclusively mediated by system y^+ (**Figure 2-35**). However, the inhibition of [^{3}H]-ADMA uptake in brain regions (albeit to a lesser degree) in the presence of the additional five transport inhibitors utilised makes it very difficult to pinpoint ADMA transport at the BBB to just one transport system. In light of the approximately equal sensitivity of [^{3}H]-ADMA to inhibition by 2 mM BCH and 500 µM α-methyl-*D*,*L*-tryptophan, ADMA may be interacting with system $B^{0,+}$ for transport from plasma to the brain. Furthermore, the sensitivity of [^{3}H]-ADMA to inhibition by 200 µM *L*-phenylalanine may indicate system L transport, while sensitivity to 5 mM *L*-leucine and 2 mM harmaline respectively indicate system y^+L and $b^{0,+}$ transport.

[^{3}H]-ADMA thus appears to be a highly promiscuous molecule with respect to interactions with transport systems at the BBB, and has a highly complex transport profile that can unfortunately not be dissected on the evidence from these experiments alone. However, it is clear that system y^+, as hypothesised, is a major contributor to [^{3}H]-ADMA transport across the BBB. The hypothesis that ADMA may use system y^+ for transport was based entirely on the observation that supraphysiological concentrations of ADMA were able to inhibit *L*-arginine accumulation *in vitro* (Closs *et al.*, 1997). However, the experiments reported in this thesis are among the first to confirm system y^+ as the main transporter for ADMA through direct empirical observation. The other publication reporting this finding was published after these experiments were performed but only relate to *in vitro* observations (Strobel *et al.*, 2012), and thus the results presented in this study represent the first identification of system y^+ mediated transport of ADMA *in vivo*.

While the canonical system y^+ transporter CAT-1 has been shown to be capable of mediating ADMA efflux (Strobel *et al.*, 2012), these experiments are not sufficient to determine if the efflux of [^{3}H]-ADMA from the CNS (described in ***section 2.5.3.2 - [^{3}H]-ADMA uptake into the CNS) is mediated by system y^+***. An interesting point of comparison would be repeating these experiments at 30 minutes to identify efflux transporters, since this would allow the detection of the transport system(s) mediating efflux following the initial accumulation of [^{3}H]-ADMA after 10 minutes. This is discussed in greater detail in ***section 2.5.8 - Future work***.

2.5.3.3C BCSFB

Accumulation of [^{3}H]-ADMA in the CSF was sensitive to inhibition by unlabelled ADMA concentrations of 3, 10 and 500 µM (**Figure 2-28**), but not 0.5 and 100 µM. The reasons for this are not entirely clear, since [^{3}H]-ADMA accumulation in the pineal gland, choroid plexus and pituitary gland was sensitive to inhibition by unlabelled ADMA at all concentrations from 0.5-500 µM - indicative of a saturable transport system at the blood-CSF barrier. One possible explanation could be that the inherent technical difficulty of obtaining CSF samples is likely to have contributed to high

variability between samples. K_m values for [^{3}H]-ADMA influx into the pineal gland, choroid plexus and pituitary gland were calculated to be 281.0 ± 166.7, 49.96 ± 17.41 and 51.41 ± 16.42 µM – all of which are higher than previously published K_m value of 25 µM for *L*-arginine at the ovine choroid plexus (Segal *et al.*, 1990; Preston & Segal, 1992). This provides yet more evidence that transporters at the BBB and BCSFB have higher affinity for *L*-arginine over ADMA.

Transport inhibitor studies revealed a similarly complex interaction for [^{3}H]-ADMA with a variety of different transport systems, as indicated by its sensitivity to inhibition by a number of different transport inhibitors (**Figure 2-37**). Despite being susceptible to self-inhibition by un-labelled ADMA, [^{3}H]-ADMA accumulation in the CSF does not appear to be sensitive to any of the transport inhibitors used in these experiments (**Figure 2-37**). The sensitivity to inhibition by all transport inhibitors used in the pineal gland and choroid plexus make identifying specific interactions with transport systems in these sub-organs of the brain very difficult. In the pituitary gland, [^{3}H]-ADMA accumulation was found to be sensitive to all inhibitors used except for 500 µM α-methyl-*D*,*L*-tryptophan, suggesting perhaps that ADMA may interact with system L at the pituitary gland, and not system $B^{0,+}$. It is however clear in that [^{3}H]-ADMA accumulation in the pineal gland, choroid plexus and pituitary gland is highly sensitive to inhibition by the system y^+ inhibitor *L*-homoarginine, being inhibited by up to 88.6% in the pituitary gland.

Since efflux of [^{3}H]-ADMA was detected at the BCSFB in multiple-time uptake experiments (**Figure 2-19**), extending the perfusion time for these experiments to 30 minutes may also be beneficial in identifying the transporters responsible.

2.5.4 ADMA does not inhibit [^{3}H]-arginine transport across the BBB and BCSFB in physiologically- or pathologically-relevant conditions

The first proposed hypothesis to explain the *L*-arginine paradox was that pathological increases in circulating levels of ADMA resulted in ADMA outcompeting *L*-arginine for transport into endothelial cells (including those of the BBB), and subsequently a reduction in NO production observed in a number of cardiovascular and cerebrovascular diseases. In this situation, oral supplementation of *L*-arginine could putatively restore the *L*-arginine:ADMA ratio in plasma to switch competition for transport back in favour of *L*-arginine (see ***section 2.1.1.4A - Competition hypothesis***).

Cross competition experiments were designed to test this hypothesis, whereby a range of unlabelled ADMA concentrations were co-perfused with [^{3}H]-arginine to measure their effect on [^{3}H]-arginine transport across the murine BBB and BCSFB.

2.5.4.1 Summary of results

Cross-competition studies (**Figure 2-38**) utilising escalating concentrations of unlabelled ADMA (0.5, 3.0, 10.0, 100 and 500 µM) were designed to determine the effect of ADMA on the movement of [^{3}H]-arginine across the blood-CNS barriers. In all brain regions sampled, only 500 µM unlabelled ADMA inhibited the uptake of [^{3}H]-arginine. Capillary depletion analysis suggests the same observation can be seen in both the whole-brain homogenate and brain parenchyma, however the observed reduction of [^{3}H]-arginine uptake in BCECs following co-perfusion with 500 µM unlabelled ADMA did not attain statistical significance (**Figure 2-39**). Unlabelled ADMA did not appear to affect the accumulation of [^{3}H]-arginine in the CSF, pineal gland or pituitary gland at any of the concentrations utilised in this study, however a significant inhibition of [^{3}H]-arginine accumulation was observed in the choroid plexus following perfusion with 500 µM unlabelled ADMA (**Figure 2-40**).

2.5.4.2 Effect of ADMA on [^{3}H]-arginine transport across the BBB

One of the earliest *in vivo* studies demonstrating cross-competition of transport between *L*-arginine and *L*-lysine revealed that each could inhibit the transport of the other into the rodent brain (Banos *et al.*, 1974). It was then theorised that all three cationic amino acids share the same transport system at the BBB. A later study revealed a preference for the transport of these three different cationic amino acids by system y^+, differing following the scheme arginine > lysine > ornithine (highest affinity first, (O'Kane *et al.*, 2006)). As the primary transport system mediating [^{3}H]-arginine uptake at the BBB has been found by this study and others to be system y^+, it would not be unreasonable to predict that system y^+ may have a differing affinity to ADMA.

ADMA has previously been shown to inhibit uptake of *L*-arginine into *Xenopus laevis* oocytes expressing the system y^+ transporters, CAT-2B (Closs *et al.*, 1997). In accordance with these earlier observations, the cross-competition experiments performed for this study show that [^{3}H]-arginine uptake in the brain regions sampled was inhibited by unlabelled 500 µM ADMA, but no concentrations below 100 µM (**Figure 2-38**). Capillary depletion analysis showed the same phenomenon in whole-brain homogenate and brain parenchyma, but not in BCECs (**Figure 2-39**). Taking into consideration that the concentration of [^{3}H]-arginine in the artificial plasma for these experiments was only 11.6 nM, it would appear that system y^+ at the BBB overwhelmingly favours transport of *L*-arginine over ADMA. These findings are in accordance with a very recent publication that observed that *L*-arginine uptake in human embryonic kidney (HEK) cells overexpressing the canonical system y^+ transporter CAT-1 is only sensitive to inhibition by ADMA at concentrations above 300 µM (Strobel *et al.*, 2012). The affinity and capacity of CAT-1 to ADMA was found to be higher than that for *L*-arginine in HEK cells, which would appear to contradict the findings shown here *in vivo* at the murine BBB. However, the IC_{50} for the inhibition of *L*-arginine uptake by ADMA in HEK cells was calculated to be 758 µM, which is unlikely to be of any direct relevance *in vivo*, since ADMA plasma concentrations have never been measured as exceeding 3 µM, even in pathological conditions (Cakir *et al.*, 2005; Bode-Boger *et al.*, 2007).

2.5.4.3 Effect of ADMA on [^{3}H]-arginine transport across the BCSFB

[^{3}H]-arginine accumulation in the CSF, pineal gland and pituitary gland was not inhibited by ADMA at any of the concentrations added to the artificial plasma (**Figure 2-40**). [^{3}H]-arginine accumulation in the choroid plexus was only sensitive to inhibition by 500 µM unlabelled ADMA, and not any of the concentrations below this. This would suggest that the $\boldsymbol{K_i}$ for ADMA's inhibitory effect on [^{3}H]-arginine transport at the BCSFB is even higher than that for the BBB.

2.5.5 *L*-arginine inhibits [^{3}H]-ADMA transport across the BBB and BCSFB under physiologically-relevant conditions

2.5.5.1 Summary of results

Cross-competition studies utilising unlabelled 100 µM *L*-arginine were designed to determine the effect of *L*-arginine on the movement of [^{3}H]-ADMA across the blood-CNS barriers. In all brain regions sampled, 100 µM unlabelled *L*-arginine inhibited the uptake of [^{3}H]-ADMA (**Figure 2-42**). Capillary depletion analysis revealed the same observation at the level of the whole-brain homogenate, but also in both the brain parenchyma and BCEC fractions (**Figure 2-43**). Unlabelled 100 µM *L*-arginine did not appear to affect the accumulation of [^{3}H]-ADMA in the CSF, however a significant inhibition of [^{3}H]-ADMA accumulation was observed in the pineal gland, choroid plexus and pituitary gland following perfusion with 100 µM unlabelled *L*-arginine (**Figure 2-44**).

2.5.5.2 Effect of *L*-arginine on [^{3}H]-ADMA transport across the BBB

Following on from the observations that only supraphysiological concentrations of ADMA never observed *in vivo* have an effect on [^{3}H]-arginine transport across the BBB and BCSFB described in ***section 2.5.4***, the present study found that [^{3}H]-ADMA transport across the BBB is highly sensitive to inhibition by physiological (100 µM) *L*-arginine. The biological implications for this are that *L*-arginine transport across the BBB from plasma into brain is likely to predominate under both physiological conditions, but also pathological conditions where plasma ADMA is elevated.

This is also very elegantly demonstrated by the almost identical respective inhibition of unlabelled 100 µM *L*-arginine and 100 µM ADMA on the distribution of [^{3}H]-ADMA in the frontal cortex, as shown in **Figure 2-45**.

2.5.5.3 Effect of *L*-arginine on [^{3}H]-ADMA transport across the BCSFB

Just as [^{3}H]-ADMA is highly sensitive to inhibition by physiological concentrations of *L*-arginine at the BBB, the same holds true for the BCSFB. This is also demonstrated

by the almost identical respective inhibition of unlabelled 100 µM *L*-arginine and 100 µM ADMA on the distribution of [^{3}H]-ADMA in the choroid plexus, as shown in **Figure 2-45**. Perhaps the lack of inhibition of [^{3}H]-ADMA accumulation in the CSF by unlabelled 100 µM *L*-arginine may be an indication that the accumulation that is observed is due to passive paracellular diffusion of [^{3}H]-ADMA across the BCSFB, although this study alone would be insufficient to make a firm conclusion.

2.5.5.4 Implications for the 'competition hypothesis' to explain the *L*-arginine paradox

In analysis of the feasibility of the 'competition hypothesis' to explain the *L*-arginine paradox (in the context of the BBB and BCSFB), there are several pieces of evidence uncovered by the studies discussed in this chapter that suggest that an alternative hypothesis is needed:

i. While transport systems that can transport ADMA into BCECs from plasma exist, it would appear that efflux of ADMA pre-dominates.

ii. $\boldsymbol{K_m}$ values for ADMA influx at the BBB and BCSFB are higher than those previously published for influx of other cationic amino acids such as *L*-arginine.

iii. The biggest contributor to ADMA and *L*-arginine transport at the BBB and BCSFB is system y^+.

iv. Neither physiological nor pathological concentrations of ADMA in plasma have any inhibitory effect on *L*-arginine transport across the BBB and BCSFB *in vivo*. ADMA concentrations must be increased to supraphysiological concentrations of 500 µM to observe any inhibition of *L*-arginine transport, in agreement with observations recently made *in vitro* (Strobel *et al.*, 2012).

It is therefore highly unlikely that the *L*-arginine paradox is due to competition for transport by system y^+ between *L*-arginine and ADMA, and this hypothesis should be discounted.

2.5.6 Trans-stimulation of *L*-arginine and ADMA transport

2.5.6.1 Trans-stimulation of [^{3}H]-arginine transport

Trans-stimulation was first proposed by (Teerlink *et al.*, 2009) to explain the *L*-arginine paradox, where it was hypothesised that supplemented *L*-arginine may trans-stimulate the removal of ADMA from the cell, and restoring influx of *L*-arginine for conversion into NO (see ***section 2.1.1.4B - Trans-stimulation hypothesis***).

Of all CAATs, y^+ is by far the most sensitive to trans-stimulation, particularly CAT-1 (Hatzoglou *et al.*, 2004), although systems y^+L (Mann *et al.*, 2003) and $b^{0,+}$ (Nguyen *et al.*, 2007) both display trans-stimulation to lesser degrees. No evidence of system $B^{0,+}$ trans-stimulation has been documented.

In vitro cell culture is more ideally suited to investigating trans-stimulation since cells essentially constitute a closed system whereby the movement of solutes between extracellular and intracellular compartments can be studied and quantified. The investigation of ADMA/*L*-arginine trans-stimulation at the BBB and BCSFB *in vivo* is complicated by the presence of several intracellular and extracellular compartments, each containing different concentrations of endogenous ADMA and *L*-arginine, and expressing different transporters, with different substrate specificities. It is therefore much more difficult to predict how the solutes of interest will equilibrate between these compartments, and analyse data from these experiments. Despite this limitation, experiments were designed to investigate the ability of high levels of intracellular ADMA to trans-stimulate [^{3}H]-arginine uptake at the BBB and BCSFB following supplementation with *L*-arginine, and are discussed below.

2.5.6.1A Summary of results

Experiments involving a 20-minute 'pre-perfusion' followed by 10-minute 'post-perfusion' were designed to investigate if [^{3}H]-arginine transport across the blood-CNS barriers is subject to trans-stimulation under conditions recreating *L*-arginine supplementation in NO-deficient patients (**Figure 2-47** and **Figure 2-49**). Trans-stimulation is a phenomenon whereby the presence of substrate on one side of a cellular

membrane, stimulates the transport of substrate on the other (*trans*) side of the membrane. [^{3}H]-arginine uptake in all brain regions except for hypothalamus and thalamus was found to be trans-stimulated by high levels of intracellular ADMA (following perfusion with 500 µM unlabelled ADMA), but only when [^{3}H]-arginine in the post-perfusion was co-perfused with 200 µM unlabelled *L*-arginine (**Figure 2-47**). This trans-stimulation of [^{3}H]-arginine uptake was also seen in the whole-brain homogenate, and very strongly in BCECs ($p < 0.001$), but not in brain parenchyma following capillary depletion (**Figure 2-48**). [^{3}H]-arginine uptake was also trans-stimulated in a similar manner in the pineal gland, choroid plexus and pituitary gland (**Figure 2-49**).

2.5.6.1B Trans-stimulation of [^{3}H]-arginine transport across the BBB

The first comparison for this batch of experiments involved determining the effect of pre-perfusing with 500 µM unlabelled ADMA on [^{3}H]-arginine transport across the BBB (**Figure 2-47**). The 'control' comparison for these experiments was a 20-minute pre-perfusion with artificial plasma containing no additives, followed by a 10-minute perfusion with artificial plasma containing [^{3}H]-arginine alone. The act of pre-loading the brain capillary endothelium with 500 µM ADMA with a 20-minute pre-perfusion caused no changed in the accumulation of [^{3}H]-arginine in any of the brain regions sampled, or capillary depletion analysis samples (**Figure 2-47**).

This comparison was then extended to more accurately reflect the situation of supplemented 200 µM unlabelled *L*-arginine – the third experimental condition for comparison in these experiments. Pre-loading the brain capillary endothelium with 500 µM ADMA, and then perfusing with [^{3}H]-arginine supplemented with 200 µM unlabelled *L*-arginine produced a significant increase in [^{3}H]-arginine distribution in all brain regions sampled, except for the hypothalamus and thalamus (**Figure 2-47**). Capillary depletion analysis appears to demonstrate this effect in the whole-brain homogenate, and BCECs, but not in the brain parenchyma itself (assuming there is no fraction-to-fraction contamination).

While system y^+ is expressed on both the luminal and abluminal membrane, with expression levels higher on the abluminal membrane (O'Kane *et al.*, 2006), the unlabelled ADMA in 'pre-perfusion' artificial plasma, and [^{3}H]-arginine and unlabelled *L*-arginine in 'post-perfusion' artificial plasma would all be exposed to transporters at the luminal membrane first. It is therefore possible that the observed effect of trans-stimulation being amplified in BCECs but not brain parenchyma following capillary depletion relates directly to the luminal system y^+ transporters. It would not be unreasonable to expect that abluminal y^+ is just as susceptible to trans-stimulation as luminal y^+, however the presence of system y^+ on both luminal and abluminal membranes means they are susceptible to different substrate concentrations on each side of the membrane. Luminal system y^+ would be subject to concentration gradients for *L*-arginine and ADMA created by differences in respective concentrations in intracellular and plasma compartments. In contrast, abluminal system y^+ is subject to entirely different concentration gradients created by differences in respective concentrations of ADMA and *L*-arginine in intracellular and ISF/CSF compartments. An additional consideration to be made relates to the nature of system y^+ transporters themselves; since they are bi-directional but still uniport transporters that do not simultaneously exchange substrates across the membrane.

These observations of trans-stimulation of *L*-arginine transport by intracellular ADMA are in accordance with currently unpublished data relating to the same experiments performed using the human BBB *in vitro* model hCMEC/D3 cell line (Watson, 2012).

A possible explanation of the observed effects presented in this section is therefore that unlabelled 500 µM ADMA accumulates inside BCECs during the 'pre-perfusion', preventing influx of [^{3}H]-arginine from the circulating artificial plasma. The introduction of 200 µM *L*-arginine may then be trans-stimulating system y^+ to remove the accumulated ADMA from BCECs until the concentration gradient favouring [^{3}H]-arginine transport into the BCECs *via* y^+ overwhelms the concentration gradient favouring efflux of ADMA *via* y^+. The experiments testing this hypothesis are discussed below in ***section 2.5.6.2 - Trans-stimulation of [^{3}H]-ADMA transport***.

2.5.6.1C Trans-stimulation of [^{3}H]-arginine transport across the BCSFB

The observed effect of apparent trans-stimulation of [^{3}H]-arginine transport across the BBB also holds true for the pineal gland, choroid plexus and pituitary gland (**Figure 2-49**). The accumulation of [^{3}H]-arginine in these organs appears to be trans-stimulated when they are pre-loaded with unlabelled 500 µM ADMA and then perfused with artificial plasma containing both [^{3}H]-arginine and unlabelled 200 µM *L*-arginine.

2.5.6.2 Trans-stimulation of [^{3}H]-ADMA transport

2.5.6.2A Summary of results

[^{3}H]-ADMA accumulation in all brain regions, pineal gland, choroid plexus and pituitary gland was significantly lower when perfusing for 20 minutes with [^{3}H]-ADMA and then 10 minutes of artificial plasma containing no additives, relative to control conditions of just a 20-minute perfusion with [^{3}H]-ADMA (**Figure 2-51** and **Figure 2-53**). Capillary depletion analysis revealed that this phenomenon was only observable in whole-brain homogenate, but not in brain parenchyma or BCECs (**Figure 2-52**).

The second comparison in this study relates to [^{3}H]-ADMA accumulation after perfusing for 20 minutes followed immediately by a 10-minute perfusion of either artificial plasma containing no additives, or artificial plasma containing unlabelled 200 µM *L*-arginine. In all brain regions sampled, pineal gland and pituitary gland, [^{3}H]-ADMA accumulation was significantly higher when including unlabelled 200 µM *L*-arginine in the 10-minute 'post-perfusion'. Comparisons for capillary depletion analysis samples between these two experimental groups again revealed no significant differences.

2.5.6.2B Trans-stimulation of [^{3}H]-ADMA transport across the BBB

For the trans-stimulation hypothesis to explain the *L*-arginine paradox to be proved correct, one would predict that the increased intracellular ADMA would trans-stimulate the influx of *L*-arginine in plasma through system y^+ at the luminal membrane. The experiments described in this study were devised to test this prediction by attempting to pre-load BCECs with [^{3}H]-ADMA with an aim of observing increased

efflux due to trans-stimulation by unlabelled 200 µM un-labelled in artificial plasma (mimicking the concentration of *L*-arginine achieved in the plasma by dietary supplementation in patients (Clarkson *et al.*, 1996; Adams *et al.*, 1997)).

Trans-stimulation of [^{3}H]-ADMA efflux by high levels of extracellular *L*-arginine was found to be robustly present in the human BBB *in vitro* model hCMEC/D3 cell line (Watson, 2012), data published as PhD thesis only at time of writing. However, the lack of this phenomenon at the murine BBB in this present study may be due to a number of reasons:

i. [^{3}H]-ADMA may have already begun to be removed from BCECs after 10 minutes of the 'pre-perfusion' phase of these experiments, as per the findings of the multiple-time uptake studies discussed in ***section 2.5.3.2***.

ii. Trans-stimulation is a difficult phenomenon to observe *in vivo* and particularly at the BBB due to the number of available compartments for substrates to equilibrate between, but also because of the number of different transporters that [^{3}H]-ADMA appears to interact with, as discussed in ***section 2.5.3.3***.

The fact that [^{3}H]-ADMA accumulation actually increases when unlabelled 200 µM *L*-arginine is included in the 'post-perfusion' phase is interesting as it suggests that *L*-arginine actually blocks the efflux of [^{3}H]-ADMA during the 10-minute 'post-perfusion' phase in that experimental group. This implies that [^{3}H]-ADMA efflux from BCECs is mediated by a transporter that can also mediate *L*-arginine influx at the BBB. The present study, and others, have identified system y^+ as the most likely candidate for this system, and as previously described, this is a bi-directional uniport transport system (White, 1985; Stoll *et al.*, 1993). Having shown that *L*-arginine outcompetes ADMA on the *cis*- side of the plasma membrane for transport *via* system y^+ in this chapter, it is entirely plausible that *L*-arginine also outcompetes ADMA on the *trans*-side of the plasma membrane. One method to test this would be to co-perfuse [^{3}H]-ADMA with 20 mM *L*-homoarginine as discussed in ***section 2.5.3.3***, but extend the perfusion time from 10 minutes to 30 minutes with an aim of observing the transport

system in the state of [^{3}H]-ADMA efflux. Should this be found to be true, and in light of the fact that trans-stimulation of [3H]-ADMA efflux was not observed in the experiments discussed here, another future experiment could be to pre-load with [^{3}H]-ADMA for only 10 minutes, rather than 20 minutes.

2.5.6.2C Trans-stimulation of [^{3}H]-ADMA transport across the BCSFB

The observed lack of trans-stimulation of [^{3}H]-ADMA efflux across the BBB also holds true for the pineal gland and pituitary gland (**Figure 2-53**). However, the efflux of [^{3}H]-ADMA in the choroid plexus appeared to be trans-stimulated by the presence of unlabelled 200 µM *L*-arginine in the artificial plasma during the 10-minute 'post-perfusion' phase of the experiment, indicated by a significant decrease relative to the experimental group where no additives were present in the artificial plasma for the 10-minute 'post-perfusion' phase. This is an interesting difference between the choroid plexus and the pineal and pituitary glands that appears to be unique to this particular set of experiments; since interactions of [^{3}H]-ADMA with the BCSFB in all other studies performed for this thesis were relatively uniform between these sub-organs of the brain (*e.g.* **Figure 2-19**, **Figure 2-28** *etc.*). Determining the biological significance of this particular difference is thus difficult on the basis of these data alone, and thus further investigation of this effect in the choroid plexus under these conditions is warranted.

2.5.7 Conclusions

A number of experimental variations to the murine *in situ* brain/choroid plexus perfusion technique were devised and performed to characterise the transport of *L*-arginine and ADMA transport across the murine BBB and BCSFB. [^{3}H]-ADMA and [^{3}H]-arginine were used as substrates in addition to their unlabelled counterparts in different combinations and concentrations, as well as a number of specific transport inhibitors to compare transport and inhibition kinetics. The principal findings for these experiments are as follows:

1. Saturable transport systems for both ADMA and *L*-arginine exist at both the BBB and BCSFB in mouse.

2. A major contributor to the transport of both ADMA and *L*-arginine at both the BBB and BCSFB is system y^+, seemingly transporting *L*-arginine from plasma into the CNS, and ADMA in both directions in a time and concentration dependent manner.

3. ADMA also has complex interactions with a wide range of transport systems expressed at the BBB and BCSFB.

4. The most likely transporter mediating ADMA efflux from the CNS at both the BBB and BCSFB is system y^+.

5. ADMA does not compete with *L*-arginine for transport under physiological or pathophysiological conditions.

6. On the basis of the data shown in this study, the trans-stimulation hypothesis is partially correct, since intracellular ADMA appears to be able to trans-stimulate *L*-arginine influx in conditions mimicking dietary supplementation. This study was unable to detect trans-stimulation of ADMA efflux at the murine BBB *in vivo*, under these conditions.

While trans-stimulation of ADMA efflux by extracellular *L*-arginine has been observed at the human BBB *in vitro* (Watson, 2012), it is currently unclear if the phenomenon

also exists at the mouse BBB and BCSFB *in vivo*. As with all *in vitro* data, the limitations of studying this phenomenon in cultured cells include culture-induced changes in transporter expression, as well as a lack of transporter polarisation into luminal and abluminal membrane microenvironments to the extent that exists *in vivo*. Furthermore, the hCMEC/D3 cells have much lower TEER values when compared to BCECs *in vivo*.

2.5.7.1 Implications of NO synthesis

As *L*-arginine is the precursor for NO synthesis, and ADMA a potent inhibitor of NO synthesis (Vallance *et al.*, 1992a; Vallance *et al.*, 1992b) the interplay between the respective transport of these two amino acids across plasma membranes has been widely predicted to relate directly to NO production. Credence is lent to this hypothesis by the fact that the canonical system y^+ transporter CAT-1 that is responsible for *L*-arginine transport across most biological membranes co-localizes with caveolae and eNOS in endothelial cells (McDonald *et al.*, 1997). Moreover, the over-expression of murine CAT-1 in bovine aortic endothelial cells has previously been shown to lead to increased *L*-arginine transport and NO production (Zani & Bohlen, 2005).

One experiment to definitively test if system y^+ transport is a rate-determining step in the production of NO (and therefore if it is likely to be involved in the *L*-arginine paradox) may be to measure the effect of inhibition of *L*-arginine transport by *L*-lysine on NO production. Since *L*-lysine is a system y^+ substrate but not an inhibitor of NOS one may predict that should the transport of *L*-arginine be a critical step in NO production, that *L*-lysine would also inhibit NO production without directly inhibiting NOS. Data relating to this has thus far been conflicting/inconclusive; with one group finding that NO production is sensitive to *L*-lysine inhibition (Wu *et al.*, 2000), while another has found the opposite is true (Zani & Bohlen, 2005).

In vitro studies appear to dominate as an approach to investigating the involvement of *L*-arginine and ADMA transport on NO production, and it has been observed that 5 µM ADMA can inhibit NO production in the presence of 100 µM *L*-arginine in bovine

endothelial cells (Cardounel *et al.*, 2007). Considering the fact that data presented in this thesis, and elsewhere (Strobel *et al.*, 2012), overwhelmingly indicates that transport of *L*-arginine by system y^+ would not be affected by ADMA at those concentrations, an alternative transport system may possibly be playing a role in the *L*-arginine paradox. While system y^+ is an important system for the transport of *L*-arginine and its related methylarginines, it is not the exclusive transport system for these substrates. Indeed, data presented here for the identification of transporters mediating [^{3}H]-ADMA transport across the murine BBB and BCSFB have identified a number of interactions with different transport systems. It has previously been proposed that *L*-arginine transport in endothelial cells has two components – a high affinity, low capacity system (y^+), and an additional low affinity, high capacity system (Preik-Steinhoff *et al.*, 1995). The exact identity of this system y^+-independent component of *L*-arginine transport was not found in that study, however one possible candidate is the y^+L system, which is known to be required for NO synthesis under certain experimental conditions (Arancibia-Garavilla *et al.*, 2003). In addition to transporting *L*-arginine (Deves & Boyd, 1998; Omidi *et al.*, 2003), system y^+L has also been shown to have the capacity to transport ADMA (Slenzka *et al.*, 2011); observations corroborated by the data presented here in the context of the murine BBB and BCSFB.

In summary, while the data presented here contribute to the current understanding of the interplay between ADMA and *L*-arginine transport across biological membranes, and particularly those of the BBB and BCSFB, further experimentation is required to solve the *L*-arginine paradox.

A schematic of the involvement of trans-stimulation in explaining the arginine paradox from the observations in this study are shown in **Figure 2-54**.

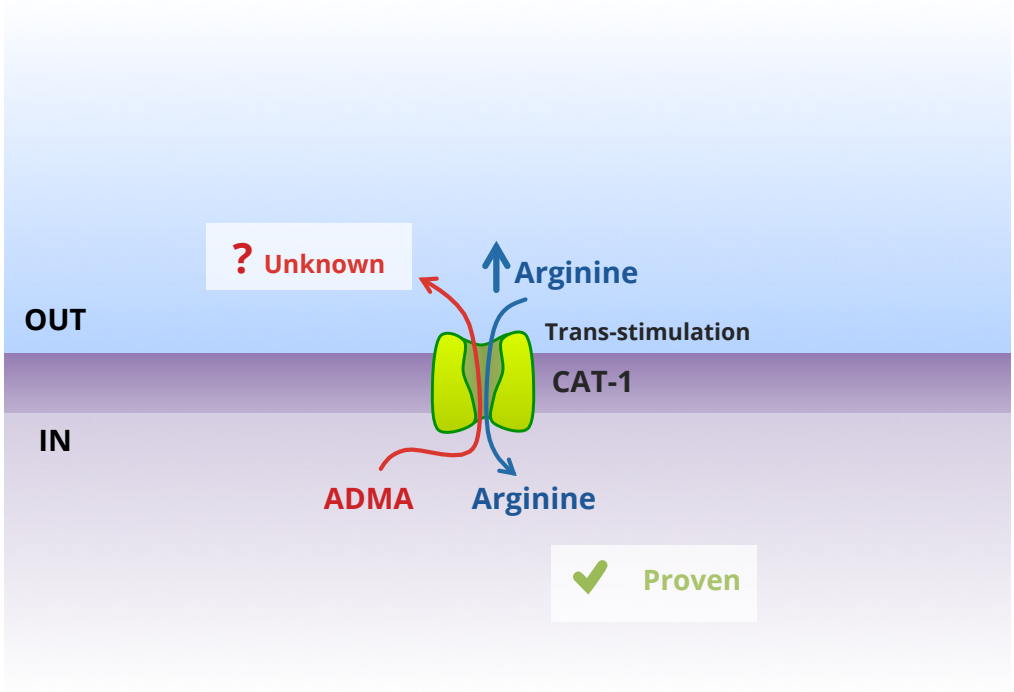

Figure 2-54: Summary of trans-stimulation involving *L*-arginine and ADMA transport across the murine BBB. An increase in the plasma concentration of *L*-arginine following oral supplementation combined with high intracellular concentrations of ADMA appears to trans-stimulate the influx of *L*-arginine into the BCEC *via* luminal CAT-1. This study was unable to measure trans-stimulated efflux of ADMA from BCECs under the same conditions, using the *in situ* brain and choroid plexus perfusion method.

2.5.8 Future work

2.5.8.1 Role of system y^+L in transport of *L*-arginine at the BBB

As mentioned above, system y^+L is a possible candidate for a second transport system regulating the transport of *L*-arginine into endothelial cells. Since system y^+L is inhibited by *L*-leucine (Estevez *et al.*, 1998; Rotmann *et al.*, 2007), this could be investigated at the BBB through the co-perfusion of *L*-leucine with [^{3}H]-arginine.

2.5.8.2 *L*-arginine transport at the apical membrane of the choroid plexus

The transport of *L*-arginine across the apical membrane of the choroid plexus could be investigated using the isolated incubated choroid plexus technique, since the greatest contributor to transport observed in the choroid plexus using the *in situ* brain/choroid plexus technique is the basolateral membrane. The isolated incubated choroid plexus technique could be expected to reveal whether or not there an apical transporter for *L*-arginine exists. The implications of these findings would be to determine if the BBB is the main transport interface for providing *L*-arginine to brain (where observed basolateral arginine transport serves to merely supply choroid plexus epithelium), or if BCSFB also contributes.

2.5.8.3 Further probing of *L*-arginine and ADMA efflux

Following the observations in this study that *L*-arginine may be effluxed from the pituitary gland after 30 minutes, extending the perfusion time of experiments where [^{3}H]-arginine was co-perfused with specific transport inhibitors to 30 minutes could be expected to identify any transport systems potentially involved in this process.

Similarly, extending the perfusion time of the same set of experiments with [^{3}H]-ADMA could also identify any transport systems involved in the efflux of ADMA (if any). It should be noted that any efflux of either ADMA or *L*-arginine could be passive and merely due to a change in concentration gradients during the perfusion.

2.5.8.4 Trans-stimulation experiments

Following the observation that the highest accumulation of [^{3}H]-ADMA in brain regions over the course of 30 minutes is after 10 minutes, a possible extension to the experiments reported here could be to reduce the 'pre-perfusion' phase from 20 minutes to 10 minutes. This could potentially reveal why the phenomenon of trans-stimulation was observed to be robust at the choroid plexus but not in brain regions.

3

Brain delivery of small molecules through specific inhibition of transporters at the blood-CNS barriers

3.1 Introduction

The efficient delivery of drugs to the CNS has proved to be a difficult task over the years, and the cumulative success rates for CNS drugs progressing through clinical development is often much lower than those seen for cardiovascular or cancer drugs (**Figure 3-1**). The underlying cause for this trend is most likely to be multi-factorial, and the topic of a number of reviews elsewhere (Alavijeh *et al.*, 2005; Pardridge, 2005). However, the presence of the blood-CNS barriers with their unique abilities to tightly and specifically regulate the movement of molecules into the CNS no doubt make the efficient delivery of CNS-active molecules to their desired site of action more challenging.

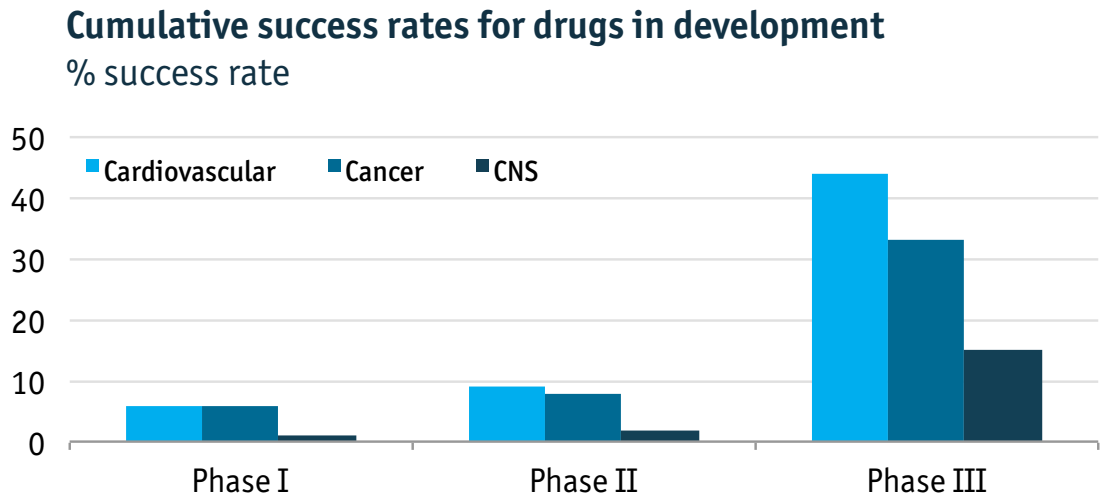

Figure 3-1: The cumulative success rates for drugs in clinical development. CNS drugs have much lower success rates during phase I, II and III clinical trials relative to cardiovascular or cancer drugs. Adapted from (Alavijeh *et al.*, 2005).

The BBB alone excludes more than 98% of small molecule diagnostics and therapeutics, and almost 100% of large biologics such as monoclonal antibodies from the CNS (Pardridge, 2005). Molecules that are known to reach the CNS in pharmacologically relevant amounts typically have a low molecular weight of approximately 0.5 kDa, and a high degree of lipid solubility (Pardridge, 2005) – characteristics that also make them more likely to be substrates for removal from the CNS by ABC efflux transporters outlined in ***chapter 1***. With the success rates shown in **Figure 3-1**, it is thought that a large number of CNS conditions could benefit from improved therapies (Pardridge, 2005). Understanding and manipulating the processes that dictate CNS entry may facilitate the rational design of drugs and drug carriers to facilitate the efficient delivery of drugs to treat CNS pathologies. One such CNS pathology that is particularly underserved by the pharmaceutical research community (more so in recent years) is Human African Trypanosomiasis (HAT), also known as 'sleeping sickness'.

3.1.1 Human African Trypanosomiasis (HAT)

HAT is a parasitic disease endemic in sub-Saharan Africa that is caused by infection with one of two protozoan extracellular organisms: *Trypanosoma brucei rhodesiense* or

Trypanosoma brucei gambiense. The parasites are transmitted by the bite of insect vectors belonging to the genus *Glossina* (Tsetse flies), and display a life cycle strategy that is equally spread between human and insect hosts (Brun *et al.*, 2010). Both parasite species cause a similar clinical disease, but with differing degrees of virulence, and can be distinguished using molecular methods (Radwanska *et al.*, 2002; Picozzi *et al.*, 2008). However, these methods are often unavailable in the field, and the differential diagnosis of HAT often relies on the parasites' discrete geographical distributions (*T.b. gambiense* in West and Central Africa, and *T.b. rhodesiense* in East Africa, shown in **Figure 3-2**), although there are concerns that the distributions may be blurring in recent years (Picozzi *et al.*, 2005). There are currently around 10,000 new cases of HAT reported each year (latest figures, (WHO, 2010)), and likely a substantial number of more cases that go unreported, with a total of 48,000 deaths due to HAT in 2008 (WHO, 2009).

The disease progression for HAT can be separated into two distinct phases, with differing symptoms. Stage 1 HAT is known as the haemolymphatic or blood phase, and is caused by the parasite invading the circulatory and lymphatic systems (Priotto *et al.*, 2007). Stage 1 HAT starts asymptomatically, but as parasitaemia increases patients often present with chronic and intermittent fever, severe itching of the skin and severe swelling of the lymph nodes (Brun *et al.*, 2010). Having entered the circulation, trypanosomes have several effective strategies to avoid the host's immune system, including a wide repertoire of genes encoding variant surface glycoproteins (VSG) that coat their outer layer and can be interchanged and even intragenetically shuffled at will to avoid antibody binding (Donelson *et al.*, 1998). Only one VSG protein is expressed on the outer layer of the parasite at any given time, and since an antibody response to this protein is raised roughly once every ten days, the parasite changes the VSG protein it expresses by antigenic variation (Turner, 1997; Cross *et al.*, 1998). This process leads to characteristic waves of parasitaemia, and eventually the disease progresses to stage 2 – the meningoencephalitic or CNS phase.

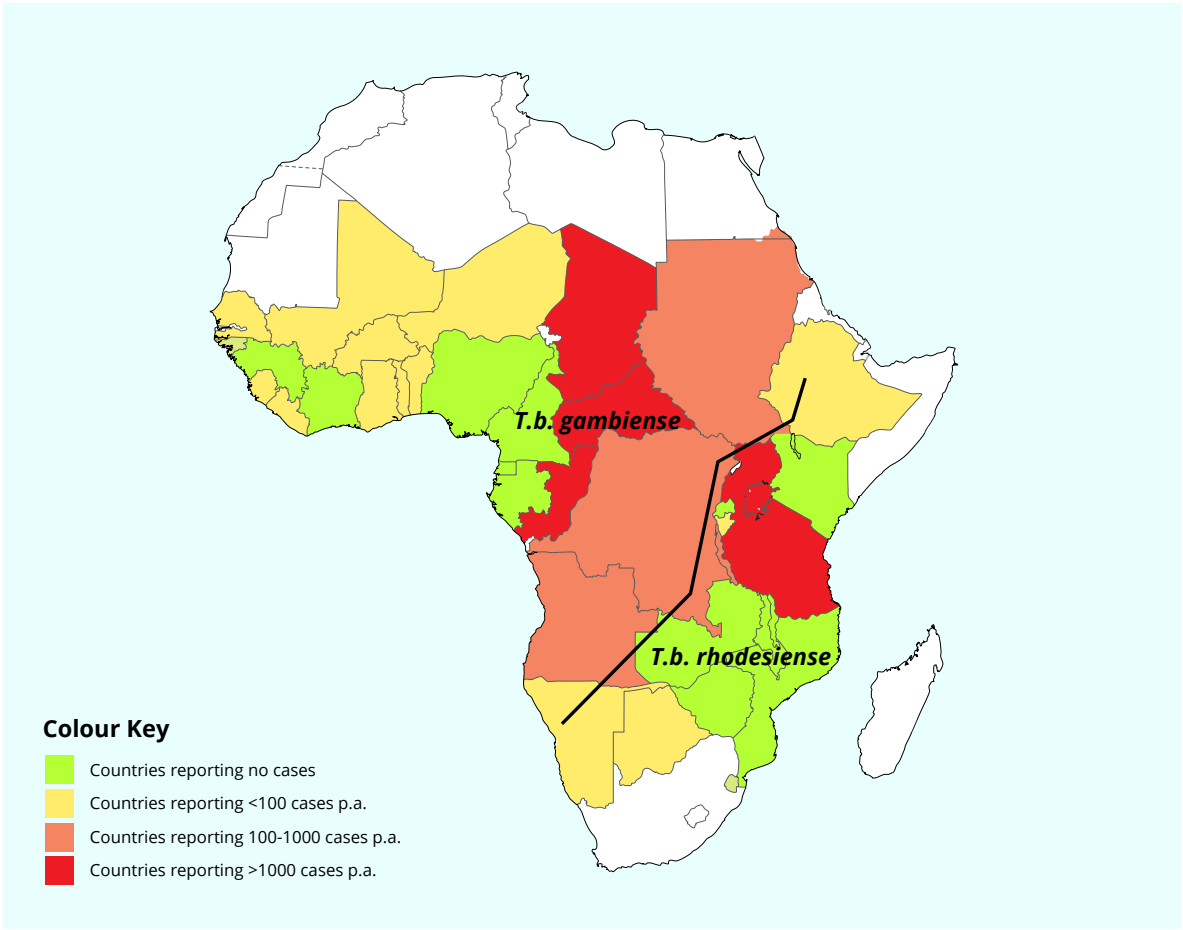

Figure 3-2: Geographical distribution of HAT in sub-Saharan Africa. Incidence of HAT caused by *T.b. gambiense* has historically been restricted to West and Central Africa, while *T.b. rhodesiense* has been restricted to East Africa. There are concerns that there may be some overlap in this distribution in recent years. Adapted from (Simarro *et al.*, 2008).

The time taken for HAT to progress to stage 2 appears to vary depending on the parasite involved. *T.b. rhodesiense* is typically the more virulent of the two, progressing to stage 2 within months; while *T.b. gambiense* can take years after the initial infection to progress to stage 2 (Odiit *et al.*, 1997; Checchi *et al.*, 2008). Stage 2 of HAT arises when the parasite leaves the circulation and lymphatic system to invade the CNS. The precise mechanism for how the parasite is able to do this is a subject of debate. One school of thought hypothesises that the parasite crosses the BBB by transcytosis without affecting paracellular permeability and TJ protein expression (Mulenga *et al.*, 2001), or by another as yet unidentified mechanism involving interferon gamma (IFN-γ) (Masocha *et al.*, 2007). Meanwhile, other groups theorise

that trypanosomes are more opportunistic and require transient increases in BBB paracellular permeability to infect the CNS (Philip *et al.*, 1994; Grab & Kennedy, 2008). Most recently, the choroid plexus has been put forward as the only site of entry for trypanosomes into the CNS, excluding the BBB, by virtue of the fact that parasites are consistently detected in the choroid plexus epithelium before the brain parenchyma (Wolburg *et al.*, 2012).

Once in the CNS, the parasites cause changes in the sleeping cycle and insomnia – characteristic features of the disease that lend themselves to the nickname 'sleeping sickness'. These symptoms are often accompanied by other neurological symptoms, such as motor weakness, limb paralysis and Parkinsonian tremors due to muscular hypertension (Kristensson *et al.*, 2010). Once established, and if left untreated, these symptoms worsen in 100% of cases until the patient falls into a coma, soon followed by death. The increased virulence in stage 1 HAT displayed by *T.b. rhodesiense* continues through to stage 2, with a much more aggressive disease progression (Balasegaram *et al.*, 2009).

3.1.1.1 Treatment of HAT

A very small number of drugs are currently available for the treatment of HAT, and these have historically been categorised as drugs for the treatment of stage 1 HAT, and drugs for the treatment of stage 2 HAT (**Table 3-1**). For stage 1 HAT, the current drug of choice for the treatment of *T.b. rhodesiense* is suramin – a potent trypanocidal drug that has been used since 1922 (Docampo & Moreno, 2003). Suramin therapy typically involves a dosing regimen of six, weekly intravenous injections and is often associated with a number of adverse reactions, including rash (incidence: 90%, not dose-limiting), adrenal cortical damage (incidence: 50%) and peripheral neuropathy (incidence: 15%) (Brun *et al.*, 2010).

Table 3-1: Standard drugs used for the treatment of stage 1 and 2 HAT, with associated adverse reactions. Adapted from (Brun *et al.*, 2010).

Parasite species	Drug	Stage	Administration route	Dosing regimen	Adverse reactions
Trypanasoma brucei gambiense	Pentamidine	1	Intramuscular	4 mg kg^{-1} once daily for 7 days	Hypoglycaemia, injection site pain, nausea, diarrhoea, vomiting
	Eflornithine	2	Intravenous infusion for >30 minutes	100 mg kg^{-1} at six hour intervals for 14 days	Diarrhoea, nausea, vomiting, convulsions, anaemia, leucopaenia and thrombocytopaenia
	Melarsoprol	2	Intravenous	2.2 mg kg^{-1} once daily for 10 days	Encephalopathic syndromes, skin reactions, peripheral motor or sensory neuropathies
Trypanosoma brucei rhodesiense	Suramin	1	Intravenous	Test dose of 4-5 mg kg^{-1} at day 1, then 5 injections of 20 mg kg^{-1} every 7 days	Hypersensitivity reactions (acute/late), albuminuria, cylinduria, haematuria, peripheral neuropathy
	Melarsoprol	2	Intravenous	3 series of 3 x 3.6 mg kg^{-1} daily, each series separated by 7 days	Encephalopathic syndromes, skin reactions, peripheral motor or sensory neuropathies

The drug used for the treatment of stage 1 *T.b. gambiense* infection is pentamidine, and will be discussed in greater detail in ***section 3.1.1.1A - Focus on Pentamidine***.

Traditionally, the most frequently used drug for the treatment of stage 2 HAT is melarsoprol – dosed intravenously at 2.2 mg kg^{-1} daily for 12 consecutive days (Burri *et al.*, 2000). However, this is due to a lack of alternatives and does not reflect the very poor safety profile of melarsoprol, which is an organic arsenic derivative that melts plastic (Lancet, 2010), and has poor solubility in water, ether or alcohol. This means that melarsoprol must be dissolved in the solvent propylene glycol for administration, which as an excipient/vehicle itself causes extreme pain upon injection (Docampo & Moreno, 2003). Furthermore, melarsoprol is extremely toxic to patients, with 5-10% developing severe encephalopathy (resulting in death in 50% of cases) (Kennedy, 2004). Such adverse reactions mean that the use of melarsoprol for the treatment of stage 2 HAT is on the decline, with either eflornithine or nifurtimox/eflornithine combination therapy (NECT, 7 days of twice daily intravenous and 10 days of 4 times daily oral therapy) preferred where possible (Simarro *et al.*, 2011). The use of eflornithine is limited both by its expense, and its inability to treat *T.b. rhodesiense* due to the parasite's high ornithine decarboxylase turnover conferring resistance (Iten *et al.*, 1997). Eflornithine is however effective in treating stage 2 *T.b. gambiense* infection, and while the absolute number of patients being treated for Stage 2 caused by *T.b. gambiense* is decreasing, it remains steady at approximately 60% of new infections annually (Simarro *et al.*, 2011).

3.1.1.1A Focus on Pentamidine

Pentamidine (1,5-4'-aidinophenoxypentane isethionate salt) is the current drug of choice for the treatment of stage 1 *T.b. gambiense* infection, and was developed after a related compound (synthalin) was discovered to have trypanocidal activity (Sands *et al.*, 1985). Pentamidine is administered *via* intramuscular injection or by slow intravenous infusion (Docampo & Moreno, 2003) and there are a number of putative mechanisms of action for its trypanocidal activity – namely through selective inhibition

of Ca^{2+}-ATPase (Benaim *et al.*, 1993) or non-specific inhibition of tRNA aminoacylation in the trypanosomal mitochondria (Sun & Zhang, 2008). While the exact mechanism of action for pentamidine trypanocidal activity is not clear (Calderano *et al.*, 2011), its success in the treatment of HAT has led to the development of other diamidine compounds (Sturk *et al.*, 2004).

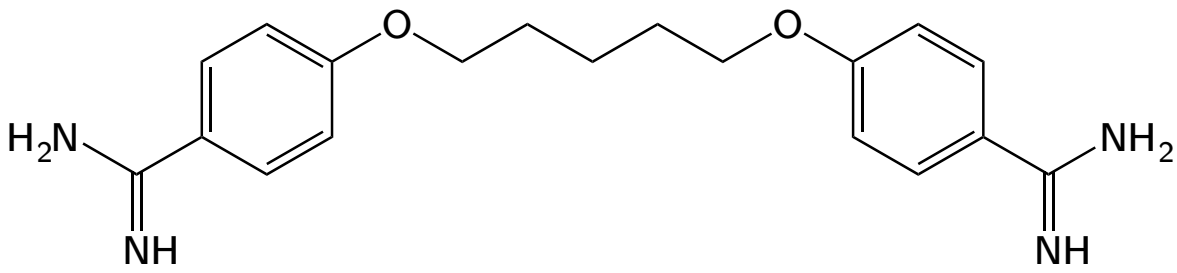

Figure 3-3: Chemical structure of pentamidine.

Pentamidine is generally considered to be one of the lesser toxic anti-HAT drugs, however peripheral side-effects include hypoglycaemia (incidence: 5-40%) and diabetes mellitus (incidence: occasional) – often dose-limiting factors that can lead to incomplete treatment (Burri, 2010). Despite being historically viewed as a stage 1 HAT drug (Raseroka & Ormerod, 1986), pentamidine has been found to be effective in treating the very early stages of stage 2 HAT (Doua *et al.*, 1996). After the first observation that trypanosomes may be accumulating in CVOs prior to infecting the CNS (Lundkvist *et al.*, 2004), later confirmed (Wolburg *et al.*, 2012), it was hypothesised that the separation of stage 1 and 2 HAT drugs (and their efficacy therein) was due to their ability or inability to cross the blood-CNS barriers (Sanderson *et al.*, 2007; Sanderson *et al.*, 2008; Sanderson *et al.*, 2009).

In the case of pentamidine, it was observed that intact drug could be detected in the brain, having crossed both the luminal and abluminal membranes of the BBB, but that a considerable amount was being trapped by the capillary endothelium (Sanderson *et al.*, 2009). Pentamidine appeared not to be metabolised to any significant degree by the

brain capillary endothelium, but brain concentrations that were attained were deemed to not be high enough to be efficacious against trypanosomes (Sanderson *et al.*, 2009). Brain concentrations of pentamidine were however significantly increased in *mdr1a/1b* -/- (P-gp double knockout) mice, as well as in the choroid plexus in wild-type mice dosed with a selective inhibitor of MRP-1 efflux (Sanderson *et al.*, 2009). Taken together, these data would suggest that a strategy that is able to attenuate these efflux mechanisms at the BBB and BCSFB should be effective in increasing CNS concentration of pentamidine.

3.1.2 Nanotechnology: Focus on Pluronic® P85

Pluronic® P85 belongs to a family of triblock copolymers characterised by a central hydrophobic block of poly(propylene oxide) (PPO) flanked by two hydrophilic blocks of poly(ethylene oxide) (PEO).

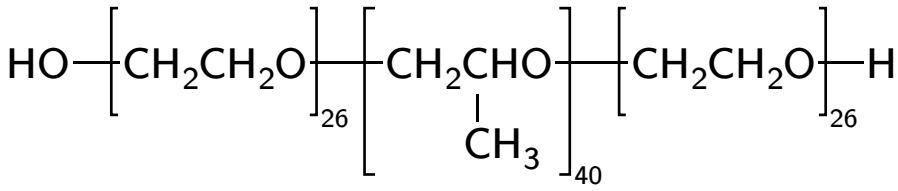

Figure 3-4: Chemical structure of Pluronic® P85.

Pluronic® P85 is thus an amphiphilic compound, as the individual PPO and PEO domains respectively have hydrophobic (water insoluble) and hydrophilic (water soluble) properties.

In very dilute conditions, Pluronics are present in solution as individual polymer chains, termed 'unimers'. As the concentration of the polymer in solution increases, a threshold point is reached whereby the unimers begin to aggregate into energetically favourable three-dimensional structures: micelles (**Figure 3-5, panel 3**). This is due to the amphiphilic nature of the molecules, which results in the molecules arranging in a conformation that reduces interactions between their hydrophobic domains and the polar water molecules. Micelles ordinarily have an anisotropic distribution of water within their structure – that is to say that the concentration of water decreases from the surface towards the hydrophobic core of the micelle; where water is largely excluded. In the case of Pluronics, however, a large fraction of water is still associated with the core.

The concentration at which micelles are formed is termed the critical micelle concentration (CMC). Above the CMC, unimers are still present at a concentration that is equal to the CMC, and any additional molecules are incorporated into micelles.

When dissolved in solution, amphiphilic molecules adsorb at the water-interface, lowering the surface tension (**Figure 3-5, panel 2**), and thus acting as surface-active-agents or 'surfactants'. This is because it is energetically more favourable for the hydrophobic domains of the molecules to avoid the contact with water. As a result, the surface tension of a liquid containing surfactants decreases with increasing surfactant concentration up to the CMC, where the interface becomes saturated and the formation of micelles in the bulk solution does not lead to further decrease of the surface tension.

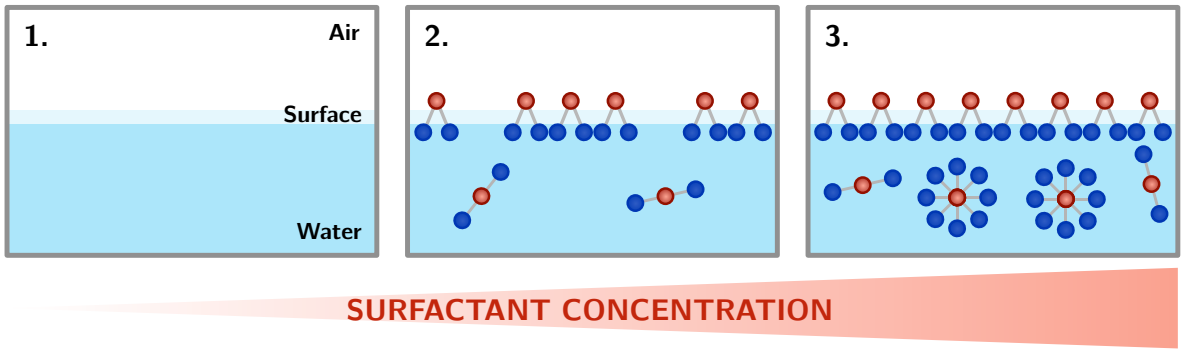

Figure 3-5: Behaviour of triblock copolymers such as Pluronic® P85 in aqueous solution. The hydrophilic domains of Pluronic® P85 are shown here in dark blue, with the hydrophobic domain in red. At low concentrations (panel 2) surfactants initially form layers on the surface of the liquid to minimise the contact of hydrophobic domains with polar water molecules. Increasing the concentration of surfactant eventually results in the formation of micelles with hydrophobic cores (panel 3). The concentration at which this occurs is termed the critical micelle concentration (CMC).

The unique structure of micelles presents a useful pharmaceutical opportunity to solubilise drugs that would ordinarily have poor solubility in aqueous solution. The spatial localisation of a drug within a micelle depends on its exact chemical structure and its polarity. Nonpolar molecules are usually solubilised within the micellar core, and drugs with intermediate polarity can be found between the exterior hydrophilic

palisade/coronal layer and the hydrophobic core (Rangel-Yagui *et al.*, 2005a), or even at the water/micelle interface, in the case of more hydrophilic drugs.

One very important consideration when designing a micellar drug delivery system is the CMC of the surfactant molecule, since this is the parameter that ultimately determines the stability of the delivery system (Kabanov & Alakhov, 2002; Rangel-Yagui *et al.*, 2005a). The biological relevance of the CMC in the context of designing an optimised drug delivery system is three-fold:

i. Circulation time
ii. Inhibitory effect of unimers on efflux transporters
iii. Decreased drug-related toxicity

These three important parameters are discussed in greater detail in the sections that follow.

3.1.2.1 Circulation time

A long systemic circulation time for an intravenous drug is often a desirable property to improve the likelihood of the drug reaching its intended target site or tissue before it is removed from the blood by the kidneys or metabolised. One possible strategy for increasing the circulation half-life of drugs is by encapsulation within specifically designed nano- or microscopic drug carriers, which include micelles (Kabanov & Alakhov, 2002; Rangel-Yagui *et al.*, 2005a).

From a pharmacological perspective, knowledge of the CMC value is of critical importance, since any micellar formulation is subject to dilution in biological fluids (*e.g.* blood) upon administration, and micelles with a high CMC can dissociate into unimers and prematurely release the drug into the blood (Yokoyama, 1992). Micelles made from a surfactant with low CMC are more likely to retain their integrity in circulation and reach the target site before decaying into unimers (Lavasanifar *et al.*, 2002; Adams *et al.*, 2003). In this prospect, polymeric surfactants such as Pluronics® are advantageous since they usually present a much lower CMC than conventional, low molecular weight surfactants.

When developing polymeric or colloidal drug delivery systems, an important consideration should be to avoid clearance by the reticuloendothelial system (RES) following protein adsorption in the blood, which typically results in accumulation of the drug carrier in the liver or spleen. It has been observed that the extent of clearance by the RES is reduced if the drug delivery system is smaller than 200 nm in diameter, facilitating a longer circulation time (Stolnik *et al.*, 1995). Micelles formed by Pluronic® P85 are approximately 20 nm in diameter, with a circulation half-life in mice of between 60 to 90 hours (Batrakova *et al.*, 2004a). The accumulation of Pluronic® P85 in the liver following systemic administration is greatly reduced if the concentration of Pluronic® P85 is above the CMC. However, the existence of Pluronic® P85 in circulation as micelles rather than unimeric form appears not to affect the overall clearance characteristics – indicating that elimination of Pluronic® P85 from the bloodstream is largely due to renal clearance rather than the disposition or disintegration of circulating micelles (Batrakova *et al.*, 2004a).

The ability of Pluronic® micelles to avoid detection and clearance by the RES is further enhanced by the hydrophilic corona formed by the PEO domain. This hydrophilic shell stabilises the micelle while also preventing the adsorption of circulating proteins, conferring it 'stealth' properties (Alvarez-Lorenzo *et al.*, 2010). Thus, the CMC is a vital consideration when designing any micelle-based drug delivery system, as is the diameter of the resulting micelles.

3.1.2.2 Inhibitory effect of unimers on efflux transporters

The high tolerability of Pluronics® *in vivo* – as well as their simple chemical structure – initially led investigators to believe that they were biologically inert compounds that could be used simply as drug solubilisers. However, there is growing evidence that some Pluronics® can have a significant effect on specific cellular responses (Kabanov *et al.*, 2005a; Kabanov *et al.*, 2005b; Kabanov, 2006). Pluronic® P85, in particular, has been shown to be remarkably effective in sensitising multi-drug resistant cancer cells and potentiating the delivery of drugs across cellular barriers, including the brain capillary endothelium (Kabanov *et al.*, 2002b; Kabanov *et al.*, 2002a). This effect appears to

mainly be due to the Pluronic® unimers (Miller *et al.*, 1997; Batrakova *et al.*, 1999a) and is thought to stem (in part) from the ability of Pluronic® 85 to be incorporated into the plasma membrane and decrease microviscosity at a local level, inhibiting active efflux transporters (Batrakova *et al.*, 2001b). As described in ***chapter 1***, the lipid microenvironment of biological membranes appears to have a critical role in the mechanisms underlying efflux mediated by ABC transporters such as P-gp and MRP (Romsicki & Sharom, 1998; Romsicki & Sharom, 1999). The inhibition of efflux transporters by Pluronics® is thought to result from conformational changes in the efflux proteins themselves and/or the steric interference with sites in the protein involved in protein-drug interactions (Batrakova *et al.*, 2004b).

In addition to the direct effect of Pluronic® P85 on efflux transporters and the surrounding lipid microenvironment described above, there appears to be an additional, indirect effect of Pluronic® P85 on multi-drug resistant cancer cells and barrier cells that may contribute to the inhibition of active efflux. Pluronic® P85 unimers are known to translocate across the plasma membrane into cells; reaching certain intracellular compartments and transiently depleting cells of ATP (Batrakova *et al.*, 2003). This transient depletion of ATP could inhibit active efflux transporters that require ATP to function (Batrakova *et al.*, 2003).

Internalisation of Pluronic® P85 unimers occurs by caveolae-mediated endocytosis, while Pluronic® P85 micelles are internalised by clathrin-mediated endocytosis (Sahay *et al.*, 2008). Caveolae trafficking often delivers endosomes to the endoplasmic reticulum (Carver & Schnitzer, 2003) but also to mitochondria (McMahon *et al.*, 2006; Bozidis *et al.*, 2008), and thus it has been proposed that this is the mechanism by which Pluronic® P85 unimers may reach mitochondria (Minko *et al.*, 2005). Pluronic® P85 concentrations as low as 0.001% have been shown to inhibit respiratory chain complexes I and IV (but not II and III) in mitochondria isolated from multi-drug resistant cancer cells (Alakhova *et al.*, 2010), and thus, by transiently disrupting the electron transport chain, less ATP is available to supply active efflux transporters. Interestingly, this phenomenon appears to be selective between cancer cells that are

multi-drug resistant or sensitive both *in vitro* and *in vivo* (Batrakova *et al.*, 2001a; Alakhova *et al.*, 2010). The proposed explanation for this selectivity relates to differences in the respiration rates and fuel sources used by multi-drug resistant and sensitive cells (fatty acids *vs.* glucose, respectively) (Harper *et al.*, 2002) as Pluronic® P85 may also be interacting with fatty acid molecules (Harper *et al.*, 2002).

In the context of the blood-CNS barriers, a precedent has already been set for the enhanced delivery of therapeutic agents across BCECs both *in vitro* (Batrakova *et al.*, 1998; Batrakova *et al.*, 1999b) and *in vivo* (Batrakova *et al.*, 2001c) using Pluronics®. Digoxin is a P-gp substrate whose CNS-delivery is greatly enhanced in P-gp knockout mice (relative to wild-type) (Batrakova *et al.*, 2001c). Furthermore, the co-formulation of digoxin with Pluronic® P85 produces a similarly enhanced delivery of digoxin to the CNS in wild-type mice (Batrakova *et al.*, 2001c). Notably, it would appear that both membrane fluidisation and ATP depletion is required for the effective inhibition of drug efflux by P-gp at the BBB (Batrakova *et al.*, 2001b).

3.1.2.3 Decreased drug-related toxicity

One of the more frequently observed side effects of pentamidine administration is hyperglycaemia (Waskin *et al.*, 1988), which often responds well to treatment upon presentation. However, pentamidine treatment can also lead to or worsen diabetes mellitus, with an incidence of approximately 10% (Jha & Sharma, 1984; Thakur *et al.*, 1991). Pentamidine has been shown to activate the hepatic T1 protein, a transport protein that is part of the glucose-6-phosphotase system (Scott & Burchell, 1991). It has been proposed that the increased activation of T1 increases the transport of glucose-6-phosphate into the lumen of the endoplasmic reticulum, where it is broken down to glucose by the enzyme glucose-6-phosphatase, and resulting in hyperglycaemia (Scott & Burchell, 1991). Furthermore, pentamidine was found to irreversibly damage pancreatic β-cells *in vitro*, leading to hyperinsulinaemia at sub-stimulatory glucose concentrations and decreased glucose-induced insulin release (Sai *et al.*, 1983; Zhou & Ipp, 1989).

Here, we propose that encapsulation of pentamidine within Pluronic® P85 micelles could reduce the exposure of pentamidine to the pancreas, as would otherwise result from systemic administration of free pentamidine through conventional needs.

3.2 Rationale and aims

As discussed in the previous sections of this chapter, pentamidine is efficacious against stage 1 HAT, but is blocked from reaching the brain by efflux mechanisms at the blood-CNS barriers. The proposed solution presented in here is to co-formulate pentamidine with Pluronic® P85 to inhibit these efflux mechanisms and increase the delivery of pentamidine to the CNS with the aim to achieve the following:

i. Effectively treat stage 2 HAT, by achieving pharmacologically relevant concentrations of pentamidine in the CNS.
ii. Reduce adverse reactions to pentamidine due to pancreatic toxicity by reducing the free fraction of pentamidine in circulation after administration.
iii. Shorten length of pentamidine treatment required to treat stage 1 disease.

One of the major benefits of this solution is that Pluronics® are FDA approved as pharmaceutical excipients. Indeed, a formulation containing Pluronics® L61 and F127 is in phase 2 clinical trials for the treatment of chemotherapy resistant oesophageal cancer (Valle *et al.*, 2011). While either Pluronics® L61 or F127 could have been selected as the first co-polymers to test as a candidate drug carrier for enhanced delivery of pentamidine to the CNS, Pluronic® P85 was selected due to its known ability to inhibit P-gp at the BBB (Batrakova *et al.*, 2003), and is known itself to cross the BBB (Price *et al.*, 2010).

Pluronic® P85 micelles and unimers are known to be internalised by cells through endocytotic mechanisms (Sahay *et al.*, 2008), and since HAT results in an increase in endocytic vesicle formation at the BBB (Sanderson *et al.*, 2008) it is hypothesised that Pluronic® P85 nanocarriers would be internalised by BCECs through similar mechanisms.

It is not anticipated that either pentamidine or Pluronic® P85 will be toxic to the brain since 5 µM pentamidine is known not to induce any neurotoxicity (Reynolds &

Aizenman, 1992), and Pluronic® P85 is also well tolerated in the brain (despite slightly altering the transport of lactate by MCT transporters (Batrakova *et al.*, 2004c)).

The precise mechanism of Pluronic® P85 micelle transport across the BBB is not currently known, however Pluronic® P85 conjugated to leptin is transported across the BBB *in vivo* using a leptin-transporter independent, non-saturable mechanism (Price *et al.*, 2010). Furthermore, Pluronic® P85 micelles enhance the delivery of the P-gp substrate, digoxin, to the brain, crossing endothelial cell monolayers *in vitro* and the BBB *in vivo* (Batrakova *et al.*, 2001c).

A summary of what is currently known about the interactions of pentamidine with the blood-CNS barriers is shown schematically in **Figure 3-6**, and the proposed solution to increase pentamidine transport into the CNS in **Figure 3-7**.

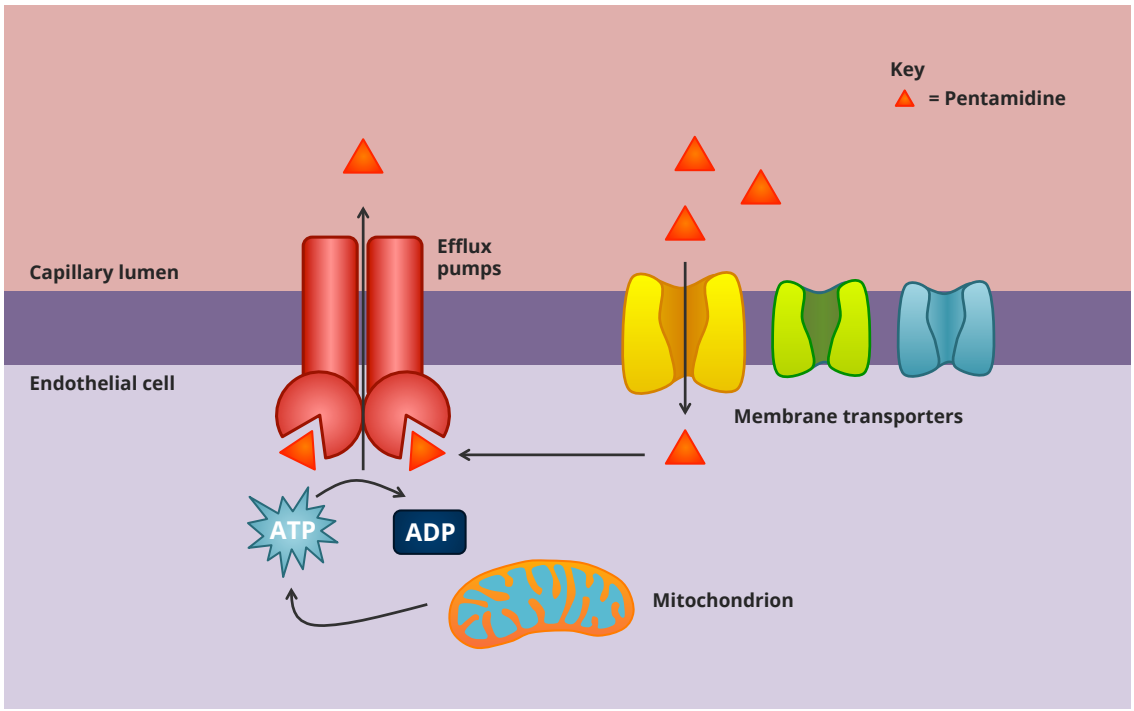

Figure 3-6: Current understanding of the interaction of pentamidine with the blood-CNS barriers. Pentamidine appears to interact with a broad range of transporters (including P-gp) expressed on the luminal side of the BBB and is removed by active efflux transporters that utilise energy from ATP hydrolysis to pump pentamidine back out into the capillary lumen.

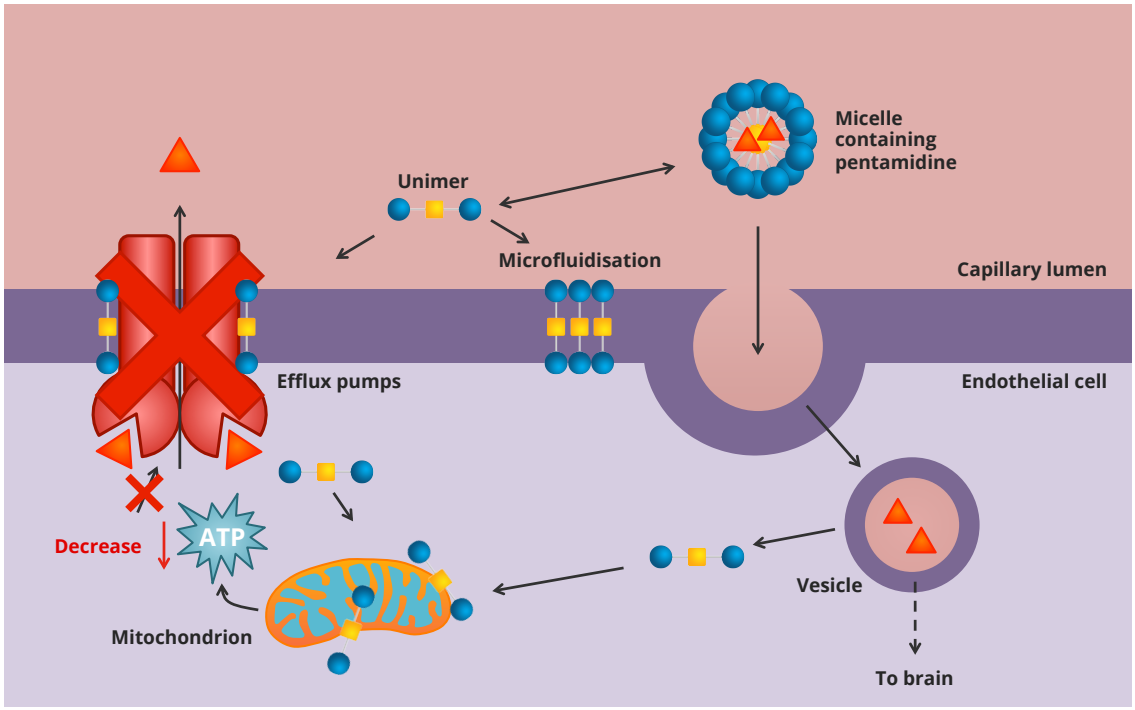

Figure 3-7: Proposed model for increasing pentamidine uptake at the blood-CNS barriers using Pluronic® P85. Pentamidine is either encapsulated within, or associated with Pluronic® P85 micelles, and taken up by clathrin-mediated endocytosis. Once in the vesicles, Pluronic® P85 unimers are translocated to mitochondria where they inhibit ATP synthesis, thus depleting the cell of ATP available for active efflux. Pluronic® P85 unimers in circulation also microfluidise the lipid membrane microenvironment surrounding efflux transporters in the luminal membrane and directly inhibit efflux. The net result is a greater delivery of pentamidine across the blood-CNS barriers.

3.3 Methods

The complexity of the blood-CNS interface, combined with limitations of the respective experimental techniques used to study it, make it difficult to predict and quantify barrier transport characteristics using one experimental approach alone. With this in mind, the hypotheses tested in this work utilised a combination of *in silico*, *in vitro* and *in vivo* procedures.

In this chapter, the different methodologies employed are presented as three broad approaches outlined below:

2.3.1. Physico-chemical characterisation of drug/polymer formulations

2.3.2. Blood-CNS model & accessory methodologies

2.3.3. Peripheral free-fraction (pancreatic toxicity) experiments

3.3.1 Physico-chemical characterisation of drug/polymer formulations

Biophysical properties of Pluronic P85® and/or drug/Pluronic P85® formulations were predicted using (a) computational (*in silico*) means and/or (b) then empirically quantified using a combination of spectrophotometry-based techniques.

The following parameters were quantified:

i. **Critical Micelle Concentration** (CMC) – The concentration at which Pluronic® P85 micelles spontaneously form in solution.

ii. **Aggregation number** (N_{agg}) – The mean number of polymeric chains present in a micelle at a given concentration above the CMC.

iii. **Drug partitioning** (P) – The partitioning of the drug within the micelles.

iv. **Mean hydrodynamic diameter** (D) – Diameter of micelles in solution as measured by dynamic light scattering.

This information was then used as a basis for a formulation rationale to take the most promising formulation(s) forward into *in vivo* studies, which also meant reducing the number of animals used in experimentation.

3.3.1.1 *In silico* simulations

Molecular dynamics modelling is a useful approach to predict structural and electronic properties of biological and chemical systems. The simulations conducted as part of this thesis were classical molecular dynamics simulation, in which the smallest individual units modelled were either atoms (atomistic) or segments of molecules (coarse-grain) represented as spheres, which can be connected together to create larger molecules.

In silico simulations were run in collaboration with Dr Chris D. Lorenz (King's College London, Department of Physics), following previously described methods (Anderson *et al.*, 2008), using the LAMMPS molecular dynamics software package (Plimpton, 1995). Two types of simulations were used:

i. Atomistic simulations to probe the detail of interactions between Pluronic® P85 unimers within a single micelle at the atomistic level.

ii. Coarse-grain simulations to determine the Critical Micelle Concentration (CMC) and aggregation number (N_{agg}) of Pluronic® P85.

3.3.1.1A General background

In essence, the behaviour of the molecules over time can be predicted from an initial set of coordinates and randomly assigned initial velocities for each of the atoms (or beads) in the simulated systems. Solving Newton's second law of motion ($F = ma$, where $\boldsymbol{F}$ is force, $\boldsymbol{m}$ is mass, and $\boldsymbol{a}$ is acceleration) for each atom or bead then allows for the calculation of trajectories in space and time (Allen, 2004).

There are a number of mathematical equations and associated constants used to describe the potential energy (whether inter- or intramolecular) between the molecules during the simulation, known as 'force fields'. The derivation of these functions is the result of both empirical and quantum mechanics calculations, and in the interest of

brevity these will not be discussed here. In its simplest terms, a force field (E_{total}) can be described as a combination of terms that relate to atoms that are either 'bonded' (linked by covalent bonds, E_{bonded}), or 'nonbonded' (van der Waals & electrostatic interactions, $E_{nonbonded}$). This relationship is represented in equation [3.1]**:**

$$E_{total} = E_{bonded} + E_{nonbonded} \quad [3.1]$$

Equation [3.2] shows the constituent terms that make up E_{bonded}, which are also diagrammatically represented in **Figure 3-8**:

$$E_{bonded} = E_{bond} + E_{angle} + E_{dihedral} \quad [3.2]$$

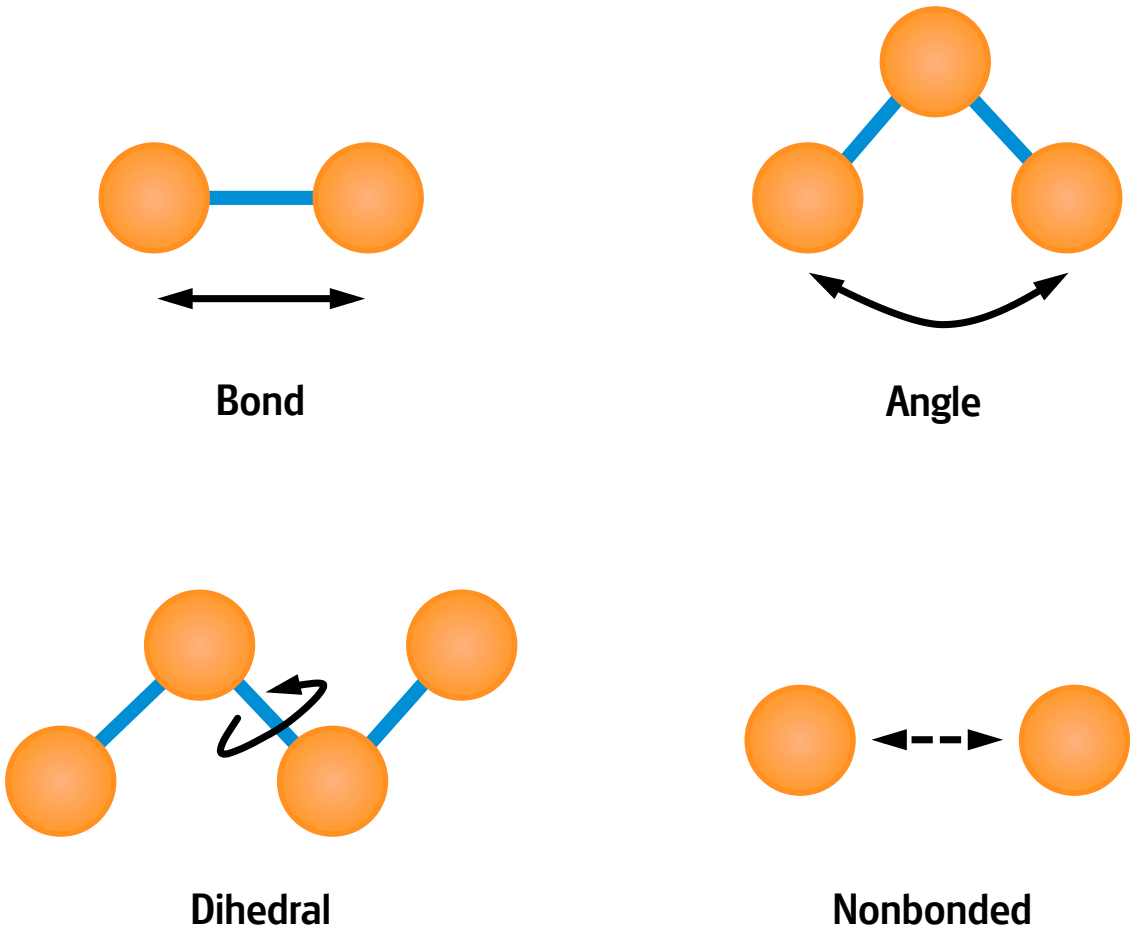

Figure 3-8: Molecular dynamics force field terms describing both intra- and intermolecular interactions.

The level of detail with which the systems can be modelled are limited to the computational power that one has at their disposal. Similarly, simulating processes that occur over long timescales can also be highly resource intensive. As such, detailed simulations where atoms are explicitly modelled typically operate over the femtosecond timescale. These simulations can be simplified and run over longer periods of time; for example by modelling hydrogen-containing groups as one "atom" (i.e. united atom model). Further simplification and thus longer timescales can be achieved by using so-called "coarse-grained" models (where the simplest representations are known as "bead-spring" models), where beads are used to represent groups of atoms and springs represent bonds between them. Coarse-graining is particularly useful for the study of reduced representations of polymeric compounds where each bead can represent several monomers.

3.3.1.1B Atomistic simulations

Atomistic molecular dynamics simulations were carried out in order to obtain a detailed description of a single micelle. These simulations utilised the aggregation number, N_{agg}, that was determined empirically for Pluronic® P85 (see ***section 3.3.1.3 - Determination of aggregation number (N_{agg})*** for method description) to define the number of Pluronic® P85 molecules to place into the simulation box.

In these simulations, each Pluronic® P85 molecule was given an interactive bead representing each individual atom in the molecule, and the interactions between the molecules modelled using the CHARMM force fields (Vorobyov *et al.*, 2007; Lee *et al.*, 2008). These simulations were carried out in a simulation box (to ensure a constant volume) such that the overall Pluronic® P85 concentration was 1.0% m/v. Simulations were first conducted with solvent implicitly modelled at 400 K (127 °C) to accelerate diffusion and allow the Pluronic® P85 molecules to self-assemble into an aggregate, before cooling the system down to 310 K (37 °C) to match body temperature. Once the structure of the aggregate had reached a constant size in the implicit solvent simulation, the simulation box was solvated with explicitly modelled water molecules to obtain a more detailed description of the interaction between the Pluronic® P85 and

water molecules. The system was then allowed to equilibrate using the Isothermal–isobaric NPT ensemble at a constant pressure of 1 atmosphere (atm) before taking aggregate size measurements.

3.3.1.1C Coarse-grain simulations

With the aim to model a solution containing Pluronic® P85 at concentrations representative of the experimental conditions, polymers are modelled by coarse-grained beads in an implicit solvent. Pluronic® are generally tri-block co-polymers with ABA arrangements, where two hydrophilic poly(ethylene oxide), A, blocks flank a hydrophobic poly(propylene oxide) block, B.

In this instance, the polymer studied (Pluronic® P85) has the following chemical structure:

$$HO(CH_2CH_2O)_{26}(CH_2CH(CH_3)O)_{40}(CH_2CH_2O)_{26}H$$

This can also be represented as:

$$A_{26}B_{40}A_{26}$$

In the coarse-grain strategy used here (Anderson & Travesset, 2006; Anderson *et al.*, 2008), one coarse-grain bead was modelled to represent ten monomers in the actual polymer, to achieve the following final bead representation:

$$A_3B_4A_3$$

This is shown more clearly in **Figure 3-9**:

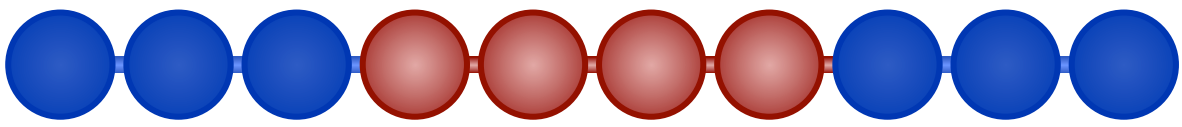

Figure 3-9: Flexible bead model of Pluronic® P85. Poly(ethylene) oxide A domains are represented as 3 repeats of 10 monomers (blue, 3 beads each), and poly(propylene) oxide B domain as 4 repeats of 10 monomers (red, 4 beads).

All non-bonded interactions between the coarse grain beads that make up the hydrophobic B block are modelled using the attractive Lennard-Jones potential (equation [3.3]), where σ and ε are the characteristic size and energy of a bead, respectively:

$$U_{BB}(r) = 4\varepsilon\left[\left(\frac{\sigma}{r}\right)^{12} - \left(\frac{\sigma}{r}\right)^{6}\right] \qquad [3.3]$$

The potential energy, $\boldsymbol{U_{BB}(r)}$, between any two beads, is a function of these two constants ($\boldsymbol{\varepsilon}$ and $\boldsymbol{\sigma}$) and the distance between the two beads, $\boldsymbol{r}$.

Meanwhile, a purely repulsive potential is used to model the nonbonded interactions between the hydrophilic coarse grain beads A and between coarse grain beads A and B:

$$U_{AABB}(r) = 4\varepsilon\left(\frac{\sigma}{r}\right)^{12} \qquad [3.4]$$

The pair potentials are cut off to zero at $\boldsymbol{r} = 3.0\boldsymbol{\sigma}$. In this study, we use the same values for the mass of the beads = 1.0, $\boldsymbol{\sigma} = 1.0$ and $\boldsymbol{\varepsilon} = 1.0$ for all coarse-grain beads in our system. Within a given Pluronic® molecule, the coarse-grain beads are connected to their neighbouring atoms via harmonic springs to represent their covalent bonds, such that the bond potential energy is given by the equation:

$$U_{bond} = k_{bond}\left(l - l_0\right)^2 \qquad [3.5]$$

For the purposes of these simulations, $\boldsymbol{k_{bond}} = 330.0$ and $\boldsymbol{l_0} = 0.84$.

The simulation boxes used here were cubic with periodic boundary conditions, and the volume of the box was held constant throughout the simulation. A timestep of $\Delta t = 0.005\left(\frac{m\sigma_2}{\varepsilon}\right)^{\frac{1}{2}}$ was used for all simulations. The simulations were conducted using the NVT canonical ensemble via Nose-Hoover dynamics (Hoover, 1985).

Simulations were carried out using seven different concentrations of Pluronic® P85, ranging from 0.03% m/v to 1.0% m/v. In doing so, the distribution of aggregate size was also measured in order to calculate the predicted CMC and N_{agg} of the resulting micelles.

3.3.1.2 Empirical measurement of critical micelle concentrations (CMC)

Two different experimental methods were used to determine the CMC of Pluronic® P85, and are outlined below. Both methods were based on a similar principle: the hydrophobic dye or fluorescent probe either change their absorption maximum wavelength (Eosin Y method), or their fluorescence emission intensity (Pyrene method) when incorporated into the hydrophobic microenvironments which are created when micelles start aggregating.

3.3.1.2A Eosin Y method to determine CMC

Experiments to measure the CMC of Pluronic® P85 using eosin Y dye (ACROS Organics; Geel, Belgium) were performed with Miss Ann-Charlott Berglar (MSc research project student, King's College London) according to a previously published method (Patist *et al.*, 2000).

Eosin Y is typically used as tissue stain, however in water it shows an absorbance maximum at 518 nm, which shifts to 542 nm upon the formation of micelles (**Figure 3-10**). As explained above, this is due to a change in the microenvironment of the dye from hydrophilic to hydrophobic, provided by the formation of a micellar core in which it preferentially partitions (**Figure 3-11**). This shift in absorbance is observed as a colour change in solution and can be measured quantitatively by spectrophotometry (Patist *et al.*, 2000).

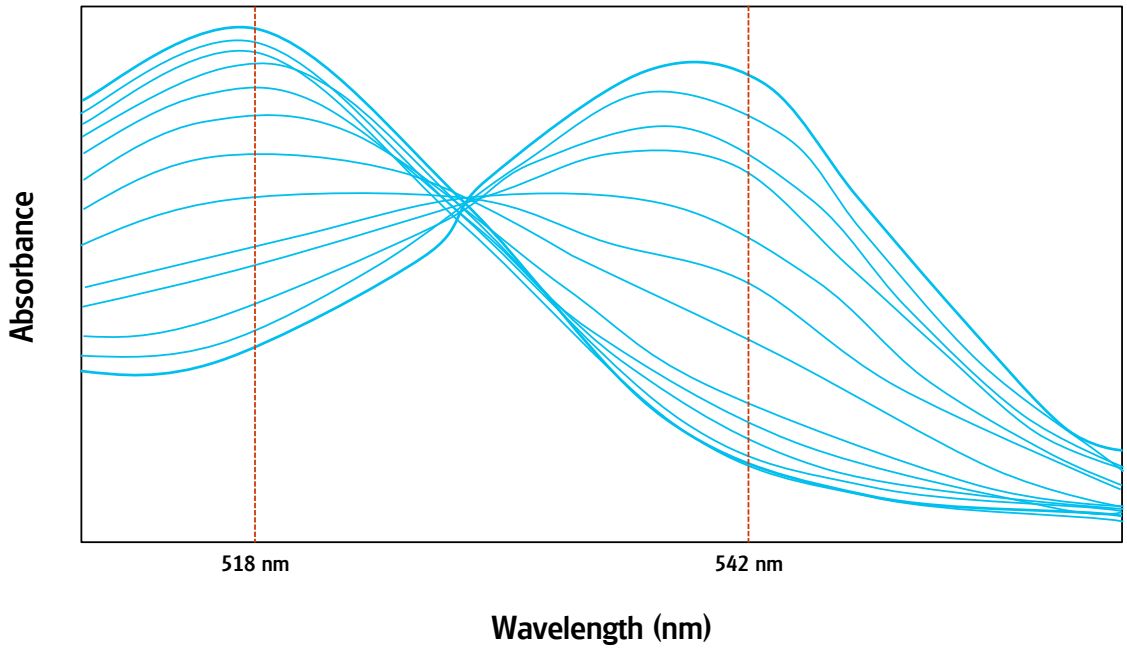

Figure 3-10: Absorbance spectrum of eosin Y in an aqueous solution (dH_2O) containing varying concentrations of Pluronic® P85. Micelle formation coincides with a shift of the wavelength maximum (λ_{max}) from 518 nm to 538 nm, however the greatest difference in the range of absorbance for given concentration range of Pluronic® P85 occurs at 542 nm. Adapted from (Patist *et al.*, 2000).

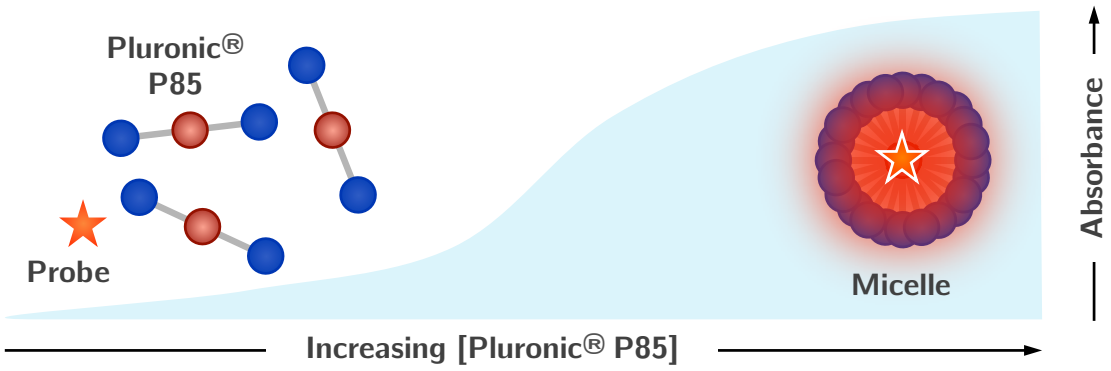

Figure 3-11: Eosin Y probe fluoresces at 542 nm when in the hydrophobic core environment of micelles.

Method optimisation

The method was first optimised in dH_2O with respect to the concentration range for Pluronic® P85 (kindly donated by BASF; NJ, USA), and temperature of sample measurements. These optimised parameters were then taken forward for determination of the CMC in Krebs-Henseleit mammalian Ringer solution (the composition of which is given in **Appendix 1**); henceforth referred to as 'artificial plasma'. Artificial plasma is the perfusate later used in the *in situ* brain perfusion technique (described in ***section 3.3.2 - Blood-CNS barrier models & accessory methodologies***), and thus it was used to better mimic micelle formation under the conditions used in the *in vivo* experiments.

However, it was observed that certain constituents of the artificial plasma in the assay were reacting with eosin Y to produce artefacts, where the same degree of colorimetric change was measured in all samples, regardless of Pluronic® P85 concentration. The precise cause of this was not determined, however it is known that eosin Y binds to albumin in solution, resulting in a change in eosin Y's fluorescence emission (Waheed *et al.*, 2000). BSA was therefore omitted from the artificial plasma for these CMC experiments, as was dextran (with which Eosin Y could also interact) and Evan's blue (a dye that would make measuring changes in fluorescence impossible). This modified form of artificial plasma will be henceforth referred to as 'optimised plasma'.

Validated method

Following optimisation of the method, the CMC of Pluronic® P85 was determined using eosin Y in the following solvents:

i) Distilled H_2O (dH_2O)

ii) Artificial plasma with dextran, BSA and Evan's Blue omitted; henceforth referred to as 'optimised plasma'.

iii) Optimised plasma with added 10 µM pentamidine (1,5-bis-4′-amidinophenoxypentane) isethionate salt (mol. wt., 592.68; 98% purity, Sigma Aldrich; Dorset, UK) to assess the effect of the drug on the CMC.

The effect of the following parameters on the CMC was investigated:

Table 3-2: Outline of factors investigated using eosin Y method for CMC determination of Pluronic® P85.

Solvent	Temperatures measured
dH_2O	25 °C; 37 °C
Optimised plasma	25 °C; 37 °C
Optimised plasma + 10 μM pentamidine isethionate	37 °C

Pluronic® P85 was dissolved in dH_2O or optimised plasma by mechanical stirring (or sonication, as shown in **Table 3-2**) at 37 °C until completely dissolved (typically a minimum of 20 minutes) to prepare a 10.0% m/v stock solution. From the stock solution, dilutions between 0% and 10.0% m/v were prepared in triplicate. The following concentrations of Pluronic® P85 solutions were prepared: 0, 0.001, 0.005, 0.01, 0.05, 0.1, 0.5, 1.0, 5.0, 10.0% m/v.

Two blank readings for each Pluronic® P85 concentration were taken in 1.5 mL disposable methacrylate UV cuvettes purchased from Fisher Scientific; Leicestershire, UK (containing 990 μL of Pluronic® P85 in dH2O or optimised artifical plasma) at 542 nm. 10 μL of 1.9 mM eosin Y aqueous solution were then added to each cuvette to achieve a final dye concentration of 19 μM. The cuvettes were mixed first by inverting them and then incubated with shaking on a platform shaker at 500rpm and 37 °C for 60 minutes. Absorbance readings at 542 nm were then taken at 20 °C or 37 °C using a Unicam UV1 spectrophotometer. Sample temperature was maintained using a Stuart S160D perspex fan incubator immediately prior to removing each cuvette individually to measure absorbance.

Absorbance at 542 nm (A_{542}) was plotted as a function of Pluronic® P85 concentration (log scale) and analysed using GraphPad Prism® 6 software. After plotting the data points, a trend line curve was fitted using the default curve-fit *log(agonist) vs. response*

– *variable slope* option in GraphPad Prism® 6. A table of XY coordinates of the fitted curve was then generated and a new graph drawn using the values from the linear part of the curve. The CMC was then derived by extrapolating from the linear part of the curve (the point at which it inflects), and determining the point at which this line intersects with the baseline (y = absorbance of the aqueous dye solution at 1.9 µM absent of Pluronic® P85). This is demonstrated more clearly in **Figure 3-12**.

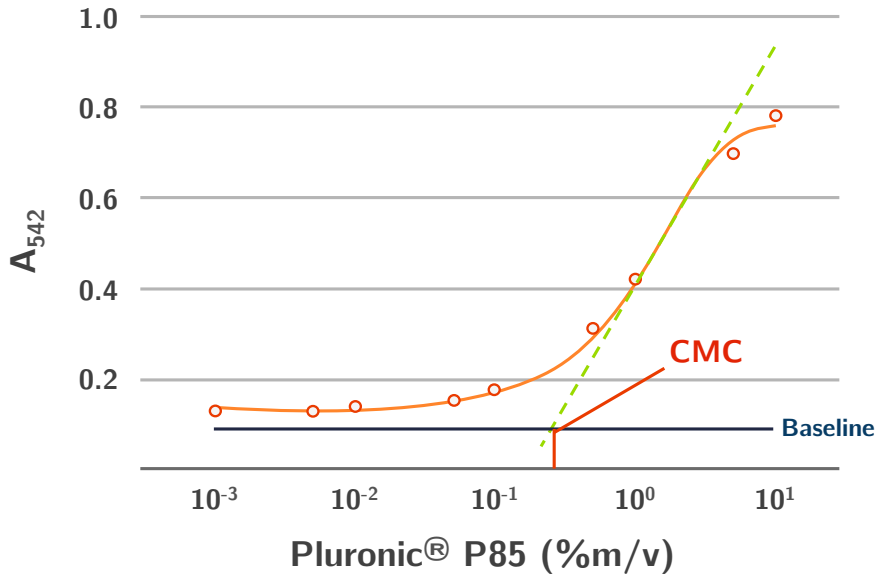

Figure 3-12: Example absorbance plot demonstrating the extrapolation of the linear portion of the curve through the inflection point. The x-intercept for the point at which the extrapolated line crosses the baseline absorbance is taken to be equal to the CMC.

3.3.1.2B Pyrene method to determine CMC

Experiments were designed in collaboration with Dr Cécile Dreiss (Institute of Pharmaceutical Science, King's College London) and Dr Margarita Valero (Department of Physical Chemistry, Universidad de Salamanca) following a previously outlined method (Wolszczak & Miller, 2002).

Pyrene (Sigma Aldrich; Dorset, UK) is a fluorophore that is sensitive to polar surroundings; its fluorescence intensity increases when it is incorporated into apolar environments (Wolszczak & Miller, 2002). This technique takes advantage of this phenomenon, using the change in fluorescence intensity as a surrogate measure for the formation of micelles once pyrene is incorporated into their hydrophobic cores.

To determine the CMC, a stock solution containing 500 nM pyrene (pyrene:dH_2O) was prepared by dissolving an appropriate volume of 10 mM pyrene in absolute ethanol into dH_2O. This stock solution was then split into two equal parts, and Pluronic® P85 added to one of the parts to achieve a final concentration of 1.0% m/v in pyrene:dH_2O. The resulting solutions of pyrene:dH_2O (with and without Pluronic® P85) were then mixed in varying mass ratios (using an OHAUS Adventurer SL microbalance for greater accuracy) to achieve the Pluronic® P85 concentrations shown in **Table 3-3**. Preparing the solutions in this way facilitates the variation in Pluronic® P85 concentrations while maintaining a constant concentration of pyrene at 500 nM in all solutions. This process was also repeated using optimised plasma in place of dH_2O to determine the CMC of Pluronic® P85 in optimised plasma.

Table 3-3: Experimental conditions and concentrations for reagents varied in the determination of CMC, partition coefficient (P) and aggregation number (N_{agg}) for Pluronic® P85.

PARAMETER INVESTIGATED	**REAGENT FOR WHICH CONCENTRATION WAS VARIED (% m/v)**
CMC	Pluronic® P85
Concentrations (% m/v)	0.00, 0.02, 0.03, 0.07, 0.10, 0.13, 0.17, 0.20, 0.23, 0.27, 0.30, 0.33, 0.37, 0.40, 0.43, 0.47, 0.60, 0.73, 0.87
Aggregation number (N_{agg})	Cetylpyridinium chloride monohydrate (Q)
Concentrations (mM)	0.000, 0.054, 0.108, 0.162, 0.216, 0.270
Partition coefficient (P)	Pluronic® P85
Concentrations (% m/v)	0.00, 0.17, 0.30, 0.43, 0.57, 0.77, 0.87

Emission spectra were obtained for each concentration of Pluronic® P85 outlined in **Table 3-3** by pipetting 1 mL of each into a Fluorescence QS 10 mm cuvette made from Suprasil© quartz (Hellma, Type 114F-QS). The cuvette was cleaned twice using dH_2O, then with absolute ethanol, and then dried between each sample. The cuvette was placed in a Varian Cary Eclipse spectrophotometer with single water thermo cell holder and temperature controller, using Cary Eclipse software. The emission spectra were obtained between 350 nm and 450 nm after excitation at 340 nm. Measurements were therefore taken using the settings: λ_{ex} = 340 nm, λ_{em} = 350-450 nm, slit = 5 nm and lamp intensity of 700 V (selected to provide optimum intensity over the broad concentration of Pluronic® P85 used). Experiments were carried out both at 20 °C and at 37 °C for Pluronic® P85 dissolved in both pyrene:dH_2O and pyrene:optimised plasma.

The resulting emission spectra typically had two peaks of maximum fluorescence intensity at approximately 374 nm and 393 nm, an example of which is shown in **Figure 3-13A**. Spectra were analysed by plotting the maximum fluorescence intensities as a function of Pluronic® P85 concentration. Two straight trend lines were then fitted through the resulting data points, and the point at which these lines intersect calculated. The abscissa (*x*-intersect) for this point is the CMC, as shown in **Figure 3-13B**.

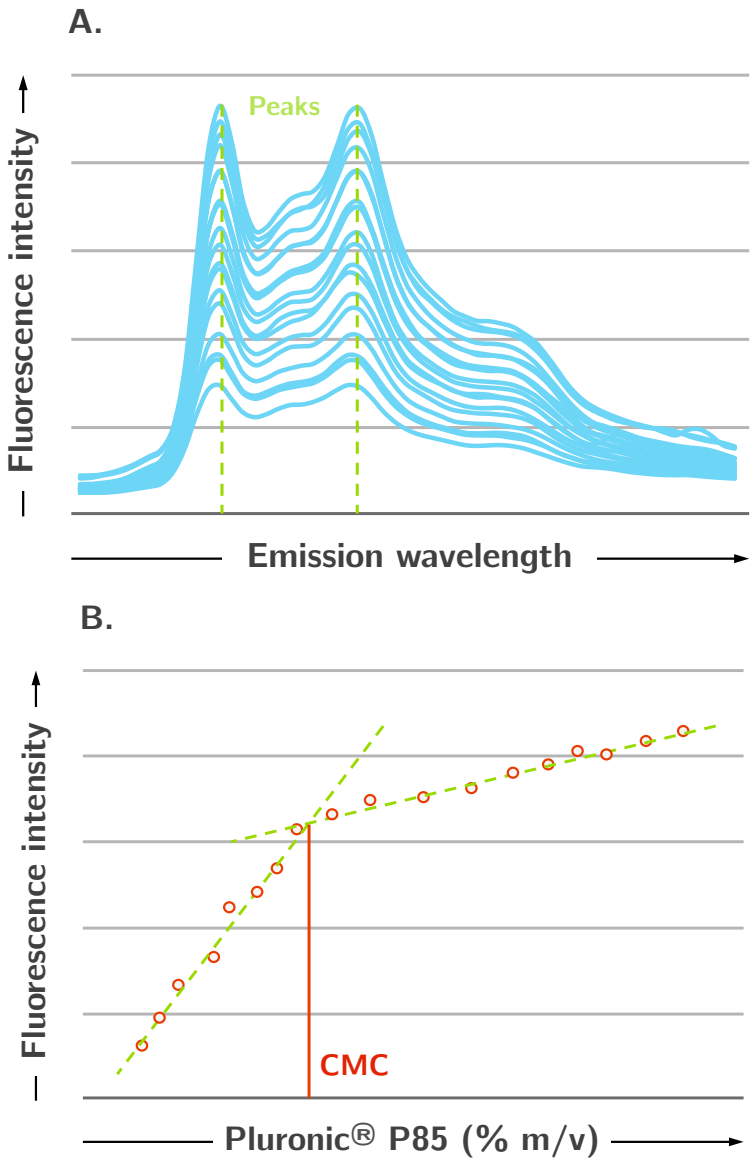

Figure 3-13: Pyrene fluorescence measurement for the determination of the Critical Micelle Concentration (CMC). A: Example of pyrene emission spectra between 350-450 nm for a range of Pluronic® P85 concentrations. Fluorescence intensity increases with increasing concentration of Pluronic® P85. **B:** Example of data analysis for the fluorescence intensity measurements taken at the peak of the emission spectra. Two straight lines are fitted through the data points on both sides of the break-point, and the intersect calculated algebraically. The abscissa (*x*-coordinate) of this intersect is defined as the CMC.

3.3.1.3 Determination of aggregation number (N_{agg})

The fluorometric determination of N_{agg} was performed following a previously published method (Junquera *et al.*, 1997). This technique utilises the fluorescent properties of pyrene (also described in the fluorometric determination of CMC using pyrene in ***section 3.3.1.2B - Pyrene method to determine CMC***). The steady-state fluorescence of pyrene within the micelles can be quenched with cetylpyridinium chloride monohydrate (Q, purchased from Sigma Aldrich; Dorset, UK), and utilised to calculate the mean number of unimers present per micelle at or above the CMC (Junquera *et al.*, 1997).

Solutions of pyrene:dH_2O was prepared as described in ***section 3.3.1.2B - Pyrene method to determine CMC.*** This solution formed the basis for the calculation of N_{agg} for Pluronic® P85 in either dH_2O or optimised plasma and was utilised to create a further stock solution including both 1.0% m/v Pluronic® P85 and 270 µM Q. This solution was then mixed with pyrene:dH_2O or optimised plasma containing 1.0% m/v Pluronic® P85 alone to create the working solutions containing varying quantities of Q, as outlined in **Table 3-3**, while keeping the concentration of pyrene and Pluronic® P85 constant.

The fluorescence intensity of all pyrene:dH_2O and pyrene:optimised plasma was then measured using the same equipment and following the same method described in ***section 3.3.1.2B - Pyrene method to determine CMC***. The natural logarithm value of the fluorescence intensity was then plotted as a function of [Q], as shown in **Figure 3-14**. A linear trend line, $y = mx + c$, was then fitted to the data, corresponding to:

$$\ln(F) = \frac{-N_{agg}}{[P85]_t - CMC} \times Q + \ln(F_0) \qquad [3.6]$$

Thus, from the slope 'm' term of the trend line defined, N_{agg} was derived as follows:

$$m = \frac{-N_{agg}}{[P85]_t - CMC}$$

$$\therefore N_{agg} = -m \times ([P85]_t - CMC) \qquad [3.7]$$

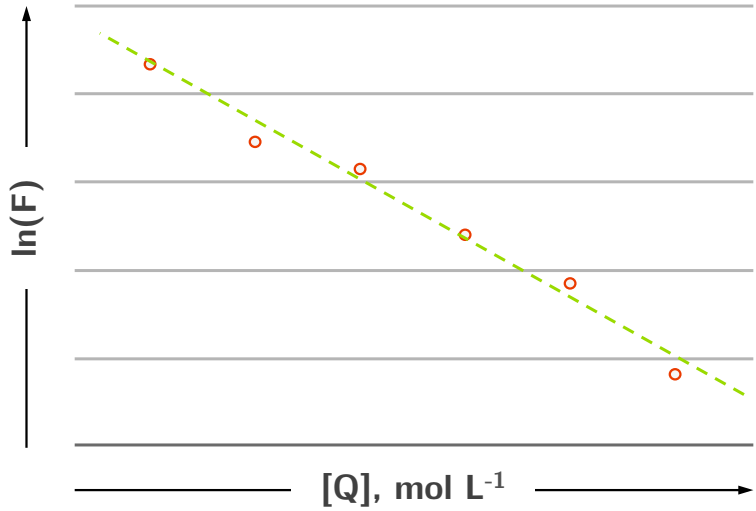

Figure 3-14: Example plot showing the natural log of the fluorescence intensity as a function of the concentration of the quencher cetylpyridinium chloride monohydrate (Q). The resulting linear trendline from these plots was used in the calculation of N_{agg}.

3.3.1.4 Determination of partition coefficient (*P*)

Measurement of the partition of pentamidine within Pluronic® P85 micelles requires the knowledge of the density and partial molar volume of Pluronic® P85 in solution. A description of the experimental steps taken to measure the partition coefficient is given below.

3.3.1.4A Measurement of Pluronic® P85 density and partial molar volume using Pycnometry

Pycnometry is a technique used to determine the density of liquids or gases as a ratio of mass to volume. By accurately measuring the mass of a known volume of a liquid, one can calculate the density of the liquid, with reference to dH_2O.

In order to measure the density of 1.0% m/v Pluronic® $P85_{(aq)}$, a glass pycnometer with an approximate volume of 10 mL was used, and the experiment carried out in its entirety at a room temperature of 22.3 °C. The glass pycnometer has a glass stopper with a glass capillary tube running through it, to allow air bubbles to escape from the flask. The flask (with stopper) was cleaned and then dried thoroughly before accurately weighing (m_{dry}). The pycnometer was then filled completely with dH_2O, and then very slowly sealed with the glass stopper. In doing so, excess dH_2O was slowly displaced (due to Archimedes Principle) by the glass stopper, and allowed to escape *via* the capillary tube in the stopper, ensuring constant volume in the pycnometer. The pycnometer was then weighed again (m_{wet}) and the exact volume of dH_2O in the pycnometer (V_{pyc}) calculated using the following equation:

$$V_{pyc} = \rho_{rt}\left(m_{wet} - m_{dry}\right) \qquad [3.8]$$

Where ρ_{rt} is the density of dH_2O at 22.3 °C = 0.997704.

This process was performed three times to obtain a mean volume for the pycnometer at room temperature.

The pycnometer was then cleaned and dried thoroughly before filling with 1.0% m/v Pluronic® $P85_{(aq)}$, and the process described above repeated again in triplicate before calculating the density of 1.0% m/v Pluronic® $P85_{(aq)}$ as follows:

$$\rho_{P85:dH_2O} = \frac{\text{mass of P85}_{(aq)}}{V_{pyc}} \quad [3.9]$$

Thus, the density of 1.0% m/v Pluronic® P85 alone (ρ_{P85}) was calculated as follows:

$$\rho_{P85} = \frac{(\text{mass of P85}_{(aq)} \times C)}{V_{pyc}} \quad [3.10]$$

Where C is the m/v concentration of P85, in this case 0.01 (1.0%).

Finally, the partial molar volume of P85 (the volume which 1 mol of P85 occupies in dH_2O, $\overline{V}_{P85}$) was calculated as follows:

$$\overline{V}_{P85} = \frac{\left(1 \div \rho_{P85:dH_2O}\right)}{\left(\text{mass of P85}_{(aq)} \times \text{M}_\text{w}\text{ of P85}\right)} = \frac{\text{M}_\text{w}\text{ of P85}}{\rho_{P85}} \quad [3.11]$$

Where M_w *is the molecular weight of P85 = 4600*

3.3.1.4B Measurement of partition coefficient (P)

Fluorometric determination of the partition coefficient of pentamidine isethionate (Sigma Aldrich; Dorset, UK) in Pluronic® P85 micelles followed a previously published method (de La Guardia *et al.*, 1991). This technique makes use of the natural fluorescence of pentamidine, which varies in intensity when incorporated into the less polar environment of Pluronic® P85 micelles. A stock solution of 10 µM pentamidine isethionate was prepared in dH_2O. Working dilutions of Pluronic® P85 shown in **Table 3-3** were then prepared, before measuring the fluorescence intensity in samples using the same equipment and following the same method for measuring the fluorescence

intensity as outlined in ***section 3.3.1.2B - Pyrene method to determine CMC***. Measurements were taken using the settings: λ_{ex} = 260 nm, λ_{em} = 300-450 nm, slit = 5 nm and lamp intensity of 800 V. Experiments were carried out at 20 °C for Pluronic® P85 dissolved in pentamidine:dH_2O and then repeated at 20 °C and 37 °C in pentamidine:optimised plasma.

When calculating the interactions of drugs with micelles, two methods are typically cited in the literature (Rangel-Yagui *et al.*, 2005b):

i. **Partition coefficient** (P) – The partition of drug between aqueous media and micellar phases.
ii. **Drug binding** (K) – The binding of drug to micelles.

For the purposes of these experiments, the true partition of drug within the micelles was deemed more relevant than the binding of the drug to micelles. Therefore the parameter selected for measurements was the **partition coefficient** (P), defined in equation [3.12] below:

$$P = \frac{[drug]_{micelle}}{[drug]_{H_2O}} \qquad [3.12]$$

Where $[drug]_{micelle}$ is referred to the micellar volume ($V_{micellar}$), and $[drug]_{H_2O}$ is referred to the overall solution volume (V_{total}), provided that the surfactant concentration (and thus the micellar volume) is very low relative to the aqueous volume ($V_{micellar} << V_{H_2O}$). This is because the overall solution volume is comprised of the micellar volume and volume of water, and in dilute surfactant solutions the overall micellar volume is negligible. In concentrated surfactant solutions where $V_{micellar}$ is high, $[drug]_{H_2O}$ should be referred to the aqueous volume ($V_{H_2O} = V_{total} - V_{micellar}$). The equation to define $V_{micellar}$ is as follows (Santos *et al.*, 2003):

$$V_{micellar} = C_s \times V_{solution} \times \gamma \qquad [3.13]$$

Where C_s is the total moles of surfactant and γ is the molar volume of Pluronic® P85 calculated from ***equation [3.11]****, also known as* $\overline{V}_{P85}$.

Determining the concentrations of the drug in each of the media by fluorescence spectroscopy requires the definition of a new parameter, α (Coutinho & Prieto, 1995):

$$\alpha = \frac{[drug]_{micelle}}{[drug]_{total}} = \frac{I - I_0}{I_\infty - I_0} \qquad [3.14]$$

Where a is detected changes in fluorescence intensity, I is the fluorescence intensity of the drug in the presence of micelles, I_0 is the fluorescence intensity of the drug in the absence of micelles, and I_∞ is the maximum possible fluorescence intensity of the drug when it is 100% solubilised. The derivation of this equation can be found in ***Appendix 2.***

Since complete solubilisation of pentamidine within the micelles cannot be achieved experimentally, fluorescence intensity at this point ($\boldsymbol{I_0}$) can also not be measured empirically. Therefore, an alternative equation was used to calculate the partition coefficient (Coutinho & Prieto, 1995):

$$\Delta I = \frac{\Delta \mathrm{I}_{\max}[P85]}{1/(P\gamma) + [P85]} \qquad [3.15]$$

Where ΔI is the change in fluorescence intensity in the absence and presence of Pluronic® P85, and $\Delta \mathrm{I}_{\max}$ the maximum possible measurable difference in fluorescence intensity. P is the partition coefficient of pentamidine between aqueous and micelle phases, and γ the molar volume of Pluronic® P85 (calculated by pycnometry, as described in ***section 3.3.1.4A - Measurement of Pluronic® P85 density and partial molar volume using Pycnometry****).*

Substituting in terms from equation [3.14] gives:

$$(I - I_0) = \frac{(I_\infty - I_0)[P85]}{1/(P\gamma) + [P85]} \quad [3.16]$$

Equation [3.16] can then be re-arranged to give:

$$\frac{1}{(P\gamma)} + [P85] = \frac{(I_\infty - I_0)[P85]}{(I - I_0)} \quad [3.17]$$

And rearranged further still:

$$\frac{1}{(P\gamma)} + \frac{1}{[P85]} + 1 = \frac{(I_\infty - I_0)}{(I - I_0)} \quad [3.18]$$

$$\frac{1}{(P\gamma)} + \frac{1}{[P85]} + 1 = \frac{(I_\infty - I_0)}{(I - I_0)} \times \frac{I_0}{I_0} \quad [3.19]$$

$$\frac{1}{(P\gamma)} \times \frac{1}{[P85]} + 1 = \left(\frac{(I_\infty - I_0)}{I_0} \right) \times \left(\frac{I_0}{(I - I_0)} \right) \quad [3.20]$$

$$\frac{I_0}{(I - I_0)} = \frac{I_0}{(I_\infty - I_0)} \times \left(\frac{1}{(P\gamma)} \times \frac{1}{[P85]} + 1 \right) \quad [3.21]$$

At this point, we have a linear equation in the format $y = c \times (mx + 1)$, where $y = \frac{I_0}{(I - I_0)}$ and $x = \frac{1}{[P85]}$ (with [P85] being the micellised surfactant). Thus, by dividing the y-intercept, c, by the slope of the line, m, one obtains $P\gamma$. Since γ is the partial molar volume calculated from pycnometry experiments, one can divide $P\gamma$ by the partial molar volume of Pluronic® P85 to obtain the partition coefficient, P.

3.3.1.5 Determination of micelle hydrodynamic diameter

A Nano ZS Zetasizer (Malvern Instruments Ltd., Malvern, Worcestershire, UK) and workspace were kindly provided by Dr Marie-Christine Jones (King's College London, Institute of Pharmaceutical Science, University of London) to measure the mean hydrodynamic diameter of Pluronic® P85 micelles. Samples were prepared in disposable 1 mL UV cuvettes in either dH_2O or optimised plasma, and the mean hydrodynamic diameter and polydispersity analysed by the zetasizer using dynamic light scattering. The zetasizer was calibrated prior to measuring the samples by defining the solvent used in the sample (*i.e.* explicitly defining contents and concentrations of salts in optimised plasma). All sample measurements were taken at 37 °C.

3.3.2 Blood-CNS barrier models & accessory methodologies

Since many of the experimental procedures utilised in the generation of data for this chapter followed the same format as those described in ***section 2.3.1 - Blood-CNS barrier model & accessory methodologies***, the reader is referred to ***chapter 2*** for information on the following:

i. Animals & anaesthesia

ii. In situ brain/choroid plexus perfusion

- **a.** Surgical preparation
- **b.** Experimental procedure
- **c.** Perfusion circuit
- **d.** Composition of artificial plasma
- **e.** CNS sampling
- **f.** Capillary depletion analysis
- **g.** Liquid scintillation analysis

In the interests of brevity, the sections that follow will only include those where there were differences in the experimental procedures performed.

3.3.2.1A Radiolabelled solutes of interest

Pentamidine

As described in ***section 3.1.1 - Human African Trypanosomiasis (HAT)***, the stage 1 drug, pentamidine, is known to treat the blood- and transition-stage of HAT, but cannot treat the CNS stage of the disease, as it does not sufficiently penetrate the blood-CNS barriers (Sanderson *et al.*, 2009). As the model drug selected to take forward in the development of a co-formulation with Pluronic® P85, [^{3}H]-pentamidine (mol. wt., 340.4 g/mol; specific activity, 5 Ci/mmol; 99% radiochemical purity) was synthesised and tritiated by Moravek Biochemicals, Brea, CA.

The inclusion of [^{3}H]-pentamidine as a radiolabelled solute of interest in the artificial plasma thus facilitated the measurement of its penetration into the CNS after perfusion.

Sucrose (baseline)

In addition to [^{3}H]-pentamidine, [^{14}C]-sucrose (mol. wt., 342.3 g/mol; specific activity, 0.412 Ci/mmol; 99% radiochemical purity; Moravek Biochemicals, Brea, CA), was also present in the artificial plasma for these experiments. The molecular weight of [^{14}C]-sucrose is comparable to that of [^{3}H]-pentamidine (340.4 g/mol), and so the inclusion of [^{14}C]-sucrose provides a useful comparison of variation between animals and indicator of BBB permeability, as it is a known compound that has poor penetration through the blood-CNS barriers. Thus, by correcting brain uptake for vascular space one also accounts for transport due to passive paracellular diffusion.

The use of [^{14}C]-sucrose as a vascular space marker was described in ***chapter 2***, and the reader is referred to ***section 2.3.1 - Blood-CNS barrier model & accessory methodologies*** should further explanation be required.

3.3.2.1B Perfusion time

The *in situ* brain/choroid plexus perfusion technique has been validated for perfusions up to 30 minutes (Sanderson *et al.*, 2007). Perfusions for these experiments were performed for either 10 or 30 minutes, as shown in **Table 3-4**.

3.3.2.1C Co-formulated drug transport experiments

As described in ***section 2.3.1.2 - In situ brain/choroid plexus perfusion***, one of the main advantages of *in situ* brain perfusion is the control the investigator has over the contents of the artificial plasma (perfusate). In addition to the radiolabelled solute of interest, the artificial plasma contents can be adjusted to also include the solute of interest in non-radiolabelled form, potential competitors of transport, and specific inhibitors of transport. Furthermore, experimental design can be altered to vary the time of perfusion and thus obtain snapshots of uptake into the brain with respect to time.

To examine the effect of co-formulating pentamidine with Pluronic® P85 on the uptake of pentamidine into the CNS, varying concentrations of Pluronic® P85 were added to

the artificial plasma, and their effects on the CNS uptake of [^{3}H]-pentamidine measured.

The CMC for Pluronic® P85 was previously found to be 0.03% m/v (Shaik *et al.*, 2009) using the fluorescence probe 1, 6- diphenyl-1, 3, 5-hexatriene (DPH, Sigma Aldrich; Dorset, UK), and a different method to those used in this study and described in ***section 3.3.1.2 - Empirical measurement of critical micelle concentrations (CMC)***. Thus our initial *in situ* brain/choroid plexus perfusion experiments with Pluronic® P85 were designed based on a CMC of 0.03% m/v. However, further evaluation by us revealed that the CMC was ten-fold higher (approximately 0.3% m/v) in our hands, both theoretically and empirically (described later in ***section 3.4.2.1 - Critical micelle concentration***). As such, and with an aim to measure [^{3}H]-pentamidine uptake into the CNS in the presence of Pluronic® P85 both below and above the CMC (*i.e.* in the absence and presence of micelles), co-formulations contained either 0.01% or 0.1% Pluronic® P85, respectively.

Un-labelled pentamidine isethionate was also included in some experiments at a concentration of 10 µM to mimic the plasma concentrations usually achieved in human patients following treatment (Waalkes & DeVita, 1970; Sanderson *et al.*, 2009). The poor water solubility of pentamidine required that it be dissolved in dimethyl sulfoxide (DMSO, Sigma Aldrich; Dorset, UK), so that the final DMSO concentration in the artificial plasma was 0.05% m/v. The inclusion of DMSO at this concentration has previously been shown not to affect blood-brain and blood-CSF barrier permeability (Sanderson *et al.*, 2009). Perfusions were initially performed for 10 minutes, and then repeated with a perfusion time of 30 minutes. Since the rationale for co-formulating with Pluronic® P85 was to reduce efflux of pentamidine from the CNS by inhibiting efflux transporters, it was hypothesised that increasing the perfusion time to 30 minutes would provide adequate time for any effects on efflux transport mechanisms to manifest.

A breakdown of the experimental conditions used for co-formulated drug transport experiments are shown in **Table 3-4**. After perfusion, the CNS was sampled and prepared for liquid scintillation counting as described earlier.

Table 3-4: Summary of experimental conditions for experiments to determine [^{3}H]-pentamidine uptake into the CNS as measured by *in situ* brain perfusion.

Additions to artificial plasma (and concentration)	**Perfusion duration (minutes)**
DMSO (0.05% m/v)	10
DMSO (0.05% m/v), un-labelled pentamidine (10 μM)	10
DMSO (0.05% m/v), un-labelled pentamidine (10 μM), Pluronic® P85 (0.01% m/v)	10
DMSO (0.05% m/v), un-labelled pentamidine (10 μM), Pluronic® P85 (0.1% m/v)	10
DMSO (0.05% m/v), Pluronic® P85 (0.01% m/v)	10
DMSO (0.05% m/v), Pluronic® P85 (0.1% m/v)	10
DMSO (0.05% m/v)	30
DMSO (0.05% m/v), Pluronic® P85 (0.01% m/v)	30
DMSO (0.05% m/v), Pluronic® P85 (0.1% m/v)	30

3.3.2.2 Isolated incubated choroid plexus technique

The isolated incubated choroid plexus technique provides a means of measuring the movement of radiolabelled solutes of interest into the choroid plexus. The technique involves the removal of the fourth ventricle of the choroid plexus from the mouse brain, which is then transferred into artificial CSF containing the radiolabelled solute of interest - allowing the study of transport *ex vivo*.

3.3.2.2A Experimental procedure

Adult male BALB/c mice (23-25 g, Harlan; Oxon, UK) were anaesthetised and heparininsed perfused transcardially as described previously (***section 2.3.1.2 - In situ brain/choroid plexus perfusion***) for 4 minutes, with artificial plasma, but not containing any radiolabelled compounds. After 4 minutes mice were decapitated, and the IVth ventricle of the choroid plexus removed from under the cerebellum using micro-forceps and Leica S4E L2 stereo-microscope. The choroid plexus was then immediately transferred to 0.65 mL warm oxygenated artificial CSF solution (contents outlined in ***Appendix 1***) and incubated at 37°C for 10 minutes in order to equilibrate ionic concentrations (equilibration incubation step). After 10 minutes the choroid plexus was removed and placed into a second 0.65 mL artificial CSF solution which also contained [^{3}H]-pentamidine and [^{14}C]-sucrose, and any other compound of interest (*e.g.* specific inhibitors of transport, or competitors for transport, solute incubation step, **Table 3-5** and **Table 3-6**). The second artificial CSF solution was also oxygenated and the choroid plexus incubated at 37 °C for 10 minutes, before removing the choroid plexus, blotting to remove excess liquid, and weighing on a microbalance (Cahn C33). As a point of reference, 50 µL samples were taken in triplicate from the final incubation medium (containing [^{3}H]-pentamidine and [^{14}C]-sucrose) both before incubation and after incubation, and these values used to calculate accumulation of [^{3}H]-pentamidine in the choroid plexus, as described below in ***section 2.3.1.2I - Expression of results***.

It should be noted that all experiments were carried out by MF with the assistance of Ms Juanita Ravindran as part of summer lab project. $N = 5$ for all treatment groups.

3.3.2.2B Expression of results

Uptake in the incubated choroid plexus was calculated as the accumulation of radiolabelled solute of interest, corrected for extracellular space (marked by [^{14}C]-sucrose) and expressed as a tissue-to-incubation medium (artificial CSF) ratio:

$$\text{Accumulation (mL/g)} = \frac{\text{radioactivity (dpm) per g of choroid plexus tissue}}{\text{radioactivity (dpm) per mL of incubation medium}} \quad [3.22]$$

3.3.2.2C Experimental design

Following a similar format to that described in ***section 2.3.1.2 - In situ brain/choroid plexus perfusion***, the isolated incubated choroid plexus technique was used to measure:

i. The effect on the movement of [^{3}H]-pentamidine between the artificial CSF and choroid plexus when co-formulated with Pluronic® P85

ii. The effect on the movement of [^{3}H]-pentamidine between the artificial CSF and choroid plexus in combination with specific transport inhibitors.

The details of these experiments are outlined below.

Co-formulated drug transport experiments

In order to measure the effect of Pluronic® P85 on the movement of pentamidine between the CSF and choroid plexus, [^{3}H]-pentamidine (0.31 µM), [^{14}C]-sucrose (0.93 µM) and DMSO (0.05% m/v) were added to the artificial CSF before incubation. In addition, varying concentrations of Pluronic® P85 (0.01%, 0.1% or 0.5% m/v) were added to measure their effect on the movement of [^{3}H]-pentamidine between the CSF and choroid plexus. An outline of the experimental plan for these experiments is shown in **Table 3-5**. After incubation for 10 minutes, samples were prepared and analysed by

liquid scintillation counting as described in ***section 2.3.1.2H - Liquid scintillation analysis***.

Table 3-5: Summary of experimental conditions for experiments to explore [^{3}H]-pentamidine accumulation in isolated incubated choroid plexus.

Added compound and concentration
DMSO (0.05%)
DMSO (0.05%), Pluronic® P85 (0.01% m/v)
DMSO (0.05%), Pluronic® P85 (0.1% m/v)
DMSO (0.05%), Pluronic® P85 (0.5% m/v)

Transport inhibitor experiments

With an aim to identify the transport system responsible for transporting pentamidine at the apical surface of the choroid plexus, specific transport inhibitors were added to the artificial CSF used in the second incubation (solute incubation step). It should however be noted that transport at the basolateral (blood-facing) membrane cannot be ruled out using this method. It is expected that any transport detected using this method is dominated by apical transport, as the surface area of the apical membrane is far greater than the surface area of the basolateral membrane. The inclusion of transport inhibitors can correlate with either an increase or decrease in the uptake of the radiolabelled solute of interest; which is respectively indicative of an efflux or influx transport system at the choroid plexus.

All transport inhibitors used were readily soluble in the artificial plasma and required no extra steps for dissolution beyond standard mechanical stirring and heating to physiological temperature (37 °C). A breakdown of the experimental conditions used for transport inhibitor experiments are shown in **Table 3-6**. After incubation, samples were prepared and analysed by liquid scintillation counting as described above.

Table 3-6: Summary of transport inhibitor experiments for [^{3}H]-pentamidine uptake between the CSF and choroid plexus as measured by the isolated incubated choroid plexus technique.

[^{3}H]-Pentamidine

Inhibitor and molar concentration	**Transporters inhibited**	**Ref**
4-aminohippuric acid (para-aminohippuric acid, PAH, 500 µM)	Oat1, Oat2, Oat3	(Sekine *et al.*, 1998; Sugiyama *et al.*, 2001; Nagata *et al.*, 2002)
Taurocholic acid (TCA, 200 µM)	Oatp1, Oatp2, Oatp3, OATPA	(Kullak-Ublick *et al.*, 1995; Abe *et al.*, 1998; Sugiyama *et al.*, 2001; Sugiyama *et al.*, 2002)
MK-571 (35 µM)	All MRPs	(Honda *et al.*, 2004; Poller *et al.*, 2008)

3.3.2.3 High Performance Liquid Chromatography (HPLC) and radiodetector analysis

HPLC analysis was performed as a means of confirming that the [^{3}H]-pentamidine used in *in vivo* experiments was intact and radiolabelled. The experimental setup for HPLC analysis was a Jasco HPLC system (HG-1580 high pressure, high performance gradient HPLC solvent delivery system, AS-1555-10 cooled autosampler, and UV-1575 UV/Vis detector, Jasco; Essex, UK), together with a Packard Radiodetector (Radiomatic 525TR Analyser, Packard; Pangbourne, UK).

The integrity of [^{3}H]-pentamidine stock isotope was confirmed by HPLC analysis to ensure no degradation had occurred over time. Samples containing either unlabelled pentamidine or [^{3}H]-pentamidine were injected onto a Zorbax RX-C8, 5 μm, 4.6 × 250-mm column following a previously published protocol (Berger *et al.*, 1991). Separation was carried out by gradient elution on the Jasco HPLC system described above. Samples were eluted using a gradient of 3.5 to 45% acetonitrile (Fisher Scientific; Leicestershire, UK) in water (1 mL/min flow rate) over a period of 30 minutes. Conditions were returned to 3.5% acetonitrile over 2 min and held to allow the column to equilibrate for 3 min (35-min total time) before running the next sample. The gradient was achieved by mixing solvents A (H_2O) and B (50% acetonitrile), both of which contained 10 mM heptane sulfonate (Fisher Scientific; Leicestershire, UK), 10 mM tetramethylammonium chloride (Sigma Aldrich; Dorset, UK), and 4.2 mM phosphoric acid (Sigma Aldrich; Dorset, UK). UV absorbance was measured at 265 nm, before passing the column eluant into a radioactive detector (Packard; Pangbourne, UK), where it was mixed 1:3 with scintillation fluid (Ultima-Flow® M, Perkin-Elmer; Boston, MA, USA) for real-time radioactive analysis. This was then repeated using 10 μM pentamidine isethionate (un-labelled, Sigma Aldrich; Dorset, UK) as a reference.

3.3.3 Peripheral free fraction / pancreatic toxicity experiments

It has been observed that up to 10% of patients receiving pentamidine treatment go on to develop hyperglycaemia and diabetes (Jha & Sharma, 1984; Thakur *et al.*, 1991). A number of possible explanations for this have been proposed:

i. Hyperglycaemia could be caused by the activation of hepatic glucose-6-phosphatase in response to pentamidine treatment (Scott & Burchell, 1991).

ii. Hyperinsulinaemia could result from irreversible damage to islet β-cells at sub-stimulatory glucose concentrations, and impaired glucose-induced insulin release (Sai *et al.*, 1983; Zhou & Ipp, 1989).

With these considerations in mind, it was hypothesised that co-formulating pentamidine within Pluronic® P85 micelles could compartmentalise and shield islet β-cells from the damaging effects of pentamidine in circulation following administration. *In vitro* experiments were designed to test this hypothesis in islet cell culture, and are described below. Experiments were performed with the assistance of Dr Bo Liu (Endocrinology and Reproduction Research Group, King's College London).

3.3.3.1 Cell culture conditions

Mouse insulinoma (MIN6) β-cells (kindly provided by Professor SJ Persaud, Endocrinology and Reproduction Research Group, King's College London) were maintained at 37 °C (95% O_2/5% CO_2) in Dulbecco's Modified Eagle's Medium (DMEM, Sigma Aldrich; Dorset, UK) supplemented with 15% v/v foetal calf serum, 2 mM glutamine, 100 U/mL penicillin and 0.1 mg/mL streptomycin (Gibco; Paisley, UK). Medium was changed every 3-4 days and cells were detached from the cell culture wells using 0.02% m/v EDTA when 80-90% confluence had been attained.

MIN6 cells were then seeded into 96-well plates at a density of 30 000 cells/well and cultured overnight in DMEM at 37 °C to adhere. DMEM was then aspirated from each well and washed twice with DMEM containing glucose at 2 mM. DMEM containing 2

mM glucose (Sigma Aldrich; Dorset, UK) was then added to each well a third time, but also to include either 10 µM pentamidine isethionate, or 1.0% m/v Pluronic® P85, or both pentamidine isethionate and Pluronic® P85 together, as outlined in the plate plan in **Table 3-7**. The poor solubility of pentamidine in water required that it be first dissolved in DMSO, resulting in a final DMSO concentration of 0.05% v/v. DMSO was also added to all other culture media used for incubation at the same concentration of 0.05% v/v.

Table 3-7: Plate plan for measuring insulin secretion from MIN6 cells after pre-exposure to pentamidine and Pluronic® P85.

1	2	3	4	5	6	7	8	9	10	11	12
2 mM glucose	2 mM glucose	2 mM glucose	2 mM glucose + 10 µM pentamidine	2 mM glucose + 10 µM pentamidine	2 mM glucose + 10 µM pentamidine	2 mM glucose + 1% m/v Pluronic® P85	2 mM glucose + 1% m/v Pluronic® P85	2 mM glucose + 1% m/v Pluronic® P85	2 mM glucose + 10 µM pentamidine + 1% m/v Pluronic® P85	2 mM glucose + 10 µM pentamidine + 1% m/v Pluronic® P85	2 mM glucose + 10 µM pentamidine + 1% m/v Pluronic® P85

Plates were then incubated at 37 °C for either 3 hours, or 24 hours, before washing twice with a bicarbonate-buffered physiological salt solution (Gey & Gey buffer, (Gey & Gey, 1936)) containing 2 mM glucose, 2 mM $CaCl_2$ and 0.5 mg/ml BSA (Sigma Aldrich; Dorset, UK) and incubated for 30 minutes at 37 °C. Following incubation, 100 µL of medium from each well was transferred to 5 mL polystyrene FACS tubes (BD Biosciences; Oxford, UK) containing 900 µL borate buffer for analysis by radioimmunoassay.

3.3.3.2 Insulin secretion as an indirect measure of cell viability

The insulin content of the incubation medium was assessed by radioimmunoassay following a previously outlined protocol (Jones *et al.*, 1988). The basic premise for this approach was that by adding known quantities of anti-insulin antibody and [^{125}I]-insulin to samples containing insulin secreted by MIN6 β-cells, the un-labelled and radiolabelled insulin would compete for binding to the antibody and form complexes, as shown in **Figure 3-15**.

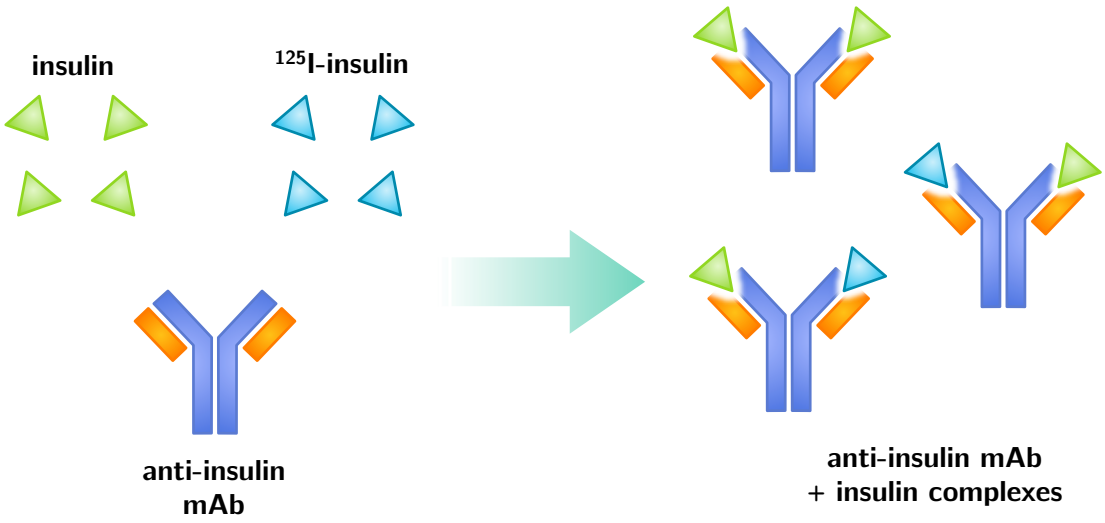

Figure 3-15: Schematic diagram of insulin-antibody interactions in radioimmunoassay. Un-labelled and radiolabelled insulin form complexes with anti-insulin monoclonal antibodies, allowing for the quantification of total un-labelled insulin in the sample. High concentrations of un-labelled insulin in a sample correlates with a reduced concentration of radiolabelled insulin within the resulting complexes due to competition for binding.

Anti-insulin monoclonal antibody was prepared at a dilution of 1:20 in borate buffer, and 100 µL added per sample. [^{125}I]-insulin tracer was also prepared in a separate solution of borate buffer, at a dilution of 1:65, and 100 µL added per sample. Samples were then incubated at 4 °C for 48 hours, before adding 1 mL of precipitant buffer containing γ-globulin, poly(ethylene glycol) and Tween 20 to each sample in order to precipitate complexes from unbound insulin. Samples were then centrifuged at 3,000 r.c.f for 15 minutes at 4 °C prior to gamma counting relative to a standard curve and corrected for non-specific binding.

3.3.4 Statistics

Data from all experiments are presented as mean ± standard error of the mean (SEM). Due to the broad range of experimental design and methods, specific details of statistical analyses performed on individual data sets will be presented in the context of the data in results chapters. Statistical significance was taken as follows: not significant (ns) $p > 0.05$, $*p < 0.05$, $**p < 0.01$, $***p < 0.001$. All statistical analyses were performed using GraphPad Prism® v6.0b graphing and statistics package for Mac.

3.4 Results: Formulation development & characterisation

As described in ***section 3.1.2 - Nanotechnology: Focus on Pluronic® P85***, the macromolecular state (unimeric vs. micellic) of Pluronic® P85 appears to dictate its effects as a biological response modifier. Therefore, an understanding of the biophysical parameters that dictate the formation of micelles in solution and their interactions with the drug (pentamidine) in solution is particularly useful when designing a drug formulation. The results of experiments to determine these biophysical properties are described below.

3.4.1 *In silico* characterisation

3.4.1.1 Critical Micelle Concentration and Aggregation number

Coarse-grained simulations containing Pluronic® P85 at seven different concentrations (0.03% - 1.00% m/v) were modelled in an implicit dH_2O-like environment (Anderson *et al.*, 2008), and the distribution of aggregates plotted relative to the probability of their existence (between 0 and 1) in the simulation box, shown in **Figure 3-16**. At 0.03% and 0.14% m/v, the majority of Pluronic exists in unimeric form (aggregation number = 1 for ≈ 90% and ≈ 50%) of Pluronic® in simulation. In the 0.29% m/v simulation one can detect the onset of micelle formation, with ≈ 75% of the simulation containing Pluronic® P85 in aggregates greater than or equal to two molecules of Pluronic® P85. Thus, these simulations give a predicted CMC of approximately 0.29% m/v in dH_2O at 37 °C.

In addition to calculating CMC from these simulations, one can clearly observe that the aggregation number increases with increasing concentrations of Pluronic® P85, where $N_{agg} = 10$ at 1.00% m/v. This is also depicted in **Figure 3-17**, which shows four snapshots of these simulations taken at Pluronic® P85 concentrations of 0.29%, 0.65%, 0.87% and 1.00% m/v.

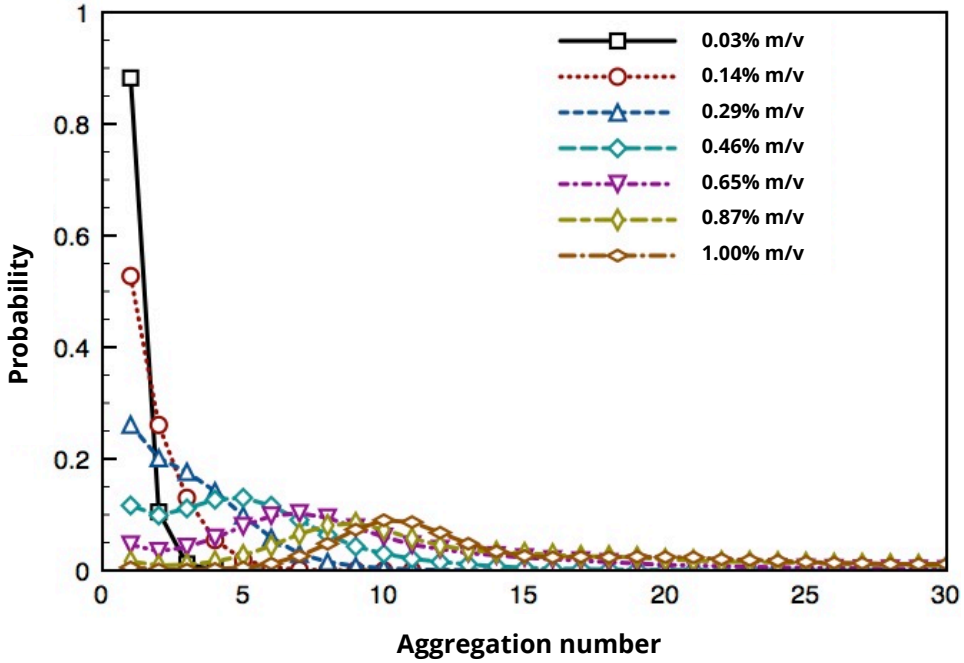

Figure 3-16: Probability of aggregates in simulation as a function of aggregation number for coarse-grained simulations of seven concentrations of Pluronic® P85. Aggregates of greater than 2 molecules can be observed at Pluronic® P85 concentrations of 0.29% and above, implying a theoretical CMC of 0.29% m/v. The modal (most frequently observed) aggregation number is detected at 1.00% m/v Pluronic® P85, where N_{agg} = 10. Simulations performed by Dr C Lorenz.

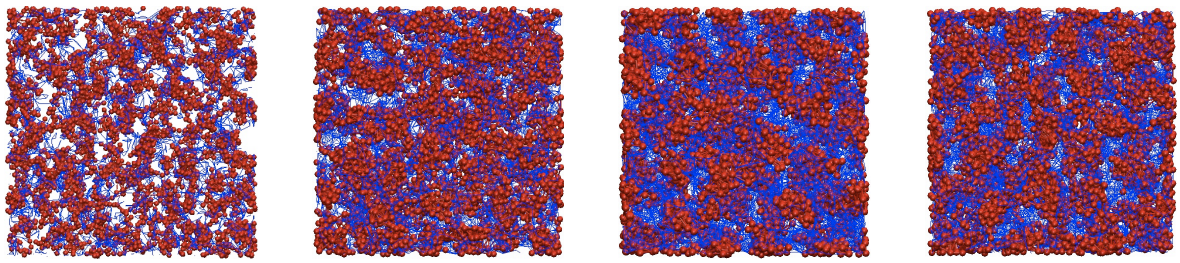

Figure 3-17: Snapshots taken from coarse-grained simulations of Pluronic® P85 at varying concentrations. Red beads represent the hydrophobic blocks of the block co-polymer and the blue beads the hydrophilic block. All simulations were run under dH_2O-like conditions at 37°C. As the concentration increases, the clusters of the hydrophobic (red) beads increase in size, which provides visual evidence of the increasing aggregation number. Simulations performed by Dr C Lorenz.

3.4.1.2 Micelle diameter

The data obtained from the coarse-grained simulations informed the design of atomistic simulations. **Figure 3-18** shows a snapshot of a single micelle modelled atomistically to contain 10 molecules of Pluronic® P85. As shown in the image, the diameter of the micelle was found to be approximately 59 Å (5.9 nm) at 310 K (37 °C).

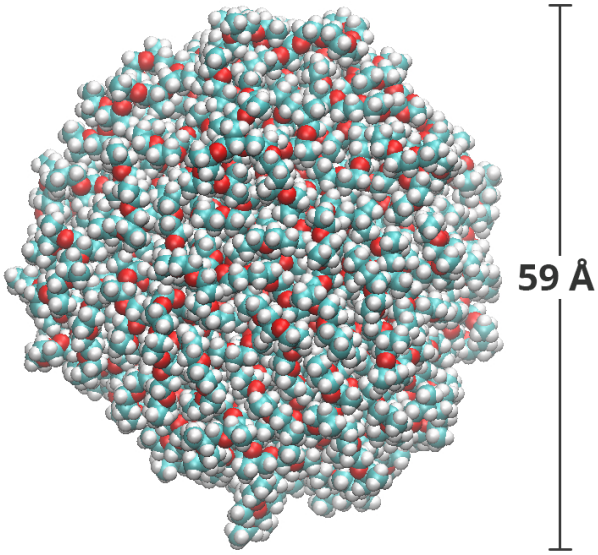

Figure 3-18: Single Pluronic® P85 micelle modelled atomistically.

3.4.2 *In vitro* characterisation

3.4.2.1 Critical micelle concentration

3.4.2.1A Eosin Y methodology

CMC measurements for Pluronic® P85 were first measured using the Eosin Y method (Patist *et al.*, 2000), as described in ***section 3.3.1.2A***. The method was first optimised with respect to the concentration range for Pluronic® P85 and its method for dissolution (whether by mechanical stirring, or sonication, data not shown). The optimised method, described in ***section 3.3.1.2A***, was then taken forward to obtain the data described below.

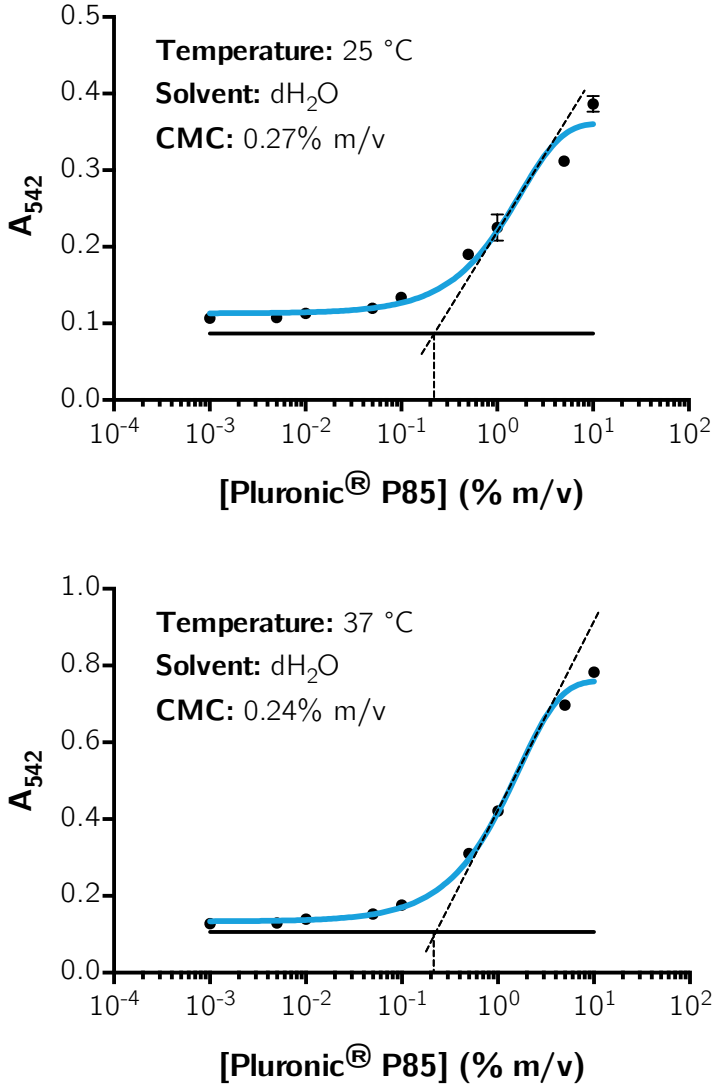

Figure 3-19: CMC measurements for Pluronic® P85 in dH_2O at 25 °C and 37 °C using the Eosin Y method. Graphs show mean±SEM, n=3 for each data point (created by GraphPad Prism v6 for Mac).

Figure 3-19 shows the CMC for Pluronic® P85 in dH_2O as measured using Eosin Y dye at 25 °C and 37 °C, calculated as being 0.27% and 0.24% m/v respectively.

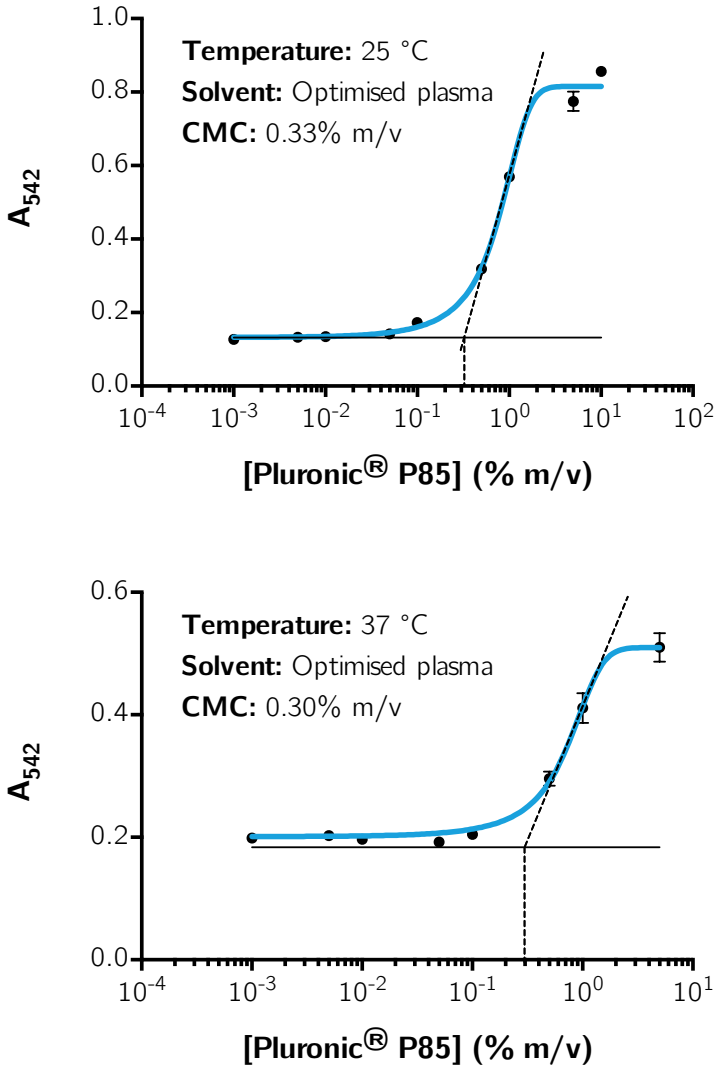

Figure 3-20: CMC measurements for Pluronic® P85 in optimised plasma at 25 °C and 37 °C using the Eosin Y method. Graphs show mean±SEM, n=3 for each data point (created by GraphPad Prism v6 for Mac).

Figure 3-20 shows the CMC for Pluronic® P85 in optimised plasma as measured using Eosin Y dye at 25 °C and 37 °C, calculated as being 0.33% and 0.30% m/v respectively.

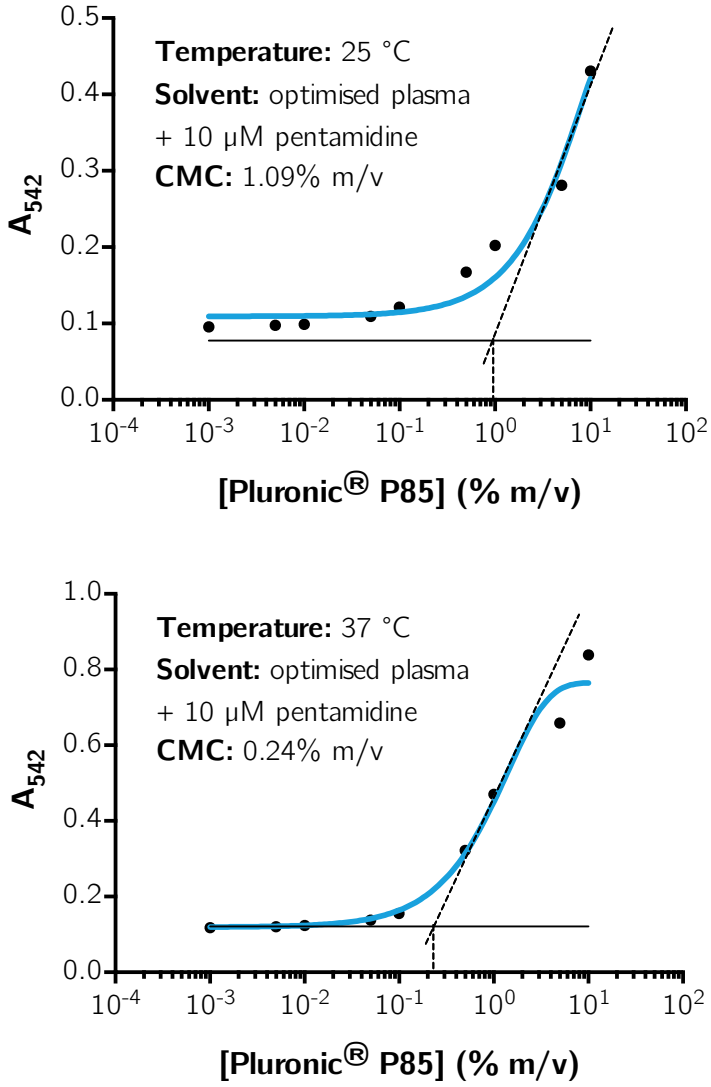

Figure 3-21: CMC measurements for Pluronic® P85 in optimised plasma + 10 µM pentamidine at 25 °C and 37 °C using the Eosin Y method. Graphs show mean±SEM, n=3 for each data point (created by GraphPad Prism v6 for Mac).

Figure 3-21 shows the CMC for Pluronic® P85 in optimised plasma as measured using Eosin Y dye at 25 °C and 37 °C, calculated as being 1.09% and 0.24% m/v respectively.

3.4.2.1B Pyrene methodology

Figure 3-22 shows representative fluorescence emission spectra for 500 nM pyrene:dH_2O at 25°C, and an example of the analysis used to calculate CMC for Pluronic® P85. Identical analyses were also applied to data collected for Pluronic® P85 in 500 nM pyrene:dH_2O at 37 °C, in 500 nM pyrene:optimised plasma at 25 °C, and at 37 °C. All experiments were performed on different days, and with different samples freshly prepared for each experimental condition.

The CMC values calculated from these data are shown together in **Table 3-8.**

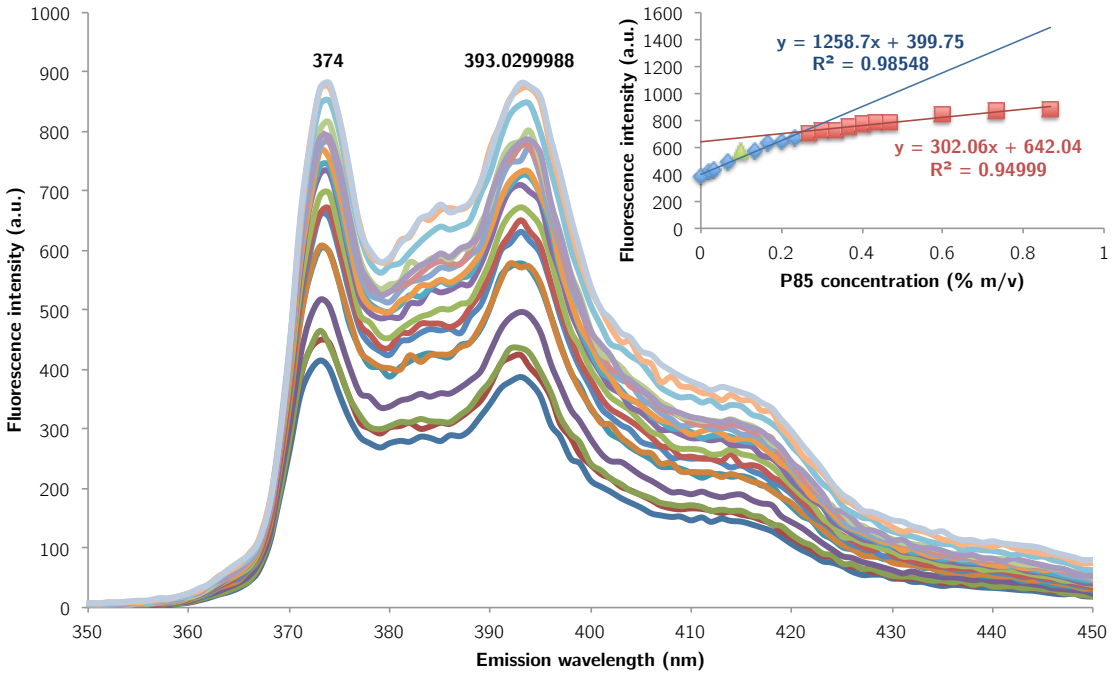

Figure 3-22: Example fluorescence emission spectra of 500 nM Pyrene in dH_2O with varying concentrations of Pluronic® P85 at 25°C. Peak fluorescence intensity increases with increasing Pluronic® P85 concentration. For a full breakdown of concentrations used please refer to **Table 3-3**. **Inset:** Fluorescence intensities measured at the emission wavelength ($\boldsymbol{\lambda_{em}}$) of 374 nm plotted *vs.* Pluronic® P85 concentration, used for the calculation of the CMC.

Table 3-8: Collated CMC values for Pluronic® P85 in either dH_2O or optimised plasma, at 25 °C or 37 °C.

Solution	Temperature	CMC (% m/v ± SEM)	n
Pyrene:dH_2O	25 °C	0.234 ± 0.010	6
	37 °C	0.170 ± 0.008	6
Pyrene:optimised plasma	25 °C	0.338 ± 0.001	3
	37 °C	0.284 ± 0.001	3

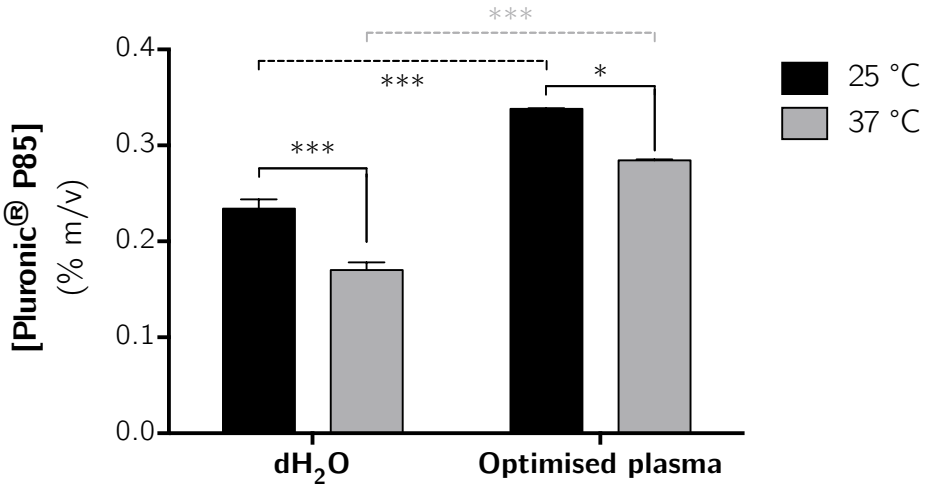

Figure 3-23: Comparison of CMC values for Pluronic® P85 calculated using pyrene in either dH_2O or optimised plasma, and at 25 °C or 37 °C. Mean ± SEM for each experimental condition were analysed by two-way ANOVA with Sidak's multiple comparisons test. *$p < 0.05$, ***$p < 0.001$.

As shown in **Table 3-8** and **Figure 3-23**, the CMC of Pluronic® P85 decreases when the temperature is increased from 25 °C to 37 °C in both solutions. Interestingly, at both temperatures studied the CMC is higher in the optimised plasma than in water ($p < 0.001$ for both comparisons).

3.4.2.2 Aggregation number

Figure 3-24 shows representative fluorescence emission spectra for 500 nM pyrene:dH_2O containing 1.0 % m/v Pluronic® P85 and varying concentrations of cetylpyridinium chloride at 25°C, and an example of the analysis used to calculate N_{agg} for Pluronic® P85. Identical analyses were also applied to data collected for Pluronic® P85 in 500 nM pyrene:dH_2O at 37 °C, in 500 nM pyrene:optimised plasma at 25 °C, and at 37 °C. All experiments were performed on different days, and with different samples freshly prepared for each experimental condition.

The N_{agg} values calculated from these data are shown together in **Table 3-9**.

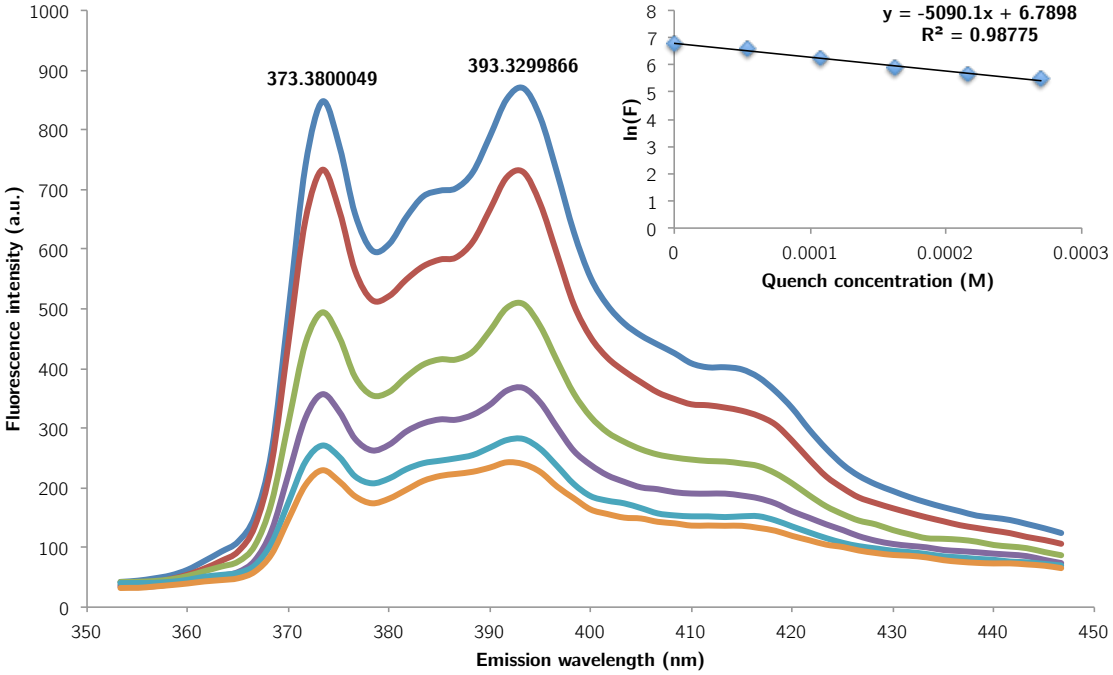

Figure 3-24: Example of fluorescence emission spectra of 500 nM Pyrene in dH_2O and 1.0 % m/v Pluronic® P85 with varying concentrations of the quench cetylpyridinium chloride. Peak fluorescence intensity is inversely proportional to concentration of cetylpyridinium chloride. For a full breakdown of concentrations used please refer to **Table 3-3**. **Inset:** Fluorescence intensities measured at the emission wavelength ($\boldsymbol{\lambda_{em}}$) of 393.3 nm, used for the calculation of N_{agg}.

Table 3-9: Collated N_{agg} values for Pluronic® P85 in either dH_2O or optimised plasma, at 25 °C or 37 °C.

Solution	Temperature	N_{agg} ± SEM	n
Pyrene:dH_2O	25 °C	8.5 ± 0.1	6
	37 °C	4.2 ± 0.2	6
Pyrene:optimised plasma	25 °C	7.1 ± 0.1	6
	37 °C	4.2 ± 0.1	6

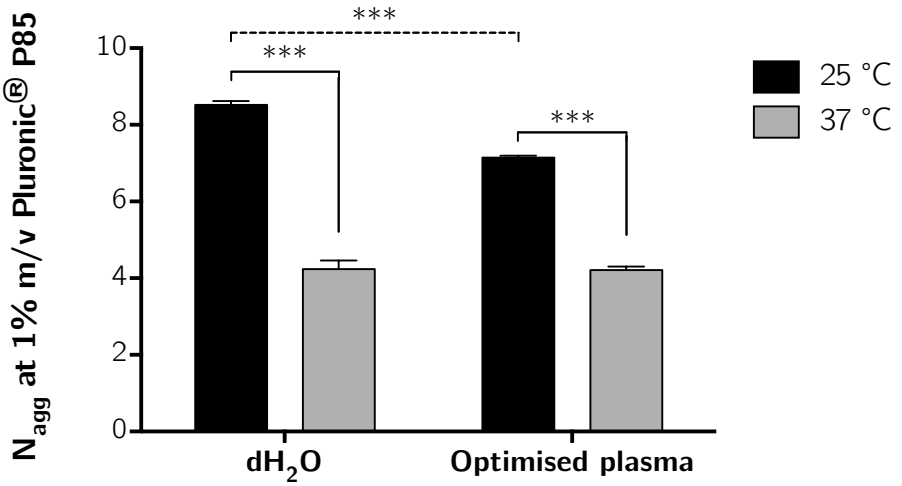

Figure 3-25: Comparison of N_{agg} values for Pluronic® P85 calculated using pyrene and cetylpyridinium chloride in either dH_2O or optimised plasma, and at 25 °C or 37 °C. Mean ± SEM for each experimental condition were analysed by two-way ANOVA with Sidak's multiple comparisons test, $***p < 0.001$.

As shown in **Table 3-9** and **Figure 3-25**, the aggregation number of Pluronic® P85 micelles decreases when increasing the temperature from 25 °C to 37 °C in both solutions. N_{agg} is lower in optimised plasma at 25 °C ($p < 0.001$), but very similar at 37 °C.

3.4.2.3 Partitioning of pentamidine into Pluronic® P85

Figure 3-26 shows representative fluorescence emission spectra for 10 µM pentamidine in aqueous solutions of Pluronic® P85 at varying concentrations at 25°C, and an example of the analysis used to calculate *P*. Identical analyses were applied to data collected for 10 µM pentamidine and Pluronic® P85 in dH_2O at 37 °C, and in optimised plasma at 25 °C, and at 37 °C. All experiments were performed on different days, and with different samples freshly prepared for each experimental condition.

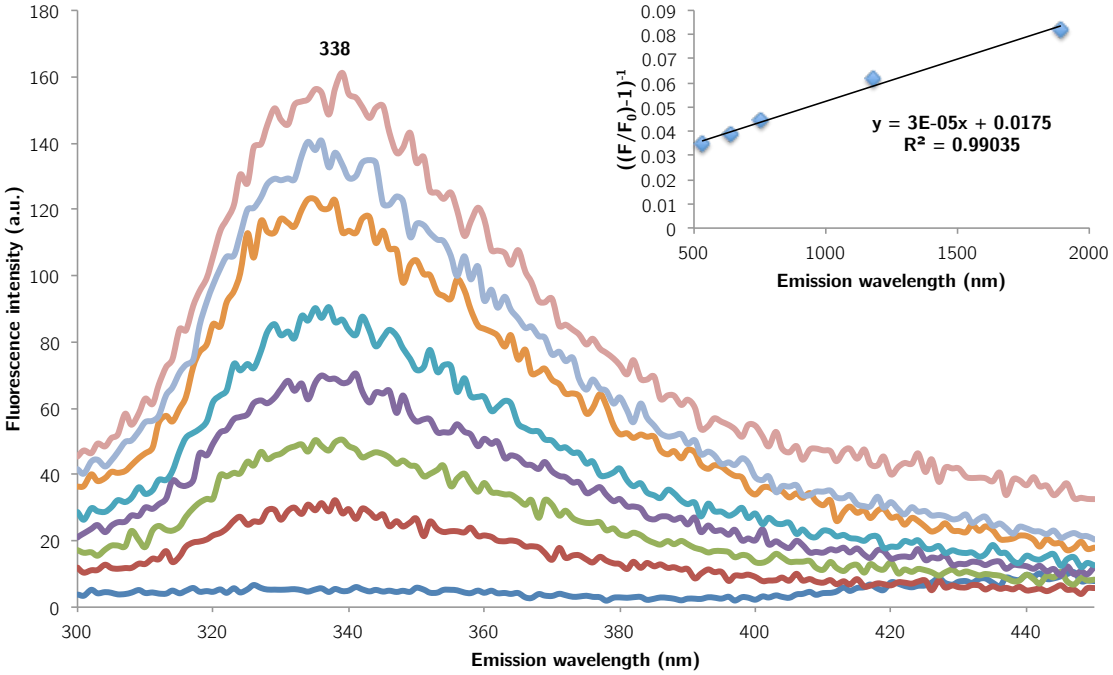

Figure 3-26: Example of fluorescence emission spectra of 10 µM pentamidine in dH_2O with varying concentrations of Pluronic® P85. Peak fluorescence intensity increases with increasing Pluronic® P85 concentration. For a full breakdown of concentrations used please refer to **Table 3-3**. **Inset:** Fluorescence intensities taken at the emission wavelength ($\boldsymbol{\lambda_{em}}$) of 338.0 nm, used for the calculation of *P*.

Table 3-10: Collated partition coefficient (*P*) values for pentamidine isethionate in Pluronic® P85 dissolved in either dH_2O or optimised plasma, at 25 °C or 37 °C.

Solution	Temperature	*P* ± SEM	n
dH_2O	25 °C	60.3 ± 3.2	8
	37 °C	60.7 ± 3.2	8
Optimised plasma	25 °C	9.2 ± 1.3	8
	37 °C	7.7 ± 0.5	8

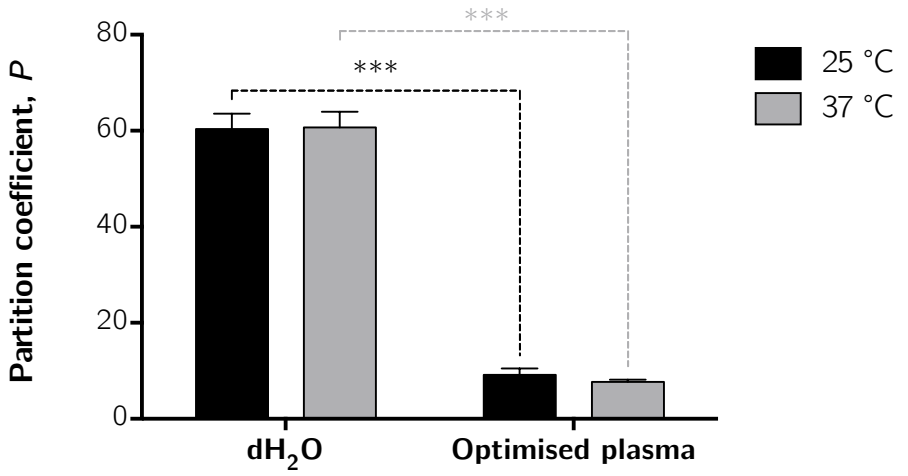

Figure 3-27: Comparison of the partition coefficient (*P*) values for pentamidine isethionate in Pluronic® P85 dissolved in either dH_2O or optimised plasma, at 25 °C and 37 °C. Mean ± SEM for each experimental condition were analysed by two-way ANOVA with Sidak's multiple comparisons test, $***p < 0.001$. NB: All partition coefficient values were calculated using the same calculated partial molar volume value (γ = 1.2059) of Pluronic® P85 in dH_2O at 25 °C using pycnometry.

As shown in **Table 3-10** and **Figure 3-27**, pentamidine partition into Pluronic® P85 micelles is substantially lower in optimised plasma relative to dH_2O ($***p < 0.001$). This phenomenon appears to be completely independent of temperature, since there is no difference between the partition coefficient measured between 25 °C and 37 °C, in either of the two solutions.

3.4.2.4 Mean hydrodynamic diameter

Figure 3-28 shows the mean hydrodynamic diameter of Pluronic® P85 micelles as measured by dynamic light scattering. No micelles were present at 0.001% m/v Pluronic® P85 dissolved either in dH_2O or optimised plasma. However, above the CMC, a single monodisperse population of micelles were formed both in dH_2O (18 nm) and artificial plasma (15 nm).

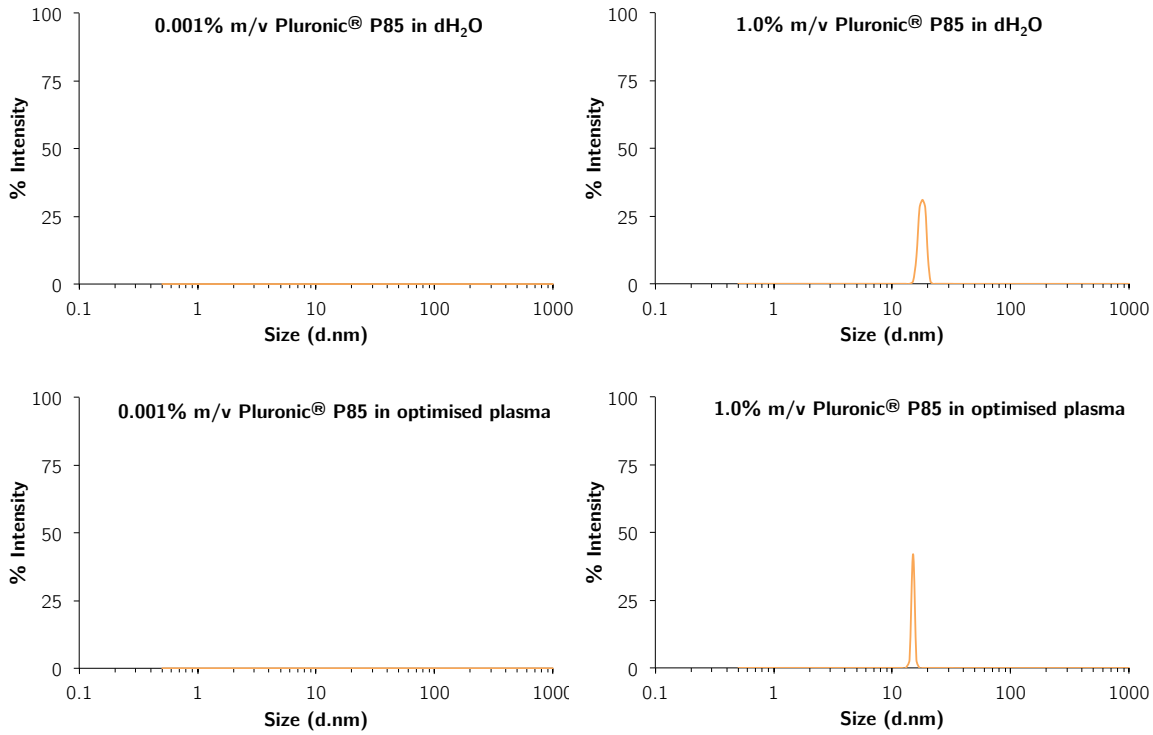

Figure 3-28: Size (mean hydrodynamic diameter) distribution of Pluronic® P85 micelles in dH_2O and optimised plasma. Solutions containing either 0.001% m/v or 1.0% m/v Pluronic® P85 were sized at 37°C using a Malvern NanoZS zetasizer. Solutions containing 0.001% m/v Pluronic® P85 displayed no observable peak, while both solutions containing 1.0% m/v Pluronic® P85 contain a single, monodisperse population of micelles of 17 nm in dH_2O and 15 nm in optimised plasma.

3.5 Results: Effect of formulation on CNS delivery of pentamidine to the CNS

3.5.1 Radiolabelled pentamidine integrity

Since both *in vivo* and *ex vivo* experimental techniques required the use of radiolabelled pentamidine for quantification by liquid scintillation counting, the integrity of [^{3}H]-pentamidine was first checked by HPLC, as described in ***section 3.3.2.3***.

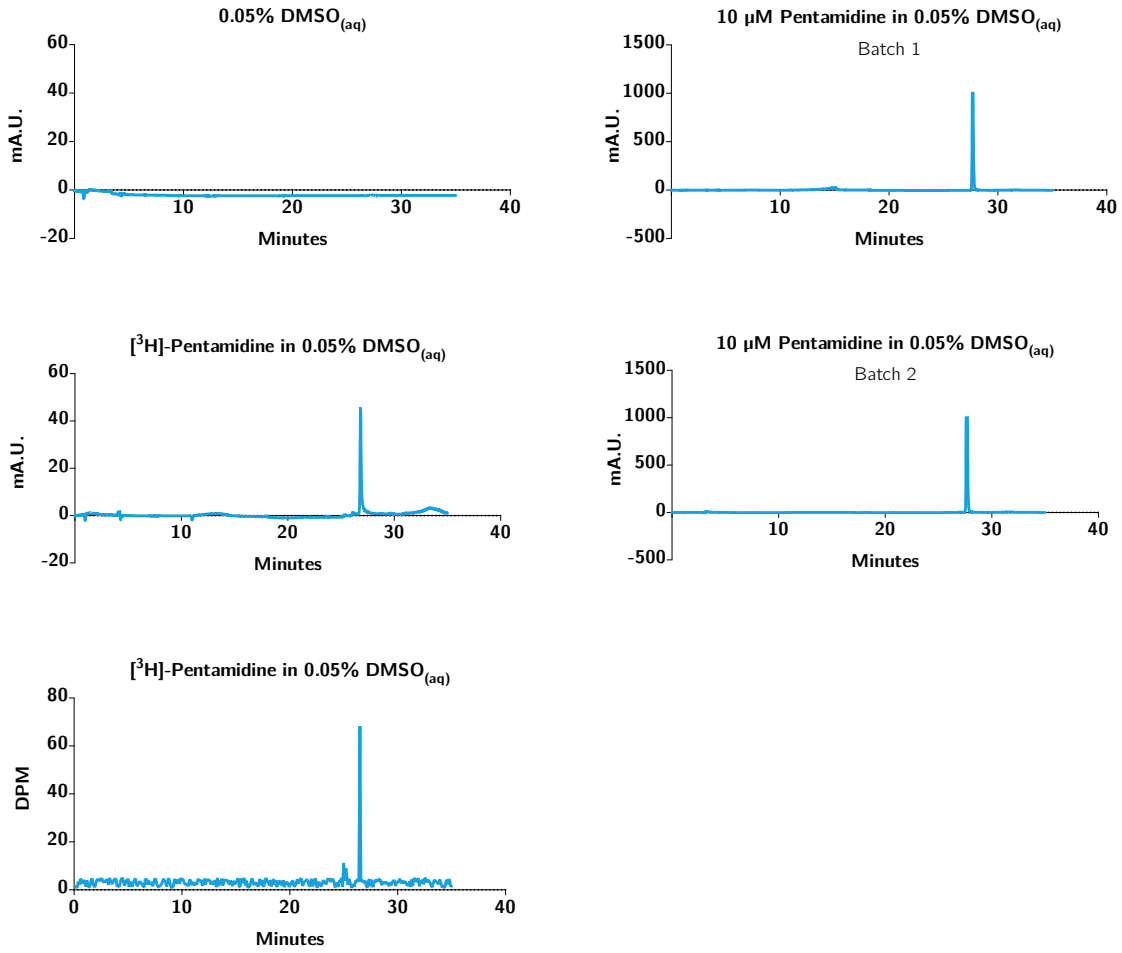

Figure 3-29: HPLC traces for two batches of unlabelled pentamidine (100 µM, batch 1 & 2), and [^{3}H]-pentamidine in 0.05% m/v DMSO$_{(aq)}$ compared to 0.05% m/v DMSO$_{(aq)}$ alone. Bottom trace shows radiodetector analysis of [^{3}H]-pentamidine in 0.05% m/v DMSO$_{(aq)}$.

A single peak, with a retention time of approximately 27 minutes (**Figure 3-29**) was detected in all three samples containing pentamidine (unlabelled or radiolabelled), in accordance with previously published data (Sanderson *et al.*, 2009). Furthermore, the fact that the majority of radioactivity detected by radiodetector analysis eluted at approximately 27 minutes also shows that the [^{3}H]-pentamidine is intact.

3.5.2 *In situ* brain/choroid plexus perfusion

3.5.2.1 Sucrose baseline

Since [^{14}C]-Sucrose can only enter the brain and CSF by simple diffusion it is a useful molecule to use as an internal control for BBB and BCSFB integrity in each experiment. It can also provide an approximation of cerebrovascular space in brain regions, and extracellular space formed between choroid plexus capillary endothelium and epithelium, and thus is a measure of variation between animals (Sanderson *et al.*, 2009). [^{14}C]-Sucrose values for all control experiments in all regions were concurrently compared to [^{14}C]-sucrose values for treatment experiments (one-way ANOVA with Dunnett's post-hoc test comparing means for each region), and found to be not significant (data not shown). Thus, none of the experimental conditions affected vascular space.

3.5.2.2 Pentamidine

In situ brain perfusion experiments involving pentamidine were first performed with a ten-minute perfusion time, and each treatment group had N=5, unless otherwise stated. As a point of comparison to all other treatments, this group of experiments contained a 'control' group containing only [^{3}H]-pentamidine and [^{14}C]-sucrose. Experiments were first performed with a 10-minute perfusion, the results of which are shown in **Figure 3-30**, **Figure 3-31** and **Figure 3-32**. These experiments were mirrored with a 30-minute perfusion, and are shown in **Figure 3-33**, **Figure 3-34** and **Figure 3-35**.

Figure 3-30 shows the effect of 0.01% m/v and 0.1% m/v Pluronic® P85 on the distribution of [^{3}H]-pentamidine into all brain regions after 10 minutes of perfusion. These data indicate that [^{3}H]-pentamidine distribution in the brain regions sampled after 10 minutes of perfusion is unaffected by the presence of Pluronic® P85 at either 0.01% or 0.1% m/v ($p > 0.05$).

However, taking the capillary depletion analysis shown in **Figure 3-31** into consideration, it would appear that the accumulation of [^{3}H]-pentamidine in the brain capillary endothelial cell-enriched pellet is enhanced by the inclusion of 0.1% Pluronic® P85 in the artificial plasma ($p < 0.01$).

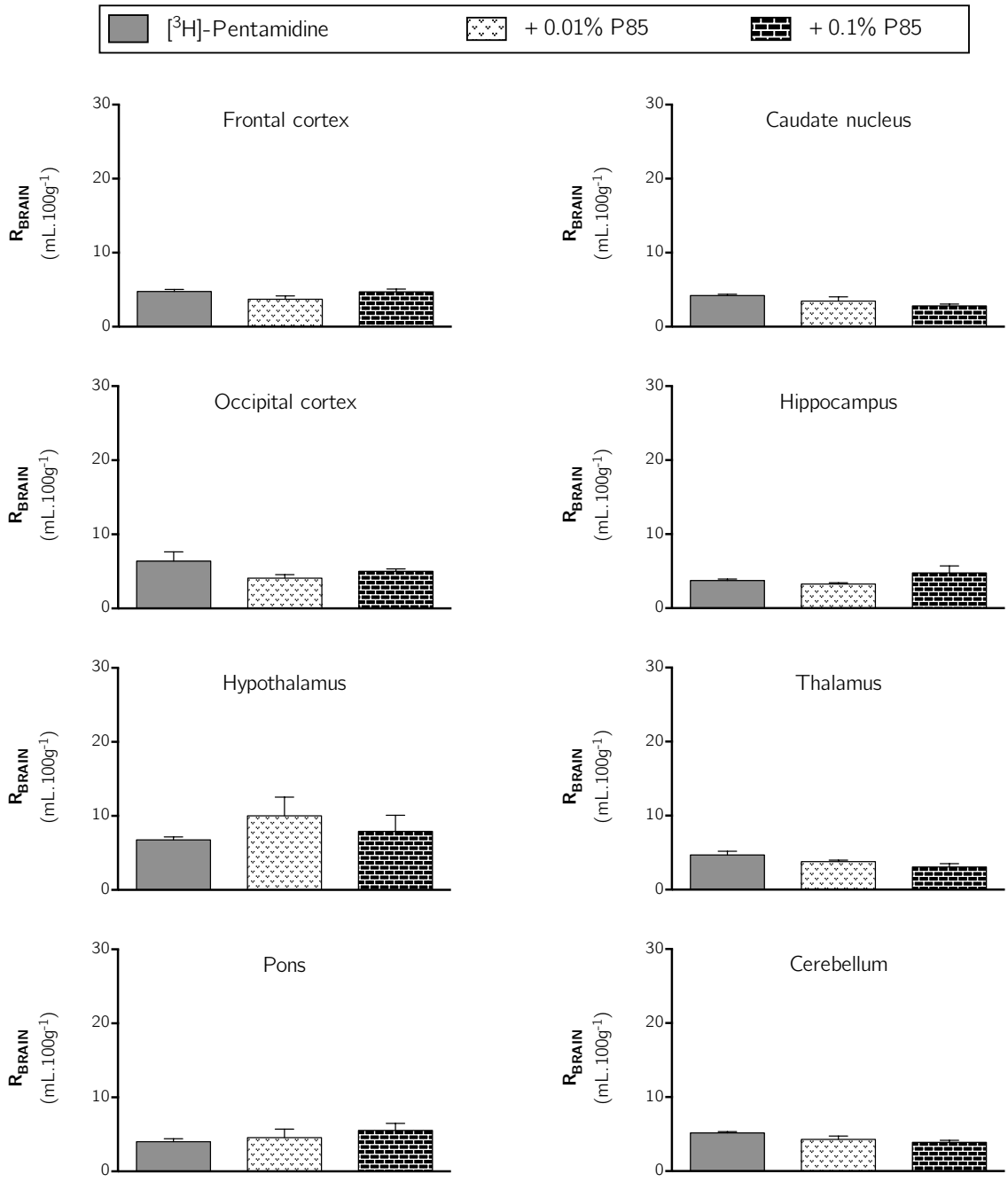

Figure 3-30: The effect 0.01% m/v and 0.1% m/v Pluronic® P85 on the distribution of [^{3}H]-pentamidine in the brain after 10 minutes of perfusion. Uptake is expressed as the percentage ratio of tissue to plasma (mL.100 g^{-1}) and is corrected for [^{14}C]-sucrose (vascular space). Each bar represents the mean ± SEM of 5 animals. Mean ± SEM for each experimental condition were analysed by two-way ANOVA with Dunnett's multiple comparisons test.

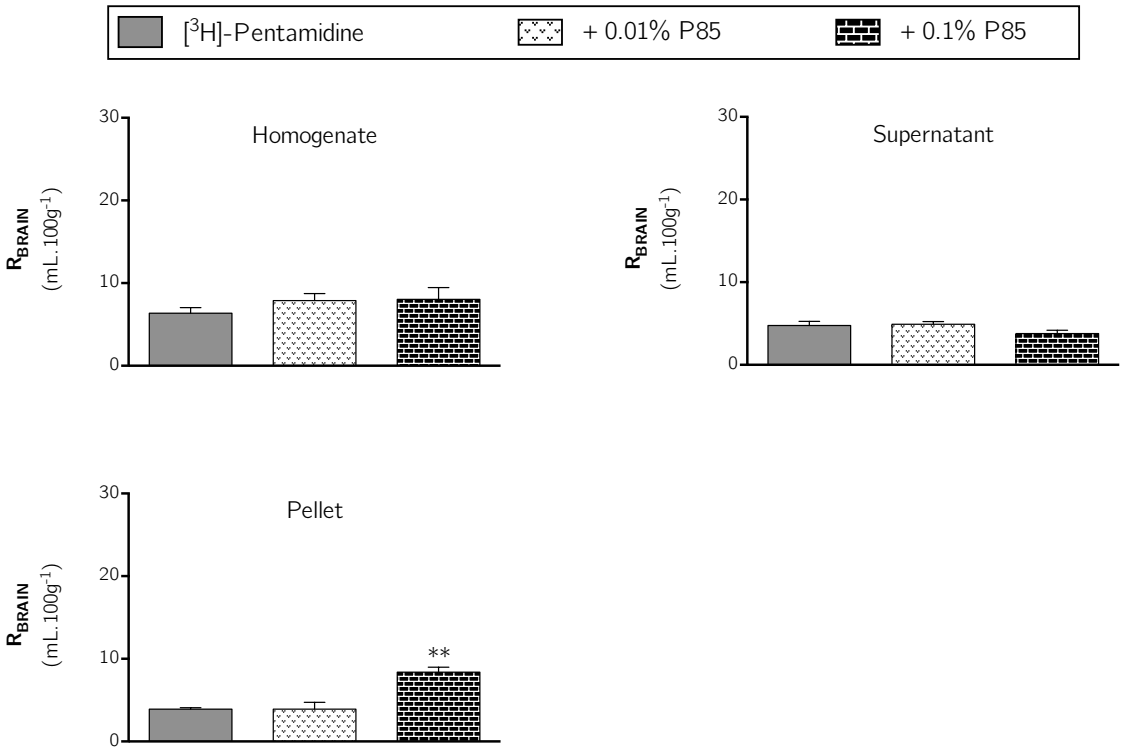

Figure 3-31: The effect 0.01% m/v and 0.1% m/v Pluronic® P85 on the distribution of [^{3}H]-pentamidine in capillary depletion samples after 10 minutes of perfusion. Uptake is expressed as the percentage ratio of tissue to plasma (mL.100 g^{-1}) and is corrected for [^{14}C]-sucrose (vascular space). Each bar represents the mean ± SEM of 5 animals. Mean ± SEM for each experimental condition were analysed by two-way ANOVA with Dunnett's multiple comparisons test, $^{**}p < 0.01$.

Figure 3-32 shows the effect of Pluronic® P85 on the distribution of [^{3}H]-pentamidine in the pineal gland, choroid plexus, and pituitary gland after 10 minutes of perfusion. These data indicate that [^{3}H]-pentamidine accumulation in the pineal gland is unaffected by Pluronic® P85. However, [^{3}H]-pentamidine accumulation in the choroid plexus is enhanced by both 0.01% m/v and 0.1% m/v Pluronic® P85, and is also enhanced in the pituitary gland, but only by 0.01% m/v Pluronic® P85.

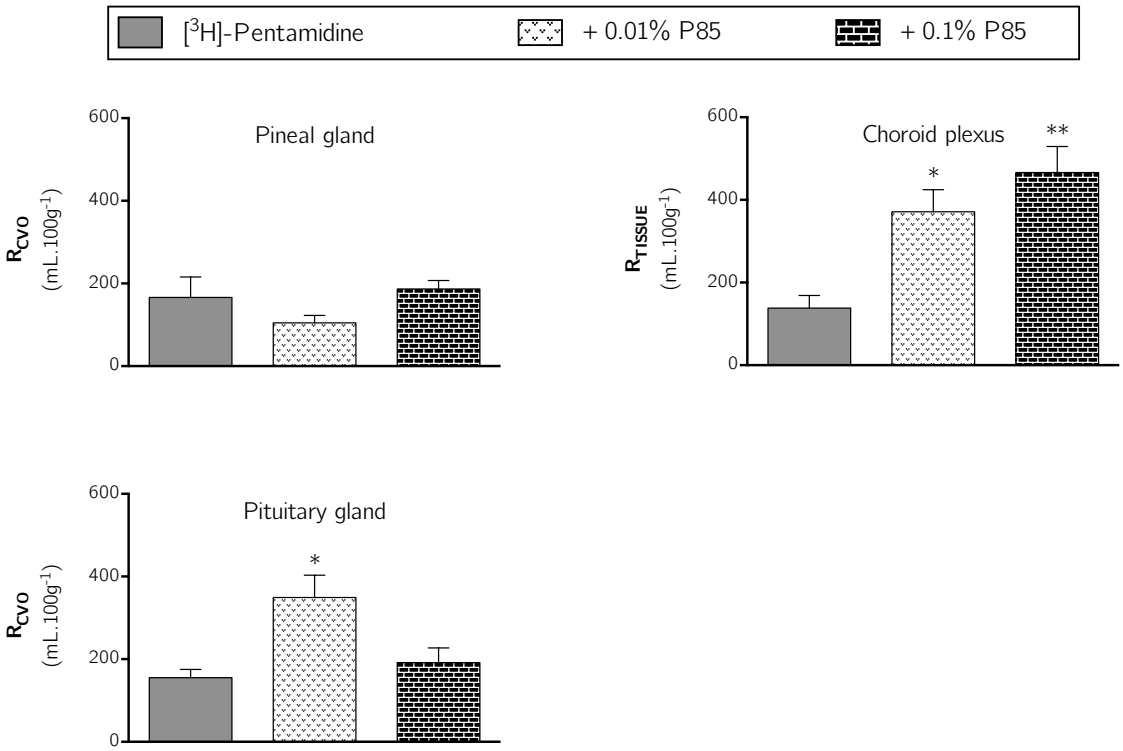

Figure 3-32: The effect 0.01% m/v and 0.1% m/v Pluronic® P85 on the distribution of [^{3}H]-pentamidine in pineal gland, choroid plexus and pituitary gland after 10 minutes of perfusion. Uptake is expressed as the percentage ratio of tissue to plasma (mL.100 g^{-1}) and is corrected for [^{14}C]-sucrose (vascular space). Each bar represents the mean ± SEM of 5 animals. Mean ± SEM for each experimental condition were analysed by two-way ANOVA with Dunnett's multiple comparisons test, $*p < 0.05$, $**p < 0.01$.

Figure 3-33 shows the effect of 0.01% m/v and 0.1% m/v Pluronic® P85 on the distribution of [^{3}H]-pentamidine into all brain regions after 30 minutes of perfusion. These data indicate that [^{3}H]-pentamidine distribution in the frontal cortex, occipital cortex, hippocampus, thalamus and cerebellum is reduced by the inclusion of 0.01% m/v Pluronic® P85 in the artificial plasma following 30 minutes of perfusion. Furthermore, the distribution of [^{3}H]-pentamidine in the hippocampus and cerebellum is also reduced after 30 minutes by the inclusion of 0.1% m/v Pluronic® P85.

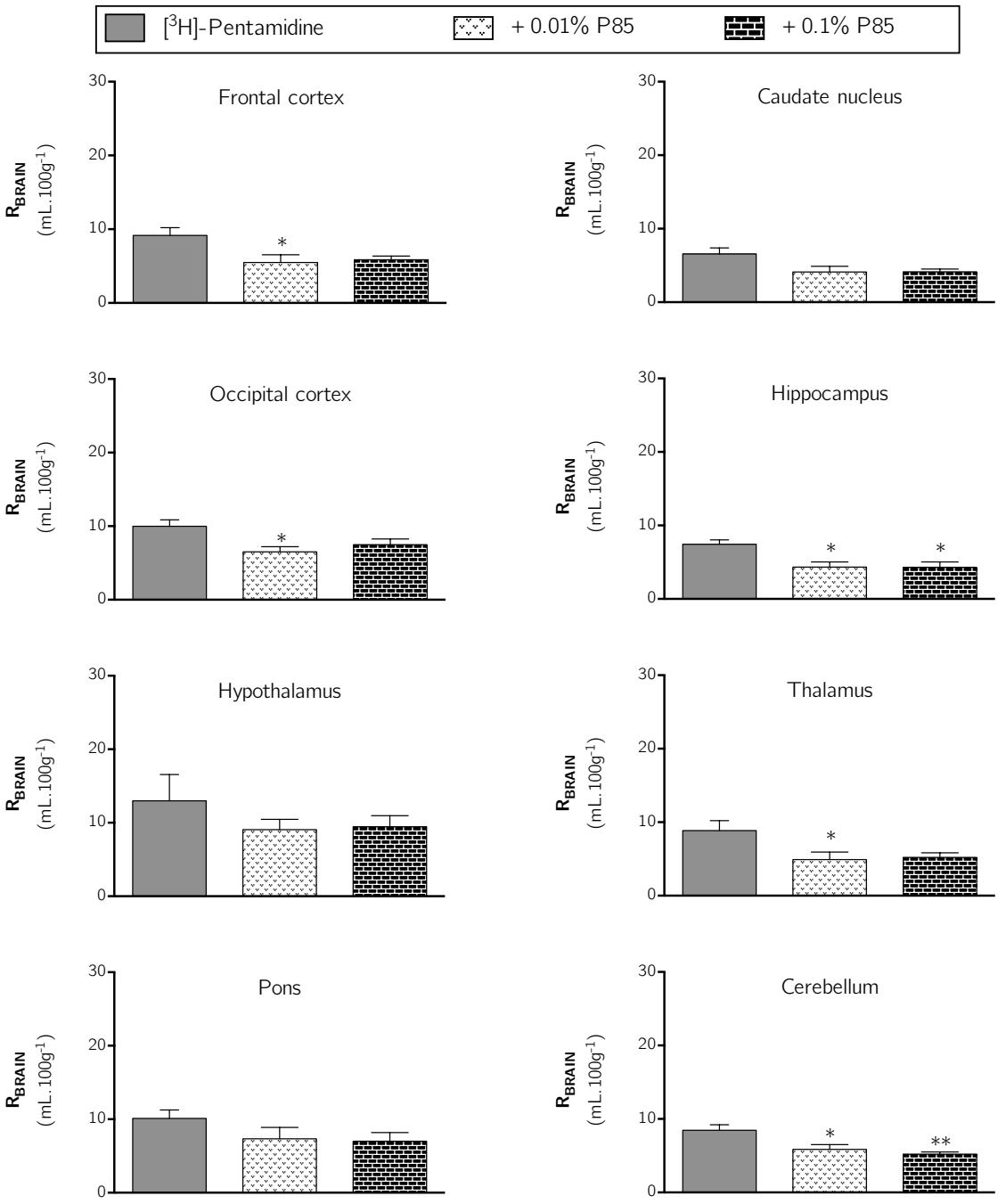

Figure 3-33: The effect 0.01% m/v and 0.1% m/v Pluronic® P85 on the distribution of [^{3}H]-pentamidine in the brain after 30 minutes of perfusion. Uptake is expressed as the percentage ratio of tissue to plasma (mL.100 g^{-1}) and is corrected for [^{14}C]-sucrose (vascular space). Each bar represents the mean ± SEM of 5 animals. Mean ± SEM for each experimental condition were analysed by two-way ANOVA with Dunnett's multiple comparisons test.

Taking the capillary depletion analysis shown in **Figure 3-34** into consideration, it would appear that [^{3}H]-pentamidine accumulation in the whole-brain homogenate and brain capillary endothelial cell-enriched pellet is unaffected by the presence of Pluronic® P85. However, the inclusion of 0.1% m/v Pluronic® P85 in artificial plasma appears to reduce the accumulation of [^{3}H]-pentamidine in the brain parenchyma after 30 minutes.

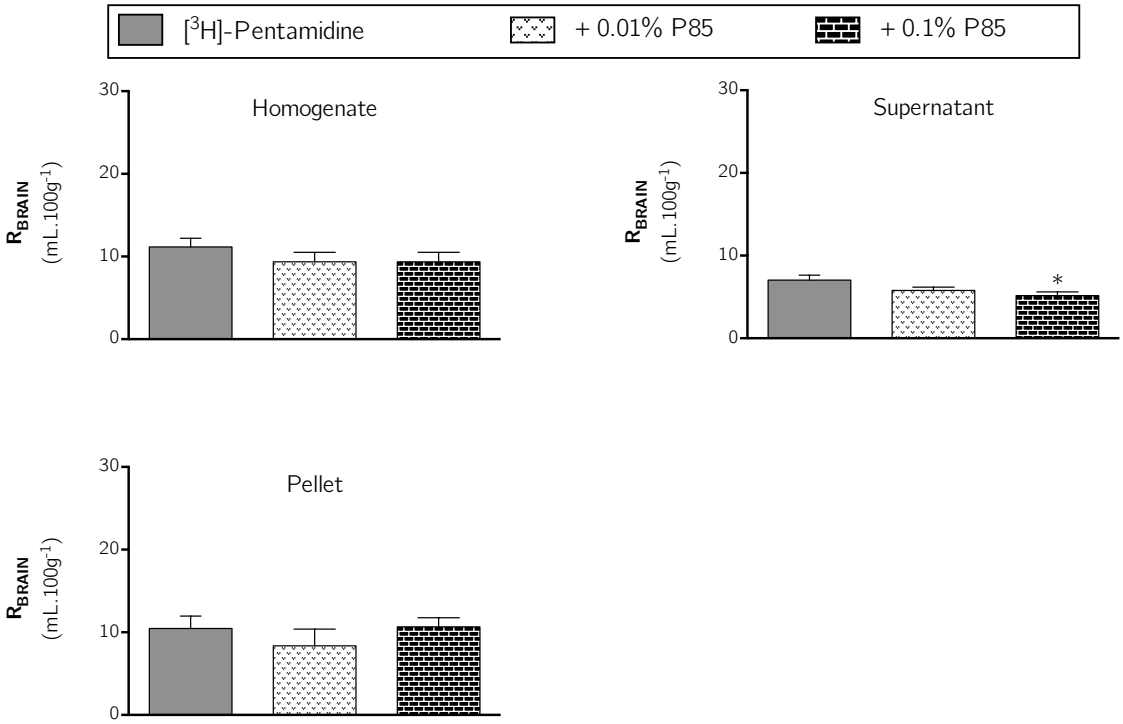

Figure 3-34: The effect 0.01% m/v and 0.1% m/v Pluronic® P85 on the distribution of [^{3}H]-pentamidine in capillary depletion samples after 30 minutes of perfusion. Uptake is expressed as the percentage ratio of tissue to plasma (mL.100 g^{-1}) and is corrected for [^{14}C]-sucrose (vascular space). Each bar represents the mean ± SEM of 5 animals. Mean ± SEM for each experimental condition were analysed by two-way ANOVA with Dunnett's multiple comparisons test, $^{**}p < 0.01$.

Figure 3-35 shows the effect of Pluronic® P85 on the distribution of [^{3}H]-pentamidine in the pineal gland, choroid plexus, and pituitary gland after 30 minutes of perfusion. These data indicate that [^{3}H]-pentamidine accumulation in all three samples is unaffected by inclusion of 0.01% m/v Pluronic® P85 in the artificial plasma following 30 minutes of perfusion. However, [^{3}H]-pentamidine accumulation in the choroid plexus and pituitary gland is enhanced by 0.1% m/v Pluronic® P85 ($p < 0.01$).

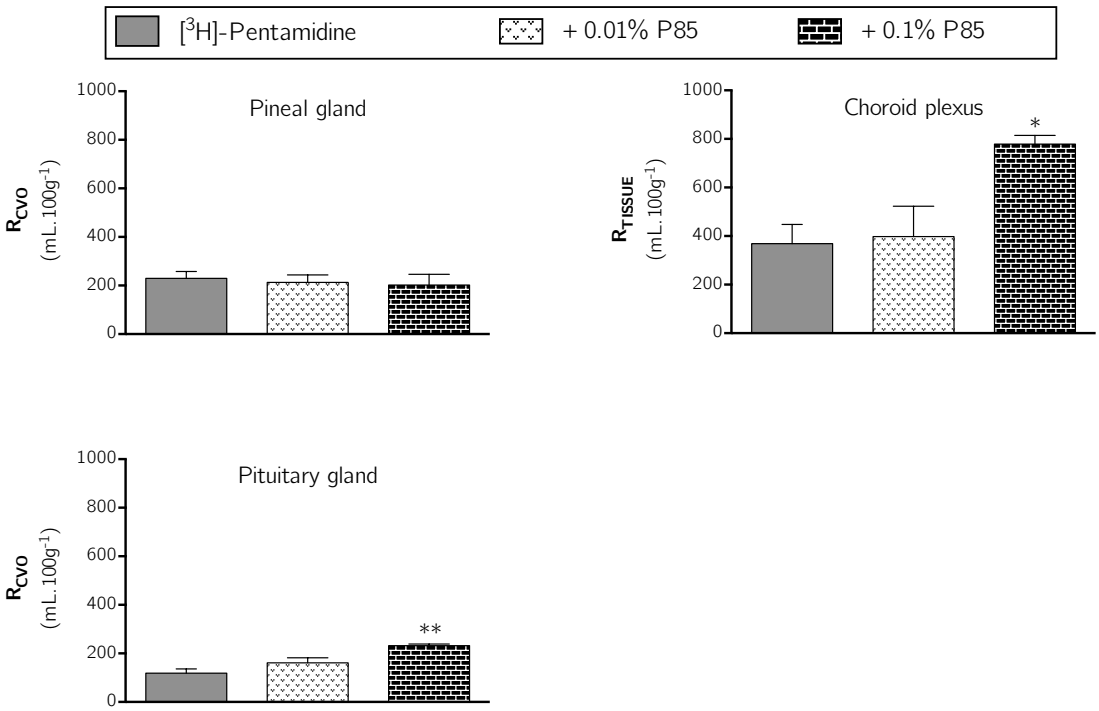

Figure 3-35: The effect 0.01% m/v and 0.1% m/v Pluronic® P85 on the distribution of [^{3}H]-pentamidine in pineal gland, choroid plexus and pituitary gland after 30 minutes of perfusion. Uptake is expressed as the percentage ratio of tissue to plasma (mL.100 g^{-1}) and is corrected for [^{14}C]-sucrose (vascular space). Each bar represents the mean ± SEM of 5 animals. Mean ± SEM for each experimental condition were analysed by two-way ANOVA with Dunnett's multiple comparisons test, *$p < 0.05$, **$p < 0.01$.

3.5.3 Isolated incubated choroid plexus

After observing the interactions of pentamidine and Pluronic® P85 with the choroid plexus using the *in situ* brain perfusion technique, these interactions were probed further using the isolated incubated choroid plexus technique.

3.5.3.1 Effect of Pluronic® P85 and transport inhibitors on choroid plexus extracellular space

[^{14}C]-Sucrose was present in each of the isolated choroid plexus incubations described in this study as a marker of extracellular space within the tissue. After the control incubations (10 minute incubations in [^{3}H]-pentamidine and [^{14}C]-sucrose alone, with no Pluronic® P85 present), [^{14}C]-sucrose accumulation was measured as 2.32 ± 0.30 mL g^{-1} and this was used as an indicator of barrier integrity. [^{14}C]-sucrose accumulation for incubations including Pluronic® P85 was also measured, and found not to be significantly different from the baseline accumulation measured in their absence (one-way ANOVA, $p > 0.05$). The accumulation of [^{14}C]-sucrose in these experiments is shown in **Figure 3-36**.

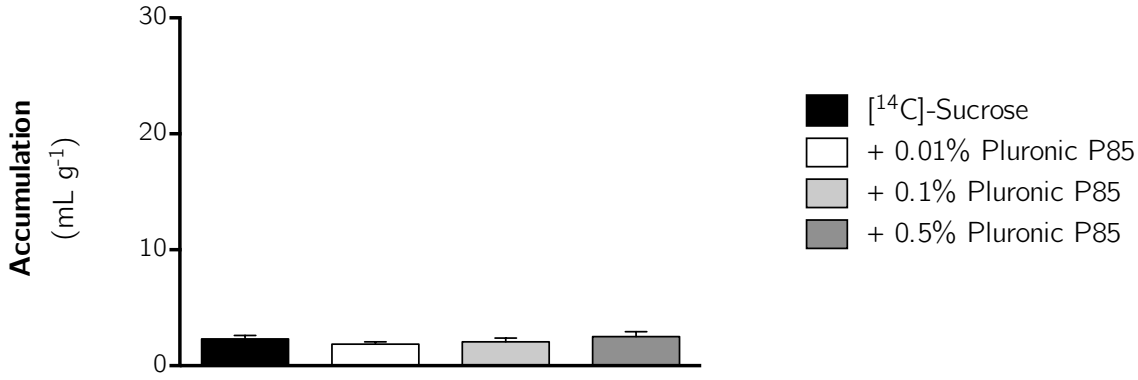

Figure 3-36: [^{14}C]-sucrose accumulation in the absence (control) and presence of Pluronic® P85 dissolved in artificial CSF and 0.05% m/v DMSO during [^{3}H]-pentamidine incubated isolated choroid plexus experiments (n=5). [^{14}C]-sucrose accumulation did not change in the presence of Pluronic® P85 at any of the concentrations used (one-way ANOVA, $P > 0.05$).

The effect of transport inhibitors on the accumulation of [^{14}C]-sucrose in isolated incubated choroid plexus was also measured, and found to not be significantly altered in the presence of any of the inhibitors used (**Figure 3-37**).

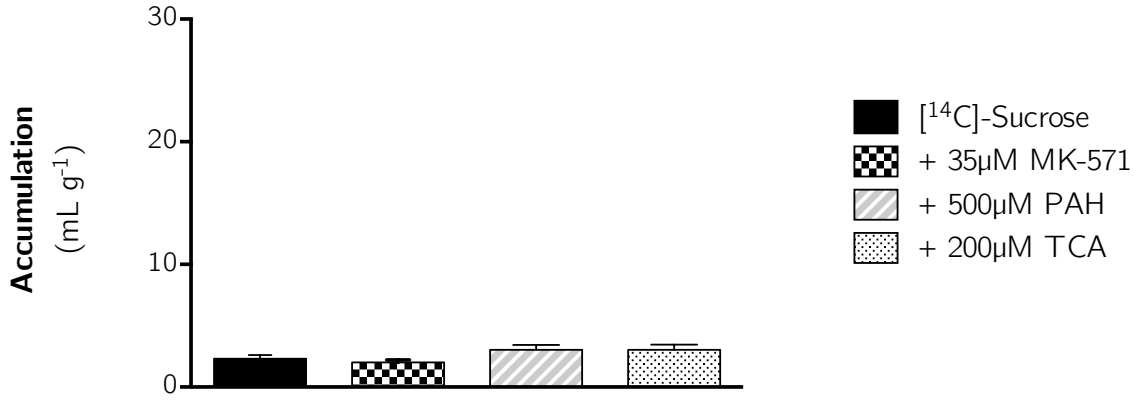

Figure 3-37: [^{14}C]-sucrose accumulation in the absence (control) and presence of transport inhibitors dissolved in artificial CSF and 0.05% m/v DMSO during [^{3}H]-pentamidine incubated isolated choroid plexus experiments (n=5). [^{14}C]-sucrose accumulation did not change in the presence of any of the inhibitors used (one-way ANOVA, $P > 0.05$).

3.5.3.2 Effect of Pluronic® P85 on the accumulation of pentamidine in the choroid plexus

The effect of Pluronic® P85 on the accumulation of [^{3}H]-pentamidine in the isolated incubated choroid plexus is shown in **Figure 3-38**. Accumulation of [^{3}H]-pentamidine is significantly reduced when co-formulating with 0.01% and 0.1% m/v Pluronic® P85, but not with 0.5% m/v Pluronic® P85.

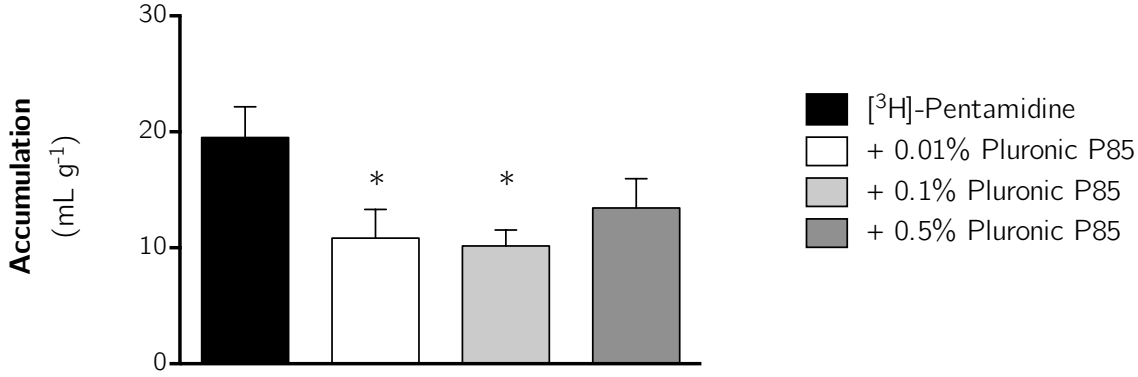

Figure 3-38: [^{3}H]-pentamidine accumulation (corrected for [^{14}C]-sucrose) in the absence (control) and presence of Pluronic® P85 dissolved in artificial CSF and 0.05% m/v DMSO during incubated isolated choroid plexus experiments (n=5). [^{3}H]-pentamidine accumulation corrected for extracellular space was decreased by the inclusion of Pluronic® P85 in the artificial CSF incubation medium, but only at concentrations of 0.01% and 0.1% m/v (one-way ANOVA with Dunnett's multiple comparisons test of means±SEM to control, $p < 0.05$).

3.5.3.3 Effect of efflux transporter inhibitors on the accumulation of pentamidine in the choroid plexus

The effect of specific inhibitors of efflux transporters on the accumulation of [^{3}H]-pentamidine in the isolated incubated choroid plexus is shown in **Figure 3-39**. Accumulation of [^{3}H]-pentamidine is significantly reduced by the inclusion of 35 µM MK-571 (MRP inhibitor), but is unaffected by the inclusion of 500 µM PAH or 200 µM TCA (OAT and OATP inhibitors, respectively).

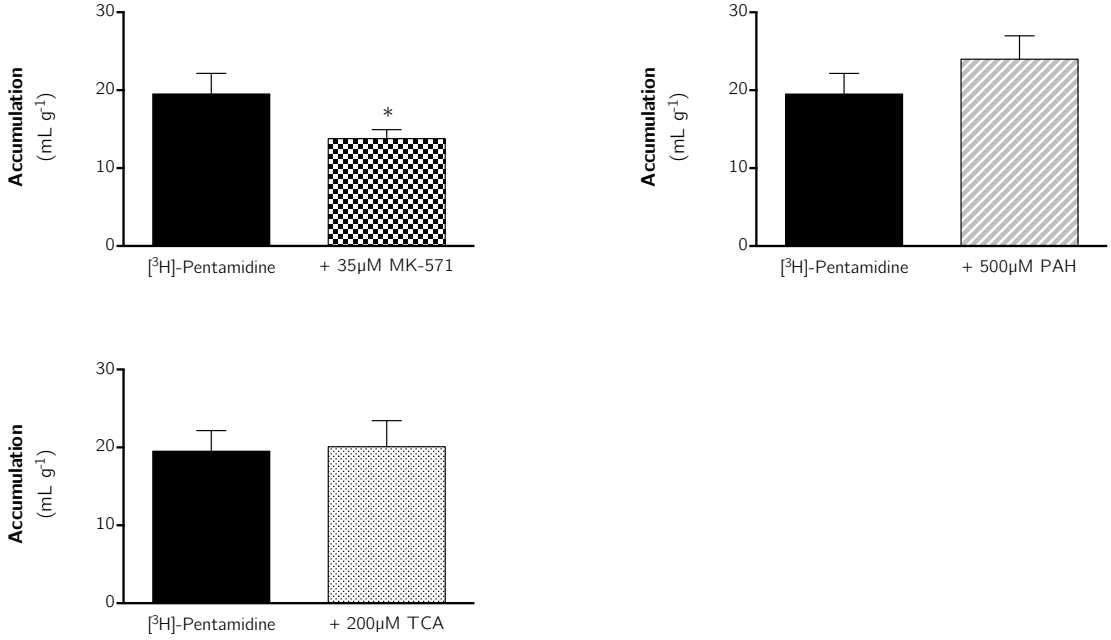

Figure 3-39: [^{3}H]-pentamidine accumulation (corrected for [^{14}C]-sucrose) in the absence (control) and presence of either MK-571 (35 µM), PAH (500 µM) or TCA (200 µM) dissolved in artificial CSF and 0.05% m/v DMSO during incubated isolated choroid plexus experiments (n=5). [^{3}H]-pentamidine accumulation corrected for extracellular space was decreased only by the inclusion of MK-571 (35 µM) in the artificial CSF incubation medium (one-way ANOVA with Dunnett's multiple comparisons test of means±SEM to control, $p < 0.05$).

3.6 Results: Effect of formulation on pentamidine-related pancreas toxicity

Figure 3-40 shows the inhibition of insulin release from MIN6 β-cells following pre-exposure to 10 µM pentamidine for either 3 or 24 hours (56.9% and 41.4% inhibition, respectively). The inhibition of insulin release was not observed when pre-exposing β-cells to 1% m/v Pluronic® P85 alone ($p > 0.05$), and was also restored to control (2 mM glucose) conditions when co-exposing β-cells to both Pluronic® P85 (1% m/v) and 10 µM pentamidine.

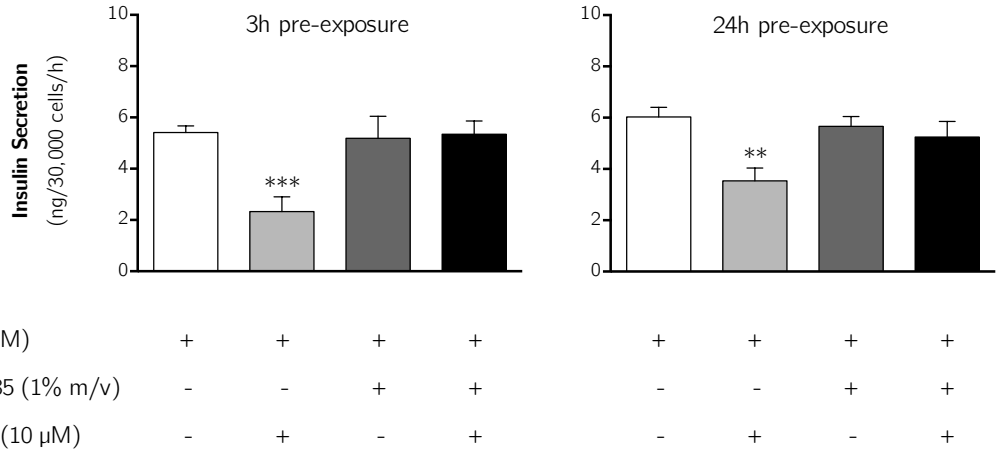

Figure 3-40: Pluronic® P85 blocks pentamidine inhibition of insulin secretion *in vitro*. Exposure of MIN6 β-cells to 10 µM pentamidine for 3 hours (left panel) or 24 hours (right panel) significantly ($p < 0.001$ or 0.01 respectively) inhibited acute insulin secretion, measured over 30 minutes. This inhibitory effect of pentamidine on β-cell exocytosis was prevented by co-exposure with 1% m/v Pluronic® P85 (one-way ANOVA with Dunnett's multiple comparisons post-hoc test relative to 2 mM glucose control). Bars shown means ± SEM, *N*=5-8.

3.7 Discussion

This chapter has examined the biophysical properties of the tri-block co-polymer Pluronic® P85 using both computational and experimental techniques. The results from both *in silico* and *in vitro* experiments were then used to inform the design of *in vivo* and *ex vivo* experiments to determine the suitability of Pluronic® P85 as a means of improving the delivery of pentamidine to the CNS through co-formulation. This multi-disciplinary approach allows for iterative improvements in formulation design assessed by *in silico, in vitro* and *in vivo* techniques that all feed back into a cyclical development pathway. Furthermore, the information obtained from *in silico* and *in vitro* methods facilitate a better informed strategic design of formulation parameters to be tested *in vivo*; reducing the number of animals that would otherwise be used following a purely empirical (trial & error) *in vivo* approach.

Results indicate that the molecular interactions of Pluronic® P85 molecules with each other and with pentamidine are sensitive to solvent and temperature, as shown by the observed changes in critical micelle concentration, aggregation number and partition coefficient both *in silico* and *in vitro*. Attempts were made to determine the biological effects of Pluronic® P85 on the blood-CNS barriers and the impact co-formulation has with the interactions of the drug pentamidine with these barriers *in vivo* and *ex vivo*.

These findings will be discussed in greater details in the sections that follow.

3.7.1 Formulation characterisation

3.7.1.1 CMC

Coarse-grained molecular dynamics simulations containing Pluronic® P85 modelled in an implicit dH_2O-like environment for the present study predicted that polymolecular aggregates (greater than or equal to two molecules of Pluronic® P85) were detectable at concentrations above 0.29% m/v (**Figure 3-16**).

While the CMC for Pluronic® P85 has been reported to be as high as 0.8% m/v in dH_2O at 30 °C (Ohashi *et al.*, 2009), previously published values are more typically found at between 0.006 – 0.03% (Kabanov *et al.*, 1995; Batrakova *et al.*, 1999a). In contrast to these published values, but in agreement with the theoretical values predicted by the coarse-grained molecular dynamics simulations, the CMC values for Pluronic® P85 in dH_2O measured using eosin Y were 0.27% m/v at 25 °C and 0.24% m/v at 37 °C (**Figure 3-19**). The CMC of Pluronic® P85 was found to decrease when increasing temperature from 25 °C to 37 °C (**Figure 3-19** and **Figure 3-20**) regardless of the solvent (water or optimised plasma), in accordance with previously published data (Kabanov *et al.*, 1995).

Interestingly, Pluronic® P85 CMC measured using the eosin Y methodology increased in optimised plasma relative to dH_2O – 0.33% m/v at 25 °C (*vs.* 0.27% m/v in water) and 0.30% m/v at 37 °C (*vs.* 0.24% m/v), shown in **Figure 3-20**. Previously published data for Pluronic® P85 found the CMC to decrease with increasing inorganic salt concentration (Ohashi *et al.*, 2009). Other tri-block co-polymers with PEO-PPO-PEO structures (such as L64, P65) have been shown to display lower CMCs in solutions containing inorganic salts (Jain *et al.*, 1999; Mata *et al.*, 2005). While it is not clear why the present study found the CMC in optimised plasma to increase relative to the CMC in dH_2O, it should be noted that previously published studies did not determine the effect that a mixture of different salts present in the solution had on the CMC.

The CMC of Pluronic® P85 in optimised plasma containing 10 µM pentamidine, as measured by the eosin Y methodology, was found to increase – reaching 1.09% m/v at 25 °C. The CMC of Pluronic® P85 in optimised plasma containing 10 µM pentamidine was lower (0.24% m/v) at 37 °C, and thus the CMC of Pluronic® P85 remains constant 37 °C. Understanding the effect of pentamidine on the CMC of Pluronic® P85 is crucial as it will ultimately relate to micelle stability and circulation time. The large increase of the CMC observed at 25°C is not clear, and further measurements at higher loadings of pentamidine would be needed to validate these measurements.

In accordance with both the theoretical CMC predicted by coarse-grained molecular dynamics simulations and the empirical values determined by the eosin Y method described in ***section 3.4.2.1A - Eosin Y methodology***, Pluronic® P85 CMC in dH_2O was measured using the pyrene method as 0.17 and 0.23 % m/v, at 25 °C and 37 °C, respectively (**Table 3-8**). As with the eosin Y method, the CMC for Pluronic® P85 in optimised plasma was higher than in dH_2O, at both temperatures measured (**Figure 3-23**).

The CMC of Pluronic® P85 in both optimised plasma and dH_2O calculated using the pyrene method also decreased with increasing temperature (from 25 °C to 37 °C, **Figure 3-23**), as found previously with the eosin Y method. **Table 3-11** shows that the CMC values for Pluronic® P85 obtained from both the Eosin Y and Pyrene method were very similar in all conditions tested.

Table 3-11: Collated CMC values for Pluronic® P85 in either dH_2O or optimised plasma, at 25 °C or 37 °C.

Solution	Temperature	CMC (% m/v)	n
Eosin Y:dH_2O	25 °C	0.27	3
	37 °C	0.24	3
Eosin Y:optimised plasma	25 °C	0.33	3
	37 °C	0.30	3
Pyrene:dH_2O	25 °C	0.234 ± 0.010	6
	37 °C	0.170 ± 0.008	6
Pyrene:optimised plasma	25 °C	0.338 ± 0.001	3
	37 °C	0.284 ± 0.001	3

3.7.1.2 N_{agg}

Coarse-grained molecular dynamics simulations containing 1% m/v Pluronic® P85 modelled in an implicit dH_2O-like environment at approximately 37 °C for the present study predicted the aggregation number to be 10 molecules per micelle (**Figure 3-16**). By comparison, the mean aggregation number for 1% m/v Pluronic® P85 in dH_2O was measured by fluorescence spectroscopy to be 8.5±0.1 at 25 °C, and decreased to 4.2±0.2 at 37 °C. Furthermore, the mean aggregation number for 1% m/v Pluronic® P85 in optimised plasma was calculated to be 7.1±0.1 at 25 °C, and decreased to 4.2±0.1 at 37 °C. Thus the aggregation number of Pluronic® P85 decreases with increasing temperature.

The aggregation number for Pluronic® P85 has previously been found using data-fitting of small-angle neutron scattering (SANS) data to increase with increasing temperature (from 20 °C to 40 °C, (Mortensen & Pedersen, 1993)). In the case of the data obtained from the present study using quenching of pyrene with cetylpyridinium chloride monohydrate, the opposite was found (**Figure 3-25**). This result is surprising, since at higher temperature, the dehydration of both PPO and PEO blocks is expected to increase micellisation and aggregation number. Further experiments would be needed to clarify this point.

3.7.1.3 Partition

Partition coefficient for pentamidine in Pluronic® P85 micelles was not found to be affected by temperature, with no significant difference between values obtained at 25 °C and 37 °C (whether in dH_2O or optimised plasma, **Figure 3-27**). However, the partition of pentamidine into Pluronic® P85 micelles appears to be greatly reduced in optimised plasma, relative to values observed for pentamidine in Pluronic® P85 micelles in dH_2O.

For simple ionic surfactants with polar head groups and hydrophobic tails, the solubilisation of drugs within micelles typically increases with increasing temperature (Alkhamis *et al.*, 2003), an observation attributed to an increase in molecular agitation

resulting from increasing the temperature that would increase micelle size and thus the space available for solubilisation within micelles (Alkhamis *et al.*, 2003). For non-ionic surfactants such as Pluronics® the effect of temperature on the partition of drug within micelles depends on whether the drug partitions exclusively into the hydrophobic core, or is distributed at the interface between the core and hydrophilic coronal/palisade layer. If aggregation number increases with increasing temperature, one would expect highly hydrophobic drugs to partition into the hydrophobic core more efficiently, however the opposite can also be true (lower partition, (Barry & El Eini, 1976)). Since aggregation number in the present study decreased with increasing temperature, and the precise location of pentamidine in the micelle structure is unknown, it is difficult to determine the significance of these findings based on the data obtained in this study alone.

A caveat from this study that further complicates the interpretation of these data is that the partial molar volume (γ) used in the calculation of these values was obtained through pycnometry performed only with Pluronic® P85 in dH_2O at 22.3 °C. The use of this value for the calculation of pentamidine partition in Pluronic® P85 micelles in dH_2O at 37 °C, but also in optimised plasma at both concentrations is an approximation. One would expect the partial molar volume of Pluronic® P85 micelles in both dH_2O and optimised plasma to decrease with increasing temperature, since individual Pluronic® P85 molecules would have a lower volume and could therefore pack more tightly (leading to a higher density, (Artzner *et al.*, 2007)).

3.7.1.4 Micelle size

Atomistic simulations of a single Pluronic® P85 micelle based on a theoretical aggregation number of 10 predicted a micelle diameter of approximately 5.9 nm (**Figure 3-18**). The mean hydrodynamic diameter of Pluronic® P85 micelles was measured at 37 °C as approximately 18 nm in dH_2O, and 16 nm in optimised plasma (**Figure 3-28**) from dynamic light scattering. Both predicted and measured values for micelle size are similar to previously published values of approximately 20 nm (Batrakova *et al.*, 2004a).

3.7.1.5 Summary

Both coarse-grained and atomistic *in silico* simulations provided useful information on the CMC, N_{agg} and micelle size. These results were further validated by spectroscopic techniques.

The data obtained from *in silico* and *in vitro* biophysical characterisation experiments presented here constitute both information that was taken forward for *in vivo* experiments (discussed below), but also a benchmark to compare to other Pluronics®, or even mixtures of multiple Pluronics® in the future.

3.7.2 Pentamidine transport across the blood-CNS barriers following co-formulation with Pluronic® P85

3.7.2.1 Radiolabelled pentamidine integrity

The integrity of radiolabelled pentamidine used in this study is of great importance. Should the radiolabel dissociate from the drug it would easily pass across the blood-CNS barriers to accumulate in the CNS and give an over-estimation of CNS uptake.

Comparison of HPLC and radiodetector analyses of solutions containing 0.05% m/v DMSO and either unlabelled 10 µM pentamidine or [^{3}H]-pentamidine clearly demonstrated that the [^{3}H]-pentamidine used in this study was intact and radiolabelled (**Figure 3-29**).

3.7.2.2 Pentamidine transport across the BBB

The motivations behind the study presented here stemmed from the initial observations of saturable influx of [^{3}H]-pentamidine into the CNS across the blood-CNS barriers, but also efflux of [^{3}H]-pentamidine from the CNS mediated by P-gp (Sanderson *et al.*, 2009). The co-formulation of [^{3}H]-pentamidine with Pluronic® P85 was hypothesised to improve the delivery of [^{3}H]-pentamidine to the brain by inhibiting the efflux transporters responsible for its removal. However, after perfusing for 10 minutes with [^{3}H]-pentamidine co-formulated either with 0.01% or 0.1% m/v Pluronic® P85 no significant difference in the distribution of [^{3}H]-pentamidine was observed in any of the brain regions relative to optimised plasma containing [^{3}H]-pentamidine alone (**Figure 3-30**).

However, capillary depletion analysis on whole-brain following a 10-minute perfusion suggests that [^{3}H]-pentamidine may be sequestered in BCECs following co-formulation with 0.1% Pluronic® P85 (**Figure 3-31**). The previously described limitations of the capillary depletion analysis technique mean that further analyses would be required to confirm this, but if it were found to be true it would imply that 0.1% m/v Pluronic® P85 inhibits the efflux of [^{3}H]-pentamidine from BCECs, although it is interesting that

this does not translate to an increase in brain distribution in the eight brain regions sampled.

Extending the perfusion time to 30 minutes produced similar results, with brain distribution of [^{3}H]-pentamidine in the frontal cortex, occipital cortex, hippocampus, thalamus and cerebellum actually decreasing when co-formulated with Pluronic® P85 (**Figure 3-33**). Capillary depletion analysis of these samples revealed the enhanced delivery of [^{3}H]-pentamidine to BCECs following co-formulation with 0.1% Pluronic® P85 seen following 10-minute perfusions is lost after 30 minutes (**Figure 3-34**).

The concentrations of Pluronic® P85 used in these experiments (0.01% and 0.1% m/v) were initially selected on the basis that previously published CMC values for Pluronic® P85 were in the range of 0.03% m/v (Kabanov *et al.*, 1995; Batrakova *et al.*, 1999a; Shaik *et al.*, 2009). The concentrations of 0.01% and 0.1% m/v would therefore represent Pluronic® P85 concentrations respectively below the CMC (only unimers present) and above the CMC (micelles and unimers present). However, on the basis of our data obtained from coarse-grained molecular dynamics simulations and biophysical characterisation experiments using pyrene and eosin Y presented in this study, both concentrations would be below the CMC.

Un-published *in vitro* BBB (hCMEC/D3) data obtained from experiments performed by members of our group show that an increase in the accumulation of [^{3}H]-pentamidine co-formulated with 0.01% and 0.1% m/v Pluronic® P85 (relative to [^{3}H]-pentamidine alone is only observed after incubation for 60 minutes and 120 minutes (Brown, 2012). No significant differences in the accumulation of [^{3}H]-pentamidine were found by co-formulating [^{3}H]-pentamidine with 0.01% and 0.1% m/v Pluronic® P85 and incubating for 5 or 20 minutes (Brown, 2012). It would therefore appear that Pluronic® P85 must first accumulate within BCECs before having any effect on the efflux of [^{3}H]-pentamidine. While one would ideally want to extend the perfusion time to mirror these *in vitro* BBB studies, the upper limit of *in situ* brain/choroid plexus perfusion time is 30 minutes before loss of BBB integrity (personal observations). It should be noted however, that co-formulation of [^{3}H]-pentamidine with 0.5% m/v

Pluronic® P85 did not alter the accumulation of [^{3}H]-pentamidine in hCMEC/D3 cells (relative to [^{3}H]-pentamidine alone) at any time point (Brown, 2012). A possible explanation for this may be that trapping of [^{3}H]-pentamidine within micelles prevents its interactions with influx transporters expressed in the membrane of the BCECs *in vitro*. This observation, combined with the cost of [^{3}H]-pentamidine (custom synthesised) and the quantities required for 10 and 30 minute *in situ* brain/choroid plexus perfusions meant that we were unable to perform these experiments *in vivo* with 0.5% m/v Pluronic® P85.

3.7.2.3 Pentamidine transport across the BCSFB

3.7.2.3A In situ brain/choroid plexus perfusion

[^{3}H]-Pentamidine accumulation in the pineal gland after 10 minutes was not affected by Pluronic® P85 at either 0.01% or 0.1% m/v (**Figure 3-32**). However, co-formulation of [^{3}H]-pentamidine with 0.01% Pluronic® P85 improved its accumulation in both the choroid plexus and the pituitary gland (**Figure 3-32**). Interestingly, co-formulating [^{3}H]-pentamidine with 0.1% m/v Pluronic® P85 improved its accumulation in the choroid plexus further, while accumulation of [^{3}H]-pentamidine when co-formulated with 0.1% m/v Pluronic® P85 returned to control levels in the pituitary gland (**Figure 3-32**).

It is not entirely obvious why this might happen. Should the CMC for Pluronic® P85 indeed fall between 0.01% and 0.1% m/v one could potentially theorise that micelles would be present at 0.1% m/v and that encapsulation of [^{3}H]-pentamidine within the micelles could prevent the interaction of [^{3}H]-pentamidine with influx transporters present in the pituitary gland. However, both *in silico* and *in vitro* characterisation of Pluronic® P85 in the present study would suggest that micelles would not be present at 0.1% m/v. However, even if the CMC value of approximately 0.3% m/v calculated in the studies presented in this chapter are true, it is somewhat difficult to explain why the enhancement of [^{3}H]-pentamidine accumulation following a 10-minute perfusion is additive in the case of the choroid plexus, but not in the case of the pituitary gland.

Data obtained following a 30-minute perfusion are shown in **Figure 3-35**, and present an additional opportunity to dissect the intricacies of the interactions of [^{3}H]-pentamidine and Pluronic® P85 and the BCSFB. As was observed after 10 minutes, Pluronic® P85 appears to have no effect on the accumulation of [^{3}H]-pentamidine in the pineal gland. In the cases of both the choroid plexus and pituitary gland, [^{3}H]-pentamidine accumulation after 30 minutes was only enhanced when co-formulated with 0.1% (**Figure 3-35**). **Figure 3-41** shows a time-dependent increase in the distribution of [^{3}H]-pentamidine in the pineal gland and choroid plexus. It is clear from presenting the data in this way that the same time-dependent increase in [^{3}H]-pentamidine distribution in the choroid plexus is also present when co-formulating with 0.1% m/v Pluronic® P85, albeit enhanced at both time-points. Interestingly, 0.01% m/v Pluronic® P85 appears to prevent the time-dependent increase in [^{3}H]-pentamidine accumulation in the choroid plexus, despite initially enhancing its accumulation after 10 minutes.

In the case of the pituitary gland, [^{3}H]-pentamidine distribution appears to decrease from 10 minutes to 30 minutes in the absence of Pluronic® P85, a phenomenon that is also true with 0.01% m/v Pluronic® P85. The co-formulation of [^{3}H]-pentamidine with 0.1% m/v Pluronic® P85 appears to reverse this effect, and facilitates a time-dependent increase in [^{3}H]-pentamidine distribution in the pituitary gland (**Figure 3-41**).

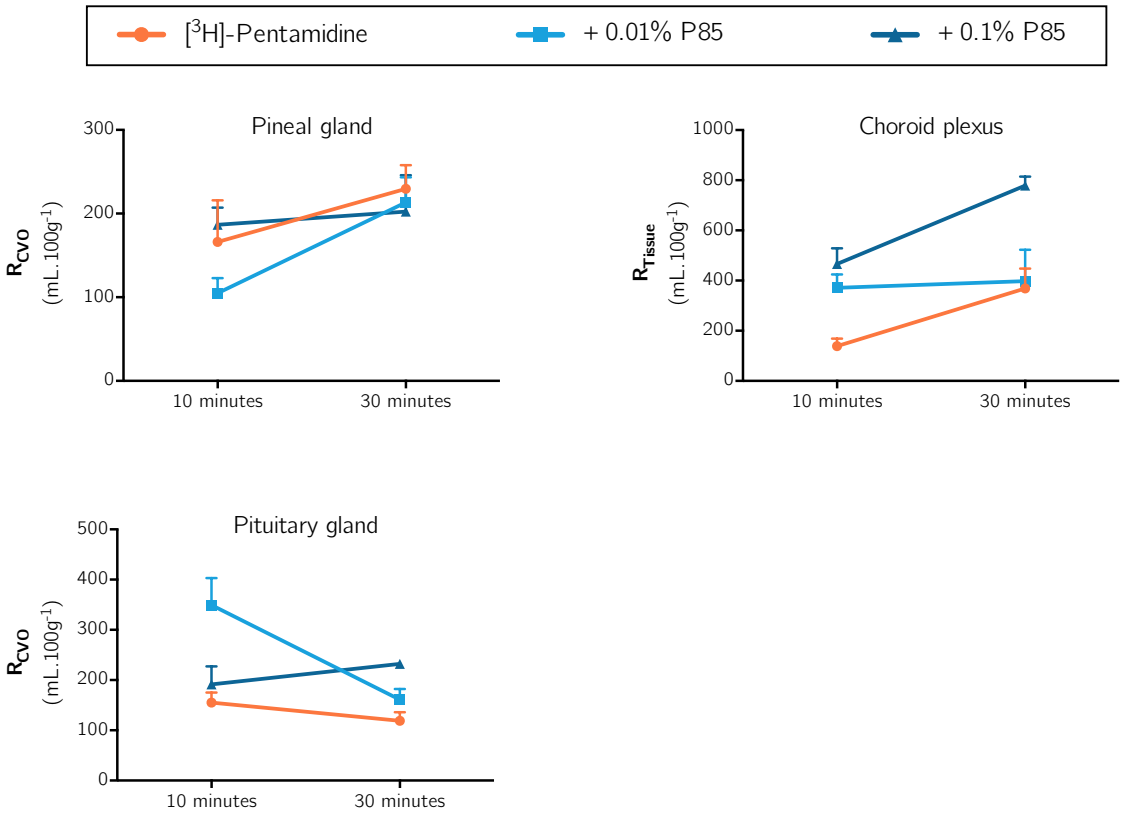

Figure 3-41: Distribution of [^{3}H]-pentamidine in the pineal gland, choroid plexus and pituitary gland in the absence or presence of Pluronic® P85 as a function of time. Uptake is expressed as the percentage ratio of tissue to plasma (mL.100 g^{-1}) and is corrected for [^{14}C]-sucrose (vascular space). Each point represents the mean+SEM of 5 animals.

3.7.2.3B Incubated choroid plexus

The inclusion of [^{14}C]-sucrose in all incubated choroid plexus experiments confirmed that extracellular space was unaffected by Pluronic® P85 at 0.01%, 0.1% and 0.5% m/v (**Figure 3-36**), or indeed any of the specific transport inhibitors (**Figure 3-37**). **Figure 3-38** shows that Pluronic® P85 at 0.01% and 0.1% m/v, but not 0.5% m/v inhibits the accumulation of [^{3}H]-pentamidine in the isolated incubated choroid plexus. The isolated incubated choroid plexus technique predominantly measures the movement of molecules from the CSF across the apical (CSF-facing) membrane of the choroid plexus. On the basis of the biological effects of Pluronic® P85 on efflux transporters described in ***section 3.1.2.2 - Inhibitory effect of unimers on efflux transporters***, it was hypothesised that the accumulation of [^{3}H]-pentamidine would be increased when co-formulated with Pluronic® P85, since both BCRP and P-gp are expressed at the apical membrane of the choroid plexus and serve to remove substrates from the choroid plexus epithelium into the CSF (Redzic, 2011). While pentamidine has been shown to be a substrate of P-gp at the murine blood-CNS barriers (Sanderson *et al.*, 2009), it would not be unreasonable to predict that pentamidine may also interact with BCRP, since there is a strong overlap in the substrate specificities of these transporters (Giacomini *et al.*, 2010). However, these data not only suggest that Pluronic® P85 does not inhibit the efflux of pentamidine from the choroid plexus by either of these transporters, but that some influx transporter for pentamidine into the choroid plexus is inhibited.

Following the observations discussed in the previous section that Pluronic® P85 may need to be exposed to cells for 60 minutes or more to affect [^{3}H]-pentamidine distribution, it may be that 10 minute incubation time utilised in these experiments was not sufficiently long enough a period of time to allow Pluronic® P85 to accumulate in the choroid plexus. A simple experiment to test this hypothesis would be to extend the incubation time to 30 or even 60 minutes.

Following the observations that Pluronic® P85 may inhibit the influx of [^{3}H]-pentamidine into the choroid plexus *via* the apical membrane, isolated incubated

choroid plexus experiments were also designed to determine the effect of specific transport inhibitors on [^{3}H]-pentamidine accumulation, and are shown in **Figure 3-39**. From the lack of inhibition by either 500 µM PAH or 200 µM TCA it would appear that pentamidine does not interact in any way with OAT-1, OAT-3, or OATP-3, which are influx transporters known to be expressed at the apical membrane of the choroid plexus. It would also suggest that pentamidine does not interact with the bi-directional transporters OATP-2 or -14 expressed at the basolateral membrane. An interesting observation was that [^{3}H]-pentamidine accumulation in the isolated choroid plexus was inhibited by the MRP-specific inhibitor MK-571 at 35 µM (**Figure 3-39**). Since MRPs are transporters that typically mediate the efflux of substrates from cells, it was hypothesised that the inclusion of MK-571 in the artificial CSF would result in reduced efflux of [^{3}H]-pentamidine from the choroid plexus and thus, greater detected accumulation. The fact that the opposite was observed here suggests that a currently unknown MRP transporter is expressed at the choroid plexus in an opposite orientation to that which is typically observed for MRP transporters, or any other transporters belonging to the ABC superfamily. Another possible explanation is that MK-571 may not be completely specific to MRP transporters alone, and may be inhibiting another transporter with [^{3}H]-pentamidine specificity.

In any case the studies presented here are insufficient to completely describe the interaction of pentamidine, or indeed Pluronic® P85 with transporters at the blood-CNS barriers. Future experiments to address these gaps in the current knowledge are described in ***section 3.7.5 - Future work***.

3.7.3 Reduced pancreatic toxicity

Pentamidine is known to cause hyperglycaemia and diabetes mellitus in approximately 10% of patients following treatment (Jha & Sharma, 1984; Waskin *et al.*, 1988; Thakur *et al.*, 1991). It was therefore hypothesised that encapsulation of pentamidine within Pluronic® P85 micelles may protect pancreatic *β*-cells from pentamidine-mediated cytotoxicity. An experiment was designed to investigate any possible benefits to co-formulating pentamidine with Pluronic® P85 that used insulin release was as a surrogate marker of pancreatic *β*-cell health, the results of which are shown in **Figure 3-40**.

As expected, insulin release from MIN6 *β*-cells was significantly reduced following both 3- and 24-hour pre-exposure to 10 µM pentamidine (**Figure 3-40**), relative to control conditions where only 2 mM glucose was present in the incubation medium. The presence of 1% m/v Pluronic® P85 and 2 mM glucose alone in the incubation medium had no effect on the release of insulin from MIN6 cells following both 3- and 24-hour pre-exposure. Most interestingly, the inhibition of insulin release mediated by pentamidine alone was prevented by co-formulating pentamidine with Pluronic® P85, which restored insulin release to control levels. It would therefore appear that encapsulation of pentamidine within Pluronic® P85 micelles does indeed protect pancreatic *β*-cells from damage by 'free' pentamidine *in vitro*.

3.7.4 Conclusions

The data presented in this chapter represent the beginnings of establishing a cyclical formulation development pathway, whereby the suitability of different Pluronic® block co-polymers for use *in vivo* can be predicted by both *in silico* and *in vitro* approaches. Having an understanding of the biophysical properties of the co-polymers allows for better initial design of experiments to measure the effect of co-formulation on pentamidine transport across the blood-CNS barriers *in vivo*, but also any subsequent optimisation of the co-formulation.

The data obtained from these experiments would suggest that a tension exists between improving delivery to brain by not having micelles present in the co-formulation, and protecting the pancreas from pentamidine by encapsulating it in micelles. Clearly there is no intermediate in this situation – micelles by definition are not present below the CMC, and are present at concentrations above the CMC. If a co-formulation of pentamidine and Pluronic® P85 was to be taken forward at sub-CMC concentrations one may consider reducing the dose of pentamidine in the co-formulation with the hopes of reducing the side-effects on the pancreas, however this is far from ideal.

While Pluronic® P85 may not be the optimal choice for improving the delivery of pentamidine to the brain a large number of alternative Pluronics® exist for consideration and use in further experiments, which are described in the section below. The co-formulation of Pluronic® P85 with pentamidine is a starting point and will form a comparison to any future work, which itself will be informed by the lessons learned in the generation of data presented in this chapter. It should also be noted that while pentamidine was selected as a model drug for the purposes of this study, it is conceivable that the same theory could be applied to any drug found to be a substrate for efflux from the CNS. Indeed, it would be expected that different drugs would interact differently with micelles, which could feasibly improve the efficacy of Pluronic® P85 as a drug vehicle.

In summary, the key findings of this study are:

1. The CMC of Pluronic® P85 was predicted to be approximately 0.29% m/v using coarse-grained molecular dynamics simulation. This was found to be highly predictive of the empirical CMC, which was calculated by two different techniques to be approximately 0.30% m/v.

2. CMC decreased with increasing temperature, but had the net effect of increasing slightly in optimised plasma relative to dH_2O.

3. Aggregation number of Pluronic® P85 micelles at 1.0% m/v was predicted using coarse-grained molecular dynamics simulations to be 10, confirmed empirically to be between 4 and 9. Aggregation number decreased with increasing temperature, contrary to previously published data, in both dH_2O and optimised plasma.

4. Partitioning of pentamidine into Pluronic® P85 micelles was found to be independent of temperature, but greatly reduced in optimised plasma relative to dH_2O.

5. Atomistic simulations of a single Pluronic® P85 micelle predicted a diameter of approximately 6 nm. The true diameter was found by dynamic light scattering to be approximately 19 nm, in accordance with previously published data for Pluronic® P85.

6. Co-formulation of pentamidine with Pluronic® P85 at sub-CMC concentrations (according to our calculation of CMC) did not enhance the delivery of pentamidine to any of the brain regions sampled, contrary to our hypothesis.

7. Pluronic® P85 may be transiently enhancing the accumulation of pentamidine in BCECs as shown by capillary depletion analysis following a 10-minute *in situ* brain/choroid plexus perfusion, but this effect is lost after 30 minutes.

8. Unpublished *in vitro* data using the human BBB cell line hCMEC/D3 suggests

that a greater exposure time may be needed to allow Pluronic® P85 to accumulate within BCECs, and that the encapsulation of pentamidine within micelles may actually negatively impact on the ability of pentamidine to interact with influx transporters at the BBB.

9. Pluronic® P85 enhances the delivery of pentamidine to the choroid plexus and pituitary gland at sub-CMC concentrations, but not to the pineal gland.

10. Pluronic® P85 at sub-CMC concentrations inhibits the transport of pentamidine into isolated incubated choroid plexus (presumably inhibiting an influx transporter at the apical membrane that is also sensitive to inhibition by the MRP-specific inhibitor MK-571).

The precise mechanism by which Pluronic® P85 enhances the transport of pentamidine from the blood into the choroid plexus and pituitary gland cannot be elucidated from the evidence presented in this study alone. It is possible that P-gp expressed sub-apical membrane epithelium for these tissues and/or MRP expressed at the basolateral membrane (Rao *et al.*, 1999) are inhibited by P85 unimers, as per the hypothesis proposed in ***section 3.2 - Rationale and aims***. That being said, an entirely different mechanism could equally be responsible for the enhanced delivery of [^{3}H]-pentamidine when combined with Pluronic® P85 at sub-CMC concentrations.

The interactions of [^{3}H]-pentamidine and Pluronic® P85 with the apical membrane of the choroid plexus were determined using the incubated isolated choroid technique. The data from these studies suggest that the movement of [^{3}H]-pentamidine back from the CSF into the choroid plexus is mediated by a transporter that is sensitive both to the MRP inhibitor MK-571, but also sub-CMC concentrations of Pluronic® P85. Since the choroid plexus is a likely major site of entry for the trypanosome parasite into the brain (Wolburg *et al.*, 2012) it might be expected that the co-formulation of pentamidine with Pluronic® P85 may be an effective treatment for early-stage 2 HAT.

A diagrammatic summary of the predicted role of Pluronic® P85 in enhancing pentamidine delivery to the choroid plexus based on the data in this study is shown in **Figure 3-42**.

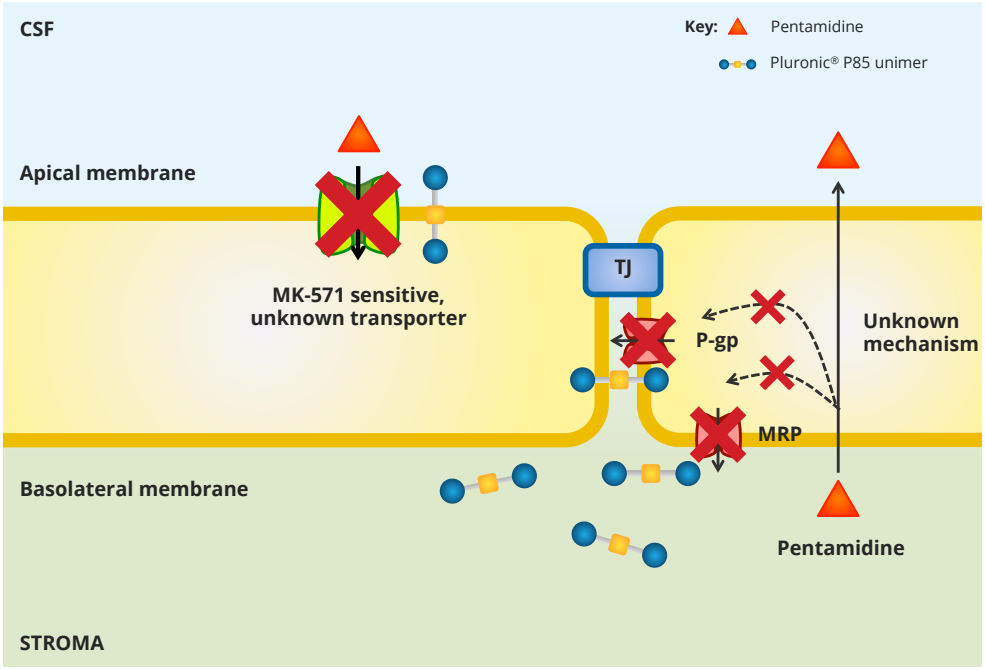

Figure 3-42: Theoretical interactions of Pluronic® P85 at sub-CMC concentrations and pentamidine with the choroid plexus epithelium. The mechanism for the movement of pentamidine across the choroid plexus epithelium cannot be elucidated from the data presented in the current study. However, it appears that removal of pentamidine from the epithelium is inhibited by Pluronic® P85, enhancing accumulation of pentamidine. Based on the isolated incubated choroid plexus data, Pluronic® P85 also inhibits the removal of pentamidine from the CSF back into the epithelium, possibly *via* a transporter that is sensitive to MK-571.

3.7.5 Future work

The data presented in this chapter formed the basis for a successful Biomedical Catalyst grant application jointly awarded by Technology Strategy Board (TSB) and Medical Research Council (MRC) in November 2012 in order to enable further evaluation of the suitability of Pluronic® block co-copolymers to enhance drug delivery to the CNS. While the application contained an extensive breakdown of a critical path for formulation evaluation and development based on milestones, a summary of future experiments to complete the present study is outlined below.

3.7.5.1 General strategy

As has already been alluded to, a number of the more than 50 Pluronic® block co-polymers could be evaluated in the same way that Pluronic® P85 was for the present study. Furthermore, it has been shown that combining different Pluronics® could enhance drug/micelle interactions and drug loading (Oh *et al.*, 2004), and thus mixtures of multiple co-polymers could also be considered. One of the most promising alternatives to Pluronic® P85 that could be considered are Pluronic® L61 and F127, which recently were combined as a blend with doxorubicin to form the drug candidate SP1049C in a phase 2 clinical trial for the treatment of oesophageal cancer (Valle *et al.*, 2011).

3.7.5.2 *In silico* experiments

Probing the effect of pentamidine and temperature on micelle size and morphology using atomistic simulations would help explain the unexpected decrease in aggregation number with increasing temperature *in vitro*, but also could help explain why the partition of pentamidine into Pluronic® P85 was found to decrease so steeply in optimised plasma. Understanding the precise location of pentamidine within the micelle structure (whether merely absorbed to the surface, or at the interface between the hydrophilic palisade layer or within the hydrophobic core itself) could help inform future optimisation to improve encapsulation. In addition to modelling where in the

micelle structure pentamidine exists, atomistic simulations could also be expected to demonstrate how many molecules of pentamidine are associated with each micelle.

The complex structure of proteins such as P-gp makes atomistic simulations unsuitable for modelling over any biologically relevant periods of time. Therefore coarse-grained molecular simulations to model how Pluronics® interact with P-gp or indeed any other ABC transporters in plasma membrane could be used to inform but also test future optimisation with different co-polymers and even blends of multiple co-polymers.

3.7.5.3 Animal experiments

While 0.5% m/v Pluronic® P85 was found not to enhance the accumulation of [^{3}H]-pentamidine into hCMEC/D3 cells *in vitro*, and this experiment was not replicated using *in situ* choroid plexus/brain perfusion due to time and financial constraints, it would be interesting to determine how the encapsulation of [^{3}H]-pentamidine within Pluronic® P85 micelles affects its transport across blood-CNS barriers *in vivo*.

An additional extension to the *in situ* perfusion experiments shown here would be to include specific transport inhibitors such as MK-571 in the artificial plasma to better understand the observed increase in [^{3}H]-pentamidine in BCECs following capillary depletion analysis of whole-brain following 10 minutes of perfusion. In carrying out these experiments one would have to be conscious of the fact that any transport inhibitors included in the artificial plasma are likely to also interact with Pluronic® P85 and this could alter the interactions of each with transporters.

In light of the un-published observations in hCMEC/D3 cells that between 60 and 120 minutes were required before any enhancements on [^{3}H]-pentamidine accumulation were detected, a natural extension to the isolated incubated choroid plexus experiments presented in this thesis would be to extend the incubation time from 10 minutes to 30 minutes, or more.

References

Abbasi, F., T. Asagmi, et al. (2001). "Plasma concentrations of asymmetric dimethylarginine are increased in patients with type 2 diabetes mellitus." *Am J Cardiol* **88**(10): 1201-1203.

Abbott, N. (2002). "Astrocyte-endothelial interactions and blood-brain barrier permeability." *J Anat* **200**(5): 527.

Abbott, N. J., A. A. Patabendige, et al. (2010). "Structure and function of the blood-brain barrier." *Neurobiol Dis* **37**(1): 13-25.

Abbott, N. J., L. Ronnback, et al. (2006). "Astrocyte-endothelial interactions at the blood-brain barrier." *Nat Rev Neurosci* **7**(1): 41-53.

Abe, T., M. Kakyo, et al. (1998). "Molecular characterization and tissue distribution of a new organic anion transporter subtype (oatp3) that transports thyroid hormones and taurocholate and comparison with oatp2." *J Biol Chem* **273**(35): 22395-22401.

Abe, T., H. Tohgi, et al. (2001). "Reduction in asymmetrical dimethylarginine, an endogenous nitric oxide synthase inhibitor, in the cerebrospinal fluid during aging and in patients with Alzheimer's disease." *Neurosci Lett* **312**(3): 177-179.

Achan, V., M. Broadhead, et al. (2003). "Asymmetric dimethylarginine causes hypertension and cardiac dysfunction in humans and is actively metabolized by dimethylarginine dimethylaminohydrolase." *Arterioscler Thromb Vasc Biol* **23**(8): 1455-1459.

Achan, V., C. T. Tran, et al. (2002). "all-trans-Retinoic acid increases nitric oxide synthesis by endothelial cells: a role for the induction of dimethylarginine dimethylaminohydrolase." *Circ Res* **90**(7): 764-769.

Adams, M. L., A. Lavasanifar, et al. (2003). "Amphiphilic block copolymers for drug delivery." *J Pharm Sci* **92**(7): 1343-1355.

Adams, M. R., R. McCredie, et al. (1997). "Oral L-arginine improves endothelium-dependent dilatation and reduces monocyte adhesion to endothelial cells in young men with coronary artery disease." *Atherosclerosis* **129**(2): 261-269.

Adle-Biassette, H., P. Olivier, et al. (2007). "Cortical consequences of in vivo blockade of monocarboxylate transport during brain development in mice." *Pediatr Res* **61**(1): 54-60.

Adriao, M., C. J. Chrisman, et al. (2004). "Arginine increases growth hormone gene expression in rat pituitary and GH3 cells." *Neuroendocrinology* **79**(1): 26-33.

Alakhova, D. Y., N. Y. Rapoport, et al. (2010). "Differential metabolic responses to pluronic in MDR and non-MDR cells: a novel pathway for chemosensitization of drug resistant cancers." *J Control Release* **142**(1): 89-100.

Alavijeh, M. S., M. Chishty, et al. (2005). "Drug metabolism and pharmacokinetics, the blood-brain barrier, and central nervous system drug discovery." *NeuroRx* **2**(4): 554-571.

Alba-Roth, J., O. A. Muller, et al. (1988). "Arginine stimulates growth hormone secretion by suppressing endogenous somatostatin secretion." *J Clin Endocrinol Metab* **67**(6): 1186-1189.

Alkhamis, K. A., H. Allaboun, et al. (2003). "Study of the solubilization of gliclazide by aqueous micellar solutions." *J Pharm Sci* **92**(4): 839-846.

Allen, M. P. (2004). Introduction to Molecular Dynamics Simulation. *In*: Computational Soft Matter: from Synthetic Polymers to Proteins. N. Attig, NIC. **23:** 1-27.

Aller, S. G., J. Yu, et al. (2009). "Structure of P-glycoprotein reveals a molecular basis for poly-specific drug binding." *Science* **323**(5922): 1718-1722.

Alvarez-Lorenzo, C., A. Rey-Rico, et al. (2010). "Poloxamine-based nanomaterials for drug delivery." *Front Biosci (Elite Ed)* **2**: 424-440.

Alvira-Botero, X. and E. M. Carro (2010). "Clearance of amyloid-beta peptide across the choroid plexus in Alzheimer's disease." *Curr Aging Sci* **3**(3): 219-229.

Amar, A. P. and M. H. Weiss (2003). "Pituitary anatomy and physiology." *Neurosurg Clin N Am* **14**(1): 11-23, v.

Anderson, J. A., C. D. Lorenz, et al. (2008). "Micellar crystals in solution from molecular dynamics simulations." *J Chem Phys* **128**(18): 184906.

Anderson, J. A. and A. Travesset (2006). "Coarse-Grained Simulations of Gels of Nonionic Multiblock Copolymers with Hydrophobic Groups." *Macromolecules* **39**(15): 5143–5151.

Anderson, R. G. (1998). "The caveolae membrane system." *Annu Rev Biochem* **67**: 199-225.

Andreeva, A. Y., E. Krause, et al. (2001). "Protein kinase C regulates the phosphorylation and cellular localization of occludin." *J Biol Chem* **276**(42): 38480-38486.

Andreeva, A. Y., J. Piontek, et al. (2006). "Assembly of tight junction is regulated by the antagonism of conventional and novel protein kinase C isoforms." *Int J Biochem Cell Biol* **38**(2): 222-233.

Anstrom, J. A., C. R. Thore, et al. (2007). "Immunolocalization of tight junction proteins in blood vessels in human germinal matrix and cortex." *Histochem Cell Biol* **127**(2): 205-213.

Arancibia-Garavilla, Y., F. Toledo, et al. (2003). "Nitric oxide synthesis requires activity of the cationic and neutral amino acid transport system y+L in human umbilical vein endothelium." *Exp Physiol* **88**(6): 699-710.

Argandona, E. G., H. Bengoetxea, et al. (2005). "Lack of experience-mediated differences in the immunohistochemical expression of blood-brain barrier markers (EBA and GluT-1) during the postnatal development of the rat visual cortex." *Brain Res Dev Brain Res* **156**(2): 158-166.

Arlt, S., F. Schulze, et al. (2008). "Asymmetrical dimethylarginine is increased in plasma and decreased in cerebrospinal fluid of patients with Alzheimer's disease." *Dement Geriatr Cogn Disord* **26**(1): 58-64.

Arluison, M., M. Quignon, et al. (2004). "Distribution and anatomical localization of the glucose transporter 2 (GLUT2) in the adult rat brain--an immunohistochemical study." *J Chem Neuroanat* **28**(3): 117-136.

Armulik, A., G. Genove, et al. (2010). "Pericytes regulate the blood-brain barrier." *Nature* **468**(7323): 557-561.

Arnold, W. P., C. K. Mittal, et al. (1977). "Nitric oxide activates guanylate cyclase and increases guanosine 3':5'-cyclic monophosphate levels in various tissue preparations." *Proc Natl Acad Sci U S A* **74**(8): 3203-3207.

Artzner, F., S. Geiger, et al. (2007). "Interactions between poloxamers in aqueous solutions: micellization and gelation studied by differential scanning calorimetry, small angle X-ray scattering, and rheology." *Langmuir* **23**(9): 5085-5092.

Balasegaram, M., H. Young, et al. (2009). "Effectiveness of melarsoprol and eflornithine as first-line regimens for gambiense sleeping sickness in nine Medecins Sans Frontieres programmes." *Trans R Soc Trop Med Hyg* **103**(3): 280-290.

Balda, M. S., J. A. Whitney, et al. (1996). "Functional dissociation of paracellular permeability and transepithelial electrical resistance and disruption of the apical-basolateral intramembrane diffusion barrier by expression of a mutant tight junction membrane protein." *J Cell Biol* **134**(4): 1031-1049.

Bamforth, S. D., U. Kniesel, et al. (1999). "A dominant mutant of occludin disrupts tight junction structure and function." *J Cell Sci* **112 (Pt 12)**: 1879-1888.

Banos, G., P. M. Daniel, et al. (1974). "Saturation of a shared mechanism which transports L-arginine and L-lysine into the brain of the living rat." *J Physiol* **236**(1): 29-41.

Barres, B. A. (2008). "The mystery and magic of glia: a perspective on their roles in health and disease." *Neuron* **60**(3): 430-440.

Barry, B. W. and D. I. El Eini (1976). "Solubilization of hydrocortisone, dexamethasone, testosterone and progesterone by long-chain polyoxyethylene surfactants." *J Pharm Pharmacol* **28**(3): 210-218.

Batrakova, E., S. Lee, et al. (1999a). "Fundamental relationships between the composition of pluronic block copolymers and their hypersensitization effect in MDR cancer cells." *Pharm Res* **16**(9): 1373-1379.

Batrakova, E. V., H. Y. Han, et al. (1998). "Effects of pluronic P85 unimers and micelles on drug permeability in polarized BBMEC and Caco-2 cells." *Pharm Res* **15**(10): 1525-1532.

Batrakova, E. V., S. Li, et al. (2003). "Optimal structure requirements for pluronic block copolymers in modifying P-glycoprotein drug efflux transporter activity in bovine brain microvessel endothelial cells." *J Pharmacol Exp Ther* **304**(2): 845-854.

Batrakova, E. V., S. Li, et al. (2001a). "Mechanism of sensitization of MDR cancer cells by Pluronic block copolymers: Selective energy depletion." *Br J Cancer* **85**(12): 1987-1997.

Batrakova, E. V., S. Li, et al. (2004a). "Distribution kinetics of a micelle-forming block copolymer Pluronic P85." *J Control Release* **100**(3): 389-397.

Batrakova, E. V., S. Li, et al. (2004b). "Effect of pluronic P85 on ATPase activity of drug efflux transporters." *Pharm Res* **21**(12): 2226-2233.

Batrakova, E. V., S. Li, et al. (1999b). "Pluronic P85 increases permeability of a broad spectrum of drugs in polarized BBMEC and Caco-2 cell monolayers." *Pharm Res* **16**(9): 1366-1372.

Batrakova, E. V., S. Li, et al. (2001b). "Mechanism of pluronic effect on P-glycoprotein efflux system in blood-brain barrier: contributions of energy depletion and membrane fluidization." *J Pharmacol Exp Ther* **299**(2): 483-493.

Batrakova, E. V., D. W. Miller, et al. (2001c). "Pluronic P85 enhances the delivery of digoxin to the brain: in vitro and in vivo studies." *J Pharmacol Exp Ther* **296**(2): 551-557.

Batrakova, E. V., Y. Zhang, et al. (2004c). "Effects of pluronic P85 on GLUT1 and MCT1 transporters in the blood-brain barrier." *Pharm Res* **21**(11): 1993-2000.

Bazzoni, G. and E. Dejana (2004). "Endothelial cell-to-cell junctions: molecular organization and role in vascular homeostasis." *Physiol Rev* **84**(3): 869-901.

Bazzoni, G., O. M. Martinez-Estrada, et al. (2000). "Homophilic interaction of junctional adhesion molecule." *J Biol Chem* **275**(40): 30970-30976.

Beck, D. W., H. V. Vinters, et al. (1984). "Glial cells influence polarity of the blood-brain barrier." *J Neuropathol Exp Neurol* **43**(3): 219-224.

Begley, D. J. (2004). "ABC transporters and the blood-brain barrier." *Curr Pharm Des* **10**(12): 1295-1312.

Begley, D. J. and M. W. Brightman (2003). "Structural and functional aspects of the blood-brain barrier." *Prog Drug Res* **61**: 39-78.

Bell, R. D., E. A. Winkler, et al. (2010). "Pericytes control key neurovascular functions and neuronal phenotype in the adult brain and during brain aging." *Neuron* **68**(3): 409-427.

Benaim, G., C. Lopez-Estrano, et al. (1993). "A calmodulin-stimulated Ca2+ pump in plasma-membrane vesicles from Trypanosoma brucei; selective inhibition by pentamidine." *Biochem J* **296 (Pt 3)**: 759-763.

Benet, L. Z. (2009). "The drug transporter-metabolism alliance: uncovering and defining the interplay." *Mol Pharm* **6**(6): 1631-1643.

Berger, B. J., V. V. Reddy, et al. (1991). "Hydroxylation of pentamidine by rat liver microsomes." *J Pharmacol Exp Ther* **256**(3): 883-889.

Bergersen, L., O. Waerhaug, et al. (2001). "A novel postsynaptic density protein: the monocarboxylate transporter MCT2 is co-localized with delta-glutamate receptors in postsynaptic densities of parallel fiber-Purkinje cell synapses." *Exp Brain Res* **136**(4): 523-534.

Bergersen, L. H. (2007). "Is lactate food for neurons? Comparison of monocarboxylate transporter subtypes in brain and muscle." *Neuroscience* **145**(1): 11-19.

Bernacki, J., A. Dobrowolska, et al. (2008). "Physiology and pharmacological role of the blood-brain barrier." *Pharmacol Rep* **60**(5): 600-622.

Betz, A. L., J. A. Firth, et al. (1980). "Polarity of the blood-brain barrier: distribution of enzymes between the luminal and antiluminal membranes of brain capillary endothelial cells." *Brain Res* **192**(1): 17-28.

Betz, A. L. and G. W. Goldstein (1978). "Polarity of the blood-brain barrier: neutral amino acid transport into isolated brain capillaries." *Science* **202**(4364): 225-227.

Black, J. A., H. Sontheimer, et al. (1993). "Spinal cord astrocytes in vitro: phenotypic diversity and sodium channel immunoreactivity." *Glia* **7**(4): 272-285.

Bobbie, M. W., S. Roy, et al. (2010). "Reduced connexin 43 expression and its effect on the development of vascular lesions in retinas of diabetic mice." *Invest Ophthalmol Vis Sci* **51**(7): 3758-3763.

Bode-Boger, S. M., R. H. Boger, et al. (1996). "L-arginine induces nitric oxide-dependent vasodilation in patients with critical limb ischemia. A randomized, controlled study." *Circulation* **93**(1): 85-90.

Bode-Boger, S. M., R. H. Boger, et al. (1998). "L-arginine-induced vasodilation in healthy humans: pharmacokinetic-pharmacodynamic relationship." *Br J Clin Pharmacol* **46**(5): 489-497.

Bode-Boger, S. M., F. Scalera, et al. (2007). "The L-arginine paradox: Importance of the L-arginine/asymmetrical dimethylarginine ratio." *Pharmacol Ther* **114**(3): 295-306.

Boffa, L. C., J. Karn, et al. (1977). "Distribution of NG, NG,-dimethylarginine in nuclear protein fractions." *Biochem Biophys Res Commun* **74**(3): 969-976.

Boger, R. H. and S. M. Bode-Boger (2001). "The clinical pharmacology of L-arginine." *Annu Rev Pharmacol Toxicol* **41**: 79-99.

Boger, R. H., S. M. Bode-Boger, et al. (1998a). "Asymmetric dimethylarginine (ADMA): a novel risk factor for endothelial dysfunction: its role in hypercholesterolemia." *Circulation* **98**(18): 1842-1847.

Boger, R. H., S. M. Bode-Boger, et al. (1998b). "Restoring vascular nitric oxide formation by L-arginine improves the symptoms of intermittent claudication in patients with peripheral arterial occlusive disease." *J Am Coll Cardiol* **32**(5): 1336-1344.

Boger, R. H., S. M. Bode-Boger, et al. (1997). "Biochemical evidence for impaired nitric oxide synthesis in patients with peripheral arterial occlusive disease." *Circulation* **95**(8): 2068-2074.

Boger, R. H., S. M. Bode-Boger, et al. (2000a). "An endogenous inhibitor of nitric oxide synthase regulates endothelial adhesiveness for monocytes." *J Am Coll Cardiol* **36**(7): 2287-2295.

Boger, R. H., K. Sydow, et al. (2000b). "LDL cholesterol upregulates synthesis of asymmetrical dimethylarginine in human endothelial cells: involvement of S-adenosylmethionine-dependent methyltransferases." *Circ Res* **87**(2): 99-105.

Bogle, R. G., R. J. MacAllister, et al. (1995). "Induction of NG-monomethyl-L-arginine uptake: a mechanism for differential inhibition of NO synthases?" *Am J Physiol* **269**(3 Pt 1): C750-756.

Bogumil, R., M. Knipp, et al. (1998). "Characterization of dimethylargininase from bovine brain: evidence for a zinc binding site." *Biochemistry* **37**(14): 4791-4798.

Boisvert, F. M., J. Cote, et al. (2003). "A proteomic analysis of arginine-methylated protein complexes." *Mol Cell Proteomics* **2**(12): 1319-1330.

Bouldin, T. W. and M. R. Krigman (1975). "Differential permeability of cerebral capillary and choroid plexus to lanthanum ion." *Brain Res* **99**(2): 444-448.

Bozidis, P., C. D. Williamson, et al. (2008). "Mitochondrial and secretory human cytomegalovirus UL37 proteins traffic into mitochondrion-associated membranes of human cells." *J Virol* **82**(6): 2715-2726.

Bradbury, M. W. (1993). "The blood-brain barrier." *Exp Physiol* **78**(4): 453-472.

Bredt, D. S. and S. H. Snyder (1990). "Isolation of nitric oxide synthetase, a calmodulin-requiring enzyme." *Proc Natl Acad Sci U S A* **87**(2): 682-685.

Brightman, M. W. and T. S. Reese (1969). "Junctions between intimately apposed cell membranes in the vertebrate brain." *J Cell Biol* **40**(3): 648-677.

Brizzee, K. R. and L. M. Neal (1954). "A re-evaluation of the cellular morphology of the area postrema in view of recent evidence for a chemoreceptor function." *J Comp Neurol* **100**(1): 41-61.

Bronger, H., J. Konig, et al. (2005). "ABCC drug efflux pumps and organic anion uptake transporters in human gliomas and the blood-tumor barrier." *Cancer Res* **65**(24): 11419-11428.

Brown, A. M., S. Baltan Tekkok, et al. (2004). "Energy transfer from astrocytes to axons: the role of CNS glycogen." *Neurochem Int* **45**(4): 529-536.

Brown, A. M. and B. R. Ransom (2007). "Astrocyte glycogen and brain energy metabolism." *Glia* **55**(12): 1263-1271.

Brown, R. C. (2012). "Accumulation of pentamidine co-formulated with Pluronic® P85 in hCMEC/D3 cells." *Un-published data*.

Bruggemann, E. P., U. A. Germann, et al. (1989). "Two different regions of P-glycoprotein [corrected] are photoaffinity-labeled by azidopine." *J Biol Chem* **264**(26): 15483-15488.

Brun, R., J. Blum, et al. (2010). "Human African trypanosomiasis." *Lancet* **375**(9709): 148-159.

Bulau, P., D. Zakrzewicz, et al. (2007). "Analysis of methylarginine metabolism in the cardiovascular system identifies the lung as a major source of ADMA." *Am J Physiol Lung Cell Mol Physiol* **292**(1): L18-24.

Burri, C. (2010). "Chemotherapy against human African trypanosomiasis: is there a road to success?" *Parasitology* **137**(14): 1987-1994.

Burri, C., S. Nkunku, et al. (2000). "Efficacy of new, concise schedule for melarsoprol in treatment of sleeping sickness caused by Trypanosoma brucei gambiense: a randomised trial." *Lancet* **355**(9213): 1419-1425.

Busch, A. E., T. Herzer, et al. (1994). "Opposite directed currents induced by the transport of dibasic and neutral amino acids in Xenopus oocytes expressing the protein rBAT." *J Biol Chem* **269**(41): 25581-25586.

Cakir, E., O. Ozcan, et al. (2005). "Elevated plasma concentration of asymmetric dimethylarginine that is reduced by single dose testosterone administration in idiopathic hypogonadotropic hypogonadism patients." *J Clin Endocrinol Metab* **90**(3): 1651-1654.

Calatozzolo, C., M. Gelati, et al. (2005). "Expression of drug resistance proteins Pgp, MRP1, MRP3, MRP5 and GST-pi in human glioma." *J Neurooncol* **74**(2): 113-121.

Calderano, S. G., P. D. de Melo Godoy, et al. (2011). "Trypanosome prereplication machinery: a potential new target for an old problem." *Enzyme Res* **2011**: 518258.

Calonge, M. J., P. Gasparini, et al. (1994). "Cystinuria caused by mutations in rBAT, a gene involved in the transport of cystine." *Nat Genet* **6**(4): 420-425.

Cammer, W., F. Tansey, et al. (1989). "Differential localization of glutathione-S-transferase Yp and Yb subunits in oligodendrocytes and astrocytes of rat brain." *J Neurochem* **52**(3): 876-883.

Cardounel, A. J., H. Cui, et al. (2007). "Evidence for the pathophysiological role of endogenous methylarginines in regulation of endothelial NO production and vascular function." *J Biol Chem* **282**(2): 879-887.

Cardounel, A. J. and J. L. Zweier (2002). "Endogenous methylarginines regulate neuronal nitric-oxide synthase and prevent excitotoxic injury." *J Biol Chem* **277**(37): 33995-34002.

Carver, L. A. and J. E. Schnitzer (2003). "Caveolae: mining little caves for new cancer targets." *Nat Rev Cancer* **3**(8): 571-581.

Chairoungdua, A., H. Segawa, et al. (1999). "Identification of an amino acid transporter associated with the cystinuria-related type II membrane glycoprotein." *J Biol Chem* **274**(41): 28845-28848.

Charles, A. C., J. E. Merrill, et al. (1991). "Intercellular signaling in glial cells: calcium waves and oscillations in response to mechanical stimulation and glutamate." *Neuron* **6**(6): 983-992.

Checchi, F., J. A. Filipe, et al. (2008). "Estimates of the duration of the early and late stage of gambiense sleeping sickness." *BMC Infect Dis* **8**: 16.

Chen, Z. S. and A. K. Tiwari (2011). "Multidrug resistance proteins (MRPs/ABCCs) in cancer chemotherapy and genetic diseases." *FEBS J* **278**(18): 3226-3245.

Chillaron, J., R. Estevez, et al. (1996). "Obligatory amino acid exchange via systems bo,+-like and y+L-like. A tertiary active transport mechanism for renal reabsorption of cystine and dibasic amino acids." *J Biol Chem* **271**(30): 17761-17770.

Choudhuri, S., N. J. Cherrington, et al. (2003). "Constitutive expression of various xenobiotic and endobiotic transporter mRNAs in the choroid plexus of rats." *Drug Metab Dispos* **31**(11): 1337-1345.

Christopherson, K. S., E. M. Ullian, et al. (2005). "Thrombospondins are astrocyte-secreted proteins that promote CNS synaptogenesis." *Cell* **120**(3): 421-433.

Cisternino, S., C. Mercier, et al. (2004). "Expression, up-regulation, and transport activity of the multidrug-resistance protein Abcg2 at the mouse blood-brain barrier." *Cancer Res* **64**(9): 3296-3301.

Cisternino, S., C. Rousselle, et al. (2003). "Apparent lack of Mrp1-mediated efflux at the luminal side of mouse blood-brain barrier endothelial cells." *Pharm Res* **20**(6): 904-909.

Clarkson, P., M. R. Adams, et al. (1996). "Oral L-arginine improves endothelium-dependent dilation in hypercholesterolemic young adults." *J Clin Invest* **97**(8): 1989-1994.

Closs, E. I., F. Z. Basha, et al. (1997). "Interference of L-arginine analogues with L-arginine transport mediated by the y+ carrier hCAT-2B." *Nitric Oxide* **1**(1): 65-73.

Closs, E. I., J. P. Boissel, et al. (2006). "Structure and function of cationic amino acid transporters (CATs)." *J Membr Biol* **213**(2): 67-77.

Colabufo, N. A., F. Berardi, et al. (2010). "Perspectives of P-glycoprotein modulating agents in oncology and neurodegenerative diseases: pharmaceutical, biological, and diagnostic potentials." *J Med Chem* **53**(5): 1883-1897.

Collins, J. M. and R. L. Dedrick (1983). "Distributed model for drug delivery to CSF and brain tissue." *Am J Physiol* **245**(3): R303-310.

Cooke, J. P., N. A. Andon, et al. (1991). "Arginine restores cholinergic relaxation of hypercholesterolemic rabbit thoracic aorta." *Circulation* **83**(3): 1057-1062.

Cooray, H. C., C. G. Blackmore, et al. (2002). "Localisation of breast cancer resistance protein in microvessel endothelium of human brain." *Neuroreport* **13**(16): 2059-2063.

Cordon-Cardo, C., J. P. O'Brien, et al. (1989). "Multidrug-resistance gene (P-glycoprotein) is expressed by endothelial cells at blood-brain barrier sites." *Proc Natl Acad Sci U S A* **86**(2): 695-698.

Cornell-Bell, A. H., S. M. Finkbeiner, et al. (1990). "Glutamate induces calcium waves in cultured astrocytes: long-range glial signaling." *Science* **247**(4941): 470-473.

Cornford, E. M., S. Hyman, et al. (1998). "Glut1 glucose transporter in the primate choroid plexus endothelium." *J Neuropathol Exp Neurol* **57**(5): 404-414.

Cornford, E. M., J. B. Varesi, et al. (1997). "Mitochondrial content of choroid plexus epithelium." *Exp Brain Res* **116**(3): 399-405.

Cottrell, G. T. and A. V. Ferguson (2004). "Sensory circumventricular organs: central roles in integrated autonomic regulation." *Regul Pept* **117**(1): 11-23.

Coutinho, A. and M. Prieto (1995). "Self-association of the polyene antibiotic nystatin in dipalmitoylphosphatidylcholine vesicles: a time-resolved fluorescence study." *Biophys J* **69**(6): 2541-2557.

Creager, M. A., S. J. Gallagher, et al. (1992). "L-arginine improves endothelium-dependent vasodilation in hypercholesterolemic humans." *J Clin Invest* **90**(4): 1248-1253.

Crone, C. and S. P. Olesen (1982). "Electrical resistance of brain microvascular endothelium." *Brain Res* **241**(1): 49-55.

Cross, G. A., L. E. Wirtz, et al. (1998). "Regulation of vsg expression site transcription and switching in Trypanosoma brucei." *Mol Biochem Parasitol* **91**(1): 77-91.

Culotta, E. and D. E. Koshland, Jr. (1992). "NO news is good news." *Science* **258**(5090): 1862-1865.

Currier, S. J., K. Ueda, et al. (1989). "Deletion and insertion mutants of the multidrug transporter." *J Biol Chem* **264**(24): 14376-14381.

Czeredys, M., C. Mysiorek, et al. (2008). "A polarized localization of amino acid/carnitine transporter B(0,+) (ATB(0,+)) in the blood-brain barrier." *Biochem Biophys Res Commun* **376**(2): 267-270.

Dagenais, C., C. Rousselle, et al. (2000). "Development of an in situ mouse brain perfusion model and its application to mdr1a P-glycoprotein-deficient mice." *J Cereb Blood Flow Metab* **20**(2): 381-386.

Dahlin, A., J. Royall, et al. (2009). "Expression profiling of the solute carrier gene family in the mouse brain." *J Pharmacol Exp Ther* **329**(2): 558-570.

Daneman, R., L. Zhou, et al. (2010). "Pericytes are required for blood-brain barrier integrity during embryogenesis." *Nature* **468**(7323): 562-566.

Daood, M., C. Tsai, et al. (2008). "ABC transporter (P-gp/ABCB1, MRP1/ABCC1, BCRP/ABCG2) expression in the developing human CNS." *Neuropediatrics* **39**(4): 211-218.

Das, I., N. S. Khan, et al. (1996). "Elevated endogenous nitric oxide synthase inhibitor in schizophrenic plasma may reflect abnormalities in brain nitric oxide production." *Neurosci Lett* **215**(3): 209-211.

Dauchy, S., F. Dutheil, et al. (2008). "ABC transporters, cytochromes P450 and their main transcription factors: expression at the human blood-brain barrier." *J Neurochem* **107**(6): 1518-1528.

de La Guardia, M., E. Peris-Cardells, et al. (1991). "Fluorimetric determination of binding constants between micelles and chemical systems." *Microchemical journal* **44**(2): 193-200.

De Robertis, E. and H. M. Gerschenfeld (1961). Submicroscopic Morphology and Function of Glial Cells. *In*: International Review of Neurobiology. C. P. Carl and R. S. John, Academic Press. **Volume 3:** 1-65.

Deane, R. and M. B. Segal (1985). "The transport of sugars across the perfused choroid plexus of the sheep." *J Physiol* **362**: 245-260.

Deeley, R. G. and S. P. Cole (2006). "Substrate recognition and transport by multidrug resistance protein 1 (ABCC1)." *FEBS Lett* **580**(4): 1103-1111.

Deeley, R. G., C. Westlake, et al. (2006). "Transmembrane transport of endo- and xenobiotics by mammalian ATP-binding cassette multidrug resistance proteins." *Physiol Rev* **86**(3): 849-899.

Deen, W. M., M. J. Lazzara, et al. (2001). "Structural determinants of glomerular permeability." *Am J Physiol Renal Physiol* **281**(4): F579-596.

Dejana, E. (2004). "Endothelial cell-cell junctions: happy together." *Nat Rev Mol Cell Biol* **5**(4): 261-270.

Del Bigio, M. R. (1995). "The ependyma: a protective barrier between brain and cerebrospinal fluid." *Glia* **14**(1): 1-13.

Demeule, M., A. Regina, et al. (2002). "Drug transport to the brain: key roles for the efflux pump P-glycoprotein in the blood-brain barrier." *Vascul Pharmacol* **38**(6): 339-348.

Deves, R. and C. A. Boyd (1998). "Transporters for cationic amino acids in animal cells: discovery, structure, and function." *Physiol Rev* **78**(2): 487-545.

Deves, R., P. Chavez, et al. (1992). "Identification of a new transport system (y+L) in human erythrocytes that recognizes lysine and leucine with high affinity." *J Physiol* **454**: 491-501.

Diaz-Flores, L., R. Gutierrez, et al. (2009). "Pericytes. Morphofunction, interactions and pathology in a quiescent and activated mesenchymal cell niche." *Histol Histopathol* **24**(7): 909-969.

Dietrich, M. O., C. Spuch, et al. (2008). "Megalin mediates the transport of leptin across the blood-CSF barrier." *Neurobiol Aging* **29**(6): 902-912.

Docampo, R. and S. N. Moreno (2003). "Current chemotherapy of human African trypanosomiasis." *Parasitol Res* **90 Supp 1**: S10-13.

Donelson, J. E., K. L. Hill, et al. (1998). "Multiple mechanisms of immune evasion by African trypanosomes." *Mol Biochem Parasitol* **91**(1): 51-66.

Dore-Duffy, P. and K. Cleary (2011). "Morphology and properties of pericytes." *Methods Mol Biol* **686**: 49-68.

Dorszewska, J., J. Florczak, et al. (2007). 1.102 Homocysteine and asymmetric dimethylarginine (ADMA) in the plasma of patients with Parkinson's disease. Abstracts of the XVII WFN Congress on Parkinson's Disease and Related Disorders, Parkinsonism & Related Disorders, 13: S34.

Doua, F., T. W. Miezan, et al. (1996). "The efficacy of pentamidine in the treatment of early-late stage Trypanosoma brucei gambiense trypanosomiasis." *Am J Trop Med Hyg* **55**(6): 586-588.

Drab, M., P. Verkade, et al. (2001). "Loss of caveolae, vascular dysfunction, and pulmonary defects in caveolin-1 gene-disrupted mice." *Science* **293**(5539): 2449-2452.

Drexler, H., A. M. Zeiher, et al. (1991). "Correction of endothelial dysfunction in coronary microcirculation of hypercholesterolaemic patients by L-arginine." *Lancet* **338**(8782-8783): 1546-1550.

Duelli, R., B. E. Enerson, et al. (2000). "Expression of large amino acid transporter LAT1 in rat brain endothelium." *J Cereb Blood Flow Metab* **20**(11): 1557-1562.

Ehrlich, P. (1885). Das Sauerstoff-Bedurfnis des Organismus; eine farbenanlytische Studie. Berlin, Germany, Hirschwald.

Eisenblatter, T., S. Huwel, et al. (2003). "Characterisation of the brain multidrug resistance protein (BMDP/ABCG2/BCRP) expressed at the blood-brain barrier." *Brain Res* **971**(2): 221-231.

el-Bacha, R. S. and A. Minn (1999). "Drug metabolizing enzymes in cerebrovascular endothelial cells afford a metabolic protection to the brain." *Cell Mol Biol (Noisy-le-grand)* **45**(1): 15-23.

Ernst, S. A., J. R. Palacios, 2nd, et al. (1986). "Immunocytochemical localization of Na+,K+-ATPase catalytic polypeptide in mouse choroid plexus." *J Histochem Cytochem* **34**(2): 189-195.

Estevez, R., M. Camps, et al. (1998). "The amino acid transport system y+L/4F2hc is a heteromultimeric complex." *FASEB J* **12**(13): 1319-1329.

Eyal, S., P. Hsiao, et al. (2009). "Drug interactions at the blood-brain barrier: fact or fantasy?" *Pharmacol Ther* **123**(1): 80-104.

Fanning, A. S., B. J. Jameson, et al. (1998). "The tight junction protein ZO-1 establishes a link between the transmembrane protein occludin and the actin cytoskeleton." *J Biol Chem* **273**(45): 29745-29753.

Faraci, F. M. (1990). "Role of nitric oxide in regulation of basilar artery tone in vivo." *Am J Physiol* **259**(4 Pt 2): H1216-1221.

Farkas, E. and P. G. Luiten (2001). "Cerebral microvascular pathology in aging and Alzheimer's disease." *Prog Neurobiol* **64**(6): 575-611.

Farrell, C. L. and W. M. Pardridge (1991). "Blood-brain barrier glucose transporter is asymmetrically distributed on brain capillary endothelial lumenal and ablumenal membranes: an electron microscopic immunogold study." *Proc Natl Acad Sci U S A* **88**(13): 5779-5783.

Feldman, G. J., J. M. Mullin, et al. (2005). "Occludin: structure, function and regulation." *Adv Drug Deliv Rev* **57**(6): 883-917.

Fenstermacher, J., P. Gross, et al. (1988). "Structural and functional variations in capillary systems within the brain." *Ann N Y Acad Sci* **529**: 21-30.

Fickling, S. A., D. P. Holden, et al. (1999). "Regulation of macrophage nitric oxide synthesis by endothelial cells: a role for NG,NG-dimethylarginine." *Acta Physiol Scand* **167**(2): 145-150.

Fields, H. M., L. Rinaman, et al. (1999). "Distribution of glucose transporter isoform-3 and hexokinase I in the postnatal murine brain." *Brain Res* **846**(2): 260-264.

Forstermann, U., E. I. Closs, et al. (1994). "Nitric oxide synthase isozymes. Characterization, purification, molecular cloning, and functions." *Hypertension* **23**(6 Pt 2): 1121-1131.

Fry, M. and A. V. Ferguson (2007). "The sensory circumventricular organs: brain targets for circulating signals controlling ingestive behavior." *Physiol Behav* **91**(4): 413-423.

Furuse, M., K. Fujita, et al. (1998). "Claudin-1 and -2: novel integral membrane proteins localizing at tight junctions with no sequence similarity to occludin." *J Cell Biol* **141**(7): 1539-1550.

Furuse, M., T. Hirase, et al. (1993). "Occludin: a novel integral membrane protein localizing at tight junctions." *J Cell Biol* **123**(6 Pt 2): 1777-1788.

Furuse, M., H. Sasaki, et al. (1999). "Manner of interaction of heterogeneous claudin species within and between tight junction strands." *J Cell Biol* **147**(4): 891-903.

Galietta, L. J., L. Musante, et al. (1998). "An electrogenic amino acid transporter in the apical membrane of cultured human bronchial epithelial cells." *Am J Physiol* **275**(5 Pt 1): L917-923.

Gao, B., B. Stieger, et al. (1999). "Localization of the organic anion transporting polypeptide 2 (Oatp2) in capillary endothelium and choroid plexus epithelium of rat brain." *J Histochem Cytochem* **47**(10): 1255-1264.

Garcia, J. G. and K. L. Schaphorst (1995). "Regulation of endothelial cell gap formation and paracellular permeability." *J Investig Med* **43**(2): 117-126.

Garthwaite, J., S. L. Charles, et al. (1988). "Endothelium-derived relaxing factor release on activation of NMDA receptors suggests role as intercellular messenger in the brain." *Nature* **336**(6197): 385-388.

Gary, J. D. and S. Clarke (1998). "RNA and protein interactions modulated by protein arginine methylation." *Prog Nucleic Acid Res Mol Biol* **61**: 65-131.

Gatlik-Landwojtowicz, E., P. Aanismaa, et al. (2006). "Quantification and characterization of P-glycoprotein-substrate interactions." *Biochemistry* **45**(9): 3020-3032.

Gazzin, S., N. Strazielle, et al. (2008). "Differential expression of the multidrug resistance-related proteins ABCb1 and ABCc1 between blood-brain interfaces." *J Comp Neurol* **510**(5): 497-507.

Gehrmann, J., Y. Matsumoto, et al. (1995). "Microglia: intrinsic immuneffector cell of the brain." *Brain Res Brain Res Rev* **20**(3): 269-287.

Gerhart, D. Z., R. J. LeVasseur, et al. (1989). "Glucose transporter localization in brain using light and electron immunocytochemistry." *J Neurosci Res* **22**(4): 464-472.

Gey, G. O. and M. K. Gey (1936). "The Maintenance of Human Normal Cells and Tumor Cells in Continuous Culture: I. Preliminary Report: Cultivation of Mesoblastic Tumors and Normal Tissue and Notes on Methods of Cultivation." *The American Journal of Cancer* **27**(1): 45-76.

Ghersi-Egea, J. F., B. Leninger-Muller, et al. (1994). "Localization of drug-metabolizing enzyme activities to blood-brain interfaces and circumventricular organs." *J Neurochem* **62**(3): 1089-1096.

Giacomini, K. M., S. M. Huang, et al. (2010). "Membrane transporters in drug development." *Nat Rev Drug Discov* **9**(3): 215-236.

Girerd, X. J., A. T. Hirsch, et al. (1990). "L-arginine augments endothelium-dependent vasodilation in cholesterol-fed rabbits." *Circ Res* **67**(6): 1301-1308.

Gjedde, A. (1981). "High- and low-affinity transport of D-glucose from blood to brain." *J Neurochem* **36**(4): 1463-1471.

Gjedde, A. (1982). "Calculation of cerebral glucose phosphorylation from brain uptake of glucose analogs in vivo: a re-examination." *Brain Res* **257**(2): 237-274.

Gold, M. E., P. A. Bush, et al. (1989). "Depletion of arterial L-arginine causes reversible tolerance to endothelium-dependent relaxation." *Biochem Biophys Res Commun* **164**(2): 714-721.

Goldman, E. E. (1913). "Vitalfarbung am Zentralnervensystem." *Abh. Preuss. Arkad. Wiss. Phys. Math.* **K1**(1): 1-60.

Gomez-Pinilla, F. (2008). "Brain foods: the effects of nutrients on brain function." *Nat Rev Neurosci* **9**(7): 568-578.

Goonasekera, C. D., D. D. Rees, et al. (1997). "Nitric oxide synthase inhibitors and hypertension in children and adolescents." *J Hypertens* **15**(8): 901-909.

Gordon, G. R., S. J. Mulligan, et al. (2007). "Astrocyte control of the cerebrovasculature." *Glia* **55**(12): 1214-1221.

Gottesman, M. M. and I. Pastan (1993). "Biochemistry of multidrug resistance mediated by the multidrug transporter." *Annu Rev Biochem* **62**: 385-427.

Gourine, A. V., V. Kasymov, et al. (2010). "Astrocytes control breathing through pH-dependent release of ATP." *Science* **329**(5991): 571-575.

Grab, D. J. and P. G. Kennedy (2008). "Traversal of human and animal trypanosomes across the blood-brain barrier." *J Neurovirol* **14**(5): 344-351.

Greenberger, L. M. (1993). "Major photoaffinity drug labeling sites for iodoaryl azidoprazosin in P-glycoprotein are within, or immediately C-terminal to, transmembrane domains 6 and 12." *J Biol Chem* **268**(15): 11417-11425.

Guo, F. H., H. R. De Raeve, et al. (1995). "Continuous nitric oxide synthesis by inducible nitric oxide synthase in normal human airway epithelium in vivo." *Proc Natl Acad Sci U S A* **92**(17): 7809-7813.

Hallemeesch, M. M., Y. L. Vissers, et al. (2004). "Acute reduction of circulating arginine in mice does not compromise whole body NO production." *Clin Nutr* **23**(3): 383-390.

Hamilton, N. B., D. Attwell, et al. (2010). "Pericyte-mediated regulation of capillary diameter: a component of neurovascular coupling in health and disease." *Front Neuroenergetics* **2**.

Harik, S. I., R. N. Kalaria, et al. (1990). "Immunocytochemical localization of the erythroid glucose transporter: abundance in tissues with barrier functions." *J Neurosci* **10**(12): 3862-3872.

Harper, M. E., A. Antoniou, et al. (2002). "Characterization of a novel metabolic strategy used by drug-resistant tumor cells." *FASEB J* **16**(12): 1550-1557.

Haseloff, R. F., I. E. Blasig, et al. (2005). "In search of the astrocytic factor(s) modulating blood-brain barrier functions in brain capillary endothelial cells in vitro." *Cell Mol Neurobiol* **25**(1): 25-39.

Hatzoglou, M., J. Fernandez, et al. (2004). "Regulation of cationic amino acid transport: the story of the CAT-1 transporter." *Annu Rev Nutr* **24**: 377-399.

Hawkins, B. T. and T. P. Davis (2005). "The blood-brain barrier/neurovascular unit in health and disease." *Pharmacol Rev* **57**(2): 173-185.

Hawkins, R. A., R. L. O'Kane, et al. (2006). "Structure of the blood-brain barrier and its role in the transport of amino acids." *J Nutr* **136**(1 Suppl): 218S-226S.

Hediger, M. A., M. F. Romero, et al. (2004). "The ABCs of solute carriers: physiological, pathological and therapeutic implications of human membrane transport proteinsIntroduction." *Pflugers Arch* **447**(5): 465-468.

Heiskala, M., P. A. Peterson, et al. (2001). "The roles of claudin superfamily proteins in paracellular transport." *Traffic* **2**(2): 93-98.

Herculano-Houzel, S. (2011). "Scaling of brain metabolism with a fixed energy budget per neuron: implications for neuronal activity, plasticity and evolution." *PLoS One* **6**(3): e17514.

Herve, F., N. Ghinea, et al. (2008). "CNS delivery via adsorptive transcytosis." *AAPS J* **10**(3): 455-472.

Higgins, C. F., R. Callaghan, et al. (1997). "Structure of the multidrug resistance P-glycoprotein." *Semin Cancer Biol* **8**(3): 135-142.

Hoglund, P. J., K. J. Nordstrom, et al. (2011). "The solute carrier families have a remarkably long evolutionary history with the majority of the human families present before divergence of Bilaterian species." *Mol Biol Evol* **28**(4): 1531-1541.

Honda, Y., F. Ushigome, et al. (2004). "Effects of grapefruit juice and orange juice components on P-glycoprotein- and MRP2-mediated drug efflux." *Br J Pharmacol* **143**(7): 856-864.

Hoover, W. G. (1985). "Canonical dynamics: Equilibrium phase-space distributions." *Phys Rev A* **31**(3): 1695-1697.

Hosokawa, H., T. Sawamura, et al. (1997). "Cloning and characterization of a brain-specific cationic amino acid transporter." *J Biol Chem* **272**(13): 8717-8722.

Huang, Y., B. N. Kang, et al. (2007). "The cationic amino acid transporters CAT1 and CAT3 mediate NMDA receptor activation-dependent changes in elaboration of neuronal processes via the mammalian target of rapamycin mTOR pathway." *J Neurosci* **27**(3): 449-458.

Huber, J. D., R. D. Egleton, et al. (2001). "Molecular physiology and pathophysiology of tight junctions in the blood-brain barrier." *Trends Neurosci* **24**(12): 719-725.

Humm, A., E. Fritsche, et al. (1997). "Crystal structure and mechanism of human L-arginine:glycine amidinotransferase: a mitochondrial enzyme involved in creatine biosynthesis." *EMBO J* **16**(12): 3373-3385.

Iten, M., H. Mett, et al. (1997). "Alterations in ornithine decarboxylase characteristics account for tolerance of Trypanosoma brucei rhodesiense to D,L-alpha-difluoromethylornithine." *Antimicrob Agents Chemother* **41**(9): 1922-1925.

Ito, K. and M. Groudine (1997). "A new member of the cationic amino acid transporter family is preferentially expressed in adult mouse brain." *J Biol Chem* **272**(42): 26780-26786.

Itoh, M., H. Sasaki, et al. (2001). "Junctional adhesion molecule (JAM) binds to PAR-3: a possible mechanism for the recruitment of PAR-3 to tight junctions." *J Cell Biol* **154**(3): 491-497.

Jager, K., S. Wolf, et al. (2013). "Differential topochemistry of three cationic amino acid transporter proteins, hCAT1, hCAT2 and hCAT3, in the adult human brain." *Amino Acids* **44**(2): 423-433.

Jain, N., A. George, et al. (1999). "Effect of salt on the micellization of pluronic P65 in aqueous solution." *Colloids and Surfaces A: Physicochemical and Engineering Aspects* **157**(1): 275-283.

Jha, T. K. and V. K. Sharma (1984). "Pentamidine-induced diabetes mellitus." *Trans R Soc Trop Med Hyg* **78**(2): 252-253.

Johnson, J. A., A. el Barbary, et al. (1993). "Glutathione S-transferase isoenzymes in rat brain neurons and glia." *J Neurosci* **13**(5): 2013-2023.

Jones, L. C., C. T. Tran, et al. (2003). "Common genetic variation in a basal promoter element alters DDAH2 expression in endothelial cells." *Biochem Biophys Res Commun* **310**(3): 836-843.

Jones, P. M. and A. M. George (2004). "The ABC transporter structure and mechanism: perspectives on recent research." *Cell Mol Life Sci* **61**(6): 682-699.

Jones, P. M., D. M. Salmon, et al. (1988). "Protein phosphorylation in electrically permeabilized islets of Langerhans. Effects of Ca2+, cyclic AMP, a phorbol ester and noradrenaline." *Biochem J* **254**(2): 397-403.

Jones, R. J., D. Jourd'heuil, et al. (2007). "iNOS regulation by calcium/calmodulin-dependent protein kinase II in vascular smooth muscle." *Am J Physiol Heart Circ Physiol* **292**(6): H2634-2642.

Jung, C. S., B. Lange, et al. (2012). "The CSF concentration of ADMA, but not of ET-1, is correlated with the occurrence and severity of cerebral vasospasm after subarachnoid hemorrhage." *Neurosci Lett* **524**(1): 20-24.

Junquera, E., L. Peña, et al. (1997). "Micellar behavior of the aqueous solutions of dodecylethyldimethylammonium bromide. A characterization study in the presence and absence of hydroxypropyl-β-cyclodextrin." *Langmuir* **13**(2): 219-224.

Kabanov, A., J. Zhu, et al. (2005a). "Pluronic block copolymers for gene delivery." *Adv Genet* **53**: 231-261.

Kabanov, A. V. (2006). "Polymer genomics: an insight into pharmacology and toxicology of nanomedicines." *Adv Drug Deliv Rev* **58**(15): 1597-1621.

Kabanov, A. V. and V. Y. Alakhov (2002). "Pluronic block copolymers in drug delivery: from micellar nanocontainers to biological response modifiers." *Crit Rev Ther Drug Carrier Syst* **19**(1): 1-72.

Kabanov, A. V., E. V. Batrakova, et al. (2002a). "Pluronic block copolymers as novel polymer therapeutics for drug and gene delivery." *J Control Release* **82**(2-3): 189-212.

Kabanov, A. V., E. V. Batrakova, et al. (2002b). "Pluronic block copolymers for overcoming drug resistance in cancer." *Adv Drug Deliv Rev* **54**(5): 759-779.

Kabanov, A. V., E. V. Batrakova, et al. (2005b). "Polymer genomics: shifting the gene and drug delivery paradigms." *J Control Release* **101**(1-3): 259-271.

Kabanov, A. V., I. R. Nazarova, et al. (1995). "Micelle formation and solubilization of fluorescent probes in poly (oxyethylene-b-oxypropylene-b-oxyethylene) solutions." *Macromolecules* **28**(7): 2303-2314.

Kaehler, S. T., N. Singewald, et al. (1999). "Nitric oxide modulates the release of serotonin in the rat hypothalamus." *Brain Res* **835**(2): 346-349.

Kakimoto, Y. and S. Akazawa (1970). "Isolation and identification of N-G,N-G- and N-G,N'-G-dimethyl-arginine, N-epsilon-mono-, di-, and trimethyllysine, and glucosylgalactosyl- and galactosyl-delta-hydroxylysine from human urine." *J Biol Chem* **245**(21): 5751-5758.

Kalaria, R. N., M. J. Mitchell, et al. (1988). "Monoamine oxidases of the human brain and liver." *Brain* **111 (Pt 6)**: 1441-1451.

Kale, G., A. P. Naren, et al. (2003). "Tyrosine phosphorylation of occludin attenuates its interactions with ZO-1, ZO-2, and ZO-3." *Biochem Biophys Res Commun* **302**(2): 324-329.

Kamouchi, M., T. Kitazono, et al. (2004). "Calcium influx pathways in rat CNS pericytes." *Brain Res Mol Brain Res* **126**(2): 114-120.

Karssen, A. M., O. Meijer, et al. (2004). "Localization of mRNA expression of P-glycoprotein at the blood-brain barrier and in the hippocampus." *Ann N Y Acad Sci* **1032**: 308-311.

Karunakaran, S., N. S. Umapathy, et al. (2008). "Interaction of tryptophan derivatives with SLC6A14 (ATB0,+) reveals the potential of the transporter as a drug target for cancer chemotherapy." *Biochem J* **414**(3): 343-355.

Katsuki, S., W. Arnold, et al. (1977). "Stimulation of guanylate cyclase by sodium nitroprusside, nitroglycerin and nitric oxide in various tissue preparations and comparison to the effects of sodium azide and hydroxylamine." *J Cyclic Nucleotide Res* **3**(1): 23-35.

Kavanaugh, M. P. (1993). "Voltage dependence of facilitated arginine flux mediated by the system y+ basic amino acid transporter." *Biochemistry* **32**(22): 5781-5785.

Keep, R. F. and H. C. Jones (1990). "A morphometric study on the development of the lateral ventricle choroid plexus, choroid plexus capillaries and ventricular ependyma in the rat." *Brain Res Dev Brain Res* **56**(1): 47-53.

Kennedy, P. G. (2004). "Human African trypanosomiasis of the CNS: current issues and challenges." *J Clin Invest* **113**(4): 496-504.

Khan, U., A. Hassan, et al. (2007). "Asymmetric dimethylarginine in cerebral small vessel disease." *Stroke* **38**(2): 411-413.

Kielstein, J. T., R. H. Boger, et al. (1999). "Asymmetric dimethylarginine plasma concentrations differ in patients with end-stage renal disease: relationship to treatment method and atherosclerotic disease." *J Am Soc Nephrol* **10**(3): 594-600.

Kim, J. W., E. I. Closs, et al. (1991). "Transport of cationic amino acids by the mouse ecotropic retrovirus receptor." *Nature* **352**(6337): 725-728.

Kirkham, M. and R. G. Parton (2005). "Clathrin-independent endocytosis: new insights into caveolae and non-caveolar lipid raft carriers." *Biochim Biophys Acta* **1745**(3): 273-286.

Kleinert, H., A. Pautz, et al. (2004). "Regulation of the expression of inducible nitric oxide synthase." *Eur J Pharmacol* **500**(1-3): 255-266.

Koehler-Stec, E. M., K. Li, et al. (2000). "Cerebral glucose utilization and glucose transporter expression: response to water deprivation and restoration." *J Cereb Blood Flow Metab* **20**(1): 192-200.

Kondo, A. and K. Suzuki (1993). "The blood brain barrier in human leukodystrophies and allied diseases. Ultrastructural and morphometric studies on the capillaries in brain biopsies." *Clin Neuropathol* **12**(3): 169-174.

Kose, N., T. Asashima, et al. (2007). "Altered expression of basement membrane-related molecules in rat brain pericyte, endothelial, and astrocyte cell lines after transforming growth factor-beta1 treatment." *Drug Metab Pharmacokinet* **22**(4): 255-266.

Kristensson, K., M. Nygard, et al. (2010). "African trypanosome infections of the nervous system: parasite entry and effects on sleep and synaptic functions." *Prog Neurobiol* **91**(2): 152-171.

Kubota, K., M. Furuse, et al. (1999). "Ca(2+)-independent cell-adhesion activity of claudins, a family of integral membrane proteins localized at tight junctions." *Curr Biol* **9**(18): 1035-1038.

Kuffler, S. W., J. G. Nicholls, et al. (1966). "Physiological properties of glial cells in the central nervous system of amphibia." *J Neurophysiol* **29**(4): 768-787.

Kullak-Ublick, G. A., B. Hagenbuch, et al. (1995). "Molecular and functional characterization of an organic anion transporting polypeptide cloned from human liver." *Gastroenterology* **109**(4): 1274-1282.

Kusuhara, H., Z. He, et al. (2003). "Expression and functional involvement of organic anion transporting polypeptide subtype 3 (Slc21a7) in rat choroid plexus." *Pharm Res* **20**(5): 720-727.

Kwan, P., G. J. Sills, et al. (2003). "Differential expression of multidrug resistance genes in naive rat brain." *Neurosci Lett* **339**(1): 33-36.

Lajer, M., L. Tarnow, et al. (2008). "Plasma concentration of asymmetric dimethylarginine (ADMA) predicts cardiovascular morbidity and mortality in type 1 diabetic patients with diabetic nephropathy." *Diabetes Care* **31**(4): 747-752.

Lam, F. C., R. Liu, et al. (2001). "beta-Amyloid efflux mediated by p-glycoprotein." *J Neurochem* **76**(4): 1121-1128.

Lamarque, D., J. Kiss, et al. (1996). "[Role of nitric oxide in maintaining the mucosal integrity and in inflammatory gastrointestinal diseases]." *Gastroenterol Clin Biol* **20**(12): 1085-1098.

Lancet, T. (2010). "Killer coma: the evolving story of sleeping sickness treatment." *Lancet* **375**(9709): 93.

Lavasanifar, A., J. Samuel, et al. (2002). "Poly(ethylene oxide)-block-poly(L-amino acid) micelles for drug delivery." *Adv Drug Deliv Rev* **54**(2): 169-190.

Lavi, S., R. Egbarya, et al. (2003). "Role of nitric oxide in the regulation of cerebral blood flow in humans: chemoregulation versus mechanoregulation." *Circulation* **107**(14): 1901-1905.

Lawson, L. J., V. H. Perry, et al. (1992). "Turnover of resident microglia in the normal adult mouse brain." *Neuroscience* **48**(2): 405-415.

Lee, H., R. M. Venable, et al. (2008). "Molecular dynamics studies of polyethylene oxide and polyethylene glycol: hydrodynamic radius and shape anisotropy." *Biophys J* **95**(4): 1590-1599.

Lee, Y. J., H. Kusuhara, et al. (2004). "Do multidrug resistance-associated protein-1 and -2 play any role in the elimination of estradiol-17 beta-glucuronide and 2,4-dinitrophenyl-S-glutathione across the blood-cerebrospinal fluid barrier?" *J Pharm Sci* **93**(1): 99-107.

Leino, R. L., D. Z. Gerhart, et al. (1999). "Monocarboxylate transporter (MCT1) abundance in brains of suckling and adult rats: a quantitative electron microscopic immunogold study." *Brain Res Dev Brain Res* **113**(1-2): 47-54.

Leiper, J., J. Murray-Rust, et al. (2002). "S-nitrosylation of dimethylarginine dimethylaminohydrolase regulates enzyme activity: further interactions between nitric oxide synthase and dimethylarginine dimethylaminohydrolase." *Proc Natl Acad Sci U S A* **99**(21): 13527-13532.

Leiper, J. M., J. Santa Maria, et al. (1999). "Identification of two human dimethylarginine dimethylaminohydrolases with distinct tissue distributions and homology with microbial arginine deiminases." *Biochem J* **343 Pt 1**: 209-214.

Levin, V. A., H. D. Landahl, et al. (1976). "The application of brain capillary permeability coefficient measurements to pathological conditions and the selection of agents which cross the blood-brain barrier." *J Pharmacokinet Biopharm* **4**(6): 499-519.

Leypoldt, F., C. U. Choe, et al. (2009). "Dimethylarginine dimethylaminohydrolase-1 transgenic mice are not protected from ischemic stroke." *PLoS One* **4**(10): e7337.

Liebner, S., M. Corada, et al. (2008). "Wnt/beta-catenin signaling controls development of the blood-brain barrier." *J Cell Biol* **183**(3): 409-417.

Lin, J. H. (2004). "How significant is the role of P-glycoprotein in drug absorption and brain uptake?" *Drugs Today (Barc)* **40**(1): 5-22.

Lin, J. H. and M. Yamazaki (2003). "Role of P-glycoprotein in pharmacokinetics: clinical implications." *Clin Pharmacokinet* **42**(1): 59-98.

Lin, K. Y., A. Ito, et al. (2002). "Impaired nitric oxide synthase pathway in diabetes mellitus: role of asymmetric dimethylarginine and dimethylarginine dimethylaminohydrolase." *Circulation* **106**(8): 987-992.

Lindvall, M. and C. Owman (1980). "Evidence for the presence of two types of monoamine oxidase in rabbit choroid plexus and their role in breakdown of amines influencing cerebrospinal fluid formation." *J Neurochem* **34**(3): 518-522.

Linnet, K. and T. B. Ejsing (2008). "A review on the impact of P-glycoprotein on the penetration of drugs into the brain. Focus on psychotropic drugs." *Eur Neuropsychopharmacol* **18**(3): 157-169.

Lorenzo, A. V. and S. R. Snodgrass (1972). "Leucine transport from the ventricles and the cranial subarachnoid space in the cat." *J Neurochem* **19**(5): 1287-1298.

Lorrain, D. S. and E. M. Hull (1993). "Nitric oxide increases dopamine and serotonin release in the medial preoptic area." *Neuroreport* **5**(1): 87-89.

Lundkvist, G. B., K. Kristensson, et al. (2004). "Why trypanosomes cause sleeping sickness." *Physiology (Bethesda)* **19**: 198-206.

Lyck, R., N. Ruderisch, et al. (2009). "Culture-induced changes in blood-brain barrier transcriptome: implications for amino-acid transporters in vivo." *J Cereb Blood Flow Metab*.

Macchi, M. M. and J. N. Bruce (2004). "Human pineal physiology and functional significance of melatonin." *Front Neuroendocrinol* **25**(3-4): 177-195.

Majano, P., E. Lara-Pezzi, et al. (2001). "Hepatitis B virus X protein transactivates inducible nitric oxide synthase gene promoter through the proximal nuclear factor kappaB-binding site: evidence that cytoplasmic location of X protein is essential for gene transactivation." *Hepatology* **34**(6): 1218-1224.

Mann, G. E., D. L. Yudilevich, et al. (2003). "Regulation of amino acid and glucose transporters in endothelial and smooth muscle cells." *Physiol Rev* **83**(1): 183-252.

Martens-Lobenhoffer, J., O. Krug, et al. (2004). "Determination of arginine and asymmetric dimethylarginine (ADMA) in human plasma by liquid chromatography/mass spectrometry with the isotope dilution technique." *J Mass Spectrom* **39**(11): 1287-1294.

Masocha, W., M. E. Rottenberg, et al. (2007). "Migration of African trypanosomes across the blood-brain barrier." *Physiol Behav* **92**(1-2): 110-114.

Mata, J. P., P. R. Majhi, et al. (2005). "Concentration, temperature, and salt-induced micellization of a triblock copolymer Pluronic L64 in aqueous media." *J Colloid Interface Sci* **292**(2): 548-556.

Matter, K. and M. S. Balda (2003). "Holey barrier: claudins and the regulation of brain endothelial permeability." *J Cell Biol* **161**(3): 459-460.

Mayer, B., M. John, et al. (1990). "Purification of a Ca2+/calmodulin-dependent nitric oxide synthase from porcine cerebellum. Cofactor-role of tetrahydrobiopterin." *FEBS Lett* **277**(1-2): 215-219.

McCann, J. C. and B. N. Ames (2005). "Is docosahexaenoic acid, an n-3 long-chain polyunsaturated fatty acid, required for development of normal brain function? An overview of evidence from cognitive and behavioral tests in humans and animals." *Am J Clin Nutr* **82**(2): 281-295.

McDermott, J. R. (1976). "Studies on the catabolism of Ng-methylarginine, Ng, Ng-dimethylarginine and Ng, Ng-dimethylarginine in the rabbit." *Biochem J* **154**(1): 179-184.

McDonald, K. K., S. Zharikov, et al. (1997). "A caveolar complex between the cationic amino acid transporter 1 and endothelial nitric-oxide synthase may explain the "arginine paradox"." *J Biol Chem* **272**(50): 31213-31216.

McMahon, K. A., M. Zhu, et al. (2006). "Detergent-free caveolae proteome suggests an interaction with ER and mitochondria." *Proteomics* **6**(1): 143-152.

Miller, D. W., E. V. Batrakova, et al. (1997). "Interactions of pluronic block copolymers with brain microvessel endothelial cells: evidence of two potential pathways for drug absorption." *Bioconjug Chem* **8**(5): 649-657.

Minko, T., E. V. Batrakova, et al. (2005). "Pluronic block copolymers alter apoptotic signal transduction of doxorubicin in drug-resistant cancer cells." *J Control Release* **105**(3): 269-278.

Minn, A., S. Leclerc, et al. (2002). "Drug transport into the mammalian brain: the nasal pathway and its specific metabolic barrier." *J Drug Target* **10**(4): 285-296.

Moncada, S., A. Higgs, et al. (1997). "International Union of Pharmacology Nomenclature in Nitric Oxide Research." *Pharmacol Rev* **49**(2): 137-142.

Morcos, Y., M. J. Hosie, et al. (2001). "Immunolocalization of occludin and claudin-1 to tight junctions in intact CNS vessels of mammalian retina." *J Neurocytol* **30**(2): 107-123.

Morrissey, J. J., R. McCracken, et al. (1994). "Location of an inducible nitric oxide synthase mRNA in the normal kidney." *Kidney Int* **45**(4): 998-1005.

Mortensen, K. and J. S. Pedersen (1993). "Structural study on the micelle formation of poly (ethylene oxide)-poly (propylene oxide)-poly (ethylene oxide) triblock copolymer in aqueous solution." *Macromolecules* **26**(4): 805-812.

Mousavi, S. A., L. Malerod, et al. (2004). "Clathrin-dependent endocytosis." *Biochem J* **377**(Pt 1): 1-16.

Mukherjee, S., R. N. Ghosh, et al. (1997). "Endocytosis." *Physiol Rev* **77**(3): 759-803.

Mulenga, C., J. D. Mhlanga, et al. (2001). "Trypanosoma brucei brucei crosses the blood-brain barrier while tight junction proteins are preserved in a rat chronic disease model." *Neuropathol Appl Neurobiol* **27**(1): 77-85.

Muller, M., E. Bakos, et al. (1996). "Altered drug-stimulated ATPase activity in mutants of the human multidrug resistance protein." *J Biol Chem* **271**(4): 1877-1883.

Murray-Rust, J., J. Leiper, et al. (2001). "Structural insights into the hydrolysis of cellular nitric oxide synthase inhibitors by dimethylarginine dimethylaminohydrolase." *Nat Struct Biol* **8**(8): 679-683.

Nabeshima, S., T. S. Reese, et al. (1975). "Junctions in the meninges and marginal glia." *J Comp Neurol* **164**(2): 127-169.

Nag, S. and D. J. Begley (2005). Blood-brain barrier, exchange of metabolites and gases. *In*: Pathology & Genetics, Cerebrovascular Diseases. H. Kalimo. Basel, ISN Neuropath. Press**:** 22-29.

Nagata, Y., H. Kusuhara, et al. (2002). "Expression and functional characterization of rat organic anion transporter 3 (rOat3) in the choroid plexus." *Mol Pharmacol* **61**(5): 982-988.

Nakajima, T., Y. Matsuoka, et al. (1971). "Isolation and identification of N-G-monomethyl, N-G, N-G-dimethyl- and N-G,N' G-dimethylarginine from the hydrolysate of proteins of bovine brain." *Biochim Biophys Acta* **230**(2): 212-222.

Nathan, C. and Q. W. Xie (1994). "Regulation of biosynthesis of nitric oxide." *J Biol Chem* **269**(19): 13725-13728.

Nawrath, H., J. W. Wegener, et al. (2000). "Voltage dependence of L-arginine transport by hCAT-2A and hCAT-2B expressed in oocytes from Xenopus laevis." *Am J Physiol Cell Physiol* **279**(5): C1336-1344.

Nedergaard, M., B. Ransom, et al. (2003). "New roles for astrocytes: redefining the functional architecture of the brain." *Trends Neurosci* **26**(10): 523-530.

Neuwelt, E. A., B. Bauer, et al. (2011). "Engaging neuroscience to advance translational research in brain barrier biology." *Nat Rev Neurosci* **12**(3): 169-182.

Ng, W. F., F. Sarangi, et al. (1989). "Identification of members of the P-glycoprotein multigene family." *Mol Cell Biol* **9**(3): 1224-1232.

Nguyen, T. V., D. E. Smith, et al. (2007). "PEPT1 enhances the uptake of gabapentin via trans-stimulation of b0,+ exchange." *Pharm Res* **24**(2): 353-360.

Nicholson, B., T. Sawamura, et al. (1998). "Increased Cat3-mediated cationic amino acid transport functionally compensates in Cat1 knockout cell lines." *J Biol Chem* **273**(24): 14663-14666.

Nies, A. T., G. Jedlitschky, et al. (2004). "Expression and immunolocalization of the multidrug resistance proteins, MRP1-MRP6 (ABCC1-ABCC6), in human brain." *Neuroscience* **129**(2): 349-360.

Nishiyama, Y., M. Ueda, et al. (2010). "Asymmetric dimethylarginine (ADMA) as a possible risk marker for ischemic stroke." *J Neurol Sci* **290**(1-2): 12-15.

Nitta, T., M. Hata, et al. (2003). "Size-selective loosening of the blood-brain barrier in claudin-5-deficient mice." *J Cell Biol* **161**(3): 653-660.

Notsu, Y., T. Nabika, et al. (2009). "Evaluation of asymmetric dimethylarginine and homocysteine in microangiopathy-related cerebral damage." *Am J Hypertens* **22**(3): 257-262.

O'Brien, F. E., T. G. Dinan, et al. (2012). "Interactions between antidepressants and P-glycoprotein at the blood-brain barrier: clinical significance of in vitro and in vivo findings." *Br J Pharmacol* **165**(2): 289-312.

O'Kane, R. L. and R. A. Hawkins (2003). "Na+-dependent transport of large neutral amino acids occurs at the abluminal membrane of the blood-brain barrier." *Am J Physiol Endocrinol Metab* **285**(6): E1167-1173.

O'Kane, R. L., J. R. Vina, et al. (2004). "Na+ -dependent neutral amino acid transporters A, ASC, and N of the blood-brain barrier: mechanisms for neutral amino acid removal." *Am J Physiol Endocrinol Metab* **287**(4): E622-629.

O'Kane, R. L., J. R. Vina, et al. (2006). "Cationic amino acid transport across the blood-brain barrier is mediated exclusively by system y+." *Am J Physiol Endocrinol Metab* **291**(2): E412-419.

Odiit, M., F. Kansiime, et al. (1997). "Duration of symptoms and case fatality of sleeping sickness caused by Trypanosoma brucei rhodesiense in Tororo, Uganda." *East Afr Med J* **74**(12): 792-795.

Ogawa, T., M. Kimoto, et al. (1987a). "Occurrence of a new enzyme catalyzing the direct conversion of NG,NG-dimethyl-L-arginine to L-citrulline in rats." *Biochem Biophys Res Commun* **148**(2): 671-677.

Ogawa, T., M. Kimoto, et al. (1989). "Purification and properties of a new enzyme, NG,NG-dimethylarginine dimethylaminohydrolase, from rat kidney." *J Biol Chem* **264**(17): 10205-10209.

Ogawa, T., M. Kimoto, et al. (1990). "Dimethylarginine:pyruvate aminotransferase in rats. Purification, properties, and identity with alanine:glyoxylate aminotransferase 2." *J Biol Chem* **265**(34): 20938-20945.

Ogawa, T., M. Kimoto, et al. (1987b). "Metabolism of NG,NG-and NG,N'G-dimethylarginine in rats." *Arch Biochem Biophys* **252**(2): 526-537.

Oh, K. T., T. K. Bronich, et al. (2004). "Micellar formulations for drug delivery based on mixtures of hydrophobic and hydrophilic Pluronic block copolymers." *J Control Release* **94**(2-3): 411-422.

Ohashi, K., K. Hashizaki, et al. (2009). "Effects of Inorganic Salts on Micellization and Solubilization in an Aqueous Solution of Poly (ethylene oxide)/Poly (propylene oxide)/Poly (ethylene oxide) Triblock Copolymer." *Journal of Dispersion Science and Technology* **30**(5): 720-724.

Oldendorf, W. H. (1971). "Uptake of radiolabeled essential amino acids by brain following arterial injection." *Proc Soc Exp Biol Med* **136**(2): 385-386.

Oldendorf, W. H. and W. J. Brown (1975). "Greater number of capillary endothelial cell mitochondria in brain than in muscle." *Proc Soc Exp Biol Med* **149**(3): 736-738.

Oldendorf, W. H., M. E. Cornford, et al. (1977). "The large apparent work capability of the blood-brain barrier: a study of the mitochondrial content of capillary endothelial cells in brain and other tissues of the rat." *Ann Neurol* **1**(5): 409-417.

Omidi, Y., L. Campbell, et al. (2003). "Evaluation of the immortalised mouse brain capillary endothelial cell line, b.End3, as an in vitro blood-brain barrier model for drug uptake and transport studies." *Brain Res* **990**(1-2): 95-112.

Padbury, J. F., S. K. Diah, et al. (2004). "Transcriptional regulation of the LAT-1/CD98 light chain." *Biochem Biophys Res Commun* **318**(2): 529-534.

Paik, W. K. and S. Kim (1968). "Protein methylase I. Purification and properties of the enzyme." *J Biol Chem* **243**(9): 2108-2114.

Palacios, M., R. G. Knowles, et al. (1989). "Nitric oxide from L-arginine stimulates the soluble guanylate cyclase in adrenal glands." *Biochem Biophys Res Commun* **165**(2): 802-809.

Palm, F., M. L. Onozato, et al. (2007). "Dimethylarginine dimethylaminohydrolase (DDAH): expression, regulation, and function in the cardiovascular and renal systems." *Am J Physiol Heart Circ Physiol* **293**(6): H3227-3245.

Pappenheimer, J. R. (1970). On the location of the blood-brain barrier. *In*: Proceedings of the Wales Symposium on the Blood-Brain Barrier. London, sponsored by the Wates Foundation, Truex Press, Oxford**:** 66-84.

Pardridge, W. M. (1977). "Unidirectional influx of glutamine and other neutral amino acids into liver of fed and fasted rat in vivo." *Am J Physiol* **232**(5): E492-496.

Pardridge, W. M. (1983). "Brain metabolism: a perspective from the blood-brain barrier." *Physiol Rev* **63**(4): 1481-1535.

Pardridge, W. M. (1998). "Blood-brain barrier carrier-mediated transport and brain metabolism of amino acids." *Neurochem Res* **23**(5): 635-644.

Pardridge, W. M. (2005). "The blood-brain barrier: bottleneck in brain drug development." *NeuroRx* **2**(1): 3-14.

Pardridge, W. M., R. J. Boado, et al. (1990). "Brain-type glucose transporter (GLUT-1) is selectively localized to the blood-brain barrier. Studies with quantitative western blotting and in situ hybridization." *J Biol Chem* **265**(29): 18035-18040.

Pardridge, W. M. and W. H. Oldendorf (1975a). "Kinetic analysis of blood-brain barrier transport of amino acids." *Biochim Biophys Acta* **401**(1): 128-136.

Pardridge, W. M. and W. H. Oldendorf (1975b). "Kinetics of blood-brain transport of hexoses." *Biochim Biophys Acta* **382**(3): 377-392.

Patist, A., S. Bhagwat, et al. (2000). "On the measurement of critical micelle concentrations of pure and technical-grade nonionic surfactants." *Journal of Surfactants and Detergents* **3**(1): 53-58.

Patlak, C. S., R. G. Blasberg, et al. (1983). "Graphical evaluation of blood-to-brain transfer constants from multiple-time uptake data." *J Cereb Blood Flow Metab* **3**(1): 1-7.

Pellerin, L. and P. J. Magistretti (2003). "Food for thought: challenging the dogmas." *J Cereb Blood Flow Metab* **23**(11): 1282-1286.

Peppiatt, C. M., C. Howarth, et al. (2006). "Bidirectional control of CNS capillary diameter by pericytes." *Nature* **443**(7112): 700-704.

Perkins, C. P., V. Mar, et al. (1997). "Anemia and perinatal death result from loss of the murine ecotropic retrovirus receptor mCAT-1." *Genes Dev* **11**(7): 914-925.

Pettersson, A., T. Hedner, et al. (1998). "Increased circulating concentrations of asymmetric dimethyl arginine (ADMA), an endogenous inhibitor of nitric oxide synthesis, in preeclampsia." *Acta Obstet Gynecol Scand* **77**(8): 808-813.

Pfeiffer, R., J. Loffing, et al. (1999a). "Luminal heterodimeric amino acid transporter defective in cystinuria." *Mol Biol Cell* **10**(12): 4135-4147.

Pfeiffer, R., G. Rossier, et al. (1999b). "Amino acid transport of y+L-type by heterodimers of 4F2hc/CD98 and members of the glycoprotein-associated amino acid transporter family." *EMBO J* **18**(1): 49-57.

Phelps, C. H. (1972). "Barbiturate-induced glycogen accumulation in brain. An electron microscopic study." *Brain Res* **39**(1): 225-234.

Philbert, M. A., C. M. Beiswanger, et al. (1995). "Glutathione S-transferases and gamma-glutamyl transpeptidase in the rat nervous systems: a basis for differential susceptibility to neurotoxicants." *Neurotoxicology* **16**(2): 349-362.

Philip, K. A., M. J. Dascombe, et al. (1994). "Blood-brain barrier damage in experimental African trypanosomiasis." *Ann Trop Med Parasitol* **88**(6): 607-616.

Philp, N. J., H. Yoon, et al. (2001). "Mouse MCT3 gene is expressed preferentially in retinal pigment and choroid plexus epithelia." *Am J Physiol Cell Physiol* **280**(5): C1319-1326.

Picozzi, K., M. Carrington, et al. (2008). "A multiplex PCR that discriminates between Trypanosoma brucei brucei and zoonotic T. b. rhodesiense." *Exp Parasitol* **118**(1): 41-46.

Picozzi, K., E. M. Fevre, et al. (2005). "Sleeping sickness in Uganda: a thin line between two fatal diseases." *BMJ* **331**(7527): 1238-1241.

Piontek, J., L. Winkler, et al. (2008). "Formation of tight junction: determinants of homophilic interaction between classic claudins." *FASEB J* **22**(1): 146-158.

Plimpton, S. J. (1995). "Fast Parallel Algorithms for Short-Range Molecular Dynamics." *J Comput Phys* **117**(1): 1-19.

Pluta, R. M. (2008). "Dysfunction of nitric oxide synthases as a cause and therapeutic target in delayed cerebral vasospasm after SAH." *Acta Neurochir Suppl* **104**: 139-147.

Poller, B., H. Gutmann, et al. (2008). "The human brain endothelial cell line hCMEC/D3 as a human blood-brain barrier model for drug transport studies." *J Neurochem* **107**(5): 1358-1368.

Powell, E. M. and H. M. Geller (1999). "Dissection of astrocyte-mediated cues in neuronal guidance and process extension." *Glia* **26**(1): 73-83.

Preik-Steinhoff, H., S. Zink, et al. (1995). "Transport of L-arginine in arginine-deprived endothelial cells." *Biochem Biophys Res Commun* **213**(2): 447-453.

Preston, J. E. and M. B. Segal (1992). "The uptake of anionic and cationic amino acids by the isolated perfused sheep choroid plexus." *Brain Res* **581**(2): 351-355.

Price, T. O., S. A. Farr, et al. (2010). "Transport across the blood-brain barrier of pluronic leptin." *J Pharmacol Exp Ther* **333**(1): 253-263.

Priotto, G., S. Kasparian, et al. (2007). "Nifurtimox-eflornithine combination therapy for second-stage Trypanosoma brucei gambiense sleeping sickness: a randomized clinical trial in Congo." *Clin Infect Dis* **45**(11): 1435-1442.

Quinton, P. M., E. M. Wright, et al. (1973). "Localization of sodium pumps in the choroid plexus epithelium." *J Cell Biol* **58**(3): 724-730.

Radwanska, M., F. Claes, et al. (2002). "Novel primer sequences for polymerase chain reaction-based detection of Trypanosoma brucei gambiense." *Am J Trop Med Hyg* **67**(3): 289-295.

Ramachandra, M., S. V. Ambudkar, et al. (1998). "Human P-glycoprotein exhibits reduced affinity for substrates during a catalytic transition state." *Biochemistry* **37**(14): 5010-5019.

Rangel-Yagui, C. O., A. Pessoa, Jr., et al. (2005a). "Micellar solubilization of drugs." *J Pharm Pharm Sci* **8**(2): 147-165.

Rangel-Yagui, C. O., A. Pessoa Jr, et al. (2005b). "Micellar solubilization of drugs." *J Pharm Pharm Sci* **8**(2): 147-163.

Rao, V. V., J. L. Dahlheimer, et al. (1999). "Choroid plexus epithelial expression of MDR1 P glycoprotein and multidrug resistance-associated protein contribute to the blood-cerebrospinal-fluid drug-permeability barrier." *Proc Natl Acad Sci U S A* **96**(7): 3900-3905.

Raseroka, B. H. and W. E. Ormerod (1986). "The trypanocidal effect of drugs in different parts of the brain." *Trans R Soc Trop Med Hyg* **80**(4): 634-641.

Rawal, N., R. Rajpurohit, et al. (1995). "Structural specificity of substrate for S-adenosylmethionine:protein arginine N-methyltransferases." *Biochim Biophys Acta* **1248**(1): 11-18.

Redzic, Z. (2011). "Molecular biology of the blood-brain and the blood-cerebrospinal fluid barriers: similarities and differences." *Fluids Barriers CNS* **8**(1): 3.

Reese, T. S., N. Feder, et al. (1971). "Electron microscopic study of the blood-brain and blood-cerebrospinal fluid barriers with microperoxidase." *J Neuropathol Exp Neurol* **30**(1): 137-138.

Reese, T. S. and M. J. Karnovsky (1967). "Fine structural localization of a blood-brain barrier to exogenous peroxidase." *J Cell Biol* **34**(1): 207-217.

Regina, A., A. Koman, et al. (1998). "Mrp1 multidrug resistance-associated protein and P-glycoprotein expression in rat brain microvessel endothelial cells." *J Neurochem* **71**(2): 705-715.

Reynolds, I. J. and E. Aizenman (1992). "Pentamidine is an N-methyl-D-aspartate receptor antagonist and is neuroprotective in vitro." *J Neurosci* **12**(3): 970-975.

Roberts, L. M., D. S. Black, et al. (2008a). "Subcellular localization of transporters along the rat blood-brain barrier and blood-cerebral-spinal fluid barrier by in vivo biotinylation." *Neuroscience* **155**(2): 423-438.

Roberts, L. M., K. Woodford, et al. (2008b). "Expression of the thyroid hormone transporters monocarboxylate transporter-8 (SLC16A2) and organic ion transporter-14 (SLCO1C1) at the blood-brain barrier." *Endocrinology* **149**(12): 6251-6261.

Romero, I. A., K. Radewicz, et al. (2003). "Changes in cytoskeletal and tight junctional proteins correlate with decreased permeability induced by dexamethasone in cultured rat brain endothelial cells." *Neurosci Lett* **344**(2): 112-116.

Romsicki, Y. and F. J. Sharom (1998). "The ATPase and ATP-binding functions of P-glycoprotein--modulation by interaction with defined phospholipids." *Eur J Biochem* **256**(1): 170-178.

Romsicki, Y. and F. J. Sharom (1999). "The membrane lipid environment modulates drug interactions with the P-glycoprotein multidrug transporter." *Biochemistry* **38**(21): 6887-6896.

Rossitch, E., Jr., E. Alexander, 3rd, et al. (1991). "L-arginine normalizes endothelial function in cerebral vessels from hypercholesterolemic rabbits." *J Clin Invest* **87**(4): 1295-1299.

Rotmann, A., A. Simon, et al. (2007). "Activation of classical protein kinase C decreases transport via systems y+ and y+L." *Am J Physiol Cell Physiol* **292**(6): C2259-2268.

Rufa, A., P. Blardi, et al. (2008). "Plasma levels of asymmetric dimethylarginine in cerebral autosomal dominant arteriopathy with subcortical infarct and leukoencephalopathy." *Cerebrovasc Dis* **26**(6): 636-640.

Russel, F. G., R. Masereeuw, et al. (2002). "Molecular aspects of renal anionic drug transport." *Annu Rev Physiol* **64**: 563-594.

Sahay, G., E. V. Batrakova, et al. (2008). "Different internalization pathways of polymeric micelles and unimers and their effects on vesicular transport." *Bioconjug Chem* **19**(10): 2023-2029.

Sai, P., D. Boillot, et al. (1983). "Pentamidine, a new diabetogenic drug in laboratory rodents." *Diabetologia* **25**(5): 418-423.

Saitou, M., K. Fujimoto, et al. (1998). "Occludin-deficient embryonic stem cells can differentiate into polarized epithelial cells bearing tight junctions." *J Cell Biol* **141**(2): 397-408.

Sanchez del Pino, M. M., D. R. Peterson, et al. (1995). "Neutral amino acid transport characterization of isolated luminal and abluminal membranes of the blood-brain barrier." *J Biol Chem* **270**(25): 14913-14918.

Sanderson, L., M. Dogruel, et al. (2008). "The blood-brain barrier significantly limits eflornithine entry into Trypanosoma brucei brucei infected mouse brain." *J Neurochem* **107**(4): 1136-1146.

Sanderson, L., M. Dogruel, et al. (2009). "Pentamidine movement across the murine blood-brain and blood-cerebrospinal fluid barriers: effect of trypanosome infection, combination therapy, P-glycoprotein, and multidrug resistance-associated protein." *J Pharmacol Exp Ther* **329**(3): 967-977.

Sanderson, L., A. Khan, et al. (2007). "Distribution of suramin, an antitrypanosomal drug, across the blood-brain and blood-cerebrospinal fluid interfaces in wild-type and P-glycoprotein transporter-deficient mice." *Antimicrob Agents Chemother* **51**(9): 3136-3146.

Sands, M., M. A. Kron, et al. (1985). "Pentamidine: a review." *Rev Infect Dis* **7**(5): 625-634.

Santos, N. C., M. Prieto, et al. (2003). "Quantifying molecular partition into model systems of biomembranes: an emphasis on optical spectroscopic methods." *Biochimica Et Biophysica Acta-Biomembranes* **1612**(2): 123-135.

Sauer, I., I. R. Dunay, et al. (2005). "An apolipoprotein E-derived peptide mediates uptake of sterically stabilized liposomes into brain capillary endothelial cells." *Biochemistry* **44**(6): 2021-2029.

Savidge, T. C., P. Newman, et al. (2007). "Enteric glia regulate intestinal barrier function and inflammation via release of S-nitrosoglutathione." *Gastroenterology* **132**(4): 1344-1358.

Scherer, P. E., T. Okamoto, et al. (1996). "Identification, sequence, and expression of caveolin-2 defines a caveolin gene family." *Proc Natl Acad Sci U S A* **93**(1): 131-135.

Schinkel, A. H. (1999). "P-Glycoprotein, a gatekeeper in the blood-brain barrier." *Adv Drug Deliv Rev* **36**(2-3): 179-194.

Schinkel, A. H. and J. W. Jonker (2003). "Mammalian drug efflux transporters of the ATP binding cassette (ABC) family: an overview." *Adv Drug Deliv Rev* **55**(1): 3-29.

Schinkel, A. H., U. Mayer, et al. (1997). "Normal viability and altered pharmacokinetics in mice lacking mdr1-type (drug-transporting) P-glycoproteins." *Proc Natl Acad Sci U S A* **94**(8): 4028-4033.

Schmidt, H. H., J. S. Pollock, et al. (1991). "Purification of a soluble isoform of guanylyl cyclase-activating-factor synthase." *Proc Natl Acad Sci U S A* **88**(2): 365-369.

Schummers, J., H. Yu, et al. (2008). "Tuned responses of astrocytes and their influence on hemodynamic signals in the visual cortex." *Science* **320**(5883): 1638-1643.

Schurr, E., M. Raymond, et al. (1989). "Characterization of the multidrug resistance protein expressed in cell clones stably transfected with the mouse mdr1 cDNA." *Cancer Res* **49**(10): 2729-2733.

Scott, D. E., G. P. Kozlowski, et al. (1974). "Scanning electron microscopy in the ultrastructural analysis of the mammalian cerebral ventricular system." *Int Rev Cytol* **37**(0): 349-388.

Scott, H. M. and A. Burchell (1991). "Pentamidine activates T1 the hepatic microsomal glucose 6-phosphate transport protein of the glucose-6-phosphatase system." *Biochim Biophys Acta* **1097**(1): 31-36.

Sedlakova, R., R. R. Shivers, et al. (1999). "Ultrastructure of the blood-brain barrier in the rabbit." *J Submicrosc Cytol Pathol* **31**(1): 149-161.

Seelig, A., X. L. Blatter, et al. (2000). "Substrate recognition by P-glycoprotein and the multidrug resistance-associated protein MRP1: a comparison." *Int J Clin Pharmacol Ther* **38**(3): 111-121.

Segal, M. B., J. E. Preston, et al. (1990). "Kinetics and Na independence of amino acid uptake by blood side of perfused sheep choroid plexus." *Am J Physiol* **258**(5 Pt 2): F1288-1294.

Seifert, G., K. Schilling, et al. (2006). "Astrocyte dysfunction in neurological disorders: a molecular perspective." *Nat Rev Neurosci* **7**(3): 194-206.

Sekine, T., S. H. Cha, et al. (1998). "Identification of multispecific organic anion transporter 2 expressed predominantly in the liver." *FEBS Lett* **429**(2): 179-182.

Selley, M. L. (2003). "Increased concentrations of homocysteine and asymmetric dimethylarginine and decreased concentrations of nitric oxide in the plasma of patients with Alzheimer's disease." *Neurobiol Aging* **24**(7): 903-907.

Selley, M. L. (2004). "Increased (E)-4-hydroxy-2-nonenal and asymmetric dimethylarginine concentrations and decreased nitric oxide concentrations in the plasma of patients with major depression." *J Affect Disord* **80**(2-3): 249-256.

Shaik, N., N. Giri, et al. (2009). "Investigation of the micellar effect of pluronic P85 on P-glycoprotein inhibition: cell accumulation and equilibrium dialysis studies." *J Pharm Sci* **98**(11): 4170-4190.

Shapiro, A. B. and V. Ling (1997). "Extraction of Hoechst 33342 from the cytoplasmic leaflet of the plasma membrane by P-glycoprotein." *Eur J Biochem* **250**(1): 122-129.

Silverman, J. A. (1999). "Multidrug-resistance transporters." *Pharm Biotechnol* **12**: 353-386.

Simarro, P. P., A. Diarra, et al. (2011). "The human African trypanosomiasis control and surveillance programme of the World Health Organization 2000-2009: the way forward." *PLoS Negl Trop Dis* **5**(2): e1007.

Simarro, P. P., J. Jannin, et al. (2008). "Eliminating human African trypanosomiasis: where do we stand and what comes next?" *PLoS Med* **5**(2): e55.

Simionescu, M., N. Ghinea, et al. (1988). "The cerebral microvasculature of the rat: structure and luminal surface properties during early development." *J Submicrosc Cytol Pathol* **20**(2): 243-261.

Simpson, I. A., N. M. Appel, et al. (1999). "Blood-brain barrier glucose transporter: effects of hypo- and hyperglycemia revisited." *J Neurochem* **72**(1): 238-247.

Slenzka, A., G. Unger, et al. (2011). "ABSTRACT: Removal of intracellular asymmetric dimethyl-L-arginine (ADMA) requires system y+L membrane transporter— despite significant activity of the metabolising enzyme dimethylarginine dimethylaminohydrolase (DDAH)." *Naunyn-Schmiedeberg´s Arch Pharmacol* **383**(Suppl 1): 1-112.

Sloan, J. L. and S. Mager (1999). "Cloning and functional expression of a human Na(+) and Cl(-)-dependent neutral and cationic amino acid transporter B(0+)." *J Biol Chem* **274**(34): 23740-23745.

Smith, Q. R., S. Momma, et al. (1987). "Kinetics of neutral amino acid transport across the blood-brain barrier." *J Neurochem* **49**(5): 1651-1658.

Smith, Q. R. and S. I. Rapoport (1986). "Cerebrovascular permeability coefficients to sodium, potassium, and chloride." *J Neurochem* **46**(6): 1732-1742.

Smith, Q. R. and J. Stoll (1998). Blood-brain barrier amino acid transport. *In*: Introduction to the blood-brain barrier. W. M. Pardridge. Cambridge, UK, Cambridge University Press**:** 188-197.

Smith, W. A., B. T. Schurter, et al. (2004). "Arginine methylation of RNA helicase a determines its subcellular localization." *J Biol Chem* **279**(22): 22795-22798.

Song, L., S. Ge, et al. (2007). "Caveolin-1 regulates expression of junction-associated proteins in brain microvascular endothelial cells." *Blood* **109**(4): 1515-1523.

Speake, T., C. Whitwell, et al. (2001). "Mechanisms of CSF secretion by the choroid plexus." *Microsc Res Tech* **52**(1): 49-59.

Sperandeo, M. P., G. Borsani, et al. (1998). "The gene encoding a cationic amino acid transporter (SLC7A4) maps to the region deleted in the velocardiofacial syndrome." *Genomics* **49**(2): 230-236.

Stamatovic, S. M., R. F. Keep, et al. (2009). "Caveolae-mediated internalization of occludin and claudin-5 during CCL2-induced tight junction remodeling in brain endothelial cells." *J Biol Chem* **284**(28): 19053-19066.

Steel, J. H. and J. Polak (1997). "Introduction to functional anatomy of the pituitary gland and alterations in disease." *Microsc Res Tech* **39**(2): 97.

Stevens, B. R., D. K. Kakuda, et al. (1996). "Induced nitric oxide synthesis is dependent on induced alternatively spliced CAT-2 encoding L-arginine transport in brain astrocytes." *J Biol Chem* **271**(39): 24017-24022.

Stoll, J., K. C. Wadhwani, et al. (1993). "Identification of the cationic amino acid transporter (System y+) of the rat blood-brain barrier." *J Neurochem* **60**(5): 1956-1959.

Stolnik, S., L. Illum, et al. (1995). "Long circulating microparticulate drug carriers." *Advanced Drug Delivery Reviews* **16**(2): 195-214.

Stratman, A. N., K. M. Malotte, et al. (2009). "Pericyte recruitment during vasculogenic tube assembly stimulates endothelial basement membrane matrix formation." *Blood* **114**(24): 5091-5101.

Strazielle, N. and J. F. Ghersi-Egea (2000). "Choroid plexus in the central nervous system: biology and physiopathology." *J Neuropathol Exp Neurol* **59**(7): 561-574.

Strazielle, N. and J. F. Ghersi-Egea (2005). "Factors affecting delivery of antiviral drugs to the brain." *Rev Med Virol* **15**(2): 105-133.

Strazielle, N., S. T. Khuth, et al. (2004). "Detoxification systems, passive and specific transport for drugs at the blood-CSF barrier in normal and pathological situations." *Adv Drug Deliv Rev* **56**(12): 1717-1740.

Strobel, J., M. Mieth, et al. (2012). "Interaction of the cardiovascular risk marker asymmetric dimethylarginine (ADMA) with the human cationic amino acid transporter 1 (CAT1)." *J Mol Cell Cardiol* **53**(3): 392-400.

Stuehr, D. J. (1997). "Structure-function aspects in the nitric oxide synthases." *Annu Rev Pharmacol Toxicol* **37**: 339-359.

Stuhlmiller, D. F. and K. M. Boje (1995). "Characterization of L-arginine and aminoguanidine uptake into isolated rat choroid plexus: differences in uptake mechanisms and inhibition by nitric oxide synthase inhibitors." *J Neurochem* **65**(1): 68-74.

Sturk, L. M., J. L. Brock, et al. (2004). "Distribution and quantitation of the anti-trypanosomal diamidine 2,5-bis(4-amidinophenyl)furan (DB75) and its N-methoxy prodrug DB289 in murine brain tissue." *Acta Trop* **91**(2): 131-143.

Sugiyama, D., H. Kusuhara, et al. (2003). "Involvement of multidrug resistance associated protein 1 (Mrp1) in the efflux transport of 17beta estradiol-D-17beta-glucuronide (E217betaG) across the blood-brain barrier." *Pharm Res* **20**(9): 1394-1400.

Sugiyama, D., H. Kusuhara, et al. (2001). "Characterization of the efflux transport of 17beta-estradiol-D-17beta-glucuronide from the brain across the blood-brain barrier." *J Pharmacol Exp Ther* **298**(1): 316-322.

Sugiyama, D., H. Kusuhara, et al. (2002). "Effect of 17 beta-estradiol-D-17 beta-glucuronide on the rat organic anion transporting polypeptide 2-mediated transport differs depending on substrates." *Drug Metab Dispos* **30**(2): 220-223.

Sun, H., D. R. Johnson, et al. (2001). "Transport of fluorescein in MDCKII-MRP1 transfected cells and mrp1-knockout mice." *Biochem Biophys Res Commun* **284**(4): 863-869.

Sun, T. and Y. Zhang (2008). "Pentamidine binds to tRNA through non-specific hydrophobic interactions and inhibits aminoacylation and translation." *Nucleic Acids Res* **36**(5): 1654-1664.

Surdacki, A., M. Nowicki, et al. (1999). "Reduced urinary excretion of nitric oxide metabolites and increased plasma levels of asymmetric dimethylarginine in men with essential hypertension." *J Cardiovasc Pharmacol* **33**(4): 652-658.

Suzuki, A., C. Ishiyama, et al. (2002). "aPKC kinase activity is required for the asymmetric differentiation of the premature junctional complex during epithelial cell polarization." *J Cell Sci* **115**(Pt 18): 3565-3573.

Sydow, K., E. Schwedhelm, et al. (2003). "ADMA and oxidative stress are responsible for endothelial dysfunction in hyperhomocyst(e)inemia: effects of L-arginine and B vitamins." *Cardiovasc Res* **57**(1): 244-252.

Tachikawa, M., M. Watanabe, et al. (2005). "Distinct spatio-temporal expression of ABCA and ABCG transporters in the developing and adult mouse brain." *J Neurochem* **95**(1): 294-304.

Taddei, A., C. Giampietro, et al. (2008). "Endothelial adherens junctions control tight junctions by VE-cadherin-mediated upregulation of claudin-5." *Nat Cell Biol* **10**(8): 923-934.

Takase-Yoden, S. and R. Watanabe (2001). "Distribution of ecotropic retrovirus receptor protein in rat brains detected by immunohistochemistry." *J Gen Virol* **82**(Pt 8): 1815-1820.

Takizawa, H., T. Gabra-Sanders, et al. (1986a). "Changes of frequency spectrum of the CSF pulse wave caused by supratentorial epidural brain compression." *J Neurol Neurosurg Psychiatry* **49**(12): 1367-1373.

Takizawa, H., T. Gabra-Sanders, et al. (1986b). "Spectral analysis of the CSF pulse wave at different locations in the craniospinal axis." *J Neurol Neurosurg Psychiatry* **49**(10): 1135-1141.

Tanaka, Y., G. Tang, et al. (2006). "Kv channels contribute to nitric oxide- and atrial natriuretic peptide-induced relaxation of a rat conduit artery." *J Pharmacol Exp Ther* **317**(1): 341-354.

Tang, Z., P. E. Scherer, et al. (1996). "Molecular cloning of caveolin-3, a novel member of the caveolin gene family expressed predominantly in muscle." *J Biol Chem* **271**(4): 2255-2261.

Teerlink, T., Z. Luo, et al. (2009). "Cellular ADMA: Regulation and action." *Pharmacol Res* **60**(6): 448-460.

Terpolilli, N. A., M. A. Moskowitz, et al. (2012). "Nitric oxide: considerations for the treatment of ischemic stroke." *J Cereb Blood Flow Metab* **32**(7): 1332-1346.

Tewes, B. J. and H. J. Galla (2001). "Lipid polarity in brain capillary endothelial cells." *Endothelium* **8**(3): 207-220.

Thakur, C. P., M. Kumar, et al. (1991). "Comparison of regimes of treatment of antimony-resistant kala-azar patients: a randomized study." *Am J Trop Med Hyg* **45**(4): 435-441.

Toda, N., K. Ayajiki, et al. (2009). "Cerebral blood flow regulation by nitric oxide: recent advances." *Pharmacol Rev* **61**(1): 62-97.

Tojo, A., W. J. Welch, et al. (1997). "Colocalization of demethylating enzymes and NOS and functional effects of methylarginines in rat kidney." *Kidney Int* **52**(6): 1593-1601.

Tomi, M., M. Mori, et al. (2005). "L-type amino acid transporter 1-mediated L-leucine transport at the inner blood-retinal barrier." *Invest Ophthalmol Vis Sci* **46**(7): 2522-2530.

Tran, C. T., M. F. Fox, et al. (2000). "Chromosomal localization, gene structure, and expression pattern of DDAH1: comparison with DDAH2 and implications for evolutionary origins." *Genomics* **68**(1): 101-105.

Triguero, D., J. Buciak, et al. (1990). "Capillary depletion method for quantification of blood-brain barrier transport of circulating peptides and plasma proteins." *J Neurochem* **54**(6): 1882-1888.

Tsai, P. S., J. P. Kaufhold, et al. (2009). "Correlations of neuronal and microvascular densities in murine cortex revealed by direct counting and colocalization of nuclei and vessels." *J Neurosci* **29**(46): 14553-14570.

Tsikas, D., R. H. Boger, et al. (2000). "Endogenous nitric oxide synthase inhibitors are responsible for the L-arginine paradox." *FEBS Lett* **478**(1-2): 1-3.

Tuomanen, E., H. Liu, et al. (1985). "The induction of meningeal inflammation by components of the pneumococcal cell wall." *J Infect Dis* **151**(5): 859-868.

Turner, C. M. (1997). "The rate of antigenic variation in fly-transmitted and syringe-passaged infections of Trypanosoma brucei." *FEMS Microbiol Lett* **153**(1): 227-231.

Uchida, Y., S. Ohtsuki, et al. (2011). "Quantitative targeted absolute proteomics of human blood-brain barrier transporters and receptors." *J Neurochem* **117**(2): 333-345.

Uhr, M., C. Namendorf, et al. (2004). "P-glycoprotein is a factor in the uptake of dextromethorphan, but not of melperone, into the mouse brain: evidence for an overlap in substrate specificity between P-gp and CYP2D6." *J Psychopharmacol* **18**(4): 509-515.

Umbarger, H. E. (1978). "Amino acid biosynthesis and its regulation." *Annu Rev Biochem* **47**: 532-606.

Usui, M., H. Matsuoka, et al. (1998). "Increased endogenous nitric oxide synthase inhibitor in patients with congestive heart failure." *Life Sci* **62**(26): 2425-2430.

Valkonen, V. P., H. Paiva, et al. (2001). "Risk of acute coronary events and serum concentration of asymmetrical dimethylarginine." *Lancet* **358**(9299): 2127-2128.

Vallance, P. and J. Leiper (2004). "Cardiovascular biology of the asymmetric dimethylarginine:dimethylarginine dimethylaminohydrolase pathway." *Arterioscler Thromb Vasc Biol* **24**(6): 1023-1030.

Vallance, P., A. Leone, et al. (1992a). "Accumulation of an endogenous inhibitor of nitric oxide synthesis in chronic renal failure." *Lancet* **339**(8793): 572-575.

Vallance, P., A. Leone, et al. (1992b). "Endogenous dimethylarginine as an inhibitor of nitric oxide synthesis." *J Cardiovasc Pharmacol* **20 Suppl 12**: S60-62.

Valle, J. W., A. Armstrong, et al. (2011). "A phase 2 study of SP1049C, doxorubicin in P-glycoprotein-targeting pluronics, in patients with advanced adenocarcinoma of the esophagus and gastroesophageal junction." *Invest New Drugs* **29**(5): 1029-1037.

Valverde, I., A. Penalva, et al. (2001). "Involvement of nitric oxide in the regulation of growth hormone secretion in dogs." *Neuroendocrinology* **74**(4): 213-219.

van Deurs, B. (1980). "Structural aspects of brain barriers, with special reference to the permeability of the cerebral endothelium and choroidal epithelium." *Int Rev Cytol* **65**: 117-191.

van Deurs, B., M. Moller, et al. (1978). "Uptake of horseradish peroxidase from CSF into the choroid plexus of the rat, with special reference to transepithelial transport." *Cell Tissue Res* **187**(2): 215-234.

van Hinsbergh, V. W. and G. P. van Nieuw Amerongen (2002). "Intracellular signalling involved in modulating human endothelial barrier function." *J Anat* **200**(6): 549-560.

Van Itallie, C. M. and J. M. Anderson (2004). "The role of claudins in determining paracellular charge selectivity." *Proc Am Thorac Soc* **1**(1): 38-41.

van Meer, G. and K. Simons (1986). "The function of tight junctions in maintaining differences in lipid composition between the apical and the basolateral cell surface domains of MDCK cells." *EMBO J* **5**(7): 1455-1464.

Van Winkle, L. J. and A. L. Campione (1990). "Functional changes in cation-preferring amino acid transport during development of preimplantation mouse conceptuses." *Biochim Biophys Acta* **1028**(2): 165-173.

Van Winkle, L. J., A. L. Campione, et al. (1990a). "Development of system B0,+ and a broad-scope Na(+)-dependent transporter of zwitterionic amino acids in preimplantation mouse conceptuses." *Biochim Biophys Acta* **1025**(2): 225-233.

Van Winkle, L. J., A. L. Campione, et al. (1990b). "Inhibition of transport system b0,+ in blastocysts by inorganic and organic cations yields insight into the structure of its amino acid receptor site." *Biochim Biophys Acta* **1025**(2): 215-224.

Van Winkle, L. J., H. N. Christensen, et al. (1985). "Na+-dependent transport of basic, zwitterionic, and bicyclic amino acids by a broad-scope system in mouse blastocysts." *J Biol Chem* **260**(22): 12118-12123.

VanWert, A. L., M. R. Gionfriddo, et al. (2010). "Organic anion transporters: discovery, pharmacology, regulation and roles in pathophysiology." *Biopharm Drug Dispos* **31**(1): 1-71.

Vekony, N., S. Wolf, et al. (2001). "Human cationic amino acid transporter hCAT-3 is preferentially expressed in peripheral tissues." *Biochemistry* **40**(41): 12387-12394.

Verrey, F. (2003). "System L: heteromeric exchangers of large, neutral amino acids involved in directional transport." *Pflugers Arch* **445**(5): 529-533.

Vestweber, D. (2008). "VE-cadherin: the major endothelial adhesion molecule controlling cellular junctions and blood vessel formation." *Arterioscler Thromb Vasc Biol* **28**(2): 223-232.

Vitalis, T., C. Fouquet, et al. (2002). "Developmental expression of monoamine oxidases A and B in the central and peripheral nervous systems of the mouse." *J Comp Neurol* **442**(4): 331-347.

Volk, B., U. Hettmannsperger, et al. (1991). "Mapping of phenytoin-inducible cytochrome P450 immunoreactivity in the mouse central nervous system." *Neuroscience* **42**(1): 215-235.

Vorbrodt, A. W. (1988). "Ultrastructural cytochemistry of blood-brain barrier endothelia." *Prog Histochem Cytochem* **18**(3): 1-99.

Vorobyov, I., V. M. Anisimov, et al. (2007). "Additive and classical drude polarizable force fields for linear and cyclic ethers." *J Chem Theory Comput* **3**(3): 1120-1133.

Voutsinos-Porche, B., G. Bonvento, et al. (2003). "Glial glutamate transporters mediate a functional metabolic crosstalk between neurons and astrocytes in the mouse developing cortex." *Neuron* **37**(2): 275-286.

Waalkes, T. P. and V. T. DeVita (1970). "The determination of pentamidine (4,4'-diamidinophenoxypentane) in plasma, urine, and tissues." *J Lab Clin Med* **75**(5): 871-878.

Wacher, V. J., C. Y. Wu, et al. (1995). "Overlapping substrate specificities and tissue distribution of cytochrome P450 3A and P-glycoprotein: implications for drug delivery and activity in cancer chemotherapy." *Mol Carcinog* **13**(3): 129-134.

Wagner, C. A., F. Lang, et al. (2001). "Function and structure of heterodimeric amino acid transporters." *Am J Physiol Cell Physiol* **281**(4): C1077-1093.

Waheed, A. A., K. S. Rao, et al. (2000). "Mechanism of dye binding in the protein assay using eosin dyes." *Anal Biochem* **287**(1): 73-79.

Walz, W. (2000). "Controversy surrounding the existence of discrete functional classes of astrocytes in adult gray matter." *Glia* **31**(2): 95-103.

Wanby, P., L. Brattstrom, et al. (2003). "Asymmetric dimethylarginine and total homocysteine in plasma after oral methionine loading." *Scand J Clin Lab Invest* **63**(5): 347-353.

Wanby, P., T. Teerlink, et al. (2006). "Asymmetric dimethylarginine (ADMA) as a risk marker for stroke and TIA in a Swedish population." *Atherosclerosis* **185**(2): 271-277.

Wang, D., S. Strandgaard, et al. (2008). "Asymmetric dimethylarginine and lipid peroxidation products in early autosomal dominant polycystic kidney disease." *Am J Kidney Dis* **51**(2): 184-191.

Wang, D., S. Strandgaard, et al. (2009). "Asymmetric dimethylarginine, oxidative stress, and vascular nitric oxide synthase in essential hypertension." *Am J Physiol Regul Integr Comp Physiol* **296**(2): R195-200.

Waskin, H., J. K. Stehr-Green, et al. (1988). "Risk factors for hypoglycemia associated with pentamidine therapy for Pneumocystis pneumonia." *JAMA* **260**(3): 345-347.

Watson, C. P. (2012). Interactions of Endogenous and Exogenous Molecules with the Human Blood–Brain Barrier. Institute of Pharmaceutical Science. London, UK, King's College London. **Ph.D. Thesis**.

Weidenfeller, C., C. N. Svendsen, et al. (2007). "Differentiating embryonic neural progenitor cells induce blood-brain barrier properties." *J Neurochem* **101**(2): 555-565.

Westholm, D. E., J. N. Rumbley, et al. (2008). "Organic anion-transporting polypeptides at the blood-brain and blood-cerebrospinal fluid barriers." *Curr Top Dev Biol* **80**: 135-170.

White, M. F. (1985). "The transport of cationic amino acids across the plasma membrane of mammalian cells." *Biochim Biophys Acta* **822**(3-4): 355-374.

White, R. P., P. Vallance, et al. (2000). "Effect of inhibition of nitric oxide synthase on dynamic cerebral autoregulation in humans." *Clin Sci (Lond)* **99**(6): 555-560.

WHO (2009) "Progress Report by the Secretariat: Control of human African trypanosomiasis."

WHO. (2010, 01-06-2010). "Human African trypanosomiasis: number of new cases drops to historically low level in 50 years." Retrieved 10-01-2013, 2013, from http://www.who.int/neglected_diseases/integrated_media/integrated_media_hat_june_2010/en/index.html.

Williams, S. A., T. J. Abbruscato, et al. (1996). "Passage of a delta-opioid receptor selective enkephalin, [D-penicillamine2,5] enkephalin, across the blood-brain and the blood-cerebrospinal fluid barriers." *J Neurochem* **66**(3): 1289-1299.

Williams, T. M. and M. P. Lisanti (2004). "The caveolin proteins." *Genome Biol* **5**(3): 214.

Wolburg, H., S. Mogk, et al. (2012). "Late stage infection in sleeping sickness." *PLoS One* **7**(3): e34304.

Wolburg, H., S. Noell, et al. (2009). "Agrin, aquaporin-4, and astrocyte polarity as an important feature of the blood-brain barrier." *Neuroscientist* **15**(2): 180-193.

Wolburg, H., K. Wolburg-Buchholz, et al. (2003). "Localization of claudin-3 in tight junctions of the blood-brain barrier is selectively lost during experimental autoimmune encephalomyelitis and human glioblastoma multiforme." *Acta Neuropathol* **105**(6): 586-592.

Wolburg, H., K. Wolburg-Buchholz, et al. (2001). "Claudin-1, claudin-2 and claudin-11 are present in tight junctions of choroid plexus epithelium of the mouse." *Neurosci Lett* **307**(2): 77-80.

Wolf, F. and F. Kirchhoff (2008). "Neuroscience. Imaging astrocyte activity." *Science* **320**(5883): 1597-1599.

Wolf, S., A. Janzen, et al. (2002). "Expression of solute carrier 7A4 (SLC7A4) in the plasma membrane is not sufficient to mediate amino acid transport activity." *Biochem J* **364**(Pt 3): 767-775.

Wolszczak, M. and J. Miller (2002). "Characterization of non-ionic surfactant aggregates by fluorometric techniques." *Journal of Photochemistry and Photobiology A: Chemistry* **147**(1): 45-54.

Wright, E. M. (1974). "Active transport of glycine across the frog arachnoid membrane." *Brain Res* **76**(2): 354-358.

Wright, E. M. (1978). "Transport processes in the formation of the cerebrospinal fluid." *Rev Physiol Biochem Pharmacol* **83**: 3-34.

Wright, P. M., G. J. Nogueira, et al. (1971). "Role of the pia mater in the transfer of substances in and out of the cerebrospinal fluid." *Exp Brain Res* **113**(3): 294-305.

Wu, A., Z. Ying, et al. (2007). "Omega-3 fatty acids supplementation restores mechanisms that maintain brain homeostasis in traumatic brain injury." *J Neurotrauma* **24**(10): 1587-1595.

Wu, F., B. Cholewa, et al. (2000). "Characterization of L-arginine transporters in rat renal inner medullary collecting duct." *Am J Physiol Regul Integr Comp Physiol* **278**(6): R1506-1512.

Wurtman, R. J. and J. Axelrod (1965). "The Pineal Gland." *Sci Am* **213**: 50-60.

Xu, L., B. Wang, et al. (2007). "NOx and ADMA changes with focal ischemia, amelioration with the chaperonin GroEL." *Neurosci Lett* **418**(2): 201-204.

Yeramian, A., L. Martin, et al. (2006). "Arginine transport via cationic amino acid transporter 2 plays a critical regulatory role in classical or alternative activation of macrophages." *J Immunol* **176**(10): 5918-5924.

Yokoyama, M. (1992). "Block copolymers as drug carriers." *Crit Rev Ther Drug Carrier Syst* **9**(3-4): 213-248.

Yoo, J. H. and S. C. Lee (2001). "Elevated levels of plasma homocyst(e)ine and asymmetric dimethylarginine in elderly patients with stroke." *Atherosclerosis* **158**(2): 425-430.

Yoshimoto, T., E. Yoshimoto, et al. (1992). "Enhanced gene expression of the murine ecotropic retroviral receptor and its human homolog in proliferating cells." *J Virol* **66**(7): 4377-4381.

Zani, B. G. and H. G. Bohlen (2005). "Transport of extracellular l-arginine via cationic amino acid transporter is required during in vivo endothelial nitric oxide production." *Am J Physiol Heart Circ Physiol* **289**(4): H1381-1390.

Zeuthen, T. and E. M. Wright (1981). "Epithelial potassium transport: tracer and electrophysiological studies in choroid plexus." *J Membr Biol* **60**(2): 105-128.

Zhang, H., Y. N. Song, et al. (2010). "Regulation and role of organic anion-transporting polypeptides (OATPs) in drug delivery at the choroid plexus." *J Clin Neurosci* **17**(6): 679-684.

Zheng, P. P., E. Romme, et al. (2010). "Glut1/SLC2A1 is crucial for the development of the blood-brain barrier in vivo." *Ann Neurol* **68**(6): 835-844.

Zheng, W. and Q. Zhao (2002). "Establishment and characterization of an immortalized Z310 choroidal epithelial cell line from murine choroid plexus." *Brain Res* **958**(2): 371-380.

Zhou, D. B. and E. Ipp (1989). "Pentamidine-induced beta cell toxicity is not preventable by high glucose." *Am J Med Sci* **298**(2): 89-92.

Zlokovic, B. V. (2005). "Neurovascular mechanisms of Alzheimer's neurodegeneration." *Trends Neurosci* **28**(4): 202-208.

Zlokovic, B. V., D. J. Begley, et al. (1986). "Measurement of solute transport across the blood-brain barrier in the perfused guinea pig brain: method and application to N-methyl-alpha-aminoisobutyric acid." *J Neurochem* **46**(5): 1444-1451.

Zoccali, C., S. Bode-Boger, et al. (2001). "Plasma concentration of asymmetrical dimethylarginine and mortality in patients with end-stage renal disease: a prospective study." *Lancet* **358**(9299): 2113-2117.

Appendices

Appendix 1 – Solutions

Modified Krebs-Henseleit Mammalian Ringer (artificial plasma, pH 7.4) solution contents:

Reagent	Mass (g)	Volume (mL)	Final concentration (mM)
NaCl	6.8375	-	117.0
KCl	0.3504	-	4.7
$MgSO_4.7H_2O$	6.7781	-	27.5
$NaHCO_3$	2.0834	-	24.8
KH_2PO_4	0.1633	-	1.2
Dextran (60,000 – 90,000)*	39.0000	-	-
$CaCl_{2(aq)}$ (1M)	-	2.5	2.5
dH_2O	-	997.5	-
Added on day of expt.			
Glucose	1.8016	-	10.0
Bovine Serum Albumin*	1.0000	-	-
Evan's Blue*	0.0551	-	57.3
Total		1000	

*= Removed to produce optimised plasma.

Artificial plasma (pH 7.4) was prepared to include clinical grade 60-90 kDa dextran (39 g/L) purchased from MP Biomedicals; CA, USA, NaCl (117.0 mM), KCl (4.7 mM), $NaHCO_3$ (24.8 mM), and KH_2PO_4 (1.2 mM) from BDH/VWR International; Leicestershire, UK, $CaCl_2$ (2.5 mM) (from a 1M stock solution, Sigma Aldrich; Dorset, UK), and $MgSO_4.7H_2O$ (27.5 mM, Sigma Aldrich; Dorset, UK).

Then, glucose (10 mM, purchased from BDH/VWR International; Leicestershire, UK), bovine serum albumin (BSA, 0.1% w/v, purchased from Sigma Aldrich; Dorset, UK) and Evan's Blue dye (57.4 µM) were added on the day of the experiment to ensure the solution remained free of bacterial and fungal growth. Glucose is included to maintain cerebral glucose metabolism and ATP production, BSA for maintenance of oncotic pressure, and to bind to Evan's Blue dye, and Evan's blue was added as a qualitative measure of BBB integrity. All reagents were freely soluble in water following gentle mechanical stirring.

Capillary depletion buffer contents (pH 7.4):

Reagent	Mass (g)	Volume (mL)	Final concentration (mM)
NaCl	8.2400	-	141.0
KCl	0.2982	-	4.0
$MgSO_4.7H_2O$	0.2465	-	1.0
HEPES	2.6030	-	10.9
$NaH_2PO_4.2H_2O$	0.1560	-	1.0
$CaCl_{2(aq)}$ (1M)	-	2.8	2.8
dH_2O		997.2	
Added on day of expt.			
Glucose	1.8016	-	10.0
Total		1000	

Artificial CSF contents (pH 7.4):

Reagent	Mass (g)	Volume (mL)	Final concentration (mM)
NaCl	0.0076	-	0.13
KCl	0.2237	-	3.00
$NaHO_3$	2.2178	-	26.4
$NaH_2PO_4.2H_2O$	0.0343	-	0.22
$MgCl_2$	0.3647	-	3.83
$CaCl_{2(aq)}$ (1M)	-	2.50	2.50
dH_2O		997.50	
Added on day of expt.			
Glucose	0.9855	-	5.47
Total		1000	

Appendix 2 – Calculating drug partition coefficient in micelles

Derivation of equation:

$$\alpha = \frac{[drug]_{micelle}}{[drug]_{total}} = \frac{I - I_0}{I_\infty - I_0} \quad [2.1]$$

Fluorescence intensity is proportional to the concentration of pentamidine (the emitting substance) and can be defined as follows:

$$I_0 = C_0 k_0 \quad [2.2]$$

Where I_0 is fluorescence intensity of pentamidine, C_0 is the concentration of pentamidine, and k_0 is the fluorescence proportionality constant, all in the absence of micelles (0 subscript).

For partition coefficient experiments the concentration of pentamidine was constant at 10 µM, and the concentration of Pluronic® P85 altered in samples. Since fluorescence intensity is typically additive (total fluorescence intensity is the summation of fluorescence emitted from pentamidine both inside and outside micelles), fluorescence intensity measured in these samples becomes:

$$I = (C_0 - C_{micelle})k_0 + C_{micelle}k_\infty \quad [2.3]$$

Where k_∞ is the proportionality constant when all drug present is inside micelles, and $C_{micelle}$ is the concentration of drug when all drug is present inside micelles.

Thus, equation [2.3] can be re-written as follows:

$$I = C_0 k_0 - C_{micelle}k_0 + C_{micelle}k_\infty \quad [2.4]$$

And then I_0 from equation [2.2] substituted for C_0k_0:

$$I = I_0 + C_{micelle}(k_\infty - k_0) \quad [2.5]$$

Subtracting I_0 from both sides:

$$I - I_0 = C_{micelle}(k_\infty - k_0) \quad [2.6]$$

Then, in the theoretical instance of pentamidine being 100% solubilised inside micelles:

$$I_\infty - I_0 = C_0(k_\infty - k_0) \qquad [2.7]$$

Thus, fluorescence intensity for a full range of samples containing varying concentrations of Pluronic® P85 (including 0% m/v) can be defined as follows:

$$\alpha = \frac{I - I_0}{I_\infty - I_0} = \frac{C_{micelle}\cancel{(k_\infty - k_0)}}{C_0\cancel{(k_\infty - k_0)}} = \frac{C_{micelle}}{C_0} = \frac{[drug]_{micelle}}{[drug]_{total}} \qquad [2.8]$$